ABSTRACT

MICROHYDRODYNAMIC, KINETIC AND THERMAL MODELING OF WET MEDIA MILLING FOR PROCESS OPTIMIZATION AND INTENSIFICATION

by
Gulenay Guner

Nanoparticle production by wet stirred media milling (WSMM) is a common method for the formulation of poorly water-soluble drugs. While most of the studies in the WSMM literature focus on the formulation aspects to overcome the stability challenges, a thorough mechanistic understanding of the process is lacking, and the process is slow, costly, and energy-intensive. This dissertation presents experimental and modeling work with the ultimate goals of (i) gaining a deeper and more mechanistic understanding of the WSMM process and breakage kinetics of the particles using a microhydrodynamic model with various improvements and advancements, (ii) examining the heat dissipation during the WSMM as a function of various process parameters, and (iii) optimizing and intensifying the WSMM using novel approaches such as bead mixtures of two different bead materials and mixtures of differently sized beads.

To achieve the aforementioned goals, an *n*th-order breakage kinetics model is formulated to provide the best representation of the experimental median particle size evolution with time upon the milling of drug suspensions. Microhydrodynamic parameters are used to predict the breakage rate constant via a subset selection method, where the predictions are improved when the packing limit of the beads is taken into account. The analysis of heat generation–transfer experimental results suggest a significant rise in temperature during the milling, and stirrer speed is the most influential parameter followed

by bead loading and bead size. An enthalpy balance model (EBM) is formulated to fit the experimental temperature profiles and determine the fraction of the mechanical power converted to heat, which is predicted using power law and machine learning approaches. As a low-fidelity alternative to the EBM, a semi-theoretical lumped-parameter model (LPM) is also formulated, which requires less experimental information though still provides a better estimation of temperature rise during WSMM as compared with the EBM. To improve the process, two novel process optimization approaches via bead mixtures are evaluated. When two bead materials, which are polystyrene and zirconia, are compared, polystyrene is found to be more efficient in terms of lower power consumption and heat generation, whereas zirconia beads are found to be better for fast breakage kinetics. Mixture of bead materials is introduced as a novel operational technique, to optimize the process from a holistic cycle time–power consumption–heat generation perspective. A decision tree for the composition of the bead mixture for various pharmaceutical application scenarios is developed. While the mixtures of polystyrene–zirconia beads help to reduce cycle time with acceptable temperature rise and power consumption, the mixtures of different bead sizes do not provide any significant benefit as compared with narrowly-sized individual beads. Overall, this dissertation addresses various process challenges of WSMM such as long cycle time and temperature rise, and formulates novel experimental solutions such as mixture of beads and predictive modeling techniques using various machine learning algorithms. Besides generating fundamental insights into the processing, the research hints at a new path to modeling the WSMM process via a combination of the microhydrodynamic model and population balance model augmented with machine learning approaches.

MICROHYDRODYNAMIC, KINETIC AND THERMAL MODELING OF WET MEDIA MILLING FOR PROCESS OPTIMIZATION AND INTENSIFICATION

by
Gulenay Guner

A Dissertation
Submitted to the Faculty of
New Jersey Institute of Technology
in Partial Fulfillment of the Requirements for the Degree of
Doctor of Philosophy in Chemical Engineering

Otto H. York Department of
Chemical and Materials Engineering

December 2022

APPROVAL PAGE

MICROHYDRODYNAMIC, KINETIC AND THERMAL MODELING OF WET MEDIA MILLING FOR PROCESS OPTIMIZATION AND INTENSIFICATION

Gulenay Guner

Dr. Ecevit A. Bilgili, Dissertation Advisor — Date
Professor of Chemical and Materials Engineering, NJIT

Dr. Lisa B. Axe, Dissertation Co-Advisor — Date
Professor and Chair of Chemical and Materials Engineering, NJIT

Dr. Piero Armenante, Committee Member — Date
Distinguished Professor of Chemical and Materials Engineering, NJIT

Dr. Murat Guvendiren, Committee Member — Date
Associate Professor of Chemical and Materials Engineering, NJIT

Dr. Kathleen McEnnis, Committee Member — Date
Assistant Professor of Chemical and Materials Engineering, NJIT

Dr. Helen F. Yao, Committee Member — Date
Investigator, GlaxoSmithKline, Collegeville, PA

BIOGRAPHICAL SKETCH

Author: Gulenay Guner

Degree: Doctor of Philosophy

Date: December 2022

Undergraduate and Graduate Education:

- Doctor of Philosophy in Chemical Engineering,
  New Jersey Institute of Technology, Newark, NJ, 2022

- Bachelor of Science in Chemical Engineering,
  Bogazici University, Istanbul, Turkiye, 2019

Major: Chemical Engineering

Presentations and Publications:

Journal Articles:

Guner, G.,Yilmaz, D., Yao, H., Clancy, D., & Bilgili, E. (2022). A semi-theoretical lumped-parameter model for predicting the temperature evolution during wet stirred media milling of drug suspensions. *Pharmaceutics*, (under preparation).

Guner, G., Elashri, S., Mehaj, M., Seetharaman, & Bilgili, E. (2022). Do mixtures of beads with different sizes improve wet stirred media milling of drug suspensions? *Advanced Powder Technology* (under preparation).

Guner, G., Seetharaman, N., Elashri, S., Mehaj, M., & Bilgili, E. (2022). Analysis of heat generation during the production of drug nanosuspensions in a wet stirred media mill. *International Journal of Pharmaceutics, 624*, 122020.

Guner, G., Yilmaz, D., Eskin, D., & Bilgili, E. (2022). Effects of bead packing limit concentration on microhydrodynamics-based prediction of breakage kinetics in wet stirred media milling. *Powder Technology*, 403, 117433.

Guner, G., Elashri, S., Mehaj, M., Seetharaman, N., Yao, H. F., Clancy, D. J., & Bilgili, E. (2022). An enthalpy-balance model for timewise evolution of temperature during wet stirred media milling of drug suspensions. *Pharmaceutical Research*, 1-18.

Guner, G., Kannan, M., Berrios, M., & Bilgili, E. (2021). Use of bead mixtures as a novel process optimization approach to nanomilling of drug suspensions. *Pharmaceutical Research*, 1-18.

Guner, G., Yilmaz, D., & Bilgili, E. (2021). Kinetic and microhydrodynamic modeling of fenofibrate nanosuspension production in a wet stirred media mill. *Pharmaceutics*, *13*(7), 1055.

Bilgili, E., & Guner, G. (2020). Mechanistic modeling of wet stirred media milling for production of drug nanosuspensions. *American Association of Pharmaceutical Scientists PharmSciTech*, *22*(1), 2.

Journal Articles Outside the Scope of This Dissertation:

Guner, G., Amjad, A., Berrios, M., Kannan, M., & Bilgili, E. (2022). Nanoseeded desupersaturation and dissolution tests for development of robust drug amorphous solid dispersions. *Pharmaceutics*, (under preparation).

Coelho, A., Schenck, L., Guner, G., Punia, A., & Bilgili, E. (2022). A combined isolation and formulation approach to convert nanomilled suspensions into high drug-loaded composite particles that readily reconstitute. *Powders*, *1*(2), 88-109.

Azad, M., Guner, G., Afolabi, A., Davé, R., & Bilgili, E. (2021). Impact of solvents during wet stirred media milling of cross-linked biopolymer suspensions. *Advanced Powder Technology*, *32*(12), 4562-4575.

Conference Proceedings:

Guner, G., Elashri, S., Mehaj, M., Seetharaman, N., Yao, H. F., Clancy, D. J., & Bilgili, E. An enthalpy-balance model for timewise evolution of temperature during wet stirred media milling of drug suspensions. *Presented at American Institute of Chemical Engineers Annual Meeting 2022.*

Guner, G., Seetharaman, N., Elashri, S., Mehaj, M., & Bilgili, E. Analysis of heat generation during the production of drug nanosuspensions in a wet stirred media mill. *Presented at American Institute of Chemical Engineers Annual Meeting 2022.*

Guner, G., Yilmaz, D., & Bilgili, E. A combined kinetic–microhydrodynamic analysis of the fenofibrate nanosuspension production in a wet stirred media mill. *Presented at American Institute of Chemical Engineers Annual Meeting 2021.*

Guner, G., Kannan, M., Berrios, M., & Bilgili, E. Use of bead mixtures as an enabling approach for optimal production of drug nanosuspensions. *Presented at American Institute of Chemical Engineers Annual Meeting 2021*.

Guner, G., Kannan, M., Berrios, M., Parker, N., & Bilgili, E. A novel intensification strategy for wet media milling of drug suspensions: bead mixtures. *Presented at the 1st International Electronic Conference on Pharmaceutics 2020.*

Ve sen, ben değirmenlere karşı ♪♫

I took this picture during my trip to Amsterdam, while I was listening to my favorite song, looking at this beautiful sunset and wind mill, full of hopes and dreams. Here I am, writing my Ph.D. dissertation about mills, proud of my achievements and self-growth all thanks to the endless support of my caring parents, the greatest sister on the earth, and my better half.

ACKNOWLEDGMENTS

I would like to express my sincere gratitude to my dissertation advisor, Dr. Ecevit A. Bilgili, who is knowledgeable, perfectionist, considerate, and always supportive. He pushes and guides me to reach my personal best. At the same time, he is always there supporting me, defending me, encouraging me, and spending time with me throughout my Ph.D. program. He is not only an advisor in my research, but also the one doing everything in his power to guide me towards a successful future career. I am truly blessed to have him as my dissertation advisor. I thank my co-advisor Dr. Lisa Axe who encouraged me when I was having self-doubts. She is a great role-model as a strong female professor and program chairperson.

I would like to express my appreciation to all my Ph.D. dissertation committee members. Special thanks to Dr. Murat Guvendiren for the collaboration opportunity. I would like to extend my thanks to other committee members, Dr. Piero Armenante, Dr. Kathleen McEnnis, and Dr. Helen F. Yao, whose guidance, constructive feedback, and suggestions significantly helped me to reach excellence in research.

I am grateful for financial support from GlaxoSmithKline in part through the G2718B0 award. I would like to thank Mr. Donald Clancy and Dr. Helen Yao for their guidance throughout the project.

I would like to recognize all the co-workers for their direct involvement in my research, either spiritually or physically: Dr. Eylul Cetindag, Dr. Guluzar Buyukgoz, Dr. Kuriakose Kunnath, Nontawat Muanpaopong, Sangah Kim, Zhixing Lin, Nathaniel Parker, Ayesha Amjad, Keanu Radgman, Christian Mangohig, Manisha Kannan, Matthew

Berrios, Sherif Elashri, Natasha Seetharman, and Mirsad Mehaj. I am especially grateful to Dr. Mahbubur Rahman for helping me develop the skills necessary to succeed in my research.

I would like to thank all my friends who were by my sides during my sorrows and joys, my ups and downs. I am fortunate enough to have such wonderful friends, special thanks to my dear friends in the department Alperen Abaci and Elif Irem Senyurt for our tea hours. Thanks to Dr. Pelin Ayranci, Uras Varolgunes, and Gokhan Yilmaz, for always giving each other motivation necessary to survive the graduate school together. Thanks to my oldest friend since the elementary school, Inci Ilgin, for always being there for me.

Finally, I would like to express my deepest gratitude to my family. To my mother Aysen, my father, Hasbi, and my sister Hilal for their endless love and support at every stage of my life, and my husband and lifelong best friend since college, Dogacan, I would not have been able to accomplish what I have without you, and I promise to continue to make you proud!

TABLE OF CONTENTS

Chapter **Page**

TABLE OF CONTENTS
(Continued)

Chapter **Page**

TABLE OF CONTENTS
(Continued)

Chapter **Page**

TABLE OF CONTENTS
(Continued)

Chapter **Page**

TABLE OF CONTENTS
(Continued)

Chapter **Page**

TABLE OF CONTENTS
(Continued)

Chapter **Page**

TABLE OF CONTENTS
(Continued)

Chapter **Page**

LIST OF TABLES

Table **Page**

LIST OF TABLES
(Continued)

Table **Page**

LIST OF TABLES
(Continued)

Table **Page**

LIST OF TABLES
(Continued)

Table **Page**

LIST OF FIGURES

Figures **Page**

LIST OF FIGURES
(Continued)

Figure **Page**

LIST OF FIGURES
(Continued)

Figure **Page**

LIST OF FIGURES
(Continued)

Figure **Page**

LIST OF FIGURES
(Continued)

Figure **Page**

LIST OF FIGURES
(Continued)

Figure **Page**

LIST OF FIGURES
(Continued)

Figure **Page**

LIST OF FIGURES
(Continued)

Figure **Page**

LIST OF FIGURES
(Continued)

Figure **Page**

LIST OF FIGURES
(Continued)

Figure **Page**

LIST OF FIGURES
(Continued)

Figure **Page**

LIST OF SYMBOLS

Nomenclature

a	average frequency of drug particle compressions, Hz
c	bead loading or fractional volumetric concentration of the beads, –
d	particle diameter (size), m
e	restitution coefficient, –
F_b^n	average max. normal force during collision of two identical elastic beads, N
g_0	radial distribution function at contact, –
K	coefficient obtained from an empirical correlation, –
p	probability for a single drug particle to be caught between the beads, –
P_w	average stirrer power per unit volume, W/m^3
R	radius, m
R_{diss}	dissipation coefficient of the bead, –
R_{diss0}	dissipation coefficient when relative motion of the bead–liquid is absent, –
t	milling time, s
u_b	average bead oscillation velocity, m/s
V_m	volume of the milling chamber, m^3
Y	Young modulus, Pa
Y^*	reduced elastic modulus for the bead–drug contact, Pa

Greek letters

α_b	radius of the contact circle formed at the contact of two beads, m

ε_{coll}	energy dissipation rate due to partially inelastic bead–bead collisions, W/m^3
ε_{ht}	power spent on shear of equivalent liquid of the slurry at the same shear rate but calculated (measured) as if no beads were present in the flow, W/m^3
ε_{m}	non-dimensional bead–bead gap thickness at which the lubrication force stops increasing and becomes a constant, –
ε_{tot}	total energy dissipation rate, W/m^3
ε_{visc}	energy dissipation rate due to both the liquid–beads viscous friction and lubrication, W/m^3
η	Poisson's ratio, –
ϑ	granular temperature, m^2/s^2
μ_L	apparent shear viscosity, Pa·s
ν	frequency of single-bead oscillations, Hz
Π	energy dissipation rate attributed to the deformation of drug particles per unit volume, W/m^3
$\Pi\sigma_y$	pseudo energy dissipation rate, J^2/m^{6}s
ρ	density, kg/m^3
σ_b^{max}	maximum bead contact pressure at the center of the contact circle, Pa
σ_y	contact pressure in drug particle when the fully plastic condition is obtained, Pa
ω	stirrer (rotational) speed, rpm
ψ	volumetric fraction of drug particles in the drug suspension, –

Indices

b	bead
L	equivalent liquid (milled drug suspension)
p	drug particle
50	median (50% passing) particle size

CHAPTER 1

INTRODUCTION

1.1 Motivation for Bioavailability Enhancement of Drugs

Formulation and delivery of Active Pharmaceutical Ingredients (APIs) in the form of efficacious, stable pharmaceutical dosages is an important objective in the drug development cycle. Improving the bioavailability, stability, and convenience of solid dosages to patients are important considerations in formulation development [1]. Bioavailability means the rate and extent to which the active substance or therapeutic moiety is absorbed from a pharmaceutical form and becomes available at the site of action [2]. According to the Biopharmaceutics Classification System (BCS), only 65% of the oral WHO essential drugs met the high solubility criterion, which requires the drug to be soluble in pH 1–7 of 250 ml aqueous fluid [2, 3]. About 30–40% of the considered set of established drugs have to be regarded as practically insoluble in water (<0.1 mg/mL according to the USP (United States Pharmacopeia) definition) [4]. While the fraction of "practically insoluble" drugs is 70% in the pharmaceutical compounds in development [5], the fraction of BCS class II and IV drugs among new molecular entities has been estimated to be as high as 90% [6]. The trend toward the identification of more lipophilic and/or larger new molecular compounds by modern drug discovery methods is generally accompanied by a decrease in aqueous solubility [7]. Challenges related to poor aqueous solubility may occur already early in the drug development process and, consequently, there are increasing efforts to link the drug discovery and development process with early formulation strategies [8].

The techniques to overcome poor solubility entails either chemical or physical modifications for which some aspects were mentioned in the following table [9].

Table 1.1 Commonly Used Techniques in Bioavailability Enhancement of Poorly Soluble Drugs

Chemical Modifications	Salt Formation	The most common method for increasing the solubility and dissolution rate of acidic and basic drugs
	Co-crystallization	Crystalline material consists of two or more molecular (& electrical neutral) species held together by non-covalent forces. Important as an alternative to salt formation for neutral drugs
	Co-solvency	Solvent used to increase solubility known as co-solvent. It is also commonly referred to as solvent blending.
	Hydrotropic	It improves solubility by complexation involving weak interaction between hydrophobic agents (e.g., sodium alginate, urea) & solute.
	Solubilizing agent	The solubility of poorly soluble drugs can also be improved by various solubilizing materials. Ex. PEG 400 is improving the solubility of hydrochlorothiazide
	Nanotechnology	For many new chemical entities of very low solubility, micronization is not sufficient because the micronized product has a very low effective surface area for dissolution and the next step taken was nanonization.
Physical Modifications	Particle size reduction	This can be done mainly by micronization & nanonization. As particle size decreases, surface area of particle increases resulting in increase in dissolution rate. Nanonization has overlap with "Nanotechnology".
	Modification of the crystal habit	Different polymorphs of drugs are chemically identical, but they exhibit different physicochemical properties including solubility, melting point, density, texture, stability. (Solubility ranking: Amorphous >Metastable polymorph >Stable polymorph)
	Complexation	Complexation is the association between two or more molecules to form a non-bonded entity with a well-defined stoichiometry which relies on relatively weak forces such as London forces, hydrogen bonding and hydrophobic interactions
	Solubilization by surfactants	The presence of surfactants may lower the surface tension but increases solubility of drug within an organic solvent.
	Drug dispersions in carriers	The dispersion of one or more active ingredients in an inert carrier in a solid-state, frequently prepared by the melting method, solvent method, or fusion solvent method. Usually, the drug is kept amorphous (ASDs).

Among these approaches, particle size reduction (wet stirred media milling, a.k.a., nanonization or nanomilling) [10] and amorphous solid dispersions (ASDs) [2] have been the most widely used and become platform approaches. Amorphous drugs lack distinct intermolecular arrangement of a crystalline structure. They exhibit lower thermodynamic stability and higher apparent solubility than their crystalline counterparts [11]. While amorphous drugs have higher solubility and dissolution rates, they are generally less stable physically and chemically than their corresponding crystal forms [12-14]. ASDs can generate significant supersaturation during *in vitro* and *in vivo* dissolution even for drugs with extremely low solubility, thus enhancing the dissolution rate [11]. On the other hand, nanomilling could lead to the formation of drug nanocrystals that have a large surface area, and such a large surface area has been shown to increase the dissolution rate and enhance bioavailability [15]. In the prevalent pharmaceutical nanotechnology literature, particles with sizes ~10 nm up to 1000 nm [16], including the colloids domain, have been broadly regarded as nanoparticles, while in most practical pharmaceutical applications nanoparticles refer to 50–300 nm particles [10, 17]. Due to their relatively stable nature in the solid-state, drug nanocrystals in dry form are advantageous to ASD-based dosages from a storage stability perspective. Besides higher dissolution rates leading to improved bioavailability, other advantages of drug nanoparticles include the elimination of food effects, safe dose escalation, and enhanced efficacy and tolerability profiles [18]. Moreover, drug nanoparticles in suspension form have been used for a multitude of delivery routes: oral, parenteral, inhalation, dermal, etc. Despite these advantages, obviously, drug nanocrystals cannot be effective if the bioavailability is limited by the extremely low solubility of the drug (thermodynamic limit).

In view of the above pros/cons and considering the widespread use and significance of drug nanoparticles, this dissertation mainly focuses on the formation of drug nanoparticles via wet stirred media milling (WSMM) process. In Section 1.2, before delving into a review of the WSMM process in Section 1.3, a quick review of drug nanoparticle production is presented. Section 1.4 will present a summary of the approaches that have been used to model the WSMM process and give the details of the microhydrodynamic model used in this dissertation. Section 1.5 presents the knowledge gaps and research needs for WSMM that are addressed in this dissertation and Section 1.6 presents the objectives.

1.2 Preparation of Drug Nanoparticles and Their Suspensions

Nanoparticles, which can be prepared in the form of nanosuspensions, have been demonstrated to improve the dissolution rate for many drugs since they have a larger specific surface area and higher overall solute transfer coefficient compared with their micro-sized counterparts [10]. If their particle size is decreased further, especially less than ~100 nm, the apparent solubility becomes higher according to the Ostwald-Freundlich theory [16]. Overall, all these features exhibited by nanoparticles improve the dissolution rate according to the Noyes–Whiney equation, where m is the mass dissolved, A is the surface area, D is diffusion coefficient of the drug, h is the diffusion layer thickness, C_s is saturation solubility and C is the concentration of the solution at time t [19]; the increase in dissolution rate, in turn, enhances the bioavailability of drugs [20].

$$\left(\frac{dm}{dt}\right) = \frac{AD(C_s - C)}{h} \tag{1.1}$$

Drug nanosuspensions can be prepared by top-down, bottom-up, or combinative methods. Top-down methods such as high-pressure homogenization (HPH) [16], wet stirred media milling [21, 22], and ball milling [23] involve high shear–impact forces to achieve size reduction of as-received drug crystals down to micro or nanometer scale. Bottom-up methods involve building up particles by precipitation of dissolved molecules via liquid anti-solvent precipitation (LASP) [24] and precipitation by supercritical fluids [25, 26]. Melt emulsification is another example of a bottom-up technique that can be used for drugs with low melting points [27, 28]. Combinative methods include a combination of bottom-up and top-down approaches [29]. Among various methods used for the production of drug nanoparticles, wet stirred media milling (WSMM) has found the most common use in the pharmaceutical industry owing to its unique advantages: WSMM is organic solvent-free, scalable, and environmentally benign [10]. Moreover, WSMM allows producing nanosuspensions with high drug loading, which exhibits low excipient side effects. Also, it has continuous processing capability and can be applied universally to any poorly water-soluble drug. Nanosuspensions also have the advantage of higher mass packing (higher dose) per injection volume and improved physical stability owing to the use of stabilizers such as polymers and/or surfactants [16, 30].

1.3 Wet Stirred Media Milling (WSMM) Process

A schematic of the WSMM process operating in the recirculation mode is illustrated in **Figure 1.1.** Inside a holding tank, a pre-suspension of the drug at 2–30% w/w loading [31] is typically prepared by adding drug powder to an aqueous solution of stabilizers such as polymers, surfactants, etc. The homogeneous pre-suspension is circulated through the milling chamber and back to the holding tank using peristaltic or other positive-

displacement pumps for accurate feeding. To minimize media contamination, the milling chamber is lined with hard, wear-resistant ceramics or stainless steel and pre-loaded typically with 50–90% *v/v* of the chamber wear-resistant media (beads) such as yttrium-stabilized zirconia (YSZ) or cross-linked polystyrene (CPS). Silica, steel, iron, and alumina balls have also been used for non-pharmaceutical applications [10, 17, 32]. Typical bead sizes range from 100 µm to 3000 µm; however, both larger and smaller beads have also been used for some specific applications or modeling purposes [33]. A screen with a nominal opening size that is about half the size of beads is located at the outlet of the milling chamber. The screen retains the beads while allowing the passage of the drug suspension. A stirrer (rotor), with mixing elements emanating from the stirrer body (**Figure 1.2**), stirs the slurry of beads and drug suspension in the chamber, causing turbulent flow and fluctuating motion of the beads [34]. As the suspension passes through the milling chamber, drug particles are captured, compressed, and broken by the beads. The rotational speed of the stirrer is scale-dependent, while the tip speeds range from 4–20 m/s [10]. Both the milling chamber and the holding tank are equipped with a chiller unit, which keeps the suspension temperature in the holding tank and the milling chamber under control.

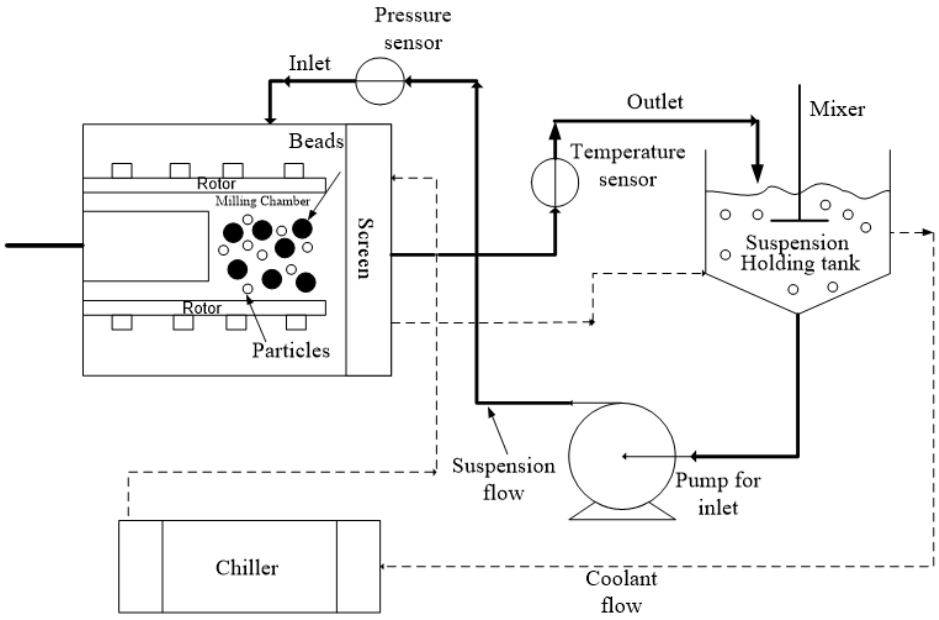

Figure 1.1 Schematic of a wet stirred media mill in recirculation mode of operation.

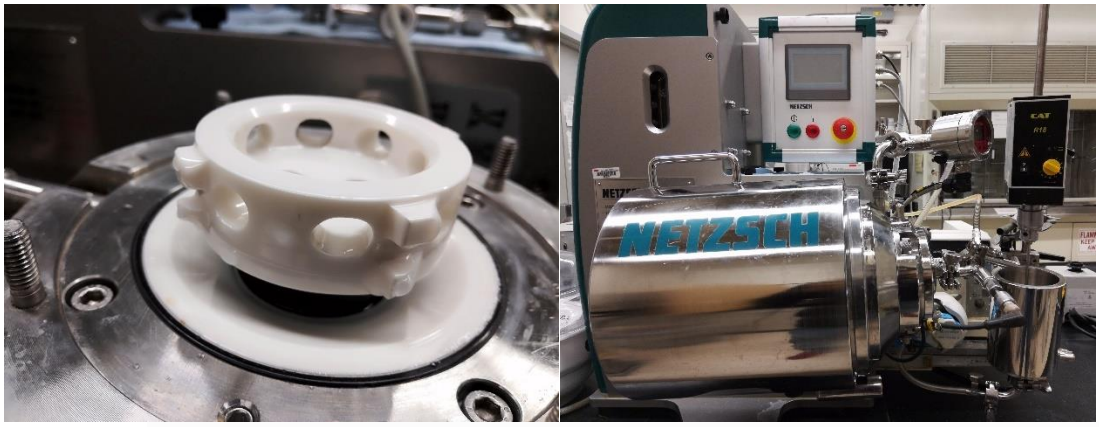

Figure 1.2 A ceramic (YSZ) stirrer with mixing elements at the periphery (left) inside a Netzsch Microcer horizontal wet stirred media mill used in the experimental work (right).

A schematic of possible particle change mechanisms occurring during the wet media milling of drugs is shown in **Figure 1.3**. [10]. Particle size during milling generally depends on (i) process–equipment parameters; (ii) mechanical and physicochemical properties of drug particles; and (iii) physical stability of the milled suspension, i.e., mitigation of aggregation and/or Ostwald ripening in the presence of various stabilizers [35, 36]. Preparation of a drug nanosuspension with desired particle size and adequate

storage stability entails selecting a proper stabilizer formulation and effective process–equipment parameters for the WSMM. The selection of optimal stabilizer formulation is a laborious and resource-demanding task, yet an important one with potentially serious consequences. A poorly formulated drug nanosuspension may undergo aggregation, Ostwald ripening, fast sedimentation of particles, and cake formation during milling/storage, which will lead to various issues in downstream processing of the respective suspensions and poor product performance from the final dosages such as unexpectedly slow dissolution (see [10] and references cited in there). Obviously, potential particle size increase/growth during milling and storage can lead to loss of high surface area associated with the drug nanoparticles, which reduces the significant benefits intended from the nanomilling process.

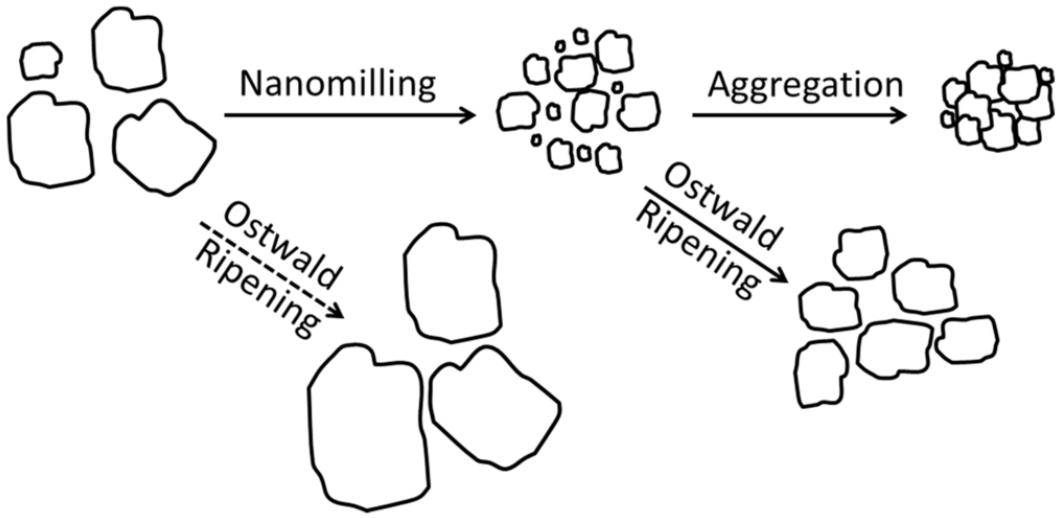

Figure 1.3 Schematic of particle change mechanisms during the WSMM process.

1.3.1 Formulation aspects

As mentioned before, WSMM is the most popular production method for nanosuspension production, however, it suffers from some challenges. A major issue is the aggregation–growth tendency of the milled drug particles in the aqueous suspensions during milling or

storage which results in loss of surface area [10]. In the milling process, two mechanisms happen conversely. While the breakage of the particle continues depending on the mechanical stress that the milling applies, aggregation takes place due to the highly attractive interparticle forces such as van der Waals and hydrophobic forces [37]. On the other hand, the drug particles in the suspension may grow due to a process called Ostwald ripening in which dissolved drug molecules from smaller drug particles are transported into larger particles as a function of increasing solubility [38]. Therefore, the physical stability of the drug nanosuspensions by various stabilizers [39, 40], also known as dispersants, is required during milling and storage for proper downstream processing and adequate shelf-life.

The physicochemical properties of drugs such as surface energy, solubility, molecular weight, type and number of the functional groups, crystal structure, mechanical and thermal properties may have an impact on the particle size distribution of the nanosuspension [39, 41, 42]. A rational criterion for the selection of excipient and process conditions according to the drug properties is not established yet, but some empirical studies find a correlation between the quality attributes of nanosuspensions and fusion enthalpy [43], surface energy [44], and molecular weight [45] of the drugs. To ensure a stable drug nanosuspension, both the type of the stabilizer and the drug-to-stabilizer mass ratio should be selected judiciously so that the stabilizer adsorbs on drug particles and its concentration is high enough to prevent aggregation and low enough not to cause Ostwald ripening [46, 47]. Depending on the type of excipient, stabilization can be provided via steric, electrosteric, or a combination of both mechanisms via the adsorption of polymers and/or surfactants on drug particle surfaces [47-50]. Nonionic polymers or nonionic

surfactants (e.g., poloxamers, cellulosic derivatives, polysorbates, and povidones, etc.) usually provide steric stability by preventing the particles from getting into the range of attractive van der Waals forces. However, a high concentration of nonionic polymer is needed to obtain a stable system which is not favorable since it lowers the drug loading if the suspension is intended for a solid dosage form. Electrostatic stabilization is usually imparted by ionic surfactants, e.g., sodium dodecyl sulfate (SDS), dioctyl sulfosuccinate sodium salt (DOSS), and benzethonium chloride (BKC). In electrosteric stabilization, nonionic polymers or surfactants along with ionic surfactants stabilize the particles, acting simultaneously. However, despite their effectiveness as dispersants, usage of surfactants should be minimized as they could pose several challenges upon usage above their critical micelle concentration (CMC) such as particle growth via Ostwald ripening due to micellar solubilization during milling/storage [46, 51-53].

In addition to polymers and surfactants, colloidal superdisintegrants such as sodium starch glycolate (SSG) and croscarmellose sodium (CCS) were shown to provide enhanced kinetic and electrostatic stability in the presence of an adsorbing polymer [54-57]. For example, a study was conducted to investigate the efficiency of three methods of fenofibrate (FNB: drug) suspension stabilization, i.e., usage of high concentrations of hydroxypropyl methylcellulose (HPMC) polymer, the combination of HPMC with SDS surfactant, and combination of HPMC with a superdisintegrant [54]. As can be seen in **Figure 1.4**, while the usage of 2% HPMC was not sufficient to prevent FNB nanoparticle aggregation, the 2% HPMC–0.075% SDS combination effectively suppressed aggregation leading to much finer sizes because electrosteric stabilization was attained due to the usage of adsorbing neutral polymer (HPMC) and the anionic surfactant (SDS). Similarly, the

colloidal superdisintegrants, SSG or CCS (wet-milled during the milling of FNB) along with HPMC resulted in a stable suspension, and the stabilization provided by superdisintegrant depends on their swelling capacity. As the superdisintegrant particles absorbed water, the actual concentration of the polymer in the suspension increased. At higher polymer concentrations, the extent of adsorption of the polymer onto the drug particles appeared to increase, which in turn enhanced steric stabilization [54]. The kinetic stabilization effect could also get more pronounced as the viscosity of the suspension became higher and the mobility of the drug particles decreased when the superdisintegrant was present.

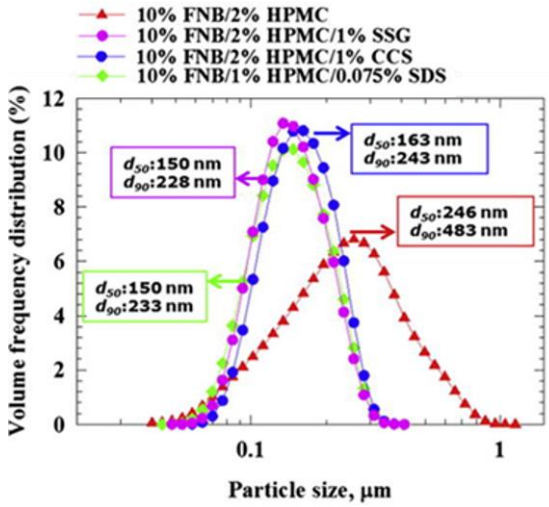

Figure 1.4 Volumetric frequency distribution of milled FNB nanosuspension with different formulations.
Source: [54]

Overall, the review of existing literature and analysis of the comprehensive review papers [10, 17] reveals that while aggregation and Ostwald ripening have a negative impact on the physical stability of drug nanosuspensions prepared by WSMM, the judicious use of stabilizer(s) and their combinations [47] as well development of novel classes of stabilizers [54, 58] such as the colloidal superdisintegrants appears to have largely

mitigated such formulation challenges. Hence, this dissertation will mainly focus on process-related challenges associated with WSMM.

1.3.2 Processing aspects and current challenges

Interestingly, while hundreds of studies generating voluminous experimental data on the formulation, stabilization, and drying of nanosuspensions exist in the pharmaceutical nanotechnology literature (see e.g., refs. [10, 18, 31, 34, 59] and the references cited therein), relatively scarce and somewhat scattered information is available on the process development–optimization of pharmaceutical WSMM [17, 57, 60]. Several challenges, technical barriers, and knowledge gaps regarding processing–operational aspects of WSMM include (bolded items are in the scope of this dissertation):

(i) the process is expensive due to its energy–intensive and inefficient nature [61];

(ii) it is relatively slow with processing times from an hour(s) to a day(s) depending on process conditions, batch size, and equipment scale [31, 57];

(iii) our understanding of the impact of stabilizers on the milling process beyond stabilization is inadequate [62];

(iv) the product (drug nanosuspension) is contaminated due to media wear, which must be minimized and controlled [10, 63, 64];

(v) the process scale-up is rather empirical (see e.g., [65]), lacking a first-principle mechanistic approach;

(vi) high heat dissipation and temperature rise during milling that may jeopardize the physicochemical stability of the drug suspensions, which necessitates a process shutdown;

(vii) Blockage of mill screen with coarse particles especially at high suspension flow rates

Solving the aforementioned processing issues entails a mechanistic understanding of the impact of process variables such as the stirrer speed, the type and size of the beads, the beads loading, the suspension flow rate, and the drug loading on the breakage kinetics,

specific energy consumption, media wear, and milling time required for the desired product fineness [57, 66].

The stirrer speed in WSMM or circumference speed in planetary ball mills plays an important role in determining the final particle size of the nanosuspensions [57]. Stirrer speeds of 2.65–14.7 m/s and circumference speeds of 150–6000 rpm have been reported [10]. The apparent breakage rate increased with an increase in the stirrer speed [57]. On the other hand, the volumetric bead loading greatly varied in the literature from 17% to 94% of the milling chamber volume. The percentage is generally expressed in terms of apparent bead volume relative to the true milling chamber volume. Afolabi et al. [57] demonstrated that a larger volume fraction of the beads resulted in faster breakage of griseofulvin particles. In terms of the impact of drug loading, Afolabi et al. [57] found that an increase in griseofulvin concentration from 5% to 30% *w*/*v* led to a sharp decrease in the milling intensity factor and consequently slower breakage. Literature review showed that the milling media (beads) made up of zirconia, alumina, or cross-linked polystyrene with various sizes have been used in wet media milling [10]. Bitterlich et al. [38] reported that the milling performance was influenced by the choice of bead material and shape. Comparing zirconia and alumina beads of the same size, they concluded that zirconia beads transferred more energy per collision due to their higher density, therefore inducing faster breakage to drug particles during milling. In addition, the milling process with spherical alumina beads was more efficient than the process with irregularly shaped alumina beads [38]. Other studies concerning the impact of process parameters will be considered in Section 1.4 within the context of modeling studies.

1.4 Mechanistic Modeling of Wet Stirred Media Milling

As mentioned in the previous sections, the formulation aspect of nanosuspensions has been addressed to a large extent and there are several formulation solutions to physical stability problems. On the other hand, process challenges (i)–(vii) mentioned in Section 1.3 have not been thoroughly investigated, which requires a mechanistic understanding of the process and well-designed process studies dedicated to the specific challenges. Of course, such an understanding cannot be gained by mere experimentation. In our recent literature review, it has been noted that there are only a few studies that made use of mechanistic models for analyzing WSMM in the pharmaceutical industry [32]. Most of the pharmaceutical WSMM studies (70%, 21 out of $N_p = 30$) used statistically-based models: empirical regression fit, response surface methodology (RSM), etc. [65, 67-86] instead of the mechanistic models (30%). Surprisingly, our literature search on *pharmaceutical WSMM* found only one study (3.3% of $N_p = 30$) with the population balance model (PBM) alone [87] and no studies with the computational fluid dynamics (CFD), discrete element method (DEM), or any coupled methods. Two studies (6.7%) with the stress intensity-number model (SI–SN model) [64, 88] and 6 studies (20%) with the microhydrodynamic model (MHD model) [33, 57, 62, 63, 89, 90] were found, where MHD turn out to be the most used mechanistic models.

Among the non-pharmaceutical WSMM studies (based on $N_{np} = 41$), there are 8 studies (19.5%) with the PBM alone [91-98], 4 studies (9.8%) with the CFD alone [99-102], 9 studies (24.4%) with the DEM alone [103-111], 13 studies (31.7%) with the coupled methods (CFD–DEM, CFD–PBM, etc.) [112-124], 13 studies (31.7%) with the SI–SN model [98, 111, 121-131], and only one study (2.4%) comparing the SI–SN model with the MHD model [127].

The statistically-based models correlated the drug particle size/specific surface area and/or predicted them based on process parameters such as milling time [65, 67-80, 86], stirrer speed [69, 71-73, 76, 77, 80-84], bead loading [74-76, 81, 82, 85, 86], bead size [80, 81, 83] or pump speed [77]. Some studies also correlated polydispersity index [74, 76, 77, 79, 80, 86], zeta potential [69, 71-74, 76, 77, 79, 80, 86], and saturation solubility [68, 73, 86] to the process parameters.

1.4.1 Comparison of the capabilities of the different modeling approaches

None of the models could simulate all aspects of the WSMM process. Each modeling approach is typically good at analyzing a certain aspect of the process, and has various pros/cons. **Table 1.2** presents the modeling approaches and respective pros/cons.

Table 1.2 Modeling Approaches Used for Simulating the WSMM Process and Their Pros/Cons

Model Type*	Pros/Cons
Eulerian-Eulerian (EE) CFD	Pros: provides the spatiotemporal variation of all flow variables
	Cons: does not consider individual beads, or stresses developed by bead–bead collisions; no microhydrodynamic information except granular temperature; does not simulate particle breakage; requires weeks of computation time
Eulerian-Lagrangian (CFD–DEM)	Pros: provides the spatiotemporal variation of all flow variables and the bead–bead collisions information with full microhydrodynamic parameters
	Cons: limitation on the number of beads (huge computer memory requirement) and computationally more expensive and demanding than EE CFD approach; may emulate particle breakage, but particle breakage for the whole milling duration is intractable in DEM
PBM	Pros: simulates evolution of the particle size distribution and describes particle breakage for the whole milling duration
	Cons: does not provide flow/motion information about the suspensions and beads; no microhydrodynamic information; limiting cases of particle mixing scenarios can be considered (well-mixed, plug flow, well-mixed cells in-series); no computational issue (very fast)
MHD	Pros: a simple semi-theoretical model that provides "average" values of microhydrodynamic parameters; no computational issue (very fast)
	Cons: no flow information, no breakage kinetics information

*The SI–SN model is purely phenomenological and inferior to the MHD model; hence, it is not worth considering in the above analysis separately.

Based on comprehensive review of the modeling approaches and their pros/cons [32] due to its simplicity and descriptive power, we use the MHD model and intend to improve and advance it for developing a deep process understanding and gaining various insights into the frequency and intensity of the bead–bead collisions and capture frequency of drug particles between the beads in this dissertation.

1.4.2 The microhydrodynamic model and impact of process parameters

Eskin et al. [34, 132] developed a comprehensive microhydrodynamic model to calculate the mean velocity of bead oscillations in a well-mixed slurry using the kinetic theory of gases and the fundamental granular energy balance [133]. Bilgili's group adapted and refined the model for application to pharmaceutical WSMM in a series of papers [33, 57, 62, 63, 89, 90]. Readers are referred to [34, 132] for full details of the model as well as the underlying assumptions, while salient features of the model will be covered here. The power applied by the mill stirrer is uniformly applied throughout the whole volume of the slurry (beads and suspension, see **Figure 1.1**) and equals the total energy dissipation rate ε_{tot}. The model inherently assumes well-mixedness (no spatial gradients), average power consumption during the milling, and a pseudo-steady-state in terms of power consumption. This power dissipates through fluctuating motions of the beads at the micro-scale. Hence, ε_{tot} is described as

$$\varepsilon_{tot} = P_w = \varepsilon_{visc} + \varepsilon_{coll} \tag{1.2}$$

where P_w is the power applied by the rotor per unit volume, ε_{visc} is the energy dissipation rate due to both the liquid–beads' viscous friction and lubrication, and ε_{coll} is the energy dissipation rate due to partially inelastic bead–bead collisions. Bilgili and Afolabi [62] added a third term, ε_{ht}, i.e., the power spent on shearing equivalent liquid (milled drug

suspension) of the slurry at the same shear rate but calculated (or measured approximately) as if no beads were present in the slurry. Then, following Eskin et al. [34], Equation (1.2) was modified as

$$P_{\mathrm{w}} = \varepsilon_{\mathrm{visc}} + \varepsilon_{\mathrm{coll}} + \varepsilon_{\mathrm{ht}} \tag{1.3}$$

$$P_w = \frac{54\mu_L c\theta R_{diss}}{d_b^2} + \frac{12}{d_b\sqrt{\pi}}(1-e^2)g_0 c^2 \rho_b \theta^{3/2} + \varepsilon_{ht} \tag{1.4}$$

where μ_{L} is the apparent shear viscosity of the equivalent liquid (drug suspension) and c is the bead loading in the milling chamber. θ is the granular temperature defined as the bead–equivalent liquid relative mean-square velocity, R_{diss} is the dissipation or effective drag coefficient, d_{b} is the bead size (taken as the median size), e is the restitution coefficient for the bead–bead collisions, ρ_{b} is the density of the beads and g_0 is the radial distribution function at contact. The dissipation coefficient R_{diss} is a function of the bead Reynolds number Re_{b}, c, and the non-dimensional bead–bead gap thickness at which the lubrication force stops increasing and becomes a constant [57]. Wylie et al. [134] give R_{diss} as

$$R_{diss} = R_{diss\,0}(c) + K(c) d_b \rho_L \theta^{0.5}/\mu_L \tag{1.5}$$

where ρ_{L} is the density of the suspension and K is a coefficient given by an empirical correlation of bead concentration c

$$K(c) = (0.096 + 0.142c^{0.121})/(1-c)^{4.45} \tag{1.6}$$

R_{diss0} in Equation (1.5) is the dissipation coefficient taking into account the squeezing of the milled suspension film between two approaching beads and is expressed as follows:

$$R_{diss\,0}(c) = k_1(c) - k_2(c)\ln \varepsilon_m \tag{1.7}$$

In Equation (1.7), ε_m is the non-dimensional bead–bead gap thickness at which the lubrication force stops increasing and becomes a constant and can be taken as 0.003 [135]. R_{diss0} was calculated by Sangani et al. [135] who employed a modified multiple method for simulation of Stokes flow in a liquid and correlations for k_1 and k_2 were found as:

$$k_1(c) = 1 + 3\sqrt{c/2} + (135/64)c\,ln\,c + 11.26c(1 - 5.1c + 16.57c^2 - 21.77c^3) \quad (1.8)$$

$$k_2(c) = cg_0 \quad (1.9)$$

Equations (1.5–1.9) were used in Equation (1.4) to calculate the granular temperature θ. The microhydrodynamic model in previous studies [33, 57, 62, 63, 90] incorporated the following Carnahan and Starling model [136] for g_0:

$$g_0 = \frac{1 - 0.5c}{(1 - c)^3} \quad (1.10)$$

The solution of Equation (1.4) for θ entails the measurement of the equivalent liquid properties, i.e., shear viscosity μ_L and density ρ_L of the drug suspension, the average stirrer power per unit volume in the presence of the beads P_w, and the energy dissipation rate for shearing the equivalent liquid ε_{ht} by viscometry and milling experiments [62]. Three approaches can be used to determine P_w or ε_{ht} (without beads). First, P_w can be directly measured by the electric motor's power consumption and/or torque measurements. Second, a general correlation for power consumption can be developed by dimensionless analysis including Euler number *Eu*, Reynolds number *Re*, and Froude number *Fr* for a specific mill and such a correlation can be used for estimating P_w [137]. Finally, P_w can also be estimated by an EL–EL (KTGF) simulation of the mill via CFD. Along with the bead material properties, μ_L, ρ_L, ε_{ht}, and P_w are incorporated into Equation (1.4), which can then

be solved for θ using any nonlinear equation solver. Finally, all MHD parameters are determined using the calculated θ as an input parameter.

The average bead oscillation velocity u_b and the frequency of single-bead oscillations ν are determined using the calculated θ and the following expressions:

$$\nu = \frac{24c}{d_b} g_0 \sqrt{\frac{\theta}{\pi}} \quad \text{and} \quad u_b = \sqrt{\frac{8\theta}{\pi}} \tag{1.11}$$

In a comprehensive microhydrodynamic model, Eskin et al. [132] considered the elastic contact deformation of the beads along with the elastic–perfectly plastic deformation of the particles caught between them. While the beads frequently collide due to their fluctuating motions in a slurry, which are characterized by θ, u_b, and ν, the beads capture and compress (deform) fine drug particles to be milled. The average maximum normal force F_b^n during the collision of two identical elastic beads, the radius of the contact circle formed at the contact of two beads α_b, and the maximum contact pressure at the center of the contact circle σ_b^{max} were calculated using

$$F_b^n = 1.96 \left(\frac{Y_b}{1-\eta_b^2} \right)^{2/5} \rho_b^{3/5} R_b^2 \theta^{3/5} \tag{1.12}$$

$$\alpha_b = \left[\frac{3(1-\eta_b^2)}{4Y_b} R_b F_b^n \right]^{1/3} \tag{1.13}$$

$$\sigma_b^{max} = \frac{3F_b^n}{2\pi\alpha_b^2} \tag{1.14}$$

where Y_b, and η_b are the Young modulus and Poisson's ratio of the bead material, R_b is the bead radius and was taken as half of d_b. The probability p of a single (drug) particle with radius R_p being caught between beads was estimated as the ratio of the volume containing

the caught particles to the volume of milled drug suspension falling on a pair of the milling beads as follows:

$$p = 0.97\frac{c}{1-c}\left[\frac{\rho_b(1-\eta_b^2)}{Y_b}\right]^{2/5}\theta^{2/5}\frac{R_p}{R_b} \tag{1.15}$$

The multiplication of the probability *p* of a single particle caught between the beads (Equation (1.15)) and the frequency of single-bead oscillations ν (Equation (1.11)) gives the average frequency of drug particle compressions *a*:

$$a = p\nu = 11.64\frac{c^2 g_0}{\sqrt{\pi}(1-c)}\left[\frac{\rho_b(1-\eta_b^2)}{Y_b}\right]^{2/5}\frac{R_p}{R_b^2}\theta^{9/10} \tag{1.16}$$

where R_p may be taken as the initial radius of the drug particles for convenience. However it should be noted that *a* decreases directly proportional with the decreasing particle size during milling as plotted in ref. [138]. The energy dissipation rate resulting from the deformation of the drug particles per unit volume Π also characterizes the grinding intensity and is expressed as follows:

$$\Pi = 4.46\frac{c^2 g_0}{\pi^{5/2}\psi\sigma_y}\left(\frac{Y_b}{1-\eta_b^2}\right)^{18/15}\left(\frac{Y^*}{Y_p}\right)^{\gamma}\rho_b^{4/5}\frac{R_p}{R_b^2}\theta^{13/10} \tag{1.17}$$

where φ, Y^*, Y_p, η_b, σ_y, R_p, and R_b respectively denote volumetric fraction of the solid (drug) particles to be ground in the slurry (the bead–drug suspension), shortly referred to as the *solid (drug) volume fraction*, reduced elastic modulus of the bead–drug particle contact, elastic modulus of the drug particles, Poisson's ratio of the beads, contact pressure in a drug particle captured when the fully plastic condition is obtained, radius of the drug particle, and radius of the bead. The reduced elastic modulus of the bead–particle contact Y^* was calculated as:

$$\frac{1}{Y^*} = \frac{1-\eta_b^2}{Y_b} + \frac{1-\eta_p^2}{Y_p} \tag{1.18}$$

In order to calculate Π using the expressions derived by Eskin et al. [132], one must either find the mechanical properties of the drug particles (Y_p, η_p, σ_y) from the literature or measure them. In general, it is difficult to find reliable mechanical properties of small drug particles as they are difficult to measure reliably [139]. For young modulus, nanoindentation experiments could be used where the load versus depth data can be fitted by using an equation developed for elastic contact of spherical surfaces [140] by inserting the Poisson's ratio, which can be assumed as 0.3 for drugs [139]. Hence, Afolabi et al. [57] factorized Π into a material-dependent factor λ, which are hard to measure, and a process-dependent factor F considering only one size of beads:

$$\lambda = 2.23 \frac{\rho_b^{4/5}}{\pi^{5/2}\sigma_y} \left(\frac{Y_b}{1-\eta_b^2} \right)^{18/15} \left(\frac{Y^*}{Y_p} \right)^{\gamma} \frac{R_p}{R_b^2} \tag{1.19}$$

$$F = \frac{c^2(2-c)}{(1-c)^3} \frac{1}{\varphi} \theta^{13/10} \tag{1.20}$$

To explain the impact of various bead sizes, Li et al. [33] suggested a slightly different factorization of Π into λ and F for multiple bead sizes as follows:

$$\lambda = 2.23 \frac{\rho_b^{4/5} R_p}{\pi^{5/2}\sigma_y} \left(\frac{Y_b}{1-\eta_b^2} \right)^{18/15} \left(\frac{Y^*}{Y_p} \right)^{\gamma} \tag{1.21}$$

$$F = \frac{c^2(2-c)}{(1-c)^3} \frac{1}{\varphi R_b^2} \theta^{13/10} \tag{1.22}$$

Both studies referred to F as the milling intensity factor and used it to gain insight into the impact of the process parameters. On the other hand, it is debatable if the bead size should be regarded as a process parameter or an equipment design parameter because beads

are an integral part of the wet media mill. In a recent study [90], instead of calculating Π, the researchers calculated a pseudo energy dissipation rate $\Pi \cdot \sigma_y$, which is directly proportional to Π, by making use of the mechanical properties of the two types of beads used: crosslinked polystyrene (CPS) and yttrium-stabilized zirconia (YSZ).

$$\Pi \sigma_y = 4.46 \frac{c^2 g_0}{\pi^{5/2} \psi} \left(\frac{Y_b}{1 - \eta_b^2} \right)^{18/15} \left(\frac{Y^*}{Y_p} \right)^{\gamma} \rho_b^{4/5} \frac{R_p}{R_b^2} \theta^{13/10} \tag{1.23}$$

The use of MHD model led to significant insights into the impact of the viscous dampening phenomenon and various process–bead parameters on the breakage kinetics, and media wear [33, 57, 62, 63, 89, 90]. The MHD-predicted effects of stirrer speed, bead size, and drug (solids) loading on the average single bead oscillation velocity u_b, to be discussed below, qualitatively agree with and exhibit similar trends to those of the experimentally measured effects [106, 107] of the same variables on the bead velocity. Unfortunately, quantitative comparisons are not possible due to different ranges of the process variables used, and these studies only reported the time-averaged bead velocity. Also, it is difficult to measure most of the microhydrodynamic parameters, but, some recent attempts to experimentally measure the stress energy–frequencies using mechanically well-characterized spherical metal particles as surrogate beads seem to be promising [131, 141]. In a recent collaborative study, EE two-phase flow simulations (two-week computation time per simulation) performed by GlaxoSmithKline and Tridiagonal [142] reveal that the spatio-temporally averaged microhydrodynamic variables from these simulations were of the same order of magnitude as those calculated with the simple MHD model, giving further credence to the MHD model.

The significant interplay between stabilization–suspension rheology and breakage kinetics has been well-established in nanomilling [62, 88, 131]. Bilgili and Afolabi [62] found an optimal polymer concentration in WSMM of griseofulvin suspensions in the presence of polymer–surfactant, which was explained by a combined MHD–polymer adsorption analysis. An increase in the polymer concentration had two counteracting effects: reduction in θ and by extension all other microhydrodynamic parameters at the higher suspension viscosity (viscous dampening) and higher polymer adsorption on drug nanoparticles, which suppressed aggregation effectively. The optimally selected stabilizer formulation for griseofulvin nanosuspensions was used in the MHD studies below to minimize any confounding effect of particle aggregation.

Several MHD studies [57, 60, 63] demonstrated that when stirrer tip speed u was increased, more mechanical energy was imparted at higher P_w, and all microhydrodynamic parameters increased monotonically, i.e., higher u led to higher θ, v, a, u_b, σ_b^{max}, and F (**Figure 1.5**). To put it differently, higher u led to higher bead velocity, which is qualitatively in line with the experimental work [106, 107, 113], more frequent and energetic/forceful bead–bead collisions, and more frequent–intense drug particle compressions. On the other hand, as can be seen from **Figure 1.6**, as the drug loading was increased, there was a slight, relatively weak, linear decrease in all microhydrodynamic parameters, except F, which exhibited a sharper decrease, thus explaining the reduced breakage rate experimentally observed at the higher drug loading [57].

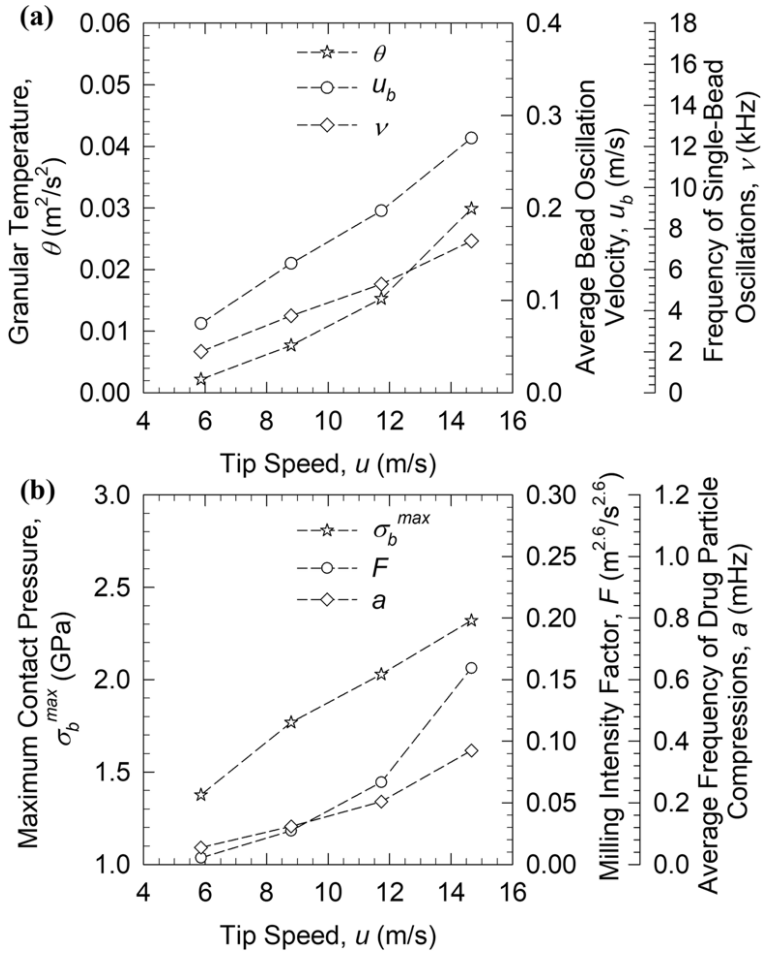

Figure 1.5 Effects of the stirrer tip speed on **(a)** the granular temperature θ, the average bead oscillation velocity u_b, and the frequency of single-bead oscillations ν and **(b)** the maximum contact pressure σ_b^{max}, the milling intensity factor F, and the average frequency of drug particle compressions a.
Source: [57]

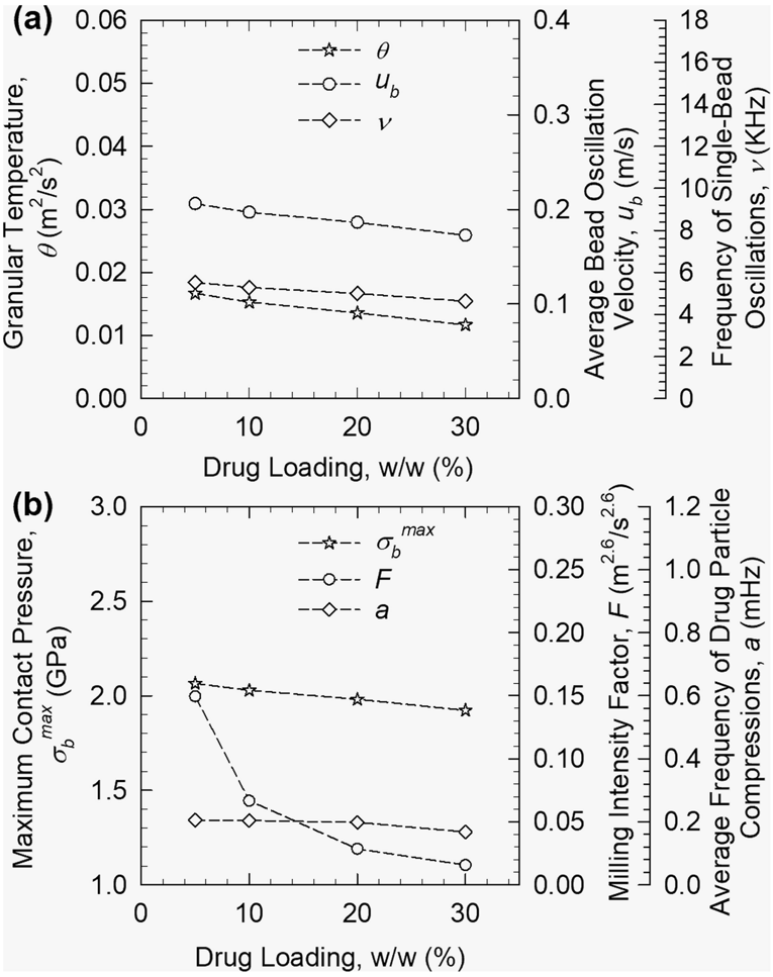

Figure 1.6 Effects of the drug loading on **(a)** the granular temperature θ, the average bead oscillation velocity u_b, and the frequency of single-bead oscillations ν and **(b)** the maximum contact pressure σ_b^{max}, the milling intensity factor F, and the average frequency of drug particle compressions a.
Source: *[57]*

Figure 1.7 presents the MHD analysis of the impact of bead size d_b. There were two major counteracting effects of d_b. A decrease in d_b led to lower θ, u_b, σ_b^{max} and higher ν and a [33, 63], i.e., more bead–bead collisions with lower collision energy–force. These counteracting effects of the MHD parameters provide a mechanistic, quantitative explanation for the origin of the optimal bead size observed experimentally [33]. Also, the differences in terms of microhydrodynamics parameters associated with small vs. large beads were largely in agreement with the findings of ref. [114] with CFD–DEM

simulations. Unlike the case for u, the overall effect of d_b on the observed breakage kinetics could not be explained by F alone; other microhydrodynamic parameters such as v and a seem to explain the bead size impact better than F. F can successfully be used to explain the impact of all process parameters such as stirrer speed, bead loading, and drug loading and correlate their combined effect on the milling time constant τ_p uniquely for a specified mill [57] (**Figure 1.8**). However, it appears that it is inadequate to explain the impact of bead size, which is usually regarded as an equipment parameter in media milling [33].

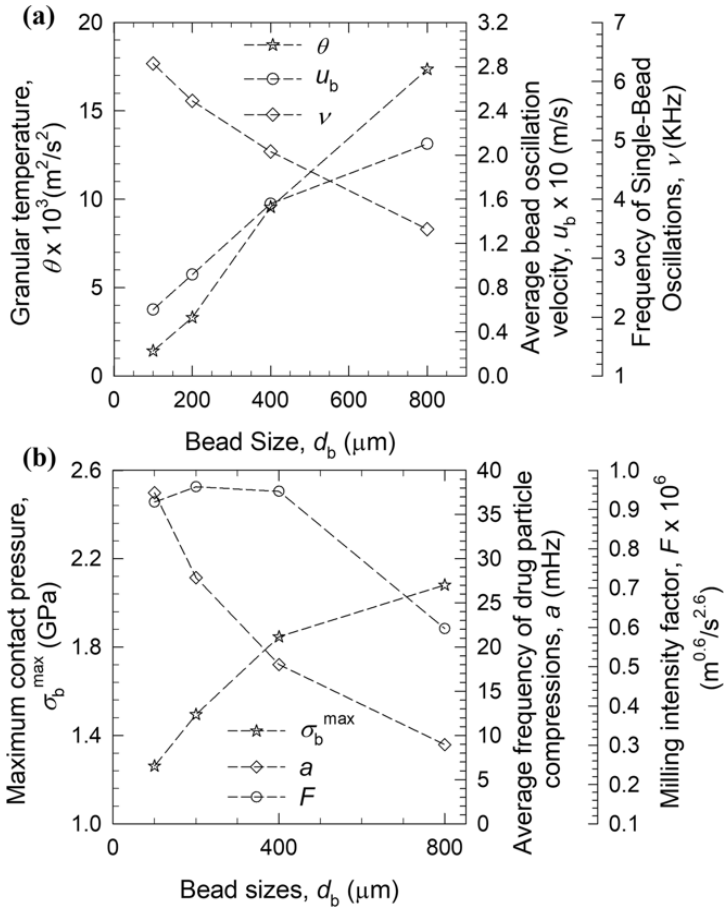

Figure 1.7 Effects of bead size d_b on **(a)** the granular temperature θ, the average bead oscillation velocity u_b, and the frequency of single-bead oscillations v at and **(b)** the maximum contact pressure σ_b^{max}, the average frequency of drug particle compressions a, and the milling intensity factor F at $\omega = 2800$ rpm.
Source: [33]

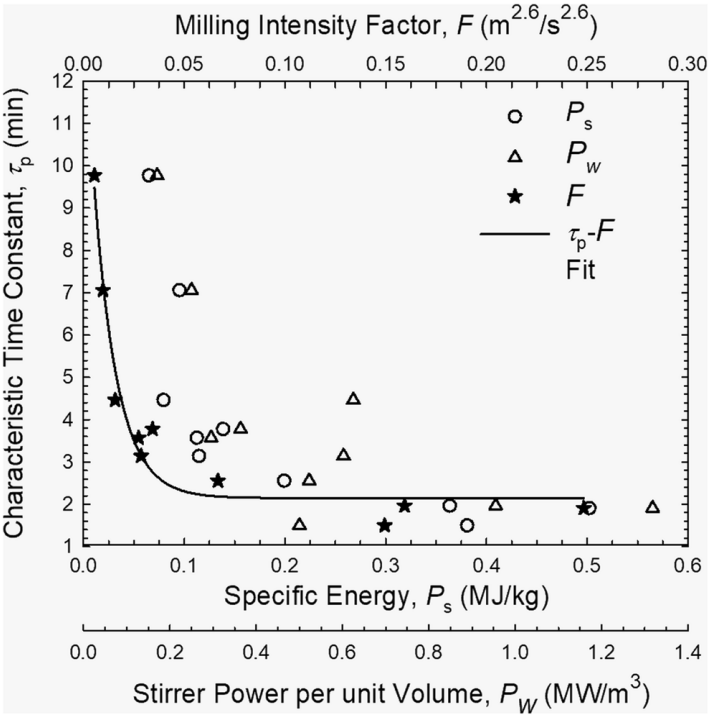

Figure 1.8 Scatter plots for the characteristic time constant τ_p *versus* the specific energy P_s, the milling intensity factor F, and the stirrer power per unit volume P_w. Fit: an exponential decay correlation.
Source: [57]

Figure 1.9. illustrates that the optimal bead size exhibited a negative power-law correlation with either the specific energy consumption or any of the MHD parameters; the fits were excellent when the MHD parameters were used as opposed to the specific energy: $R^2 \geq 0.997$ vs. $R^2 = 0.947$ [33]. Hence, the MHD model has rationalized the use of smaller beads for more energetic wet media milling and provided an overarching explanation as to the use of smaller beads in WSMM than in low-energy mills such as ball mills including centrifugal or planetary ball mills. Moreover, such a relationship between optimal bead size and the MHD parameters guided the design of an intensified WSMM process to produce drug nanosuspensions of two drugs with $d_{50} < 100$ nm at reduced energy consumption and low media contamination [63]. The same study [63] revealed drastically lower media wear and product contamination upon use of smaller beads (50 µm vs. 800

μm beads), which could be explained by the lower σ_b^{max} and higher strength of the smaller beads.

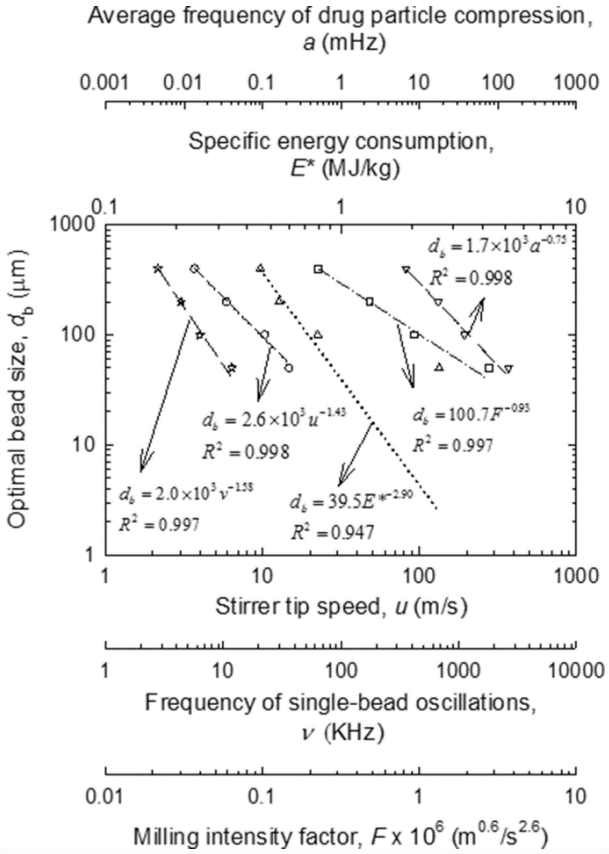

Figure 1.9 Scatter plots and power-law scaling for the dependence of optimal bead size on the stirrer tip speed *u*, the specific energy consumption *E**, the frequency of singe-bead oscillations *v*, the average frequency of drug particle compression *a*, and the milling intensity factor *F*.
Source: [33]

Similar to the case for db, two counteracting effects of volumetric bead concentration c were noted. The MHD analysis reveals that for all three stirrer speeds, ν and a were higher, whereas θ, u_b, and σ_b^{max} were lower when *c* was increased [57, 90] (**Figure 1.10**). In other words, more bead–bead collisions and drug particle compressions occurred albeit with less energetic/forceful collisions/compressions at higher *c*. Higher speeds led to a monotonic increase in all MHD parameters, as discussed earlier. The overall positive impact of *c* on the breakage kinetics, i.e., faster breakage of the drug particles at

higher c, could be explained by the increase in the milling intensity factor F [57] or $\Pi \cdot \sigma_y$ [90].

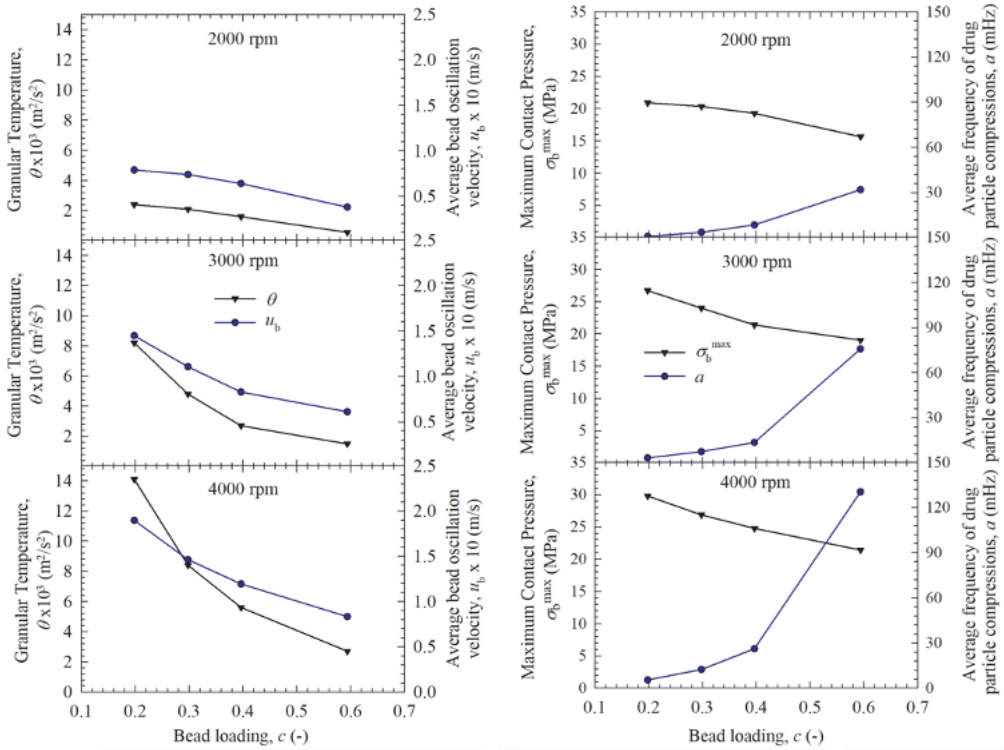

Figure 1.10 Effects of CPS bead loading c on granular temperature θ and average bead oscillation velocity u_b (left panel) as well as on the maximum contact pressure σ_b^{max} and the average frequency of drug particle compressions a at various three different stirrer speeds.
Source: [90]

In a rare analysis in WSMM literature, Parker et al. [90] compared the performance of crosslinked polystyrene (CPS) beads and yttrium-stabilized zirconia (YSZ) beads with similar sizes. Faster breakage occurred with YSZ beads as compared with CPS beads because all MHD parameters, except the radius of contact circle α_b, were higher for YSZ than for CPS (**Figure 1.11**), favoring YSZ over CPS. With higher fluctuating kinetic energy, YSZ beads having a higher modulus of elasticity ($Y_b \cong 200$ GPa) than the CPS beads ($Y_b \cong 1.5$ GPa) experienced a higher maximum contact pressure σ_b^{max} and a lower radius of contact circle α_b than the CPS beads at the same stirrer speed. This is the first

quantitative verification of the commonly held notion that softer beads (CPS) should allow for a larger contact circle than harder beads (YSZ), which is advantageous to capturing fine drug particles during the milling. However, despite this advantage of the CPS beads, due to their lower θ and u_b, their use led to smaller frequency of drug particle compressions a than the YSZ beads (except at ω = 2000 rpm). For ω = 2000 rpm, CPS beads had a slightly higher a than YSZ; yet they caused a lower breakage rate. This can possibly be explained by the lower σ_b^{max} and $\Pi \cdot \sigma_y$ generated by CPS beads at the lowest stirrer speed used [90].

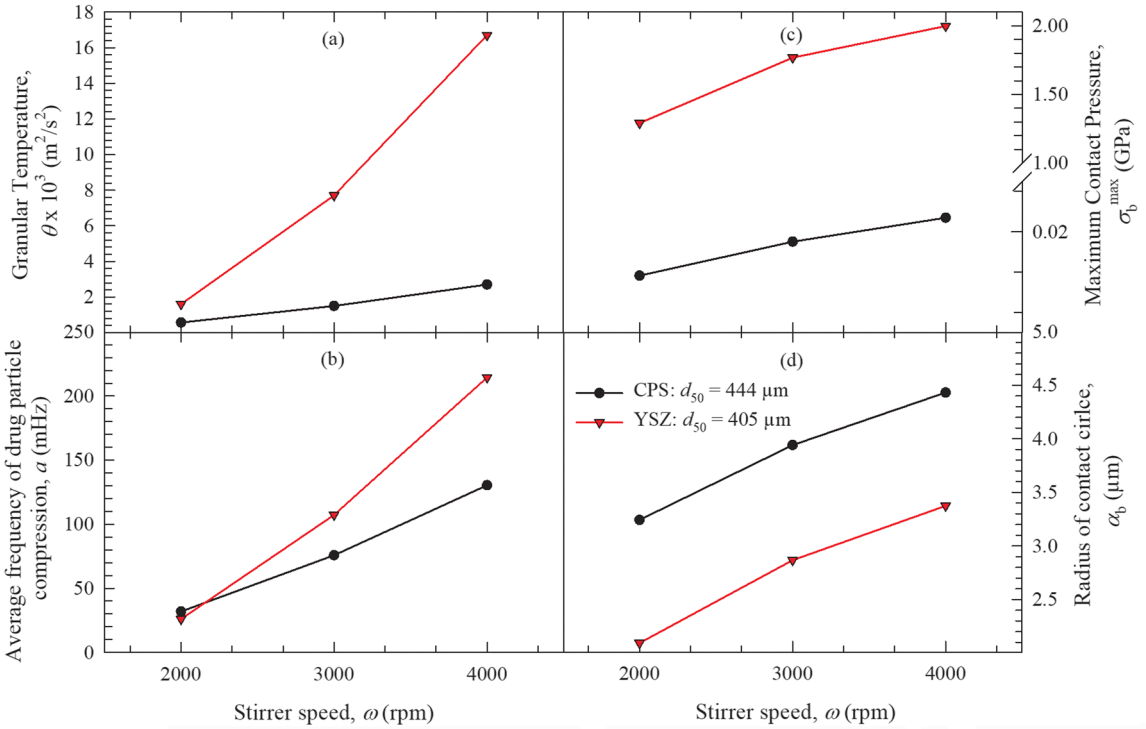

Figure 1.11 Effects of stirrer speed on **(a)** granular temperature θ, **(b)** the average frequency of drug particle compressions a, **(c)** the maximum contact pressure σ_b^{max}, and **(d)** radius of the contact circle α_b when CPS and YSZ beads were used.
Source: [90]

1.5 Research Needs and Approaches

In this section, the knowledge gaps in the literature that were addressed in this dissertation along with detailed approaches taken in each chapter will be introduced.

1.5.1 Breakage kinetics in wet stirred media milling

Despite its significant advantages, development of a WSMM poses several challenges. Most studies on WSMM have focused on formulation challenges such as aggregation and crystal growth via Ostwald ripening (see [10, 17] and references cited therein). In contrast, relatively scant information is available about the processing–operational challenges such as energy-intensive operation, high cost due to high energy consumption, long operation time, and contamination of drug particles by the beads [10, 32, 61]. Overcoming them entails a mechanistic understanding of the impact of process variables such as the stirrer speed, the size–material of the beads, and the bead loading on the breakage kinetics, milling time required for a desired product fineness, energy consumption, and media wear [57, 66]. The breakage kinetics is important to pharmaceutical industry as it relates to production cycle time: faster breakage results in shorter processing to achieve a desired nanoparticle size of the poorly soluble drugs.

Pharmaceutical engineers–formulators and academia have used various modeling approaches to investigate the WSMM process [32]. A recent survey [32] revealed that statistically-based methods such as empirical regression and response surface method methodology are the most widely-used modeling approaches. On the other hand, breakage kinetics during WSMM of drugs was also investigated using phenomenological and mechanistic models such as the population balance model (PBM) [143] and the microhydrodynamic model [33, 57, 90]. The effects of the bead size [33, 63], the stirrer speed [57, 90], the bead material [90], the bead loading [33, 57, 90], and the drug loading [33] on the particle size distribution of griseofulvin particles and a breakage time constant were investigated. In these studies, the use of the microhydrodynamic model shed light on the roles of bead–bead collisions in WSMM. However, in general, these studies did not

attempt to directly correlate the microhydrodynamic model parameters to the breakage rate constant, which determines the cycle time in the manufacturing of drug suspensions. Another issue is that all these studies and others [92, 144] used a first-order breakage kinetic model. This model is known to have a limitation, i.e., the need to eliminate the kinetic data obtained during early milling times of WSMM [62, 92]. Hence, a head-to-head fair comparison and discrimination of several breakage kinetic models for WSMM is highly warranted.

In view of the literature review above, Chapter 2 examined the impact of stirrer speed and bead material–loading on the breakage kinetics during WSMM via three breakage kinetic models and a microhydrodynamic model. Experimentally, the evolution of drug median particle size was tracked during WSMM operating at 3000–4000 rpm stirrer speed with 35–50% (v/v) loading of polystyrene or zirconia beads in a 3-factor, 2-level full-factorial design of experiments (DOE). In addition to the well-known first-order kinetic model, *n*th-order and warped-time kinetic models were developed; all kinetic models were fitted to the experimental data with the objective of identifying the best kinetic model based on statistical analysis and physical plausibility considerations. The microhydrodynamic model parameters were calculated using the measured process variables, power consumption, and suspensions viscosity–density. A subset selection algorithm was used along with Multiple Linear Regression Model (MLRM) to delineate how the breakage rate constant k was affected by the microhydrodynamic parameters. As a comparison, a purely empirical correlation for k in terms of the process parameters and bead properties was also developed. Four additional WSMM experiments were conducted at the center points and outside the domain of the DOE to test the predictive capability of

the kinetic–microhydrodynamic correlation and the purely empirical correlation. The limitations of the models as well as future strategies for the development and improvement of predictive models were discussed. Overall, this chapter offers the first comprehensive treatment of breakage kinetics during WSMM in view of the fundamental physics (microhydrodynamics) and explores the microhydrodynamic parameters that govern the breakage kinetics. It is expected that such a comprehensive analysis of breakage kinetics with consideration of the actual physics in the mill will provide insights, quantitative process understanding regarding the impact process parameters–bead material on the breakage kinetics and cycle time, as well as some predictive capability.

1.5.2 Improvement of microhydrodynamic (MHD) model

Unfortunately, previous MHD studies [33, 34, 57, 62, 90, 132] did not consider the possible impact of high bead concentrations, especially close to the packing limit, and the packing limit concentration on the breakage kinetics during WSMM. This impact can be accounted for by the radial distribution function at contact (RDF), which adjusts the collision probability of two beads as a function of the bead concentration [145]. Eskin et al. [34, 132] developed their microhydrodynamic model using the Carnahan–Starling RDF [136], which has been used in most subsequent MHD studies. The Carnahan–Starling RDF is a commonly used equation for rigid-sphere dense fluids in the kinetic theory of gases. It predicts unrealistically smooth variations of the RDF at concentrations close to the packing limit concentration [146]. Wang et al. [145] showed that the difference between an RDF that accounts for and an RDF that does not account for the packing limit gets larger when the concentration approaches the packing limit volume fraction for mono-dispersed systems (~0.63) [147]. Since the RDF affects almost all microhydrodynamic parameters,

the impact of the packing limit needs a thorough investigation via comparative assessment of various RDFs in the MHD modeling, which has not been done before. The Lun RDF [148] has been used very recently for microhydrodynamic analysis of the WSMM process for the first time [149-151]. However, the impact of the bead packing limit, as modeled by different RDFs, on the microhydrodynamic parameters and the breakage kinetics has not been examined.

In Chapter 3, we investigated the impact of bead packing limit on the breakage kinetics and microhydrodynamic parameters during WSMM of a drug (fenofibrate) suspension. The timewise evolution of the median particle size was tracked by offline laser diffraction measurements. To quantify the breakage kinetics, an *n*th-order breakage kinetics model was fitted to the median particle size evolution data; thus, enabling us to estimate the breakage kinetic parameters. For various process conditions and bead types, we calculated the microhydrodynamic parameters using three RDFs: the Carnahan–Starling RDF [136], the Lun RDF [148], and the Ma–Ahmadi RDF [146]. The Lun RDF and the Ma-Ahmadi RDF take into account the packing limit concentration of the beads, whereas the Carnahan–Starling RDF does not. Analysis of the MHD parameters enables us to evaluate the impact of the stirrer speed, the bead loading, and the bead type on milling and elucidate the effects of the bead packing limit at the bead–bead collision scale. Moreover, advancing our earlier work [150], we formulated a new subset selection algorithm with a leave-one-out cross-validation (LOOCV) technique. This algorithm allowed us to determine the best multiple linear regression models (MLRMs) of the breakage rate constant k with the microhydrodynamic parameters (semi-theoretical MLRM) or the process–bead parameters (empirical MLRM) as predictors. Experimental k

data from 10 milling runs were used to calibrate and cross-validate the MLRMs; then, these MLRMs were used to predict the median particle size evolution in four additional milling experiments that had not been used as part of the model calibration/cross-validation to discern the predictive capability. Overall, this comprehensive experimental–theoretical study presented in Chapter 3 is expected to yield fundamental insights about the role/impact of bead concentration limit on the microhydrodynamic parameters and breakage rate in WSMM.

1.5.3 Understanding heat generation–transfer during WSMM

One aspect that received no attention in the WSMM literature is the high heat generation inside the mill during WSMM [149], which could lead to a significant temperature rise. Only a small fraction of the mechanical energy spent on mixing the drug suspension–bead mixture is used to deform the drug particles [34]. Most is eventually converted into heat through dissipative processes such as viscous losses, inelastic bead–bead and bead–wall collisions, etc. [62]. Temperature plays an important role and needs to be controlled during the WSMM of drug suspensions because the physical and/or chemical stability of a drug suspension could be susceptible to temperature. A higher temperature during WSMM or storage could facilitate Ostwald ripening and growth of drug nanoparticles [46, 53, 152, 153]. Surface modification and amorphization occurred when temperature was raised from 25 ^{o}C to 37 ^{o}C in the case of a bezafibrate nanosuspension [154]. Moreover, a polymer like hydroxypropyl cellulose (HPC), which is a commonly used steric stabilizer in drug nanosuspensions, has a gelation temperature of ~44–50 ^{o}C [155]. HPC may start precipitating out of aqueous solution at or above this temperature, which may, in turn, cause physical destabilization of drug nanosuspensions.

Despite the significant potential impact of temperature on the product quality and process performance, some WSMM studies [156-158] did not even report the milling temperature. Other studies attempted to keep the milling/processing temperature below a set value such as 40 ^{o}C [159], 35 ^{o}C [57], and 25 ^{o}C [160]. In some milling studies, researchers milled the drug suspension intermittently to be able to keep the temperature below the set value; they shut down the mill, cooled it without further milling, and repeated this cycle several times [33, 90, 149, 161]. It must be emphasized that none of the above-mentioned studies investigated the impact of process parameters on heat generation and temperature rise during the WSMM. This situation is similar regarding the production of non-pharmaceutical suspensions by WSMM; the temporal evolution of temperature during the WSMM has been rarely explored. Garcia et al. [162] reported the evolution of temperature in a *batch* WSMM of calcite; however, batch milling is not used for industrial operations. Moreover, they did not investigate the impact of processing variables on the temperature rise during the milling. Hence, there is a huge gap in the general WSMM literature regarding heat generation–temperature evolution and understanding the factors that govern heat generation.

As a first attempt in the pharmaceutical nanotechnology literature, Chapter 4 examined the timewise evolution of the suspension temperature as a function of intermittent milling and cooling time and examine the impact of the milling parameters on the temperature rise. We hypothesized that the temperature is a strong function of power consumption. To this end, the precursor suspensions of fenofibrate, a model BCS Class II drug, were milled at three different stirrer speeds, bead loadings, and bead sizes. The power consumption and the suspension temperature at the mill outlet were measured and

recorded; the particle sizes after 60 min milling were measured by laser diffraction. Moreover, a newly defined thermal desirability score was used to evaluate and compare the performance of the milling runs. A connection between process conditions, power supplied by the mill stirrer, and thermal characteristics were established by utilizing dimensionless numbers such as the power number and the Reynolds number. Overall, this heat generation analysis will yield significant insights into temperature rise during the WSMM and the governing process variables. An optimal set of milling conditions will be identified based on a holistic analysis of the thermal desirability score, cycle time, power consumption, and median drug particle size.

1.5.4 Enthalpy balance model (EBM) for simulation and prediction of heat generation during milling

As discussed and addressed in Chapter 4, the temperature of drug suspensions during WSMM must be monitored and controlled because high temperatures can cause physical instability as well as chemical degradation and/or amorphization of drugs [163, 164]. Ostwald ripening and growth of drug nanoparticles are facilitated at a higher temperature during WSMM or storage [46, 53, 152]. To this end, modeling could significantly help engineers to gain fundamental insights into the WSMM process, which could facilitate process development and optimization. Bilgili and Guner [32] surveyed various modeling approaches used for WSMM, and found that about 70% of the models in pharmaceutical WSMM are based on statistically-based approaches; 30% of the models are of phenomenological or mechanistic nature. For example, the breakage kinetics can be represented with first-order exponential decay [151] or *n*th-order models [150] through empirical fits, where breakage rate constants delineate the breakage trends with respect to

varying process parameters. Recently, the breakage rate constants have been correlated with the microhydrodynamic parameters [150, 165], which enabled the inclusion of physics at the bead–bead collision scale in a modeling framework that enabled some good predictive capability for the evolution of particle size at various milling conditions. Unfortunately, to the best of our knowledge and based on the review paper [32], the literature is devoid of a model for simulating and predicting the temperature evolution during the WSMM.

Chapter 5 presents a first attempt in the WSMM literature to explore the temperature evolution during nanomilling of drug suspensions in a wet stirred media mill within the context of a simple enthalpy balance model. To this end, fenofibrate suspensions were milled at various stirrer speeds, bead loadings, and bead sizes; the mill outlet temperature was recorded over time during the milling. A dynamic enthalpy balance model was developed for simulating the temperature at the mill outlet, and the holding tank, including the temperatures of the beads and/or the stirrers in the mill chamber and the holding tank. This model is simple, with only one unknown parameter, i.e., the fraction of mechanical power converted to heat ξ, as it is ultimately intended for practical engineering use in the pharmaceutical industry. Out of the 32 milling runs, 27 runs were used as a training set for model calibration, and the remaining 5 runs formed the test set. In the model calibration, ξ was estimated for each run in the training set by fitting the simulated mill outlet temperature profile obtained from the enthalpy balance model to the experimentally measured profile. To test the predictive capability of the model, initial and final power consumptions P_0, P_f, and ξ for the five test runs were predicted by a power-law (PL) correlation and machine learning (ML) algorithms. Then, the enthalpy balance model

augmented with these predicted P_0, P_f, and ξ was used to generate the temperature profile, which was compared to the measured temperature profile in the test runs. This systematic, comprehensive experimental–modeling chapter is expected to generate significant practical and theoretical insights into heat generation and its controlling milling parameters during the WSMM.

1.5.5 Lumped parameter model (LPM) for semi-theoretical modeling of heat generation during WSMM

Chapter 5 presents the first modeling attempt of the temperature profile during WSMM [166] by using an enthalpy balance model (EBM). The EBM necessitates the simultaneous solution of five ordinary differential equations along with a sophisticated optimizer for parameter estimation. The EBM considers all salient physical features of the process such as the recirculating suspension, the configuration of the mill, the jacketed cooling of the mill and the holding tank, while necessitating the all physical–thermal properties of the suspension and mill–bead materials of construction as input [166]. It is fair to state that the EBM is not a simple model and requires some notable time and effort, justifying the development of simpler models.

In Chapter 6, we present a simple semi-theoretical lumped-parameter model (LPM), which can be easily adopted by pharmaceutical scientists and engineers, to simulate and predict the temperature evolution during the WSMM and compare its performance to the EBM. The LPM parameters, i.e., the apparent heat generation rate Q_{gen} and the apparent overall heat transfer coefficient times surface area UA, were obtained by direct fitting of the LPM to the experimentally measured temperature profiles. Then, these parameters were estimated as a function of the process parameters for the 27 training runs and predicted as

a function of the process parameters for the five test runs using a power law (PL) model and a machine learning (ML) model. The advantages and disadvantages of the LPM and the EBM as well as the limitations of the LPM were discussed. Not only will this study reveal the fitting capability of the LPM as compared with the EBM, but it will also enable us to assess their comparative predictive capabilities and usefulness for process development and understanding.

1.5.6 Optimization of the WSMM process via bead mixtures of different materials

The optimization of the WSMM process has been performed by solely considering the process parameters and milling time in prior studies [69, 71]. However, such an optimization approach is quite limited and does not offer much flexibility when the optimization entails multiple objectives such as low cycle time, low power consumption, and low heat generation. Unlike any study in the WSMM literature including non-pharmaceutical fields, as a major novelty, Chapter 7 explored the feasibility of cross-linked polystyrene (CPS)–yttrium-stabilized zirconia (YSZ) bead mixtures as a novel optimization approach for fast, efficient production of drug nanosuspensions via WSMM. While both CPS and YSZ beads were utilized in prior WSMM studies [70, 90], they have not been used in a bead mixture. We hypothesize that bead mixtures allow for optimal milling of drug suspensions from a combined energy–cycle time–heat dissipation perspective. While this hypothesis is proven, as a corollary, we aim to rationalize the use of bead mixtures as opposed to single type of beads based on judicious balancing of particle breakage kinetics–cycle time, power consumption, and heat dissipation considerations. Fenofibrate (FNB) was selected as a poorly water-soluble model drug. A total of 20 experiments were conducted at two stirrer speeds (3000 and 4000 rpm) and two volumetric

fractional bead loadings (0.35 and 0.50) with five CPS–YSZ bead mixtures including CPS alone and YSZ alone (CPS:YSZ 0:1–1:0 v/v). To characterize the breakage kinetics, three different kinetic measures were defined and analyzed including the apparent breakage rate constant of an *n*th-order kinetic model. A modified microhydrodynamic model was used to elucidate the different microhydrodynamic behavior of the CPS vs. YSZ beads and their pros/cons. Various optimization criteria based on industrial considerations were adopted and relevant merit scores were calculated. Kinetic parameters and specific power–energy consumption were used together to assess the impact of bead mixtures. This combined experimental–modeling chapter will reveal various insights as to why bead mixtures vs. YSZ or CPS beads alone offer much needed flexibility for WSMM optimization and enable development of a decision tree for bead mixture selection.

1.5.7 Impact of bead mixtures of different bead sizes

Patel et al. [167] investigated a possible synergistic effect in combining smaller and larger beads and performed experiments in varying ratios of smaller (200 and 400 μm) and larger beads (800 μm), while keeping all other process parameters of the WSMM constant. That study concluded that adding smaller beads to larger beads achieved smaller particles with lower energy consumption during milling. Moreover, they stated that it can lead to some other advantages such as savings on grinding media costs since a small amount of costly small-sized media can be used in mixtures. Additionally, Altun et al. [168] used a mixture of 1.5–2.5 mm and 3.0–4.0 mm alumina balls in *dry stirred ball milling* of limestone and compared their performance to those of the single ball size fractions in terms of milled particle size at various specific energy consumptions. The mixture performance lay in between the two individual ball size fractions although some caveats were mentioned for

the extremes of low and high energy consumption. While Patel et al. study has been the first attempt at assessing the feasibility of mixtures of beads with different nominal sizes, shortly referred to as bead mixtures hereafter, in the WSMM literature [167], it did not examine the impact of various stirrer speeds and bead loadings, and no microhydrodynamic explanation has been provided regarding the impact of various bead sizes. Moreover, the temperature and heat generation during the milling was not discussed at all.

Chapter 8 provides a comprehensive analysis of the impact of bead sizes and bead mixtures on the breakage rate, power consumption, and number of intermittent milling cycles experimentally and theoretically using a microhydrodynamic model. To this end, we used narrowly-sized zirconia beads with 100, 200 and 400 μm nominal sizes, and their half-and-half mixture combinations under 3000 and 4000 rpm stirrer speeds and 0.35 and 0.50 fractional bead loadings. The pre-suspensions of 10% griseofulvin, 7.5% hydroxypropyl cellulose, and 0.05% sodium dodecyl sulfate were milled for 3 h, while the particle sizes were measured at certain intervals via laser diffraction along with mill outlet temperature and average power consumption. The breakage kinetics was analyzed by fitting an *n*th-order breakage kinetics model to the experimentally measured median particle sizes. Microhydrodynamic parameters were calculated to examine the impact of process parameters and average bead sizes. Then, machine learning models were employed to predict the breakage kinetics in the test runs based on the microhydrodynamic parameters and process conditions. A merit score that factors in breakage rate, power consumption and number of intermittent milling was defined to compare the performance of different processing conditions and enable us to assess the impact of bead mixtures. This comprehensive analysis allows us to test the hypotheses that (i) bead mixtures can

significantly improve the WSMM process through synergistic effects in terms of breakage kinetics, power consumption, and number of intermittent milling cycles and that (ii) they will be superior to the narrowly-sized constituent beads.

1.6 Objectives, Hypotheses, and Dissertation Outline

In this dissertation, a better understanding of wet stirred media milling (WSMM) is aimed, and each chapter focuses on a different process optimization–intensification problem and associated modeling approach. Chapter 1 provides a review of the drug nanosuspension studies and clearly revealed that WSMM is the most widely used process both in industry and academia. Moreover, Chapter 1 presents challenges in WSMM process research and various modeling approaches used for process modeling. While there are formulation/stabilization challenges in developing drug nanosuspensions, most of these issues have been resolved via judicious stabilizer selection strategies with about 30 years of extensive research. However, the chemical engineering challenges associated with "processing" drug nanosuspensions have remained largely unresolved: the process is energy intensive and costly; it entails long cycle times even for small batch sizes, and high heat dissipation could either cause unacceptable temperature rise or limit the optimization domain of the process. Although these processing challenges are well-known for a long time, a great majority of the pharmaceutical nanotechnology literature has been devoted to formulation/stabilization aspects. Only during the last decade, more mechanistic understanding of the process has started to emerge. Hence, this dissertation present experimental and modeling work with the ultimate goals of (i) gaining a deeper and more mechanistic understanding of the WSMM process and breakage kinetics of the particles using the existing MHD model with various improvements and advancements, (ii)

examining the heat dissipation during the WSMM extensively with both experimental and modeling approaches, and (iii) optimizing and intensifying the WSMM using novel approaches such as bead mixtures of two different bead materials and mixtures of differently sized beads.

Toward achieving the above goals, breakage kinetics of drug particles during WSMM at different stirrer speeds and loadings of two different bead materials was investigated, and various kinetic models were developed/calibrated, while the breakage rate constant was correlated with various MHD parameters (Chapter 2). In Chapter 2, we hypothesize that not only can a statistically significant *n*th-order kinetic model–MHD model describe and explain the observed breakage kinetics, but also such a combined model has superior predictive capability as compared with a standard, purely empirical model. Chapter 3 examines the impact of bead packing limit on the microhydrodynamic parameters and breakage kinetic constant–MHD model correlations when different radial distribution functions at contact are used in the MHD model. In Chapter 2, bead packing has been considered for the first time by incorporating the Lun model [148] instead of the Carnahan-Starling model [136] of the radial distribution function at contact into the MHD model. This was a significant improvement in the accurate estimation of the microhydrodynamic parameters. However, the extent to which different radial distribution functions at contact affect the MHD parameters and the kinetics–MHD model correlations have not been examined before. Chapter 3 presents a comparative assessment of the Carnahan-Starling model [136] (no bead packing limit) with the models that incorporate bead packing limit, i.e., the Lun model [148] and the Ahmadi model [146]. We hypothesized that models that factor in the bead packing predict significantly different

microhydrodynamic parameters, which also affects the predictive capability of the kinetic–microhydrodynamic correlations.

In Chapter 4, we hypothesize that the mechanical energy conversion into heat can be modulated by judicious selection of WSMM parameters in a model-guided fashion. Then, we showed and compared how the selection of process parameters could drastically alter the temperature rise during WSMM. Toward gaining a more mechanistic understanding, Chapter 5 hypothesizes that the process could be simulated by an enthalpy balance model and the derived model could successfully fit the experimental data, which allows one to find what fraction of the power is converted to heat during the milling. That fraction was correlated with process conditions, and predictions were made by simulating the temperature profiles during test milling runs. The hypothesis that a simpler semi-theoretical model could also simulate and predict the time-wise temperature evolution was tested in Chapter 6, where the fitting and prediction capability of the derived Lumped Parameter Model (LPM) was as good as the Enthalpy Balance Model (EBM). Besides, the LPM is more advantageous as it entails obtaining less information about the mill set up and the physicochemical properties of the materials.

In Chapter 7, we hypothesize that bead mixtures allow for optimal milling of drug suspensions from a holistic energy–cycle time–heat dissipation perspective. While this hypothesis is tested, as a corollary, we aim to rationalize the use of bead mixtures as opposed to single type of beads based on judicious balancing of particle breakage kinetics–cycle time, power consumption, and heat dissipation considerations. Chapter 7 also presents a decision tree in terms of using various single beads vs. bead mixtures depending on various industrial considerations. Finally, Chapter 8 hypothesizes that mixtures of

different bead sizes could improve WSMM from a combined energy–cycle time–heat dissipation perspective. Chapter 9 discusses the overall conclusions and presents ideas for potential future work.

CHAPTER 2

BREAKAGE KINETICS MODELS AND MICROHYDRODYNAMIC CORRELATIONS FOR WET STIRRED MEDIA MILLING

This chapter aims to examine the impact of stirrer speed and bead material type–concentration on fenofibrate particle breakage during wet stirred media milling (WSMM) via three kinetic models and a microhydrodynamic model. Evolution of fenofibrate median particle size was tracked via laser diffraction during WSMM operating at 3000–4000 rpm with 35–50% (v/v) concentration of polystyrene or zirconia beads. First-order, *n*th-order, and warped-time breakage kinetic models were developed and fitted to the data. Main effects plots helped to visualize the influence of the milling variables on the breakage kinetics and microhydrodynamics parameters. A subset selection algorithm was used along with Multiple Linear Regression Model (MLRM) to delineate how the breakage rate constant is affected by the microhydrodynamic parameters. Our experimental and fitting results suggests that the *n*th-order model was found to be the best model to describe the temporal evolution; a nearly second-order kinetics ($n \cong 2$) was observed. When the process was operated at the higher stirrer speed and/or bead concentration with zirconia beads as opposed to polystyrene beads, the breakage occurred faster. A statistically significant (p value ≤ 0.01) MLRM of three microhydrodynamic parameters explained the variation in the breakage rate constant best ($R^2 \geq 0.99$). The average frequency of drug particle compressions interacting with the pseudo energy dissipation rate and the radius of the bead–bead contact circle governed the breakage kinetics in WSMM. The combined breakage kinetic model–microhydrodynamic model was demonstrated to have reasonable predictive power. Hence, the kinetic models and kinetic–microhydrodynamic correlation

enable deeper process understanding toward developing a WSMM process with reduced cycle time.

2.1 Materials and Methods

2.1.1 Materials

Fenofibrate (FNB, BP grade), which is a BCS Class II drug with an aqueous solubility of 0.8 mg/L at room temperature [169], was purchased from Jai Radhe Sales (Ahmedabad, India). The suspension formulation included a non-ionic cellulosic polymer (HPC: hydroxypropyl cellulose, L grade, Nisso America Inc, New York, NY, USA) and an anionic surfactant (SDS: sodium dodecyl sulfate, ACS grade, GFS chemicals, Columbus, OH, USA). Zirmil Y grade YSZ beads with a density of 6000 kg/m^3 were purchased from Saint Gobain ZirPro (Mountainside, NJ, USA). CPS beads with a density of 1040 kg/m^3 were purchased from Norstone Inc. (HCC grade, Bridgeport, PA, USA). While the nominal sizes of both beads are 400 µm, the actual median sizes of CPS and YSZ beads were measured as 444 µm and 405 µm, respectively, via laser diffraction using a Helos/Rodos particle size analyzer (Sympatec, NJ, USA) in dry dispersion mode. Microhydrodynamic calculations were performed using the actual median sizes of the beads. Drug suspensions were prepared in deionized water as the liquid medium.

2.1.2 Wet stirred media milling

The formulation was selected according to the detailed stability studies by our group on FNB [46, 47, 54]. 235 g pre-suspensions that have 10% FNB, 7.5% HPC-L, and 0.05% SDS with respect to 200 g DI water were prepared under constant shear mixing (Cat#. 14-503, Fisher Scientific, Pittsburgh, PA, USA) for 2 h at 300 rpm. As will be demonstrated

in Section 2.2, not only did this particular formulation ensure physical stability and mitigate aggregation and growth of FNB particles via ripening, but also it built up sufficiently high suspension viscosity, which in turn led to an accurate measurement of the power consumption during the milling and accurate calculation of the microhydrodynamic parameters. After overnight storage at 8 ^{o}C, the pre-suspensions were milled by Microcer wet stirred media mill (Netzsch Fine Particle Size Technology, LLC, Exton, PA, USA) for 180 min using the process variables presented in **Table 2.1.** Runs 1–8 correspond to a 3-factor, 2-level, full-factorial DOE.

Table 2.1 Process Variables and Bead Materials Used in the Wet Media Milling of the Fenofibrate Suspensions

Run No.	Stirrer Speed, ω (rpm)	Bead Loading, c (-)	Bead Material
1[a]	3000	0.35	CPS
2[a]	3000	0.35	YSZ
3[a]	3000	0.50	CPS
4[a]	3000	0.50	YSZ
5[a]	4000	0.35	CPS
6[a]	4000	0.35	YSZ
7[a]	4000	0.50	CPS
8[a]	4000	0.50	YSZ
9[b]	3500	0.425	CPS
10[b]	3500	0.425	YSZ
11[c]	2550	0.298	CPS
12[c]	2550	0.298	YSZ

[a]3-factor, 2-level, full-factorial DOE used in the parameter estimation of the models. [b]Center points of the original DOE for the CPS and the YSZ beads. [c]Experiments whose variables are outside the domain of the DOE.

The experimental data from these runs were used in the kinetic parameter estimation. The low–high values of the stirrer speed and the bead loading as well as the total milling time for the DOE were selected based on our prior wet milling studies using FNB [46, 54], limitations of our equipment, and the requirements of the breakage kinetic models (refer to Section 2.1.4). The design limit of the equipment (4200 rpm) dictates 4000

rpm as the high value with a safety margin, while the bead loading above 0.50 would entail more frequent, additional intermittent cooling; hence, it was not selected.

Runs 9 and 10, corresponding to the center points of the DOE for CPS and YSZ, as well as Runs 11 and 12, whose variables were selected outside the domain of the DOE, were used to test the predictive capability of the *n*th-order kinetic model–microhydrodynamic model correlation, i.e., $k = k(a, \sigma_b^{max}, \alpha_b, \Pi\sigma_y)$ and the purely empirical correlation, i.e., $k = k(\omega, c, \rho_b, Y_b)$. As ω was close to the design limit, we could not increase it beyond the high value (4000 rpm) of the DOE. Hence, for Runs 11 and 12, ω and c were both selected to be 15% smaller than the respective low values in the DOE (Runs 1 and 2). As will be demonstrated later, Runs 11 and 12 were quite different from Runs 1–8 in terms of the observed breakage kinetics. Practically, such low energetic conditions, inducing relatively low power consumption and heat dissipation, may be used to handle temperature-sensitive drugs, minimize the extent of amorphization and form conversion [4], and reduce YSZ bead contamination [24]. As we expected a slower breakage in Runs 11 and 12, based on the kinetic results from Runs 1–8, we purposefully prolonged the milling to 7 h for CPS (Run 11) and 6 h for YSZ (Run 12), thus attempting to meet the requirements in Section 2.1.4.

The mill has a chamber volume V_{mc} of 80 mL, lined with zirconia and a zirconia shaft. The bead loadings were calculated by dividing the true volumes of the beads by the volume of the milling chamber *(v/v)*. Suspensions were recirculated between the holding tank and the milling chamber at a volumetric flow rate of 126 mL/min, using a peristaltic pump (Cole-Palmer, Master Flex, Vermont Hills, IL, USA). A 200 μm nominal-sized stainless-steel screen was used to hold the beads in the milling chamber. The temperature

of the milling chamber and the holding tank was kept below 35 ^{o}C by using a chiller (Model M1-.25A-11HFX, Advantage Engineering, Greenwood, IN, USA). Due to the limited cooling capacity of our chiller, YSZ beads caused overheating especially at the high stirrer speed; hence, intermittent cooling was applied, like in [63, 90, 161], to keep the temperature below 35 ^{o}C. Samples were taken from the outlet of the mill at certain time intervals (2^{s}, s = 0, 1, 2,...7) with additional time points of 40 s, 24 min, 48 min, 96 min, and 180 min. The sampling procedure was modified to accommodate longer milling in Runs 11 and 12. The final sample was taken from the holding tank and all samples were characterized.

2.1.3 Characterization techniques

Particle size distribution (PSD) of the FNB suspensions at various milling times was determined by laser diffraction using LS 13-320 Beckman Coulter instrument (Brea, CA, USA). Polarized intensity differential scattering (PIDS) was kept between 40% and 50% while the obscuration was maintained below 8% in all measurements. The software computed the PSD using Mie scattering theory by taking the refractive indices of FNB and the measurement medium (water) 1.55 and 1.33, respectively. Prior to each measurement, about 1.0 mL suspension sample was dispersed into 5.0 mL of the stabilizer solution of the used formulation using a vortex mixer (Fisher Scientific Digital Vortex Mixer, Model No: 945415, Pittsburgh, PA) at 1500 rpm for a minute. Measurements were repeated four times (n = 4) and the average and standard deviation (SD) of these measurements were calculated. To assess the physical stability after 7 days and assess aggregation–Ostwald ripening upon aging, the milled nanosuspensions were stored at 8 ^{o}C in the refrigerator. They were mixed for 30 min prior to the particle size measurement and allowed to reach room temperature.

The apparent shear viscosities μ_L of the milled suspensions were measured using R/S plus rheometer (Brookfield Engineering, Middleboro, MS, USA) with a water jacket assembly Lauda Eco (Lauda-Brinkmann LP, Delran, NJ, USA). A CC40 coaxial cylinder with a jacketed setup was used to impart a controlled shear rate on the samples from 0 to 1000 1/s in 60 s at 25 ± 0.5 °C. The raw data were analyzed using the Rheo3000 software and the apparent shear viscosity at 1000 1/s was used in the microhydrodynamic model. The density was calculated in triplicate based on the weight of 35 ml nanosuspension.

Run 10 was selected for solid state characterization since it was milled using the center point of the DOE with the YSZ beads. The nanosuspension was poured into a petri dish as a thin layer and it was let dry overnight in a vacuum chamber. About 6–7 mg sample of the milled and dried particles, the physical mixture, the as-received fenofibrate, and HPC-L was weighed, put in an aluminum pan of 40 µL, and sealed. A Mettler–Toledo polymer analyzer DSC (Model DSC 3, Columbus, OH, USA) was used to determine the fusion enthalpy and the melting point of FNB. All samples were heated at a rate of 5 °C/min with a temperature range of 25–150 °C. Nitrogen was used at a flow rate of 60 mL/min. Data analysis was performed using the STARe V16.20 software provided by Mettler–Toledo.

Before scanning electron microscope imaging (SEM), 0.1 mL of the Run 10 nanosuspension was diluted with 10 ml deionized water and centrifuged (Compact II centrifuge, Clay Adams® Brand, Sparks, MD, USA) at 3200 rpm for 10 min to separate the drug from the aqueous phase with excess polymer. This dilution-centrifugation process was repeated two more times where 8 mL of the aliquot was decanted and replaced with fresh deionized water. After the third step, a droplet from the aliquot of the sample was put

on top of a carbon specimen holder, and it was placed in a desiccator for overnight drying under vacuum. The dried sample was then sputter coated with gold using BAL-TEC MED020 (BAL-TEC, Balzers, Switzerland) to reduce possible charging during SEM imaging. The morphology of the particles was examined using a JEOL JSM 7900F field emission SEM (JEOL USA, Inc., Peabody, MA, USA) operated at 2 kV. SEM images were taken at x15k and x30k magnification.

2.1.4 Breakage kinetic models

In the preparation of drug nanosuspensions via WSMM, breakage of the particles in a *well-stabilized suspension* is expected to be the dominant mechanism as compared to aggregation and particle growth (due to ripening) [94]. Therefore, the median particle size d_{50} monotonically decreases over time t until a limiting size d_{lim}, a.k.a. grinding limit, is attained or approached during prolonged milling [46]. Two experimental requirements emerge for an accurate and meaningful kinetic analysis: (i) the experimental d_{50}–t profile should attain or approach to an asymptote (limiting size) at sufficiently long, yet practically feasible, milling times and (ii) it should not exhibit a size increase regardless of the underlying mechanism. As will be demonstrated in Section 2.2, these requirements were largely met due to judicious selection of the formulation and process conditions. When these requirements are met, the breakage rate may be described by a breakage rate constant k and the difference between the median particle size and the limiting size raised to the power n:

$$\frac{dd_{50}(t)}{dt} = -k[d_{50}(t) - d_{\text{lim}}]^n \text{ with } d_{50}(0) = d_{50,0} \tag{2.1}$$

In previous investigations, *n* was commonly taken as 1 (first-order kinetics), and application of separation of variables followed by integration of both sides yielded the following widely used model [33, 90, 170, 171]:

$$d_{50}(t) = d_{\lim} + (d_{50,0} - d_{\lim}) \exp(-kt) \tag{2.2}$$

Here, $d_{50,0}$ is the initial median size. Equation (2.2) with a single process time constant $\tau_p = 1/k$ was not able to fit the whole experimental data governed by two or potentially more characteristic time constants [172]. Hence, in many studies (see e.g., [62, 92]) the initial median particle size at 0th min was discarded, thus making the first time point (e.g., 1st min median size) the initial size for better fitting capability. Depending on the initial PSD and initial breakage kinetics, even eliminating one data point may not allow accurate fitting of the experimental data.

As a commonly used approach in chemically reacting systems [173, 174], an *n*th-order kinetic model may be considered with the objective of resolving the inadequacy of the first-order kinetic model. Separation of the variables in Equation (2.1) with $n \neq 1$ followed by integration of both sides yielded the following equation:

$$d_{50}(t) = d_{\lim} + \left[\left(d_{50,0} - d_{\lim}\right)^{1-n} - (1-n)kt\right]^{1/(1-n)} \tag{2.3}$$

To the best of authors' knowledge, this general *n*th-order model has not been used for describing the breakage kinetics in WSMM before. Note that in ref. [174], *a second-order kinetic model* was assumed without fitting *n* to describe the mass fraction of only coarse particles as a function of time, not the median size of the whole PSD, and it was only applied to the *dry ball milling* of narrow, coarse sieve cuts > 2.5 mm. It did not consider the grinding limit and $d_{\lim}$ either.

Another kinetic modeling approach entails consideration of a time-dependent breakage rate parameter $k(t)$ as follows:

$$\frac{dd_{50}(t)}{dt} = -k(t)[d_{50}(t) - d_{\lim}] \text{ with } d_{50}(0) = d_{50,0} \quad (2.4)$$

with $k(t) = k_0\kappa(t)$. Unlike the constant k in Equations (1–3), here, k_0 is a breakage rate constant. The time-dependent function $\kappa(t)$ can be obtained from a first-order differential equation $d\phi/dt = \kappa(t)$ with $\phi(0) = 0$ at $t = 0$, where ϕ is referred to as the warped- (false-) time. This warped-time concept was introduced in the context of a population balance model before [175, 176], but it has not been used to derive the evolution of median size, as done here for the first time. With the above defining differential equation for ϕ, Equation (2.4) was transformed to a first-order differential equation in ϕ as follows:

$$\frac{dd_{50}(\phi)}{d\phi} = -k_0[d_{50}(\phi) - d_{\lim}] \text{ with } d_{50}(0) = d_{50,0} \quad (2.5)$$

We take, without loss of generality, $\phi = t^n$ as it is the simplest relation with one parameter (n), which satisfies the initial condition for ϕ and simply reduces to the first-order model when $n = 1$. Hence, the breakage rate parameter takes the form: $k(t) = k_0 n t^{n-1}$ and the solution of Equation (2.5) leads to the following warped-time kinetic model:

$$d_{50}(t) = d_{\lim} + \left(d_{50,0} - d_{\lim}\right)\exp(-k_0 t^n) \quad (2.6)$$

Marquardt-Levenberg algorithm was used to fit the three models described by Equations (2.2), (2.3), and (2.6) to the experimental median sizes and $d_{\lim}$, k or k_0, and n were estimated by SigmaPlot software. In the fitting, $d_{\lim}$ was constrained to be smaller

than the final median particle size [90]. Statistical analysis of the fits was performed to discriminate the models and main effects plots of the parameters were prepared.

2.1.5 Microhydrodynamic analysis

The microhydrodynamic parameters, i.e., granular temperature θ, average bead oscillation velocity u_b, frequency of a single bead oscillation ν, maximum contact pressure σ_b^{max}, radius of contact circle α_b, average frequency of drug particle compressions a, and pseudo energy dissipation rate for the drug particles $\Pi\sigma_y$ for all 8 runs were calculated as described in Section 1.4.2 via Equations (1.2)–(1.23). The restitution coefficient for the bead–bead collisions e was taken as 0.9 and 0.76 for YSZ and CPS beads, respectively [177, 178]. Unlike [34, 132], we used a more accurate g_0 model here, i.e., the Lun model [148]. As the bead loadings are high, the bead volume fraction at random packing c_{lim} = 0.63 [147] must be factored in for the g_0 calculation as follows:

$$g_0 = \left[1 - (c/c_{\lim})^{1/3}\right]^{-1} \tag{2.7}$$

We measured μ_L, ρ_L, and P_w (reported in **Table A.1.** of *Appendix A*); ε_{ht} was found to be negligibly small and disregarded, similar to [90]. The fsolve function in MATLAB (see Section A.1 in *Appendix A* for a sample MATLAB code) was used to solve for the only unknown in Equation (1.4), i.e., θ, which was then used to calculate the frequency of single-bead oscillations ν and the average oscillation velocity of the beads u_b. The values of η_b and Y_b were taken as 0.33 and 1.5 GPa for CPS beads [179] and 0.2 and 200 GPa for YSZ beads [180], respectively. ψ is the fraction of the drug particles in the suspension (0.074), and γ is a coefficient which can be taken as 1/3 for elastic contact between the particle and the bead [132]. Young modulus and Poisson's ratio for FNB particles were

taken as 8.93 GPa and 0.3 [181]. Since a reliable value for σ_y of FNB particles were not found in the literature, a pseudo energy dissipation rate was used.

2.1.6 Multiple linear regression and subset selection algorithm

Main effects plots were drawn to visualize how the microhydrodynamic parameters varied upon changes in the stirrer speed and loading of the beads with different materials (CPS and YSZ) in the 3-factor, 2-level DOE. In addition, a relationship between the calculated microhydrodynamic parameters and the breakage rate constant *k* of the *n*th-order kinetic model of the general form $k = k(a, \sigma_b^{max}, \alpha_b, \Pi\sigma_y)$ was sought for by the subset selection algorithm (see Algorithm 1 below), which was modified from ref. [182].

Algorithm 1: Subset Selection

Input: Training Data: $(x_i^1, x_i^2, \dots, x_i^T; y_i)_{i=1}^I$

For each $j = 1, 2, \dots, J$:

(a) Fit linear regression model for all combinations $\binom{T}{j}$ of predictors.

(b) Set the best model BM_j as the one with the highest coefficient of determination R^2

Select overall best models (BMs) among $BM_1, BM_2, \dots, BM_J$ as the one(s) that have adjusted $R^2 \geq 0.99$ and all predictors have a statistically significant relationship ($p\ value\ \leq 0.01$) with the response.

Our analysis includes three multiple linear regression model (MLRM) approaches to determine the relationship between the breakage rate constant *k* (response) and 4 microhydrodynamic parameters σ_b^{max}, α_b, a, and $\Pi\sigma_y$, i.e., first-order MLRM, second-order MLRM, and MLRM with interaction terms. For all three approaches, the training set

consists of $I = 8$ observations (runs) and the available number of predictors T varies in each approach. In the first-order MLRM, we assume that the response and 4 predictors have a direct relation such that there is no interaction or second order term ($T = 4$). The second-order MLRM includes the squared values of the predictors when fitting to the regression ($T = 8$). The MLRM with interaction terms incorporates the pairwise interactions of the predictors ($T = 10$) to the linear regression model. We considered MLRMs that have a maximum of 4 predictors ($J = 4$) because the number of data was limited and a better understanding of the impact of the predictors without forming too complex relations was desired. In fact, even without considering more than 4 predictors in each model, many models had predictors whose coefficients were statistically insignificant (p value > 0.01) due to limited data set, as will be discussed later. Our analysis was done on R 4.0.3 using lm function to fit the MLRMs [183]. We utilized ggplot2 package to plot the selected MLRM [184] (see Section A.2 in *Appendix A* for the R code).

Besides the kinetic–microhydrodynamic model, a purely empirical correlation between k and the process parameters–bead properties of the general form $k = k(\omega, c, \rho_b, Y_b)$ was sought for using the subset selection algorithm. As this correlation does not use any microhydrodynamic variable that directly connects with some aspect of the bead–bead collisions, we refer to it as the purely empirical correlation.

2.2 Results and Discussion

2.2.1 Elucidation of the particle change mechanisms

Figure 2.1 presents the particle sizes in the FNB suspensions after 180 min milling and after 7-day refrigerated storage (Runs 1–8, DOE runs). The median sizes d_{50} were all below

200 nm and the 90% volume passing sizes d_{90} were all below 300 nm. As the particle sizes did not change significantly upon 7-day storage, all milled FNB suspensions were physically stable, and impact of nanoparticle aggregation and/or particle growth through ripening processes was negligible. As will be shown in Section 2.2.2., the timewise evolution of d_{50}–t profiles were all monotone-decreasing, which also confirms the mitigation of particle aggregation–growth to a large extent. Hence, the requirements (refer to Section 2.1.4) for an accurate analysis of the breakage kinetics were generally satisfied by our experiments; the particle breakage was the dominant particle change mechanism during the WSMM runs.

Earlier work on the WSMM of FNB suspensions stabilized by hydroxypropylmethyl cellulose (HPMC) and SDS revealed critical insights about the roles of the stabilizers [46, 54]: excessive HPMC was required to suppress FNB nanoparticle aggregation in the absence of SDS; an optimal concentration of SDS exists (~0.05% w/w), which minimizes aggregation without facilitating Ostwald ripening. Ripening process was rather slow (occurred over days) and quite dependent on the SDS concentration as the solubility of FNB increased with an increasing SDS concentration [169]. Knieke et al. [46] demonstrated via laser diffraction and SEM imaging of the milled/stored fenofibrate nanoparticles in suspension form that the ripening process had no impact on the milled particle size during the milling time-scale at the SDS concentration range of 0.05%–0.25% w/w. Only at 0.25% w/w SDS and upon 7-day storage, notable particle growth (significant increase in d_{50} and d_{90}) and formation of new rhombohedron shape crystals were reported [46]. Considering that our current study used 0.05% w/w SDS, based on Knieke et al. [36] alone, one would not expect that ripening process would have any effect on the breakage

kinetics. Indeed, the monotone decreasing profile of d_{50} during the milling (Section 2.2.2), invariance of d_{50} and d_{90} during the 7-day storage (**Figure 2.1**), and absence of large rhombohedron shape drug crystals in the SEM images (**Figure 2.2**) clearly refute that aggregation or Ostwald ripening played a significant role during the milling–storage.

Apparently, 7.5% HPC–0.05% SDS combination mitigated nanoparticle aggregation without facilitating Ostwald ripening. Such neutral polymer–anionic surfactant combinations have been successfully used to stabilize a multitude of drug nanosuspensions and their success has been attributed to an electrosteric stabilization mechanism as well as enhanced wettability of the relatively hydrophobic drug and deaggregation of drug nanoparticle clusters during the milling [39, 46, 47, 54, 62, 185]. Moreover, besides their steric stabilizing action upon adsorption on drug nanoparticles, cellulosic polymers such as HPC and HPMC are well-known to inhibit nucleation and/or crystal growth (see e.g., [41]), which could have helped to mitigate Ostwald ripening [46].

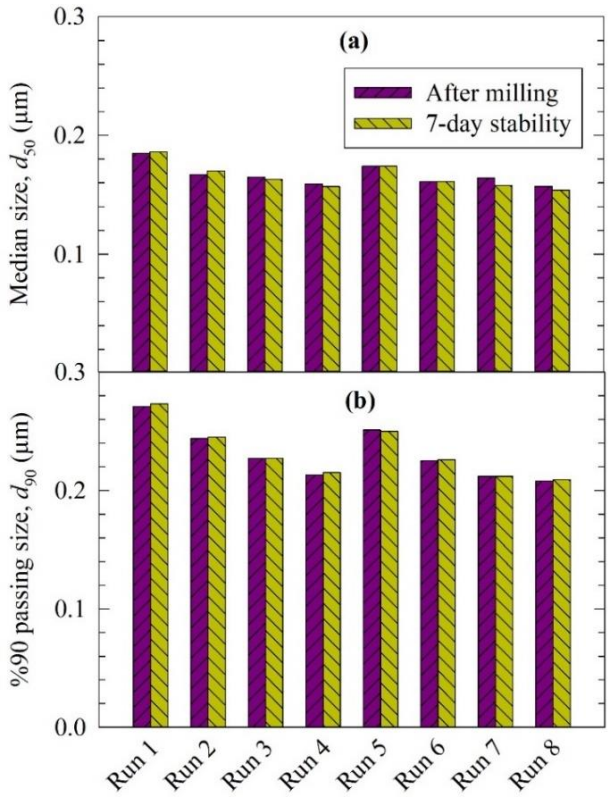

Figure 2.1 Volume-based particle size statistics of the milled FNB suspensions after milling (180 min) and after 7-day storage at 8 °C: (a) median particle size d_{50} and (b) 90% cumulative passing size d_{90}.

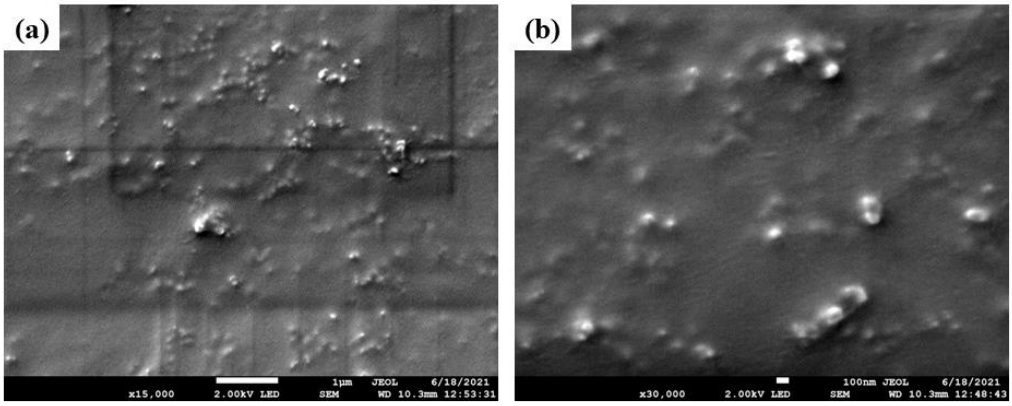

Figure 2.2 SEM image of 180 min milled FNB particles in Run 10 (ω = 3500 rpm, c = 0.425, and YSZ beads): (a) ×15k magnification (scale bar: 1 μm) and (b) ×30k magnification (scale bar: 100 nm).

Milling can change the solid state of a material due to mechanically induced defects and disorder of the crystal lattices and even conversion of the crystalline material to

amorphous form [186-188]. The DSC traces in **Figure 2.3** depicts an endothermal event (fusion) for the as-received crystalline FNB particles, while such an event was absent from the amorphous polymer (HPC). The fusion enthalpy of FNB was reduced approximately in proportion to the amount of amorphous HPC in the physical mixture and the dried nanosuspension. The comparison of the DSC traces of the physical mixture and the dried nanosuspension reveals a 2.4 ^{o}C melting point depression, which could be attributed to nanocrystalline nature of the FNB and the presence of mechanically-induced defects.

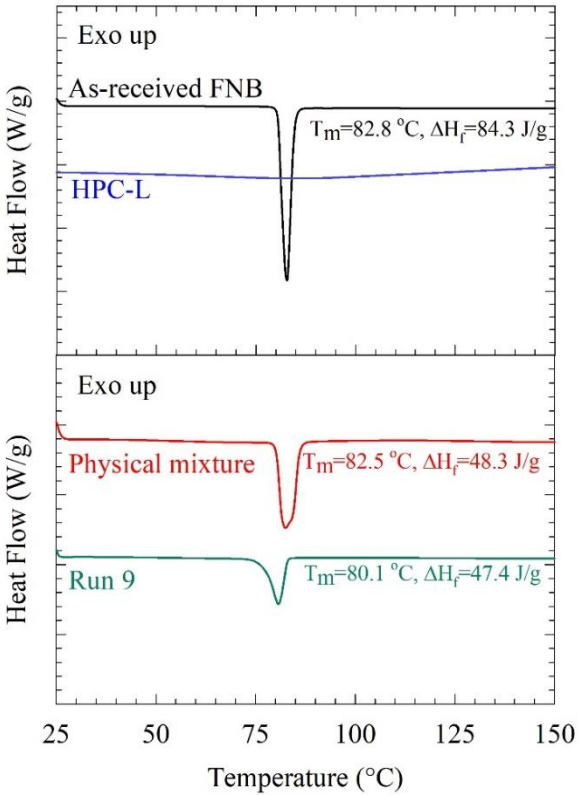

Figure 2.3 DSC traces, with the fusion enthalpy ΔH_f and the peak melting point temperature T_m, of as-received FNB, HPC-L, the unmilled physical mixture, and the dried nanosuspension prepared in Run 10 (ω = 3500 rpm, c = 0.425, and YSZ beads).

2.2.2 Breakage kinetic analysis via first-order, *n*th-order, and warped-time models

The kinetics of FNB particle breakage during WSMM was examined using three kinetic models, i.e., the first-order model, the *n*th-order model, and the warped-time model. To

discriminate these models and identify the best model, the experimental temporal evolution of the median size d_{50} as well as the fittings of the models are presented for CPS beads and YSZ beads in **Figures 2.4** and **2.5**, respectively.

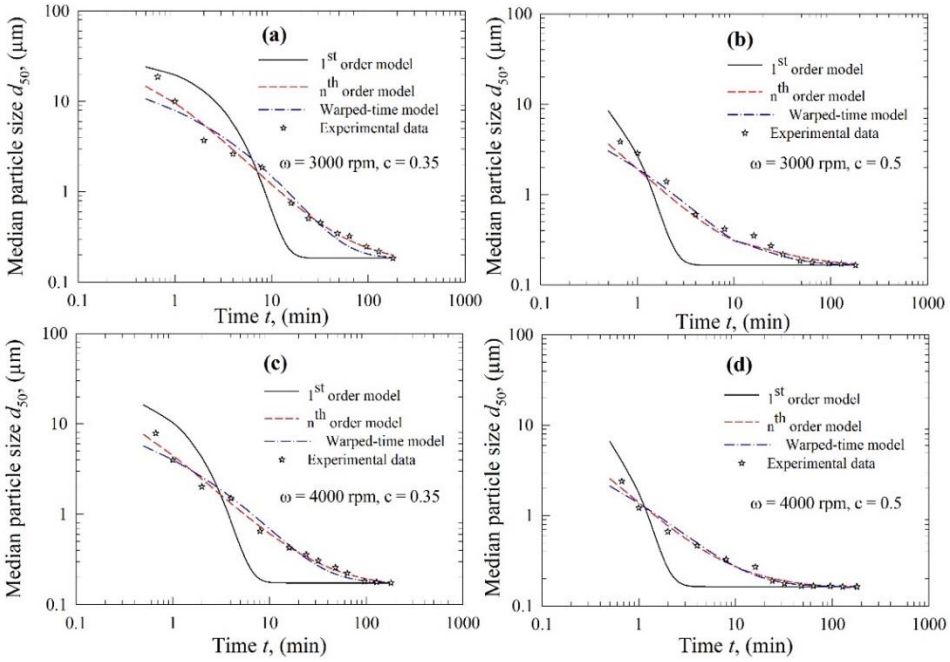

Figure 2.4 Temporal evolution of the median particle size d_{50} during the wet milling of fenofibrate with CPS beads and fitting of the data by various breakage kinetic models: (a) ω = 3000 rpm and c = 0.35, (b) ω = 3000 rpm and c = 0.5, (c) ω = 4000 rpm and c = 0.35, and (d) ω = 4000 rpm and c = 0.5.

Figures 2.4 and **2.5** depict that the coarse FNB particles break much faster (within the first 2–10 min) than the particles in the colloidal size range (< 1 μm). It should be noted that the time axis is logarithmic. The median size decreased monotonically in time and tended toward or attained a limiting size, which is the typical dynamic behavior for a well-stabilized suspension, which confirms the judicious selection of the stabilizers based on our earlier studies. As the impact of particle aggregation and growth was negligible (refer to Section 2.2.1), these observations can be explained by slowing breakage kinetics during WSMM, which can be attributed to the higher strength of the finer particles than the coarser

particles and the reduced probability of capturing the finer particles between the beads [57, 62, 90].

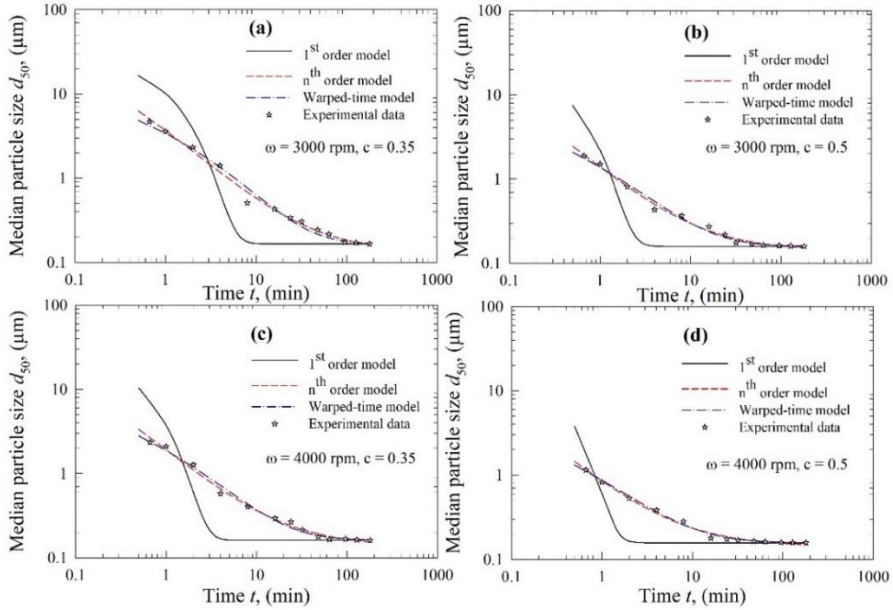

Figure 2.5 Temporal evolution of the median particle size d_{50} during the wet milling of fenofibrate with YSZ beads and fitting of the data by various breakage kinetic models: (a) ω = 3000 rpm and c = 0.35, (b) ω = 3000 rpm and c = 0.5, (c) ω = 4000 rpm and c = 0.35, and (d) ω = 4000 rpm and c = 0.5.

Regardless of the used bead material, the trends in **Figures 2.4** and **2.5** also suggest that the first-order kinetic model failed to fit the experimental data for all conditions. This observation was supported by the fitting statistics in **Table 2.2**, where the model parameters were found to be statistically significant (p value $\leq$ 0.01); however, the fitting was poor with adjusted R^2 < 0.90 for all conditions. Even though the first-order kinetic model is popular, as discussed earlier, it was inadequate to represent the whole experimental kinetic data governed by two or potentially more breakage rate constants [172]. As we want to perform a fair, head-to-head comparison of all models, all experimental data collected were used in the parameter estimation. While the fitting may be improved by removing some of

the initial data points [62, 92], this would come at the expense of reduced robustness of the model. Therefore, no experimental data was disregarded here.

Table 2.2 Statistical Summary of Parameter Estimation Using the First-Order Kinetic Model

Run	Parameter	Value	p value	R^2	Adj. R^2	SSR
1	d_{lim} (μm)	0.185	0.0036	0.818	0.803	1.32
	k (min^{-1})	0.420	0.0006			
2	d_{lim} (μm)	0.166	0.0013	0.805	0.789	1.16
	k (min^{-1})	0.992	0.0002			
3	d_{lim} (μm)	0.165	<0.0001	0.866	0.854	0.786
	k (min^{-1})	1.70	<0.0001			
4	d_{lim} (μm)	0.159	0.0001	0.851	0.838	0.767
	k (min^{-1})	2.54	<0.0001			
5	d_{lim} (μm)	0.174	0.0009	0.832	0.818	1.04
	k (min^{-1})	0.91	0.0002			
6	d_{lim} (μm)	0.161	0.0005	0.820	0.805	0.994
	k (min^{-1})	2.09	<0.0001			
7	d_{lim} (μm)	0.164	<0.0001	0.884	0.875	0.600
	k (min^{-1})	2.80	<0.0001			
8	d_{lim} (μm)	0.157	<0.0001	0.889	0.880	0.554
	k (min^{-1})	4.17	<0.0001			
9	d_{lim} (μm)	0.166	0.0010	0.817	0.802	1.09
	k (min^{-1})	1.10	0.0002			
10	d_{lim} (μm)	0.161	0.0004	0.823	0.809	0.934
	k (min^{-1})	2.18	<0.0001			
11	d_{lim} (μm)	0.190	0.0001	0.838	0.830	1.728
	k (min^{-1})	0.115	<0.0001			
12	d_{lim} (μm)	0.174	0.0001	0.796	0.794	1.710
	k (min^{-1})	0.445	<0.0001			

The first-order model performed poorly compared to the *n*th-order and the warped-time models (refer to **Figures 2.4** and **2.5**). The latter two models followed the experimental breakage trends very well. The fitting statistics presented in **Tables 2.3** and **2.4** confirm that the *n*th-order model and the warped-time model had both statistically significant parameters and their fitting capability was excellent: adjusted $R^2 \geq 0.99$, except

for the fitting of Run 1 data by the warped-time model. When all 12 runs were considered, the *n*th-order model fitted the experimental data better than the warped-time model, as can be inferred from the higher R^2 and adjusted R^2 as well as the lower sum-of-squared residuals (SSR) (except for Runs 8 and 12).

Table 2.3 Statistical Summary of Parameter Estimation Using the *n*th-order Kinetic Model

Run	Parameter	Value	p value	R^2	Adj. R^2	SSR
1	d_{lim} (μm)	0.161	0.0015			
	k ($\mu m^{(n-1)} min^{-1}$)	0.105	0.0002	0.989	0.987	0.077
	n (-)	1.86	<0.0001			
2	d_{lim} (μm)	0.132	<0.0001			
	k ($\mu m^{(n-1)} min^{-1}$)	0.217	<0.0001	0.995	0.994	0.029
	n (-)	2.06	<0.0001			
3	d_{lim} (μm)	0.158	<0.0001			
	k ($\mu m^{(n-1)} min^{-1}$)	0.432	<0.0001	0.996	0.996	0.022
	n (-)	1.90	<0.0001			
4	d_{lim} (μm)	0.142	<0.0001			
	k ($\mu m^{(n-1)} min^{-1}$)	0.686	<0.0001	0.997	0.997	0.013
	n (-)	2.08	<0.0001			
5	d_{lim} (μm)	0.152	<0.0001			
	k ($\mu m^{(n-1)} min^{-1}$)	0.215	<0.0001	0.995	0.994	0.030
	n (-)	1.95	<0.0001			
6	d_{lim} (μm)	0.137	<0.0001			
	k ($\mu m^{(n-1)} min^{-1}$)	0.461	<0.0001	0.997	0.997	0.016
	n (-)	2.10	<0.0001			
7	d_{lim} (μm)	0.154	<0.0001			
	k ($\mu m^{(n-1)} min^{-1}$)	0.806	<0.0001	0.996	0.995	0.023
	n (-)	1.96	<0.0001			
8	d_{lim} (μm)	0.143	<0.0001			
	k ($\mu m^{(n-1)} min^{-1}$)	1.28	<0.0001	0.998	0.998	0.009
	n (-)	2.12	<0.0001			
9	d_{lim} (μm)	0.142	<0.0001			
	k ($\mu m^{(n-1)} min^{-1}$)	0.264	<0.0001	0.996	0.995	0.023
	n (-)	2.00	<0.0001			
10	d_{lim} (μm)	0.136	<0.0001			
	k ($\mu m^{(n-1)} min^{-1}$)	0.527	<0.0001	0.996	0.995	0.023
	n (-)	2.12	<0.0001			
11	d_{lim} (μm)	0.093	<0.0001			
	k ($\mu m^{(n-1)} min^{-1}$)	0.023	<0.0001	0.999	0.998	0.015
	n (-)	2.09	<0.0001			
12	d_{lim} (μm)	0.125	<0.0001			
	k ($\mu m^{(n-1)} min^{-1}$)	0.092	<0.0001	0.994	0.993	0.050
	n (-)	2.11	<0.0001			

Table 2.4 Statistical Summary of Parameter Estimation Using the Warped-Time Kinetic Model

Run	Parameter	Value	p value	R^2	Adj. R^2	SSR
1	d_{lim} (μm)	0.185	0.0003			
	k_0 (min^{-n})	1.34	<0.0001	0.976	0.972	0.173
	n (-)	0.368	<0.0001			
2	d_{lim} (μm)	0.166	<0.0001			
	k_0 (min^{-n})	2.12	<0.0001	0.992	0.991	0.045
	n (-)	0.281	<0.0001			
3	d_{lim} (μm)	0.165	<0.0001			
	k_0 (min^{-n})	2.49	<0.0001	0.990	0.989	0.056
	n (-)	0.281	<0.0001			
4	d_{lim} (μm)	0.159	<0.0001			
	k_0 (min^{-n})	3.06	<0.0001	0.996	0.996	0.020
	n (-)	0.231	<0.0001			
5	d_{lim} (μm)	0.174	<0.0001			
	k_0 (min^{-n})	1.89	<0.0001	0.987	0.985	0.078
	n (-)	0.313	<0.0001			
6	d_{lim} (μm)	0.161	<0.0001			
	k_0 (min^{-n})	2.83	<0.0001	0.996	0.996	0.020
	n (-)	0.240	<0.0001			
7	d_{lim} (μm)	0.164	<0.0001			
	k_0 (min^{-n})	3.09	<0.0001	0.992	0.991	0.039
	n (-)	0.250	<0.0001			
8	d_{lim} (μm)	0.157	<0.0001			
	k_0 (min^{-n})	3.71	<0.0001	0.999	0.999	0.005
	n (-)	0.203	<0.0001			
9	d_{lim} (μm)	0.166	<0.0001			
	k_0 (min^{-n})	2.17	<0.0001	0.992	0.991	0.047
	n (-)	0.287	<0.0001			
10	d_{lim} (μm)	0.160	<0.0001			
	k_0 (min^{-n})	2.88	<0.0001	0.995	0.994	0.025
	n (-)	0.236	<0.0001			
11	d_{lim} (μm)	0.190	<0.0001			
	k_0 (min^{-n})	0.948	<0.0001	0.989	0.987	0.120
	n (-)	0.343	<0.0001			
12	d_{lim} (μm)	0.174	<0.0001			
	k_0 (min^{-n})	1.59	<0.0001	0.996	0.995	0.032
	n (-)	0.306	<0.0001			

2.2.3 Effects of process variables on the kinetic parameters

As both the *n*th-order model and the warped-time model were found to have excellent fitting capability, the impact of process variables on their model parameters, i.e., the limiting size d_{lim}, the breakage rate constant k or k_0, and the exponent n was explored. For the *n*th-order model parameters, the main effects plots in **Figure 2.6** and the fitted parameters in **Table 2.3** (DOE Runs 1–8) suggest the following major trends: (i) the breakage rate constant k was significantly higher at the higher stirrer speed, the higher bead loading, and upon the use of the YSZ beads as opposed to the CPS beads; (ii) d_{lim} varied in a narrow range from 132–161 nm with an 8-run average of 148±11 nm (RSD = 7.4%); it decreased slightly at the higher speed and with the use of the YSZ beads and increased slightly at the higher bead loading; (iii) n slightly increased upon an increase in the stirrer speed and the use of the YSZ beads, and the bead loading had almost no effect. The changes were so small that the breakage kinetics was nearly second order overall (n = 2.00±0.06 from an 8-run average, RSD = 3.0%). As compared to the drastic variation in k, the variation in n and d_{lim} for a given bead material (CPS or YSZ) was relatively small, thus, justifying one to use constant, average values of n and d_{lim} for a specific bead material.

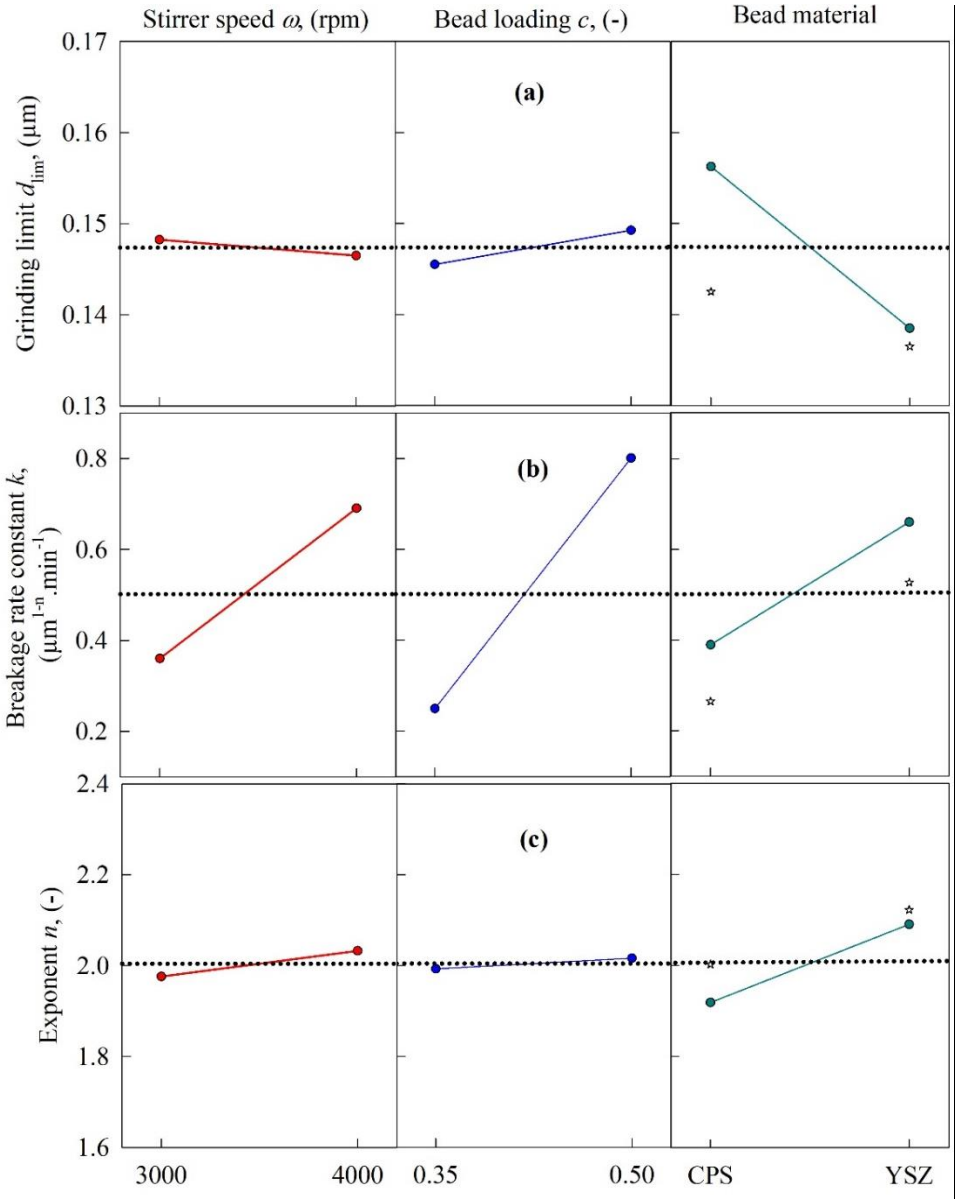

Figure 2.6 Main effects plots for the parameters of the *n*th-order kinetic model as a function of the process variables: (a) grinding limit d_{lim}, (b) breakage rate constant *k*, and (c) exponent *n*. The center point experimental data (Runs 9 and 10) were added to the right-most panel.

The variation of the breakage rate constant k_0 of the warped-time model with the process parameters (see **Figure 2.7** and refer to **Table 2.4**) was like that of *k* of the *n*th-order model. However, both d_{lim} and *n* were lower at the higher stirrer speed, the higher bead loading, and upon the use of the YSZ beads as opposed to the CPS beads. While d_{lim}

again varied in a narrow range from 157–185 nm with an 8-run average of 166±9 nm and the impact of the process parameters was rather limited (RSD = 5.4%), the relative change in *n* was notable for different processing conditions: 8-run average of 0.271±0.03 (RSD = 11%).

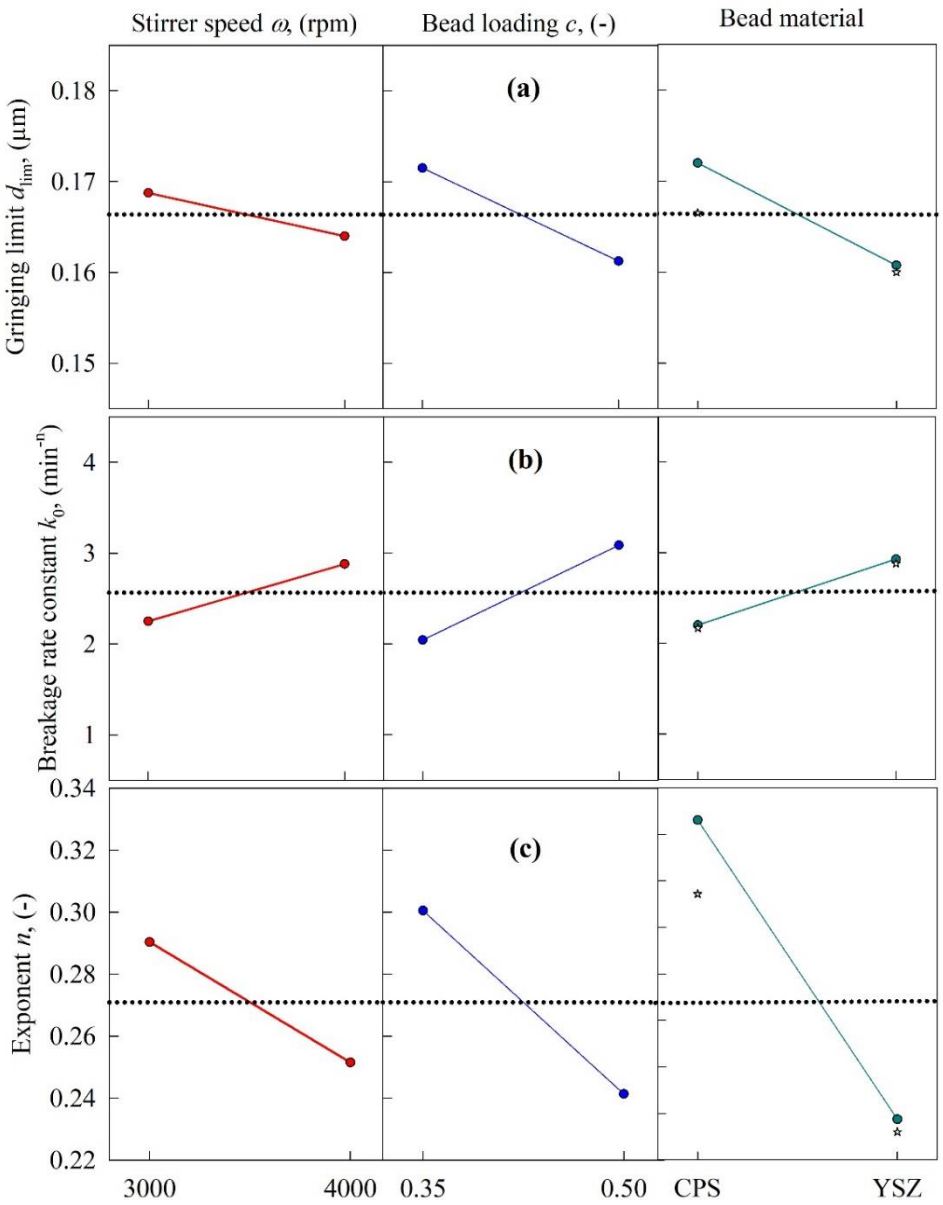

Figure 2.7 Main effects plots for the parameters of the warped-time kinetic model as a function of the process variables: (a) grinding limit d_{lim}, (b) breakage rate constant k_0, and (c) exponent *n*. The center point experimental data (Runs 9 and 10) were added to the right-most panel.

Although the warped-time model has excellent fitting capability, two issues warrant discussion. First, the grinding limit d_{lim} was found to be equal to the final milled particle size at 180 min, which is somewhat unrealistic as in the limit $t \to \infty$ the limiting particle size must be smaller than that at 180 min. This was correctly captured by the smaller d_{lim} of the *n*th-order model (see **Table 2.3** vs. **Table 2.4**). Second, unlike the case for *k* and *n* of the *n*th-order model, both k_0 and n drastically changed in opposite directions and considering the time-dependence of $k(t) = k_0 n t^{n-1}$, the impact of the processing variables on the overall breakage rate is hard to interpret without further quantitative analysis. Along with the better fitting capability of the *n*th-order model, these physical considerations led us to choose the *n*th-order model as the best kinetic model and use it for the microhydrodynamic correlations. If we were to choose the warped-time model, there would be two separate kinetic–microhydrodynamic correlations, one for *k* and another for *n*, and this would clearly be undesirable situation.

Figures 2.6 and **2.7** (right-most panel) show that the center-point responses (Run 9 for CPS and Run 10 for YSZ) and the mean values for CPS (Runs 1, 3, 5, and 7) and YSZ (Runs 2, 4, 6, and 8) deviated although they yielded similar trends in terms of increase/decrease of the kinetic parameters upon use of the CPS beads vs. the YSZ beads. We have not used the main effects plots to establish a quantitative model between the kinetic parameters and the process parameters. The kinetic–microhydrodynamic correlation of the form $k = k(a, \sigma_b^{max}, \alpha_b, \Pi\sigma_y)$ implicitly achieves that task (see Section 2.2.4). As will also be shown in Section 2.2.5, the purely empirical correlation of the form $k = k(\omega, c, \rho_b, Y_b)$ was not linear; there exist several interactions among the independent variables.

2.2.4 Microhydrodynamic origin of the calculated breakage rate constant

The microhydrodynamic parameters, i.e., granular temperature θ, average bead oscillation velocity u_b, frequency of a single bead oscillation ν, maximum contact pressure σ_b^{max}, radius of contact circle α_b, average frequency of drug particle compressions a, and pseudo energy dissipation rate for the drug particles $\Pi\sigma_y$ for all 8 runs were calculated and presented in **Table A.1** of *Appendix A*. The main effects plots (**Figures 2.8** and **2.9**) and **Table A.1** show that all microhydrodynamic parameters were significantly higher at the higher stirrer speed, signifying more frequent collisions of the beads with higher stress intensity and ensuing higher frequency of drug particle compressions. This is the microhydrodynamic origin of the higher breakage rate k at the higher stirrer speed (refer to **Figure 2.6** and **Table 2.3**). The use of the YSZ beads as opposed to the CPS beads also led to significantly higher microhydrodynamic parameters due to the much higher density of the YSZ beads, albeit with two notable exceptions (**Figures 2.8** and **2.9**). Owing to their lower modulus of elasticity, CPS beads had higher α_b than the YSZ beads (**Figure 2.9b**); hence, the CPS beads could capture more drug particles per CPS–CPS bead collision. This effect was counteracted by the higher θ, u_b, ν, σ_b^{max}, and $\Pi\sigma_y$ of the YSZ beads, signifying a higher number of more energetic/forceful YSZ bead–bead collisions. These two counteracting effects led to a slight increase in the frequency of drug particle compressions a when the YSZ beads vs. the CPS beads were used (**Figure 2.9c**), which favored breakage (refer to **Figure 2.6** and **Table 2.3**). We also note from **Figures 2.8** and **2.9** (right-most panel) that the center-point responses (Run 9 for CPS and Run 10 for YSZ) and the mean values for CPS (Runs 1, 3, 5, and 7) and YSZ (Runs 2, 4, 6, and 8) yielded similar trends

in terms of increase/decrease of the microhydrodynamic parameters upon use of CPS vs. YSZ.

When a higher bead loading c was used, two counteracting effects were observed (**Figures 2.8** and **2.9**). Due to the occurrence of higher drag forces and more bead–bead squeezing events at the higher c, the energy dissipation due to viscous losses and inelastic collisions were higher, which led to lower θ, u_b, α_b, and σ_b^{max} (lower energy/less forceful bead collisions) and did not favor particle breakage. However, the dramatic increase in the number concentration of the beads along with higher g_0 led to more frequent collisions, signified by higher ν, a, and $\Pi\sigma_y$, which favors breakage. It appears that higher ν, a, and $\Pi\sigma_y$ (favorable for breakage) is much more influential on k than lower θ, u_b, α_b, and σ_b^{max} (unfavorable for breakage), as inferred from the positive impact of c on k (refer to **Table 2.3** and **Figure 2.6**).

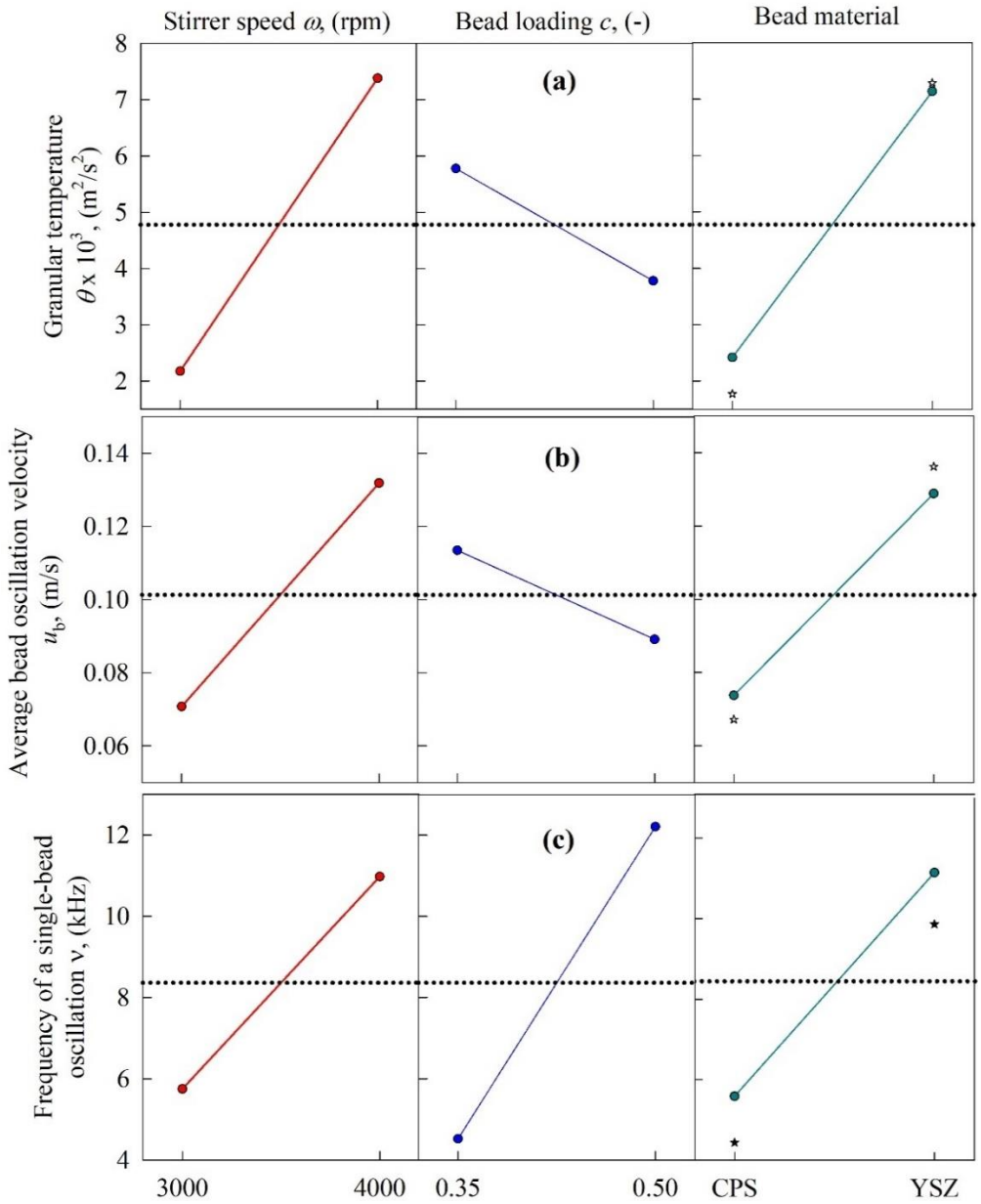

Figure 2.8 Main effects plots for the microhydrodynamic parameters as a function of the process variables: (a) granular temperature θ, (b) average bead oscillation velocity u_b, and (c) frequency of a single-bead oscillation ν. The center point experimental data (Runs 9 and 10) were added to the right-most panel.

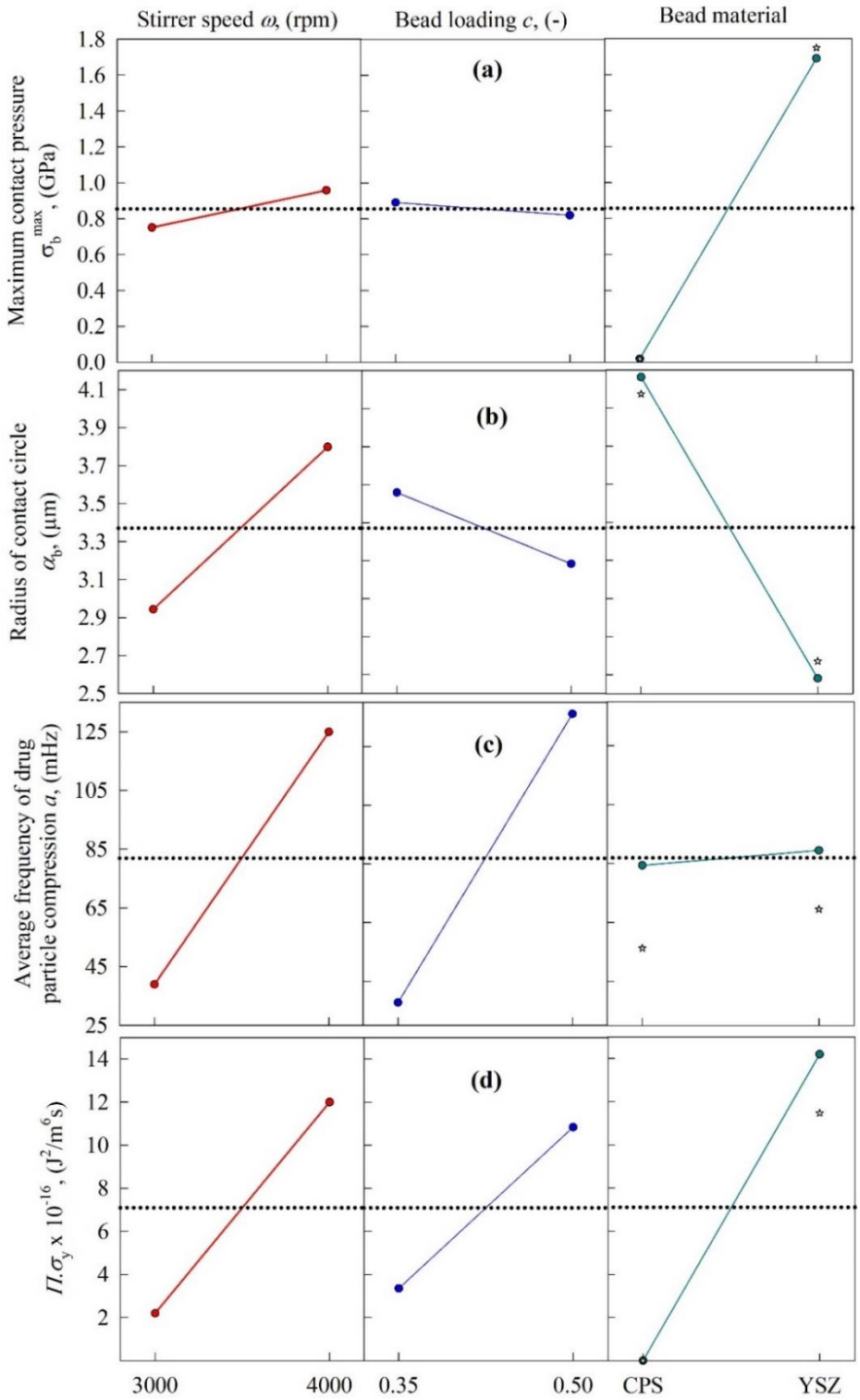

Figure 2.9 Main effects plots for the microhydrodynamic parameters as a function of the process variables: (a) maximum contact pressure σ_b^{max}, (b) radius of contact circle α_b, (c) average frequency of drug particle compression a, and (d) the pseudo energy dissipation rate $\Pi\sigma_y$. The center point experimental data (Runs 9 and 10) were added to the right-most panel.

A statistically and physically significant relationship between the microhydrodynamic parameters and the breakage rate constant k was expected based on the microhydrodynamic insights and was examined via multiple linear regression models (MLRMs). Three different MLRM approaches were investigated, i.e., the first-order MLRM, where the microhydrodynamic parameters are considered to have a linear relationship with k; the second-order MLRM, where the squares of the microhydrodynamic parameters are considered to have an impact on k as well; and the MLRM with interaction terms, where the multiple of two microhydrodynamic parameters may affect k. On purely physical grounds, k must be zero if any microhydrodynamic parameter is zero, suggesting a zero intercept. Indeed, when the intercept was included in the models, one or more MLRM coefficients, including the intercept, were generally found to be statistically insignificant (see **Table A.2** in *Appendix A*). Hence, the intercept was set to zero in the models. We selected σ_b^{max}, α_b, a, and $\Pi\sigma_y$ as the predictive microhydrodynamic parameters since they are not directly correlated to each other and each of them represents a different aspect of the bead–bead collisions (σ_b^{max} and α_b) and the compression frequency/energy of the captured drug particles (a and $\Pi\sigma_y$).

As the maximum allowed number of predictors J was chosen as 4, the algorithm considers 4 best models (BM_1, BM_2, BM_3, and BM_4) for each MLRM. As can be seen from **Table 2.5**, BM_1 has the average frequency of drug particle compression a as the predictor with the adjusted R^2 of 0.91 for all three MLRMs. BM_2 was found to have the same two predictors for all MLRMs again where maximum contact pressure σ_b^{max} and a were found to have the most impact on k. For BM_3, the algorithm selected radius of contact circle α_b in addition to the predictors used in BM_2 when the first-order MLRM was used. On the other

hand, when the second-order MLRM was used, the algorithm selected a^2 in addition to the predictors used in BM_2 for BM_3. Besides, BM_3 of MLRM with interaction term model suggests a should be used together with its interaction with α_b and $\Pi\sigma_y$. For BM_4, the selected predictors contain all available predictors of the first-order MLRM. For the second-order MLRM, the algorithm removed σ_b^{max} from BM_3 and added $\Pi\sigma_y$ and α_b^2 for BM_4. Finally, for the MLRM with interaction terms, the algorithm kept all BM_3 predictors for BM_4 with the addition of $\Pi\sigma_y$. To select the best model among all the models presented in **Table 2.5**, the following criteria were used: adjusted $R^2 \geq 0.99$ and p value ≤ 0.01. Only the following 3-parameter MLRM with interaction terms satisfied the criteria:

$$k = 1.87 \times 10^{-2} a - 3.25 \times 10^{-3} \alpha_b a - 9.77 \times 10^{-5} (\Pi\sigma_y) a \tag{2.8}$$

The k predicted by Equation (2.8) vs. the actual k of the nth-order kinetic model is presented in **Figure 2.10**. Overall, these results corroborate that a is the most important microhydrodynamic parameter that explains most of the process related variation of the breakage rate constant k along with its interaction with α_b and $\Pi\sigma_y$.

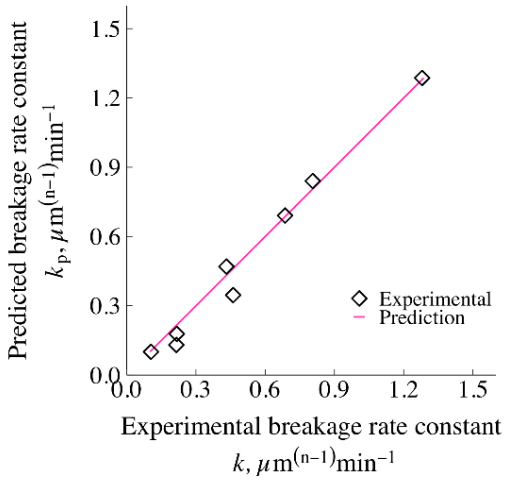

Figure 2.10 The breakage rate parameter k of the nth-order model predicted with the MLRM with interaction terms, 3-parameter (Equation (2.8)) vs. the experimentally determined k. This is the only MLRM that satisfied adjusted $R^2 \geq 0.99$ and p value ≤ 0.01 for all coefficients.

Table 2.5 Statistical Summary of the Estimated MLRM Coefficients Correlating the Breakage Rate Constant *k* of The *n*th-order Kinetic Model to the Microhydrodynamic Parameters

Approach	Best Model	Parameter			Model			
		Symbol[a]	Coefficient[b]	p value	R^2	Adj. R^2	SSR	p value
First-order MLRM	BM_1	a (mHz)	5.66×10^{-3}	3.91×10^{-5}	0.922	0.911	0.253	3.91×10^{-5}
	BM_2	σ_b^{max} (GPa)	1.52×10^{-1}	8.45×10^{-3}	0.978	0.970	0.073	1.12×10^{-5}
		a (mHz)	4.68×10^{-3}	4.05×10^{-5}				
	BM_3	$\boldsymbol{\sigma_b^{max}}$ (GPa)	1.52×10^{-1}	1.86×10^{-2}	0.978	0.964	0.073	1.50×10^{-4}
		$\boldsymbol{\alpha_b}$ (μm)	1.86×10^{-3}	9.24×10^{-1}				
		a (mHz)	4.64×10^{-3}	6.88×10^{-4}				
	BM_4	$\boldsymbol{\sigma_b^{max}}$ (GPa)	1.51×10^{-1}	1.08×10^{-1}	0.978	0.955	0.073	1.47×10^{-3}
		$\boldsymbol{\alpha_b}$ (μm)	2.07×10^{-3}	9.41×10^{-1}				
		$\boldsymbol{a}$ (mHz)	4.63×10^{-3}	1.19×10^{-2}				
		$\boldsymbol{\Pi\sigma_y}$ ($\times10^{-16}$ J^2/m^6s)	1.06×10^{-4}	9.90×10^{-1}				
Second-order MLRM	BM_1	a (mHz)	5.66×10^{-3}	3.91×10^{-5}	0.922	0.911	0.253	3.91×10^{-5}
	BM_2	σ_b^{max} (GPa)	1.52×10^{-1}	8.45×10^{-3}	0.978	0.970	0.073	1.12×10^{-5}
		a (mHz)	4.68×10^{-3}	4.05×10^{-5}				
	BM_3	$\boldsymbol{\sigma_b^{max}}$ (GPa)	1.40×10^{-1}	1.90×10^{-2}	0.982	0.971	0.060	9.14×10^{-5}
		a (mHz)	6.11×10^{-3}	7.74×10^{-3}				
		$\boldsymbol{a^2}$ **(mHz^2)**	-7.38×10^{-6}	3.39×10^{-1}				
	BM_4	a (mHz)	1.22×10^{-2}	1.27×10^{-3}	0.994	0.988	0.020	1.14×10^{-4}
		$\boldsymbol{\Pi\sigma_y}$ **($\times10^{-16}$ J^2/m^{6}s)**	1.19×10^{-2}	1.81×10^{-2}				
		$\boldsymbol{\alpha_b^2}$ **(μm^2)**	-1.16×10^{-2}	4.14×10^{-2}				
		a^2 (mHz^2)	-3.64×10^{-5}	4.88×10^{-3}				
MLRM with interaction terms	BM_1	a (mHz)	5.66×10^{-3}	3.91×10^{-5}	0.922	0.911	0.253	3.91×10^{-5}
	BM_2	σ_b^{max} (GPa)	1.52×10^{-1}	8.45×10^{-3}	0.978	0.970	0.073	1.12×10^{-5}
		a (mHz)	4.68×10^{-3}	4.05×10^{-5}				
	BM_3	a (mHz)	1.87×10^{-2}	2.74×10^{-4}	0.992	0.988	0.024	9.98×10^{-6}
		$\alpha_b a$ (μm.mHz)	-3.25×10^{-3}	1.20×10^{-3}				
		$a\Pi\sigma_y$ ($\times10^{-16}$ mHz J^2/m^6s)	-9.77×10^{-5}	6.67×10^{-3}				
	BM_4	a (mHz)	1.53×10^{-2}	3.20×10^{-4}	0.998	0.997	0.005	6.50×10^{-6}
		$\boldsymbol{\Pi\sigma_y}$ **($\times10^{-16}$ J^2/m^{6}s)**	1.86×10^{-2}	1.54×10^{-2}				
		$\alpha_b a$ (μm.mHz)	-2.48×10^{-3}	1.31×10^{-3}				
		$a\Pi\sigma_y$ ($\times10^{-16}$ mHz J^2/m^6s^2)	-1.51×10^{-4}	8.96×10^{-4}				

[a]Statistically insignificant (p value > 0.01) parameters are bolded. $\Pi\sigma_y$ is treated as a single parameter as σ_y is a constant. [b]The coefficients have the units that make the MLRM equation dimensionally homogeneous.

To gauge the usefulness of the proposed kinetic–microhydrodynamic correlation in Equation (2.8), we compared it to a purely empirical correlation, which does not require

any fundamental understanding of the underlying microhydrodynamics. The breakage rate constant was simply assumed to be a function of the process parameters ω and c as well as the bead properties ρ_b and Y_b, i.e., $k = k(\omega, c, \rho_b, Y_b)$. The bead properties were different for different bead materials.

Table 2.6 Statistical Summary of the Estimated MLRM Coefficients Correlating the Breakage Rate Constant k of the nth-order Kinetic Model to the Process Parameters–Bead Properties (The Purely Empirical Model)

Approach	Best Model	Parameter			Model			
		Symbol[a]	Coefficient[b]	p value	R^2	Adj. R^2	SSR	p value
First-order MLRM	BM_1	c (-)	1.31	1.51×10^{-3}	0.783	0.752	0.707	1.51×10^{-3}
	BM_2	c (-)	1.08	2.71×10^{-2}	0.809	0.745	0.623	6.96×10^{-3}
		$\boldsymbol{Y_b}$ (GPa)	4.02×10^{-3}	4.03×10^{-1}				
	BM_3	c (-)	3.68	2.43×10^{-2}	0.908	0.853	0.299	5.02×10^{-3}
		$\boldsymbol{\rho_b}$ (kg/m^3)	-1.17×10^{-3}	6.76×10^{-2}				
		$\boldsymbol{Y_b}$ (GPa)	3.07×10^{-2}	6.17×10^{-2}				
	BM_4	ω (rpm)	3.31×10^{-4}	3.03×10^{-2}	0.975	0.950	0.081	1.81×10^{-3}
		c (-)	3.68	5.37×10^{-3}				
		ρ_b (kg/m^3)	-2.33×10^{-3}	7.04×10^{-3}				
		Y_b (GPa)	5.95×10^{-2}	6.62×10^{-3}				
Second-order MLRM	BM_1	c^2 (-)	2.98	4.78×10^{-4}	0.843	0.820	0.512	4.78×10^{-4}
	BM_2	c^2 (-)	2.52	8.13×10^{-3}	0.868	0.824	0.431	2.30×10^{-3}
		$\boldsymbol{Y_b^2}$ (GPa^2)	4.81×10^{-6}	3.27×10^{-1}				
	BM_3	$\boldsymbol{c}$ (-)	-4.23	5.86×10^{-2}	0.930	0.888	0.228	2.57×10^{-3}
		$\boldsymbol{\omega^2}$ (rpm^2)	4.72×10^{-8}	8.03×10^{-2}				
		c^2 (-)	9.30	2.45×10^{-2}				
	BM_4	ω (rpm)	3.31×10^{-4}	3.03×10^{-2}	0.975	0.950	0.081	1.81×10^{-3}
		c (-)	3.68	5.37×10^{-3}				
		Y_b (GPa)	-1.56	7.06×10^{-3}				
		Y_b^2 (GPa^2)	7.77×10^{-3}	7.04×10^{-3}				
MLRM with interaction terms	BM_1	ωc (rpm)	3.83×10^{-4}	5.38×10^{-4}	0.838	0.814	0.530	5.38×10^{-4}
	BM_2	ω (rpm)	-3.01×10^{-4}	4.44×10^{-2}	0.922	0.895	0.256	4.83×10^{-4}
		ωc (rpm)	1.07×10^{-3}	8.10×10^{-3}				
	BM_3	Y_b (GPa)	-8.32×10^{-1}	2.44×10^{-3}	0.980	0.969	0.063	1.07×10^{-4}
		ωc (rpm)	9.56×10^{-4}	4.51×10^{-4}				
		$\rho_b Y_b$ (GPa.kg/m^3)	1.38×10^{-4}	2.43×10^{-3}				
	BM_4	ω (rpm)	-3.01×10^{-4}	2.49×10^{-3}	0.993	0.985	0.024	1.61×10^{-4}
		ωc (rpm)	1.50×10^{-3}	7.58×10^{-4}				
		$c\rho_b$ (kg/m^3)	-1.87×10^{-3}	1.42×10^{-2}				
		cY_b (GPa)	5.02×10^{-2}	1.17×10^{-2}				

[a]Statistically insignificant (p value > 0.05) parameters are bolded. [b]The coefficients have the units that make the MLRM equation dimensionally homogeneous.

The statistical results from the MLRM and the subset selection algorithm are presented in **Table 2.6**. As most MLRMs for the purely empirical correlation have

relatively low R^2, high SSR, and mostly statistically insignificant parameters (at 99% confidence level), we relaxed the statistical significance criterion from 99% confidence level to 95% confidence level, i.e., $p \leq 0.05$, which has also been used widely in the literature. Hence, BM_4 with the interaction terms was selected as it satisfied adjusted $R^2 \geq 0.99$ with all statistically significant coefficients at the 95% confidence level. This purely empirical correlation, Equation (2.9), signifies multiple binary interactions among the independent variables.

$$k = -3.01 \times 10^{-4}\omega + 1.50 \times 10^{-3}\omega c - 1.87 \times 10^{-3} c\rho_{\mathrm{b}} + 5.02 \times 10^{-2} cY_{\mathrm{b}} \tag{2.9}$$

2.2.5 Predictive capability of the kinetic-microhydrodynamic model and the purely empirical model

The timewise evolution of the median size in Runs 9–12, which were not used in the calibration of the kinetic–microhydrodynamic correlation and the purely empirical correlation, was directly fitted by the *n*th-order kinetic model first (**Figure 2.11a**). **Table 2.7** presents the statistical summary. As expected, **Figure 2.11a** and **Table 2.7** show that the kinetic model fitted the data well ($R^2 > 0.99$). Then, we estimated the *k* value of the *n*th-order model using the kinetic–microhydrodynamic correlation (Equation (2.8)) and the purely empirical correlation (Equation (2.9)). As the *n* and d_{lim} values varied in a much smaller range than the *k* values for the DOE (Runs 1–8), in the predictions, we assumed constant values for *n* and d_{lim} by calculating their average values for the CPS beads (Runs 1, 3, 5, and 7) and the YSZ beads (Runs 2, 4, 6, and 8). A comparison of these average *n* and d_{lim} values in the predictions vs. the directly fitted *n* and d_{lim} values for Runs 9–12 (**Table 2.7**) reveals that this assumption was generally valid, and the deviations from the

fitted values were reasonable small with the only exception of Run 11 d_{lim}. The relatively low estimated d_{lim} value was most likely related to the fact that even after 7 h milling, the profile did not attain or approach to a plateau under the lowest energetic conditions with the CPS beads. In general, the alternative approach of developing correlations for n and d_{lim}, like those for k, appears to be unwarranted.

Figure 2.11b presents the temporal evolution of the median size in Runs 9–12 predicted by the kinetic–microhydrodynamic correlation (Equation (2.8)), while **Figure 2.11c** presents the same predicted by the purely empirical model (Equation (2.9)). Having a cursory look at **Table 2.7** and visual assessment of these figures, we find that the purely empirical correlation did not even predict the evolution at the center point conditions (Runs 9 and 10). The reason for this is that the empirical correlation needs many more data points or experimental milling runs: e.g., 18 runs for a 3-level (low-medium-high) values of the stirrer speed and the bead loading with the CPS and YSZ beads, which would increase the resources, time, and effort by 125% as compared with the current 8-run DOE. Such an expanded DOE could enable the empirical model to have statistically more reliable parameters and perhaps additional terms in Equation (2.9) for better fitting capability. However, it is unclear if that could resolve the second major issue with the purely empirical model, i.e., its utter failure to predict the profiles of Runs 10 and 11 with the experimental conditions outside the domain of the 8-run DOE. In fact, it predicts a negative k value for Run 11 (no prediction curve presented in **Figure 2.11c**)! Hence, as expected, the purely empirical model had little to no predictive capability. In contrast, the kinetic–microhydrodynamic correlation has remarkable prediction capability for Runs 9 and 10, as signified $R^2 > 0.99$ and low SSR values that are close to those of the direct fitting. Similarly

excellent prediction was made for Run 12, which was outside the DOE. Although the kinetic–microhydrodynamic model underpredicted the median size after 10 min milling in Run 11, this prediction was reasonable and certainly superior to that by the purely empirical model, which predicted a negative *k*.

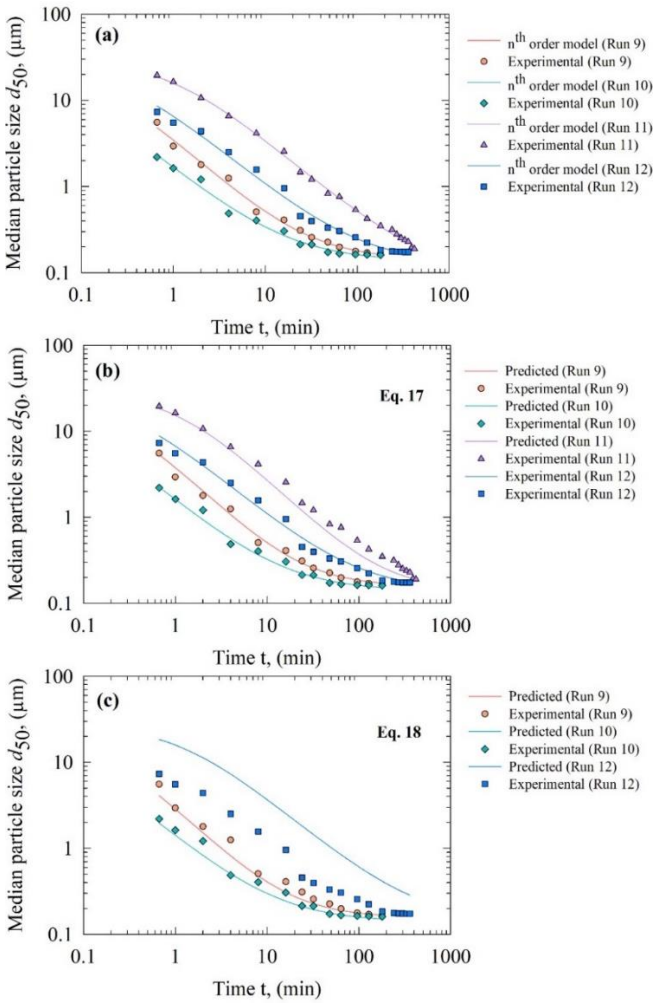

Figure 2.11 Temporal evolution of the median particle size d_{50} during the wet milling of fenofibrate and (a) its direct fit by the *n*th-order kinetic model in Equation (2.3), (b) the predicted evolution of d_{50} using k estimated by Equation (2.8), and (c) the predicted evolution of d_{50} using k estimated by Equation (2.9).

Table 2.7 Statistical Summary of the Parameters of the *n*th-order Model Fitting vs. Predictions by the Kinetic–Microhydrodynamic Model (Equation (2.8)) and the Purely Empirical Model (Equation (2.9))

Run	Direct fit, Prediction	d_{lim} (μm)	k ($\mu m^{n-1}min^{-1}$)	n (-)	R^2	SSR
9	n^{th} order model fit	0.142	0.264	2.00	0.996	0.023
	Prediction by Equation (2.8)	0.156	0.280	1.92	0.995	0.028
	Prediction by Equation (2.9)	0.156	0.383	1.92	0.986	0.086
10	n^{th} order model fit	0.136	0.527	2.12	0.996	0.023
	Prediction by Equation (2.8)	0.139	0.574	2.09	0.995	0.026
	Prediction by Equation (2.9)	0.139	0.676	2.09	0.837	0.257
11	n^{th} order model fit	0.093	0.023	2.09	0.999	0.015
	Prediction by Equation (2.8)	0.156	0.041	1.92	0.978	0.156
	Prediction by Equation (2.9)	0.156	-0.185	1.92	N/A	N/A
12	n^{th} order model fit	0.125	0.092	2.11	0.994	0.050
	Prediction by Equation (2.8)	0.139	0.093	2.09	0.993	0.055
	Prediction by Equation (2.9)	0.139	0.021	2.09	0.644	2.65

2.2.6 Limitations of the models

The main assumptions and limitations of the microhydrodynamic model have been mentioned in Section 2.2.6. Here, we focus on those related to the kinetic models. In the DOE, we considered a fixed batch size and suspension flow rate, and investigated the impact of the stirrer speed, bead loading, and bead type. Hence, the models in this chapter are strictly valid only at the respective experimental scale–batch size for the given flow rate in the recirculation mill. In the recirculation mill, two separate characteristic times exits: the mean residence time in the mill ($\tau_m = V_{sm}/Q$), where Q is the suspension flow rate and V_{sm} is the suspension volume in the mill, and the mean residence time in the holding tank ($\tau_T = V_T/Q$), where V_T is the volume (or batch size) in the holding tank. Hence, the milled particle size distribution (PSD) and the overall breakage kinetics depend on these two characteristic times. Unfortunately, our simple kinetic models cannot rigorously capture the impact of recirculation. A rigorous analysis of the recirculation could be made using a population balance model (PBM) for both the mill and the holding tank by

assuming well-mixedness or determining the residence time distribution experimentally. Interestingly, even most of the existing PBMs for the recirculation mode of WSMM used the equations valid for a batch mill without any consideration of the holding tank and two different mean residence times (e.g., [96, 97]). We found two PBM studies that correctly accounted for the recirculation effects [87, 189]. However, Diemer [189] did not consider WSMM; Annapragada and Adjei [87] used a specific breakage rate kernel that incorporated an unrealistic physical model (see [32]). To the best knowledge of the authors [32], a PBM that incorporates underlying microhydrodynamic parameters does not exist.

In this chapter, we did not investigate the impact of the batch size and the suspension flow rate, which can be rigorously examined using a PBM. The batch size is typically set; it has rarely been varied and examined in the pharmaceutical WSMM literature [10]. A comparison of the first-order time constants estimated for the breakage kinetics of identical griseofulvin suspensions under nearly identical process conditions in the same recirculation mill [62, 89] suggests that the particles were coarser at any given time when the batch size was 440 mL vs. 220 mL, except when the milling time was long enough for the particles to reach the limiting size. At any milling time, the number of theoretical passes of the holding tank content through the mill was halved (mean residence time doubled) when the batch size was doubled. For a fixed batch size, an increase in the suspension flow rate led to a higher number of theoretical passes of the entire mill content through the mill as well as a lower mean residence time both in the mill and in the holding tank, which was found to result in finer particles [87] and a sharper PSD at a given time [87, 89].

2.3 Conclusions

This chapter aimed to examine the FNB breakage rate in WSMM operating at various stirrer speeds and volumetric loading of CPS–YSZ beads via three kinetic models. The newly developed *n*th-order kinetic model with $n \cong 2$ turned out to be the best overall model that described the temporal evolution of the median size well. While the emergence of nearly second-order kinetics is interesting, further research is warranted if this finding has general applicability to multiple drugs and broader range of processing conditions. The breakage rate constant of this model was found to be higher at the higher stirrer speed, the beads loading, and upon use of YSZ vs. CPS beads. Hence, cycle time will be greatly reduced by running the WSMM at 4000 rpm with 50% YSZ beads. The microhydrodynamic parameters provided valuable insights and a physical basis for the observed breakage behaviors under different operating conditions. A statistically significant ($p \leq 0.01$) MLRM of three microhydrodynamic parameters explained the variation in the breakage rate constant best ($R^2 \geq 0.99$). The average frequency of drug particle compressions interacting with two other microhydrodynamic parameters, i.e., pseudo energy dissipation rate and the radius of the bead–bead contact circle govern the breakage kinetics in WSMM. These models are expected to be useful to pharmaceutical engineers who can (i) describe the breakage kinetics for the WSMM process quantitively and (ii) gain advanced process understanding and insights through modeling during pharmaceutical development of a WSMM process with reduced cycle time. This chapter also hints the need for developing a microhydrodynamically inspired population balance model to predict the timewise evolution of the whole drug particle size distribution, not just the median particle size, during the WSMM.

CHAPTER 3

EFFECTS OF BEAD PACKING LIMIT CONCENTRATION ON MICROHYDRODYNAMICS-BASED PREDICTION OF BREAKAGE KINETICS IN WET STIRRED MEDIA MILLING

This chapter evaluated wet-milling kinetics of a drug in a stirred mill using a microhydrodynamic model with various radial distribution functions at contact (RDFs). An *n*th-order kinetics model was fitted to the median size evolution data at several stirrer speeds and loadings of polystyrene/zirconia beads to identify the breakage rate constant *k*. Microhydrodynamic parameters were calculated using three RDFs: Carnahan–Starling, Lun, and Ma–Ahmadi. The first one, used in previous microhydrodynamic studies, does not account for the bead packing limit concentration. The Lun and the Ma–Ahmadi RDFs similarly predicted much higher frequency of less energetic–forceful bead–bead collisions than the Starling RDF. A subset selection algorithm determined the best multiple linear regression models (MLRMs) of *k* with the microhydrodynamic parameters (semi-theoretical) or the process–bead parameters (empirical) as predictors. The Lun RDF-based MLRM had the best fitting–predictions of the kinetics among the semi-theoretical MLRMs, which outperformed the empirical MLRMs.

3.1 Materials and Methods

3.1.1 Materials

The model poorly water-soluble drug used in this chapter was fenofibrate (BP grade), purchased from Jai Radhe Sales (Ahmedabad, India). The aqueous solubility of FNB is 0.8 mg/L at room temperature [169]. Hydroxypropyl cellulose (HPC, L grade, Nisso America Inc, New York, NY, USA) was used as a non-ionic polymeric stabilizer, and sodium

dodecyl sulfate (SDS, ACS grade, GFS chemicals, Columbus, OH, USA) was used as an anionic surfactant. Zirmil Y grade yttrium-stabilized zirconia (YSZ) beads (Saint Gobain ZirPro, Mountainside, NJ, USA) and HCC grade crosslinked polystyrene (CPS) beads (Norstone Inc., Bridgeport, PA, USA) with a nominal size of 400 µm were selected as they have distinctly different density and mechanical properties. While both having 400 µm nominal sizes, YSZ beads have 6000 kg/m^3 density and 405 µm actual median size, whereas CPS beads have 1040 kg/m^3 and 444 µm, respectively. The actual particle sizes were measured via laser diffraction in dry dispersion mode by Helos/Rodos particle size analyzer (Sympatec, NJ, USA).

3.1.2 Wet stirred media milling

A suspension of FNB, HPC-L, and SDS was prepared using a shear mixer (Cat.# 14-503, Fisher Scientific, Pittsburgh, PA, USA) at 300 rpm for 2 h. The formulation was selected as 10% FNB, 7.5% HPC-L, and 0.05% SDS based on a prior study [150]. The coarse suspensions were stored at 8 ^{o}C overnight prior to the milling in a Microcer wet stirred media mill (Netzsch Fine Particle Size Technology, LLC, Exton, PA, USA) for 180 min with the parameters presented in **Table 3.1**. The experimental design (Runs 1–8) is based on OFAT (one-factor-at-a-time) with three parameters at two-levels: low–high and YSZ–CPS. Runs 9 and 10 were appended to the design to emphasize practically achievable high values of the bead loading (0.60) without serious heat dissipation problem in our set-up. Experimental *k* data from Runs 1–10 were used to "calibrate" the MLRMs; then, these MLRMs were used to predict the median particle size evolution in Runs 11–14, which had not been used as part of the model calibration, to test the predictive capability.

Table 3.1 Experimental Conditions of the WSMM Process

Run no.	Stirrer speed, ω (rpm)	Bead loading, c (-)	Bead material
1[a]	3000	0.35	CPS
2[a]	3000	0.35	YSZ
3[a]	3000	0.50	CPS
4[a]	3000	0.50	YSZ
5[a]	4000	0.35	CPS
6[a]	4000	0.35	YSZ
7[a]	4000	0.50	CPS
8[a]	4000	0.50	YSZ
9[a]	3500	0.60	CPS
10[a]	3500	0.60	YSZ
11[b]	3500	0.425	CPS
12[b]	3500	0.425	YSZ
13[b]	2550	0.298	CPS
14[b]	2550	0.298	YSZ

[a]Runs used for training the models. [b]Runs used for testing the prediction capability of the models.

The bead loading was calculated as the true volume of the beads over the mill chamber volume V_m = 80 ml (*v/v*). A peristaltic pump (Cole-Palmer, Master Flex, Vermont Hills, IL, USA) recirculated the suspension between the holding tank and the milling chamber at a volumetric flow rate Q of 126 ml/min. Stainless-steel screen with openings that have half size of the nominal bead size (200 μm) was used to keep the beads in the milling chamber. The setup was cooled with the help of a chiller (Model M1-.25A-11HFX, Advantage Engineering, Greenwood, IN, USA) to keep the temperature under control; intermitting milling cycles were applied when/if the temperature reached 35 ^oC [149, 150]. The average power consumption P was determined by dividing the cumulative energy consumption read from the control panel of the mill by the milling time. The average stirrer power per unit volume P_w was calculated for all runs by $P_w = P/V_m$. The power consumption during the stirring of the suspension in the absence of the beads ε_{ht} was found by the same method. The power consumption when there was no material in the mill (no-load) was obtained and subtracted during the calculation of P_w and ε_{ht}.

3.1.3 Characterization techniques

PSD of the drug suspensions at various milling times was determined by laser diffraction using LS 13-320 Beckman Coulter instrument (Brea, CA, USA). The samples were taken from the outlet of the mill at certain time intervals (2^s, s = 0, 1, 2,...8) with the addition of 40 s, 24 min, 48 min, and 96 min. The final sample was taken from the holding tank. Before each measurement, a ~1.0 mL suspension sample was diluted with 5.0 mL of the respective stabilizer solution using a vortex mixer (Fisher Scientific Digital Vortex Mixer, Model No: 945415, Pittsburgh, PA) at 1500 rpm for one min. During measurements, polarized intensity differential scattering (PIDS) was maintained between 40% and 50% while the obscuration was maintained below 8%. PSD was provided by the software which used the Mie scattering theory. The refractive indices of FNB and water were taken as 1.55 and 1.33, respectively. Measurements were repeated four times and the average and standard deviation (SD) of these measurements were determined.

The apparent shear viscosities μ_L of the milled suspensions were measured using R/S plus rheometer (Brookfield Engineering, Middleboro, MS, USA) with a water jacket assembly Lauda Eco (Lauda-Brinkmann LP, Delran, NJ, USA). A CC40 coaxial cylinder with a jacketed setup was used to impart a controlled shear rate on the samples from 0 to 1000 1/s in 60 s. The jacket temperature was kept constant at 25 ± 0.5 °C. The raw data were analyzed using the Rheo3000 software and the apparent shear viscosity at the maximum shear rate was taken. The density of the milled suspension was measured by weighing 35 ml of the milled suspension and dividing the mass of the suspension by its volume. The measurements were performed thrice, and the average value was reported.

3.1.4 Microhydrodynamic model

In most studies that employed the MHD model for the WSMM [33, 57, 62, 63, 89, 90, 127], the following Carnahan–Starling RDF was used:

$$g_0 = \frac{1 - 0.5c}{(1 - c)^3} \tag{3.1}$$

In addition to the Carnahan-Starling RDF, we used the Lun RDF, mathematically expressed in Equation (3.2), which was suggested for multiphase flow systems that have high solids concentrations [148, 190], where c_{lim} is the bead volume fraction at random close packing assuming mono-dispersed spheres.

$$g_0 = \left[1 - (c/c_{\text{lim}})^{1/3}\right]^{-1} \tag{3.2}$$

Ma and Ahmadi proposed another RDF, Equation (3.3), that is similar to the Lun RDF, in which the complexity in the denominator ensures the proper asymptotic behavior at the limiting concentration [146].

$$g_0 = 1 + 4c\frac{1 + 2.5c + 4.5904c^2 + 4.515439c^3}{[1 - (c/c_{\text{lim}})^3]^{0.67802}} \tag{3.3}$$

For mono-dispersed spherical particles (beads here), a random packing fraction of 0.63 has been used [147]. While the YSZ and CPS beads are perfectly spherical and smooth and they have a relatively narrow PSD [90, 149], they are not mono-dispersed. The potential impact of bead size polydispersity was not considered here or in refs. [31,32]. The MHD model must be reformulated to account for the size polydispersity, which is outside the scope of this chapter. The MHD parameters were found for each RDF, as described in Section 1.4.2 and 2.2.5.

3.1.5 Breakage kinetics and multiple linear regression models (MLRMs)

Breakage of the particles during the WSMM of a well-stabilized suspension is expected to

be the dominant mechanism compared to particle aggregation [10, 94]. Our recent study established that (i) the fenofibrate suspensions were stable during the milling and storage and that (ii) the *n*th-order breakage kinetics model could fit the temporal evolution of the median particle size d_{50} better than the first-order model and the warped-time model [150]. Therefore, the following *n*th-order breakage kinetics model was used to describe the median size d_{50} evolution in time *t*:

$$d_{50}(t) = d_{\lim} + \left[\left(d_{50,0} - d_{\lim}\right)^{1-n} - (1-n)kt\right]^{1/(1-n)} \tag{3.4}$$

wherein $d_{50,0}$ is the initial median size, $d_{\lim}$ is the limiting median size, and *k* is the breakage rate constant. Marquardt–Levenberg optimization algorithm in Sigmaplot (Version 12.5) was used to fit the log-transformed experimental median sizes at various time points by Equation (3.4), and $d_{\lim}$, *n*, and *k* were estimated. In the fitting, a constraint was placed on the limiting particle size, which should be smaller than the final median particle size [90]. As will be discussed in Section 3.2, $d_{\lim}$ and *n* were relatively insensitive to the changes in the processing conditions and bead type (Runs 1–10) unlike *k*. Hence, average values of $d_{\lim}$ and *n* for CPS and YSZ beads were calculated and used in the MLRMs for *k*, as described below.

A relationship between the estimated breakage rate constant *k* of the *n*th-order kinetic model and either the calculated MHD parameters with various RDFs (semi-theoretical MLRM) or the process parameters–bead properties (the purely empirical MLRM) was sought for by a subset selection algorithm with leave-one-out cross-validation (LOOCV, see Algorithm 1 in *Appendix B* for all details). Our analysis focused on the use of various MLRMs to predict the breakage rate constant *k*, using "features" of the system such as the microhydrodynamic parameters σ_b^{max}, α_b, a, and $\Pi\sigma_y$ or the empirical parameters

of the process–beads (ω, c, ρ_b, and Y_b). In all fits, the constant term in the MLRMs was set to zero as it was found to be statistically insignificant (similar to [150]). The first-order MLRM assumes a linear relationship between 4 predictors (T = 4) and response. In the second order MLRM, we have included the squared values of predictors to be considered in the calculation of the linear relationship (T = 8). Finally, in the MLRM with interaction terms, we have incorporated the pairwise interaction terms into our dataset to measure the non-additive relationship (T = 10). Our milling experiments consist of 14 observations (runs). First 10 runs were used for subset selection with LOOCV algorithm (I = 10) and remaining 4 runs were used as an independent test set to assess the predictive power of the selected MLRMs. Our analysis was done on R 4.0.3 using lm function to fit the MLRMs [183]. We utilized ggplot2 package to plot the selected MLRM [184].

3.2 Results and Discussion

3.2.1 Production of drug nanoparticles using the WSMM process and the breakage kinetics

All fenofibrate suspensions were successfully milled to reach a median size d_{50} below 0.185 µm after 180 min milling, as can be seen in **Figure 3.1a**. While d_{50} and d_{90} of the 180 min milled suspensions were slightly lower for the YSZ beads than for the CPS beads at the higher stirrer speed ω and the higher bead loading c, their values did not vary significantly among Runs 1–10: d_{50} was 0.164 ± 0.01 µm and d_{90} was 0.229 ± 0.02 µm. The values of d_{50} and d_{90} in Runs 1–10 followed a distribution that is not statistically different from a normal distribution, as signified by the Anderson–Darling normality test results: p values of 0.088 and 0.140, respectively. These findings overall suggest that the particle size statistics of the final product suspensions alone do not yield much information

about the milling process and the breakage kinetics. They are not surprising at all because given sufficiently long milling time (180 min), the median size of the particles tends to approach and/or attain a grinding limiting size [57].

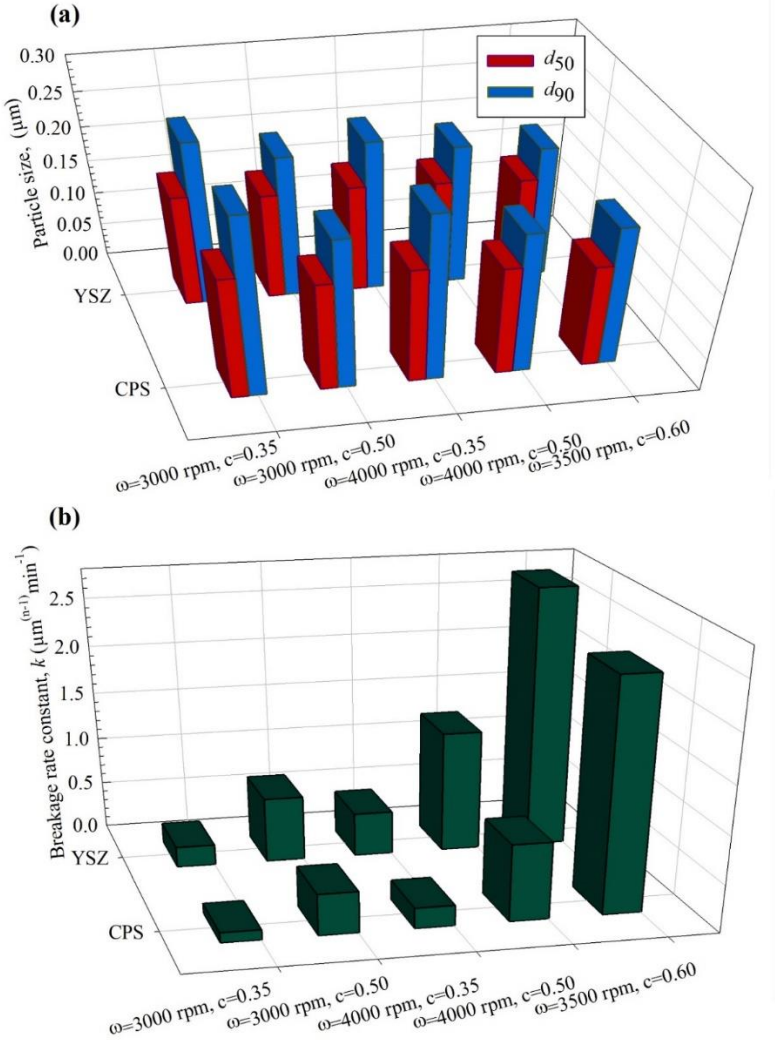

Figure 3.1 Milling characteristics of Runs 1–10: (a) Median particle size d_{50} and 90% passing size d_{90} after 180 min milling and (b) breakage rate constant k obtained from fitting nth-order breakage kinetics model.

In the previous studies of our group that used similar formulations, we found that the sizes of the fenofibrate particles in the SEM images closely matched the laser diffraction measurements, which suggested minimal aggregation of the particles in the

suspensions [46, 47, 54]. The fenofibrate suspensions were physically stable at least for a week [150], which is not surprising considering the synergistic stabilization action of the HPC–SDS combination for multiple drugs [46, 47]. Hence, the present chapter focused only on the breakage kinetics as significant confounding from any aggregation and/or Ostwald ripening of the fenofibrate particles is especially unlikely at the time scale of the milling experiments from which the kinetic parameters were estimated.

The timewise evolution of the median size d_{50} and its fitting by *n*th-order kinetic model as well as the MLRM predictions are depicted in **Figures B.1** and **B.2** (*Appendix B*), which illustrate the characteristic breakage kinetic profile for a well-stabilized suspension [62], i.e., a monotonic decrease of d_{50} and the breakage rate with an approach to a grinding limiting size [46, 57]. This could be attributed to formation of finer particles, especially colloidal/nanoparticles, with lower capture probability between the beads and their higher strength as compared with the coarser particles [94, 191, 192]. The *n*th-order kinetic model successfully fitted the timewise evolution in Runs 1–10 well, as indicated by adjusted $R^2 \geq 0.99$ (refer to **Table B.5** of the *Appendix B*). Based on **Table B.5**, we calculated the mean±SD values of d_{lim}, k, and n for all Runs 1–10 as 0.144±0.01 μm, 0.935±0.93 $\mu m^{n-1} min^{-1}$, and 2.11±0.24 μm, respectively. The Anderson–Darling normality tests indicate that the d_{lim} values obeyed a distribution that is not statistically different from a normal distribution (p value: 0.538 > 0.05), whereas k and n values originated from a non-normal distribution (p values of 0.020 and 0.027, respectively). These statistics and **Table B.5** clearly indicate that d_{lim} and n were much less sensitive to the changes in the processing conditions–bead type than k, which varied remarkably among Runs 1–10 (**Figure 3.1b**). **Figure 3.1b** illustrates that when the milling was carried out at a higher

stirrer speed and/or higher bead loading with the YSZ beads vs. the CPS beads, k was higher. Since n and d_{lim} varied in a narrower range than k, as a first approximation, the impact of the process parameters and bead type on the breakage kinetics was directly described by k alone: higher k signified faster breakage.

The stirrer power P_w was higher at the higher stirrer speed ω and/or the higher bead loading c of the (denser) YSZ beads vs. the CPS beads (**Figure 3.2a**). Under turbulent conditions, the power number correlations for various mixers and stirred vessels [137, 193] suggest that P_w increases with ω and ρ_m only, while in the transition region the viscosity μ_m plays a role too. The viscosity μ_m and density ρ_m of the bead–milled suspension mixtures were estimated using the following correlations [194]:

$$\mu_m = \mu_L[1 + 2.5c + 10c^2 + 0.0019\,exp(20c)] \quad (3.5)$$

$$\rho_m = \rho_b c + \rho_L(1 - c) \quad (3.6)$$

The values of μ_m and ρ_m were shown in **Figure 3.2b and c**. As can be seen, both the density and the viscosity of the mixtures were higher at the higher YSZ bead loadings; thus, explaining the higher P_w. Additionally, ρ_m was significantly higher for the YSZ mixtures vs. the CPS mixtures owing to the density differences of the respective bead materials (6000 vs. 1040 kg/m^3). Therefore, P_w was higher for the YSZ mixtures than that for the CPS mixtures at the same ω and c.

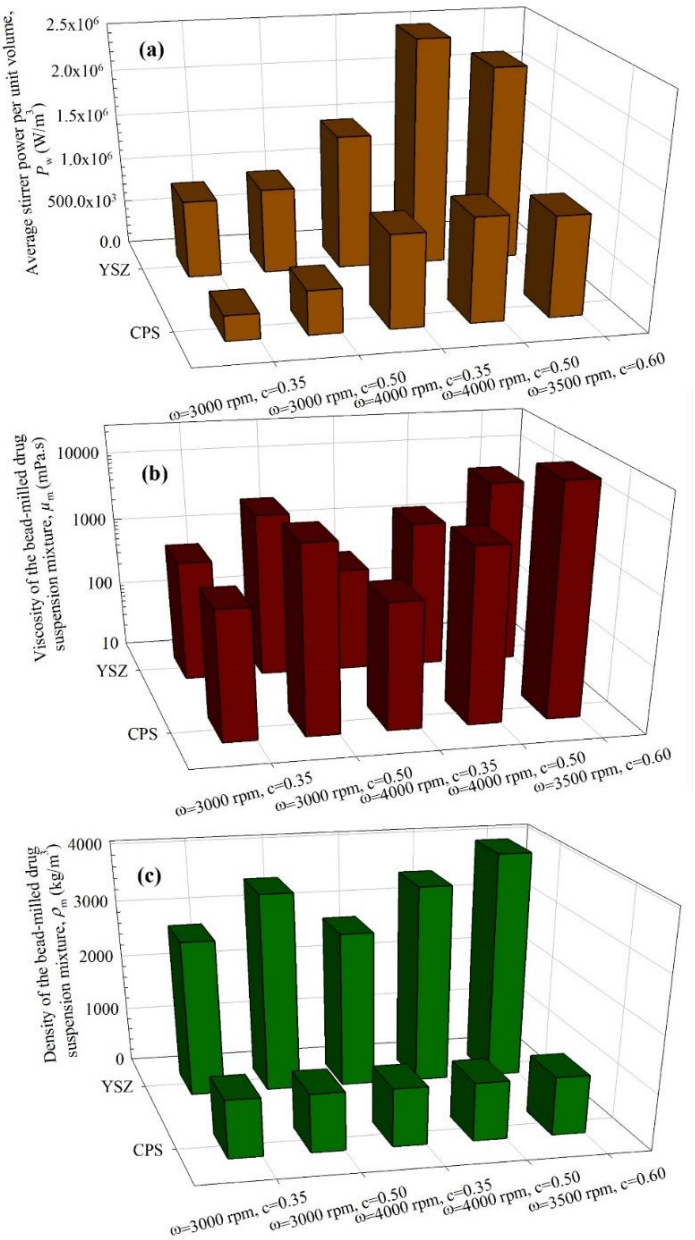

Figure 3.2 Milling characteristics of Runs 1–10: (a) the average stirrer power per unit volume P_w, (b) the viscosity of the bead–milled drug suspension mixture μ_m, and (c) the density of the bead–milled drug suspension mixture ρ_m.

3.2.2 Variation of the stressing frequency and the impact of bead packing limit concentration

The MHD parameters were calculated using three RDFs, i.e., Carnahan–Starling, Lun, and Ma–Ahmadi, considering the processing conditions, bead properties, and suspension properties in Runs 1–14.

Frequency of single-bead oscillations v and the average frequency of drug particle compressions a were calculated and their values are presented in **Figure 3.3**. A cursory look at **Figure 3.3** from the perspective of the different RDFs suggests that all three RDFs provide a similar impact of the stirrer speed and the bead type/loading qualitatively. Overall, regardless of the RDF used in the MHD calculations, both v and a increased when the stirrer speed and/or the bead loading were increased, which can explain the faster breakage depicted in **Figure 3.1b**. This observation could be partly explained by the higher P_w at the respective conditions (refer to **Figure 3.2a**) and partly by the higher bead concentration and the ensuing higher g_0 (see **Figure 3.4**) in the mill chamber at the higher bead loading. Under the specific conditions studied here, we note that an increase in the bead loading has a more pronounced effect on v and a than the stirrer speed.

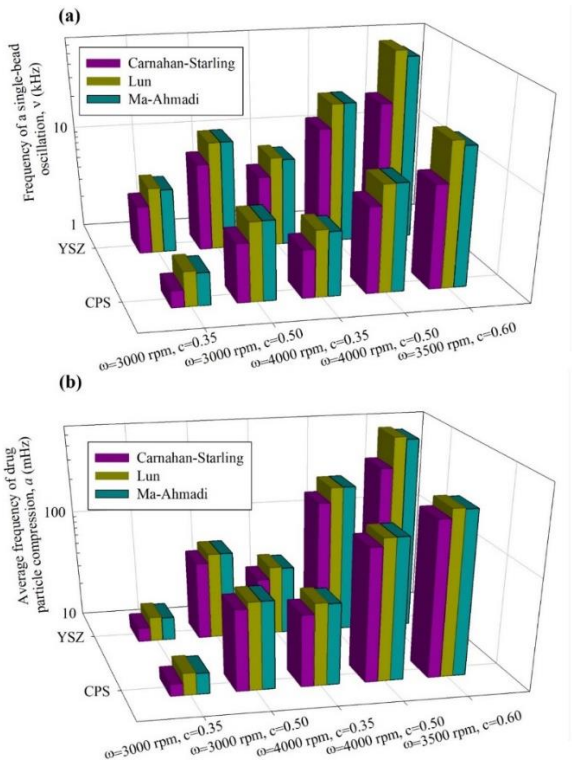

Figure 3.3 Effects of the bead type–loading c and the stirrer speed ω on (a) the frequency of a single-bead oscillation v and (b) the average frequency of drug particle compression a calculated using various RDFs in the microhydrodynamic model.

Another general trend depicted in **Figure 3.3** is that v and a values calculated with the Lun RDF and the Ma–Ahmadi RDF were similar as both RDFs took into account the bead packing limit concentration c_{lim}, whereas the Carnahan–Starling RDF significantly underpredicted v and a. The Lun RDF led to higher v and a compared to the Carnahan–Starling RDF and slightly higher compared to the Ma–Ahmadi RDF. The Lun and Ma–Ahmadi RDFs markedly differed from the Carnahan–Starling RDF, especially at the higher bead loadings. For example, while the Carnahan-Starling RDF provided around 30% and 20% lower v and a compared to the Lun RDF at ω = 3000 rpm–c = 0.35, the differences rose to around 60% and 30%, respectively, at ω = 3500 rpm–c = 0.6.

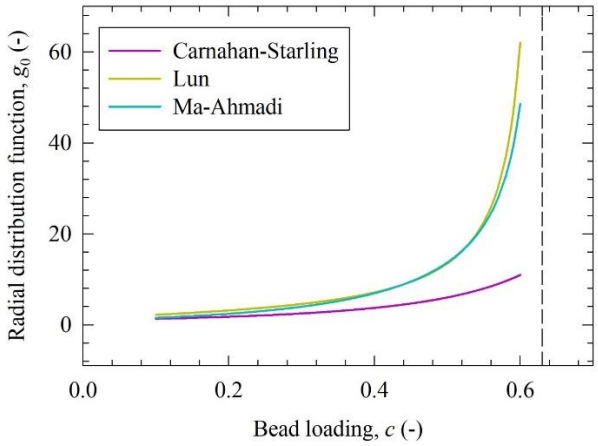

Figure 3.4 Variation of the radial distribution function at contact g_0 with the bead loading c according to the Carnahan–Starling, Lun, and Ma–Ahmadi models. Note that the Lun and Ma–Ahmadi models predict a vertical asymptote (dashed line) as $c \rightarrow c_{lim} = 0.63$.

As the RDF is a dimensionless measure of the distance s between the beads, g0 = 1+Db/s, a higher g0 corresponds to a smaller inter-bead distance and the higher bead collision probability. Overall, as can be seen from Figure 3.4, both the Lun RDF (Equation (4.4)) and the Ma–Ahmadi RDF (Equation (3.3)) predicted a much sharper increase in g0 at the higher bead loading, especially as c approaches the vertical asymptote at c_{lim}, as compared with the Carnahan–Starling RDF (Equation (3.1)). Such sharp increase in g_0 at

high solids concentrations ($0.4 < c < 0.6$) has been experimentally confirmed in gas–solids multiphase flows [145], which is very difficult to measure in WSMM. Our microhydrodynamic calculations suggest that the Carnahan–Starling RDF is less realistic than the Lun RDF and the Ma–Ahmadi RDF for denser bead–drug suspensions especially near the bead packing limit. This finding is in line with studies on liquid–solid fluidized beds and suspension flows wherein the Lun RDF and/or the Ma–Ahmadi RDF have been preferentially used [147, 195, 196]. The differences among the RDFs illustrated in **Figure 3.4** provide the fundamental theoretical basis for the bead packing effects on the v and a values. Overall, the Ma–Ahmadi RDF was close to the Lun RDF, the Carnahan–Starling RDF deviated from them drastically at $c > 0.4$.

3.2.3 Variation of the stress intensity and the impact of bead packing limit concentration

The microhydrodynamic parameters that determine how forceful the bead collisions are, i.e., the stress intensity, are the granular temperature θ, the average bead oscillation velocity u_b, and the maximum contact pressure σ_b^{max} (**Figure 3.5**). Similarly for the stress frequency parameters, all three RDFs predicted qualitatively the same pattern in terms of the impact of the stirrer speed and the bead type/loading on the stress intensity related parameters. These parameters θ, u_b, and σ_b^{max} were all higher for the YSZ beads and increased with the stirrer speed. An increase in P_w provides an increase in the fluctuating energy source to the beads, which leads to more forceful/intense collisions between the beads causing faster breakage of the drug particles. On the other hand, an increase in bead loading resulted in a decrease in the stress intensity despite the concomitant increase in P_w. This can be explained mainly by an increase in the total drag force (interphase momentum exchange)

between the drug suspension and the bead phase at higher *c*. This energy dissipation differences are governed by the different g_0 given by different RDFs.

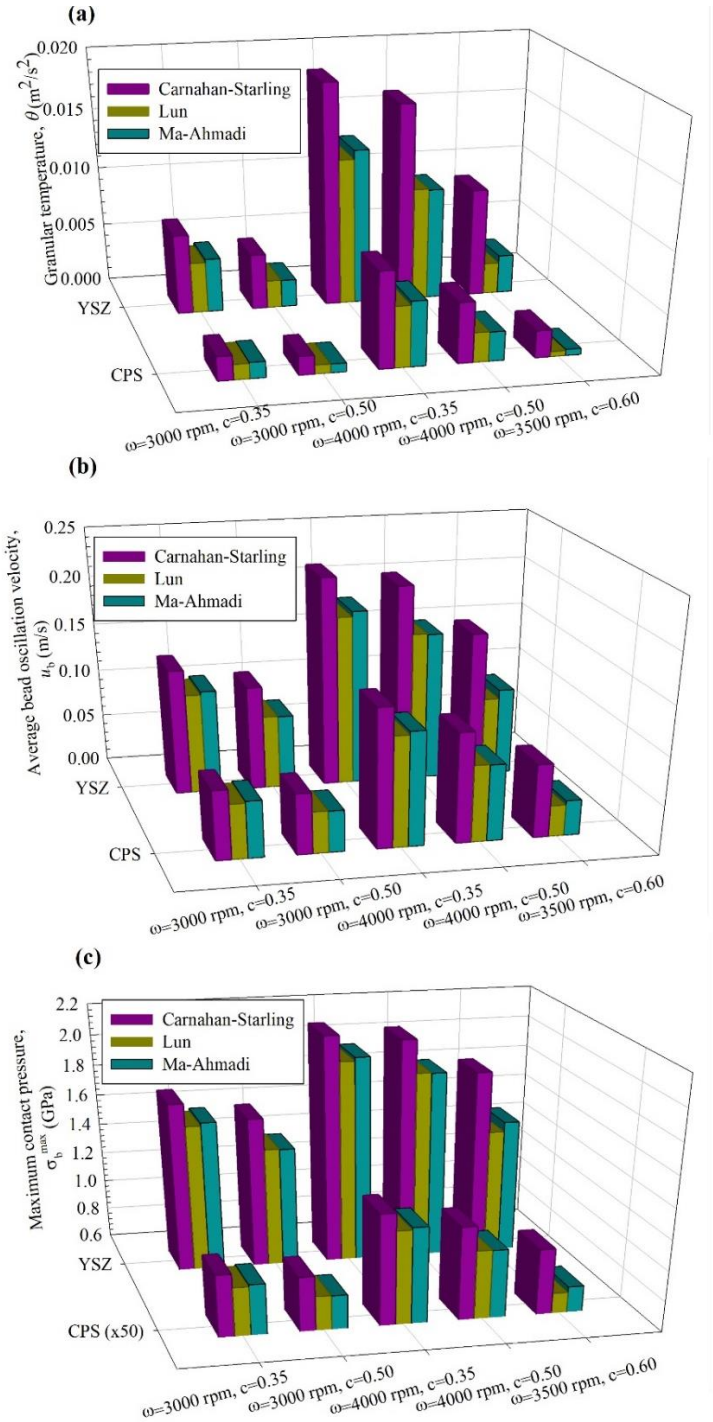

Figure 3.5 Effects of the bead type–loading *c* and the stirrer speed ω on (a) the granular temperature θ, (b) the average bead oscillation velocity u_b, and (c) the maximum contact pressure σ_b^{max} calculated using various RDFs in the microhydrodynamic model.

The MHD parameters θ, u_b, and σ_b^{max} estimated with the Lun RDF were significantly smaller than those with the Carnahan–Starling, and slightly smaller than those estimated with the Ma–Ahmadi RDF. The Carnahan–Starling RDF overpredicted the stress intensity due to its inability to account for the bead packing effects at high bead loadings and its associated impact on the energy dissipation mechanisms (viscous losses and losses due to inelastic collisions). Again, the difference got more pronounced at the higher bead loadings. For example, the Carnahan–Starling RDF provided correspondingly around 55%, 25%, and 9% higher values of θ, u_b, and σ_b^{max} than the Lun RDF at ω = 3000 rpm–c = 0.35. These differences increased to about 300%, 100% and 30%, respectively, at ω = 3500 rpm–c = 0.6, close to the bead packing limit concentration.

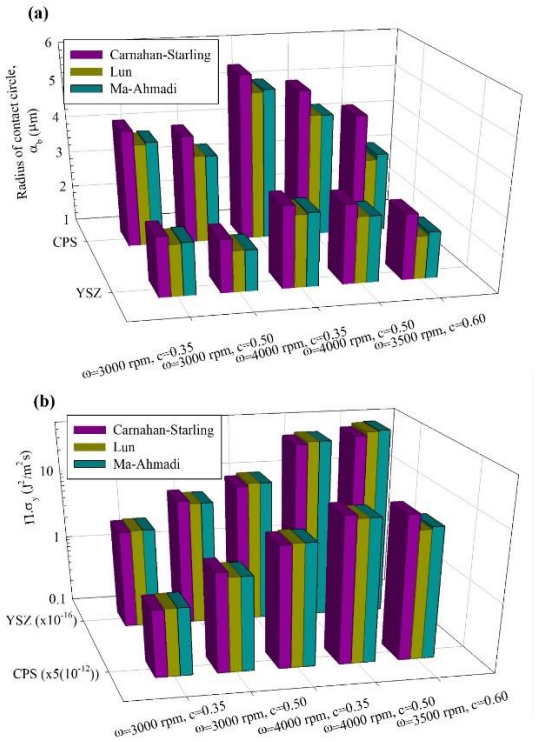

Figure 3.6 Effects of the bead type–loading c and the stirrer speed ω on (a) the radius of contact circle α_b and (b) the pseudo energy dissipation rate $\Pi{:}\sigma_y$ calculated using various RDFs in the microhydrodynamic model.

3.2.4 Other microhydrodynamic (MHD) parameters

Radius of the contact circle α_b and the pseudo energy dissipation rate $\Pi \cdot \sigma_y$ are examined separately from other MHD parameters because they could not be grouped with them (see **Figure 3.6**). Unlike any other MHD parameter, at the same ω and c, α_b was always higher for the CPS beads than for the YSZ beads (**Figure 3.6a**), which made CPS beads more favorable in terms of capturing small particles. This observation can be explained by the fact that the CPS beads deform more than the YSZ beads due to their lower Young's modulus. With an increase in the stirrer speed, α_b increased, whereas with an increase in the bead loading, it decreased. These observations are in line with the positive impact of the stirrer speed and the negative impact of the bead loading on the stress intensity, i.e., at the higher stress intensity, α_b was higher. For all the runs, the Lun RDF provided the smallest α_b, albeit close to the Ma–Ahmadi RDF, but the Carnahan–Starling RDF significantly overpredicted α_b. The α_b difference between the Carnahan–Starling RDF and the Lun RDF was more pronounced at the high bead loadings: 9% at ω = 3000 rpm–c = 0.35, and 30% at ω = 3500 rpm–c = 0.6. The pseudo energy dissipation rate $\Pi \cdot \sigma_y$ was higher at the higher ω and c (**Figure 3.6b**). The YSZ beads had four-orders of magnitude higher $\Pi \cdot \sigma_y$ than the CPS beads due to their much higher Young's modulus and density. Moreover, the higher P_w and the smaller number of drug particles captured by the YSZ beads with lower α_b led to increased work done on deforming the drug particles captured. Regarding the effect of the RDFs on $\Pi \cdot \sigma_y$, unlike other MHD parameters: there were no clear trends. This could be due to the fact $\Pi \cdot \sigma_y$ is associated with both the stress intensity and the stress frequency, which are oppositely affected by the choice of the three RDFs.

3.2.5 Overall impact of the MHD parameter changes on the breakage kinetics

An increase in the stirrer speed led to higher P_w and higher MHD parameter values, which signifies more intense collisions of the beads as well as capturing and compressing the drug particles more frequently and more forcefully. These MHD parameters qualitatively explain why and how the higher k values occurred at the higher stirrer speed. Two counteracting effects of the bead loading on the MHD parameters were observed: dramatically higher frequency of stressing events signified by the higher v and a (note the log-scale in **Figure 3.3**) and the smaller stress intensity signified by the lower values of θ, u_b, and σ_b^{max} (note the linear scale in **Figure 3.5**). It appears that the first effect was stronger than the second, which led to the higher k at the higher bead loading overall. Due to their higher density and Young's modulus, the YSZ beads led to higher stress intensity (higher θ, u_b, and σ_b^{max}) than the CPS beads. The CPS beads deformed more (higher α_b) than the YSZ beads, which counteracted the impact of the higher θ on a. Consequently, both types of beads are characterized by a of the same order-of-magnitude, which appears to be the dominant MHD parameter for the breakage kinetics. This can explain why CPS beads remain competitive to the YSZ beads while the YSZ beads overall cause faster breakage (refer to **Figure 3.1b**). All these findings on the milling of fenofibrate suspensions agree well with those on the milling of griseofulvin suspensions, another poorly soluble drug [57, 90]. This appears to confirm the generality of our findings for the milling of relatively soft materials like drugs. It is supposed that the drug particles are broken due to fatigue caused by repeated bead–bead compressions even at the relatively low stress intensities. This hypothesis is supported by the fact that despite exerting relatively low stress intensity, the CPS beads provide smaller, albeit the same order-of-magnitude k compared with the YSZ

beads (refer to **Figure 3.1b**), and a is the governing MHD parameter (see Section 3.2.3) in comparison with the stress intensity related parameters, i.e., σ_b^{max} and $\Pi\sigma_y$.

3.2.6 Semi-theoretical MLRMs vs. empirical MRLMs and prediction of the breakage rate constant

To simplify the development of MLRMs for prediction of the breakage kinetics, mean values of d_{lim} and n, i.e., 0.152 μm and 2.04 for the CPS beads and 0.137 μm and 2.18 for the YSZ beads, were assumed in the MLRMs and only k was predicted. A statistically significant correlation between the breakage rate constant k and the MHD parameters (σ_b^{max}, α_b, a, and $\Pi\sigma_y$), which were calculated using the three RDFs, was sought for by using the subset selection algorithm with LOOCV. Besides these semi-theoretical MLRMs, a purely empirical MLRM was also sought for by considering the process–bead parameters as predictors similarly. **Table 3.2** presents a statistical summary of the fitting of the breakage rate constant k in Runs 1–10 by the best semi-theoretical MLRMs with the Carnahan–Starling, Lun, and Ma–Ahmadi RDFs (Equations (3.7–3.9), respectively), the best empirical MLRM (Equation (3.10)), and other empirical MLRMs (Equations (3.11) and (3.12).

$$k = 2.80 \times 10^{-2} a - 4.39 \times 10^{-3} \alpha_b a - 1.67 \times 10^{-20} (\Pi\sigma_y) a \tag{3.7}$$

$$k = 1.61 \times 10^{-2} a + 1.58 \times 10^{-18} \Pi\sigma_y - 2.65 \times 10^{-3} \alpha_b a - 1.45 \times 10^{-20} (\Pi\sigma_y) a \tag{3.8}$$

$$k = 1.79 \times 10^{-2} a + 1.12 \times 10^{-18} \Pi\sigma_y - 3.05 \times 10^{-3} \alpha_b a - 1.42 \times 10^{-20} (\Pi\sigma_y) a \tag{3.9}$$

$$k = -44.1c + 5.82 Y_b + 56.3c^2 - 2.89 \times 10^{-2} Y_b^2 \tag{3.10}$$

$$k = 4.70 \times 10^{-4}\omega - 12.2c + 22.1c^2 \quad (3.11)$$

$$k = -8.01 \times 10^{-4}\omega + 2.24 \times 10^{-3}\omega c + 4.14 \times 10^{-7}\omega Y_b \quad (3.12)$$

For the sake of completeness, the statistical analysis summary for the subset selection algorithm with LOOCV is provided for each RDF and the empirical MLRM in **Tables B.6–B.9** of the *Appendix B.* Moreover, the prediction of the temporal evolution of d_{50} by each MLRM for Runs 1–10 is provided in **Figures B.1** and **B.2** of the *Appendix B.*

Table 3.2 The Statistical Summary of the Fitting of the Breakage Rate Constant k for Runs 1–10 by the Semi-Theoretical MLRMS and the Empirical MLRMS.

Type of MLRM	R^2	Adj. R^2	SSR	p value
MHD-based with the Starling RDF, Equation (3.7)	0.995	0.993	0.446	1.81×10^{-8}
MHD-based with the Lun RDF, Equation (3.8)	1.000	0.999	0.034	1.35×10^{-10}
MHD-based with the Ahmadi RDF, Equation (3.9)	0.999	0.998	0.146	2.94×10^{-9}
Empirical, Equation (3.10)	0.982	0.970	0.715	2.35×10^{-5}
Empirical, Equation (3.11)	0.946	0.923	1.780	8.28×10^{-5}
Empirical, Equation (3.12)	0.905	0.864	3.402	5.97×10^{-4}

The best MHD-based, semi-theoretical MLRMs have the same common predictors: a, $\alpha_b a$ and $a\Pi\sigma_y$. While the MLRM with the Carnahan–Starling RDF, Equation (3.7), has three MHD parameters as predictors, the MLRMs with the Lun RDF and the Ma–Ahmadi RDFs, Equations (3.8) and (3.9), respectively, have four predictors with the common addition of $\Pi\sigma_y$. The average number of drug particle compressions a turned out to be the dominant MHD parameter in predicting k, which supports the probable fatigue mechanism discussed in Section 3.2.5. In fact, even a as a single MHD parameter led to R^2 of 0.969, 0.941, and 0.945 for the statistically significant MLRMs with the Carnahan–Starling RDF,

the Lun RDF, and the Ma–Ahmadi RDF, respectively (BM1 in **Tables B.6–B.8**). The deviation between the experimental *k*, obtained from the *n*th-order model fitting, and the *k* predicted by the MLRMs is displayed in **Figure 3.7**, along with the statistical summary presented in **Table 3.2**. Overall, the MHD-based semi-theoretical MLRMs outperformed the purely empirical MLRMs as indicated by higher R^2, higher adjusted R^2, and lower SSR (**Table 3.2**) as well as more data points falling onto the equivalency line (**Figure 3.7**). The goodness-of-fit was rank-ordered as follows: MLRM with the Lun RDF > MLRM with the Ma–Ahmadi RDF > MLRM with the Carnahan–Starling RDF > the empirical MLRMs.

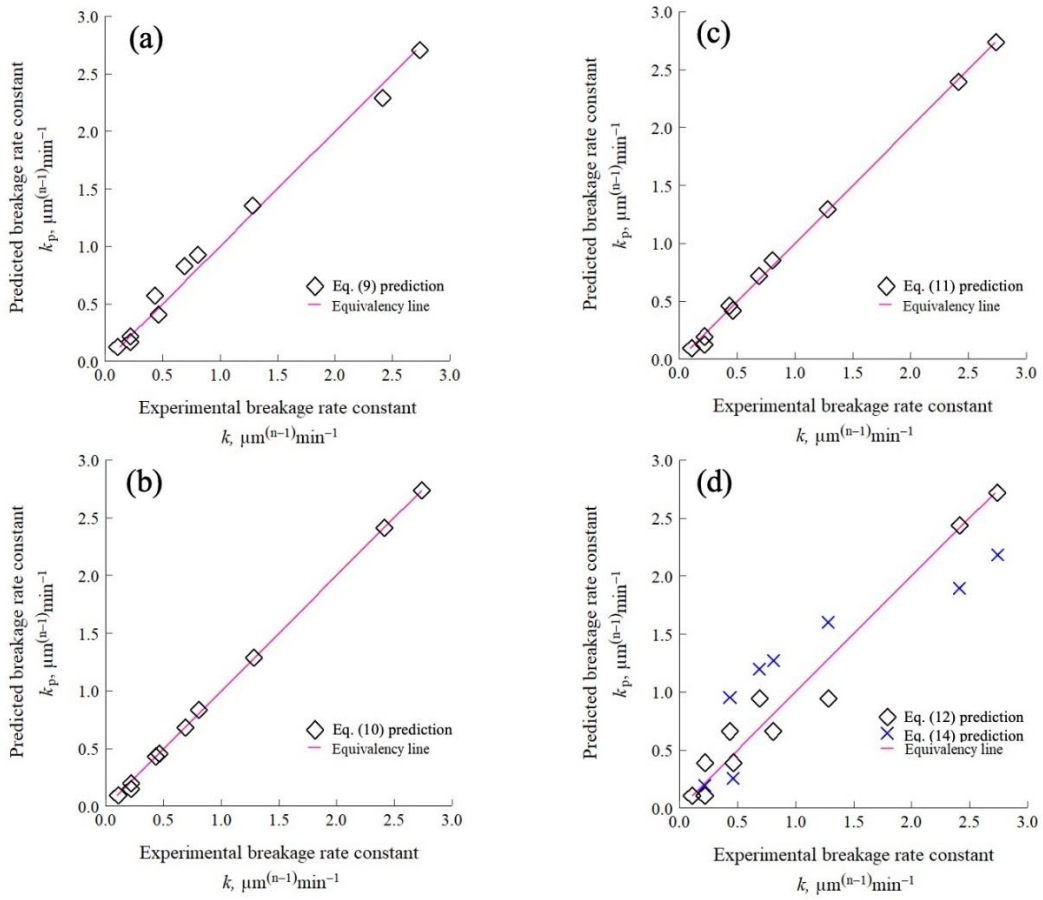

Figure 3.7 Experimental values of the breakage rate constant *k* in Runs 1–10 and its prediction by the best semi-theoretical MLRMs of the microhydrodynamic parameters, which were calculated using (a) the Carnahan–Starling RDF, (b) the Lun RDF, and (c) the Ma–Ahmadi RDF, as well as (d) the empirical MLRMs of the process variables–bead properties.

A discerning way to assess the predictive capability of the MLRMs is to see how they predict the experimental d_{50}–t data (Runs 11–14), which were not used in the calibration of the MRLM coefficients (Runs 1–10). The k value predicted by each MLRM was used to predict the temporal evolution of the median size. In this prediction, the d_{lim} and n values were taken as the average of the nth-order kinetic model fits of all CPS runs (see **Table B.5**) for the prediction of Runs 11 and 13 and all YSZ runs for the prediction of Runs 12 and 14. **Figures 3.8** and **3.9** present the experimental d_{50} evolution and its *direct fitting* by the nth-order kinetic model vs. the d_{50} evolution *predicted* by the MHD-based semi-theoretical MLRMs and the purely empirical MLRMs, respectively. The data presented in **Table 3.3** and **Figures 3.8** and **3.9** suggest that the empirical MLRMs have poor predictive capability. The best empirical MLRM given by Equation (3.10) and the empirical MLRM given by Equation (3.12) predicted a negative breakage rate constant for Runs 12 and 14 and Runs 13 and 14, respectively. Moreover, even though Equation (3.10) has better overall fitting capability for Runs 1–10 than Equation (3.12), Equation (3.12) predicted the median size evolution better than Equation (3.10) whenever these two empirical MLRMs did not yield a negative k in Runs 11–14, which is unexpected. Hence, the empirical MLRMs are unreliable in prediction. On the other hand, all semi-theoretical MLRMs predicted positive k and reasonable prediction of the experimental data (**Figure 3.8**). The small deviations could be partly ascribed to the use average values of d_{lim} and n for the CPS and YSZ beads. It is likely that the prediction could be improved by developing an additional MLRM especially for n, which has non-normal distribution; however, such an approach is not warranted as the predictions by Equations (3.8) and (3.9) are reasonably good and n variations are small. The semi-theoretical MLRMs that considered bead

packing limit concentration (the Lun RDF and the Ma–Ahmadi RDF) have better prediction capability compared to the Carnahan–Starling RDF that does not account for the bead packing limit concentration, as reflected by the higher R^2 and lower SSR values in **Table 3.3**. **Figure 3.8** illustrates the same findings visually.

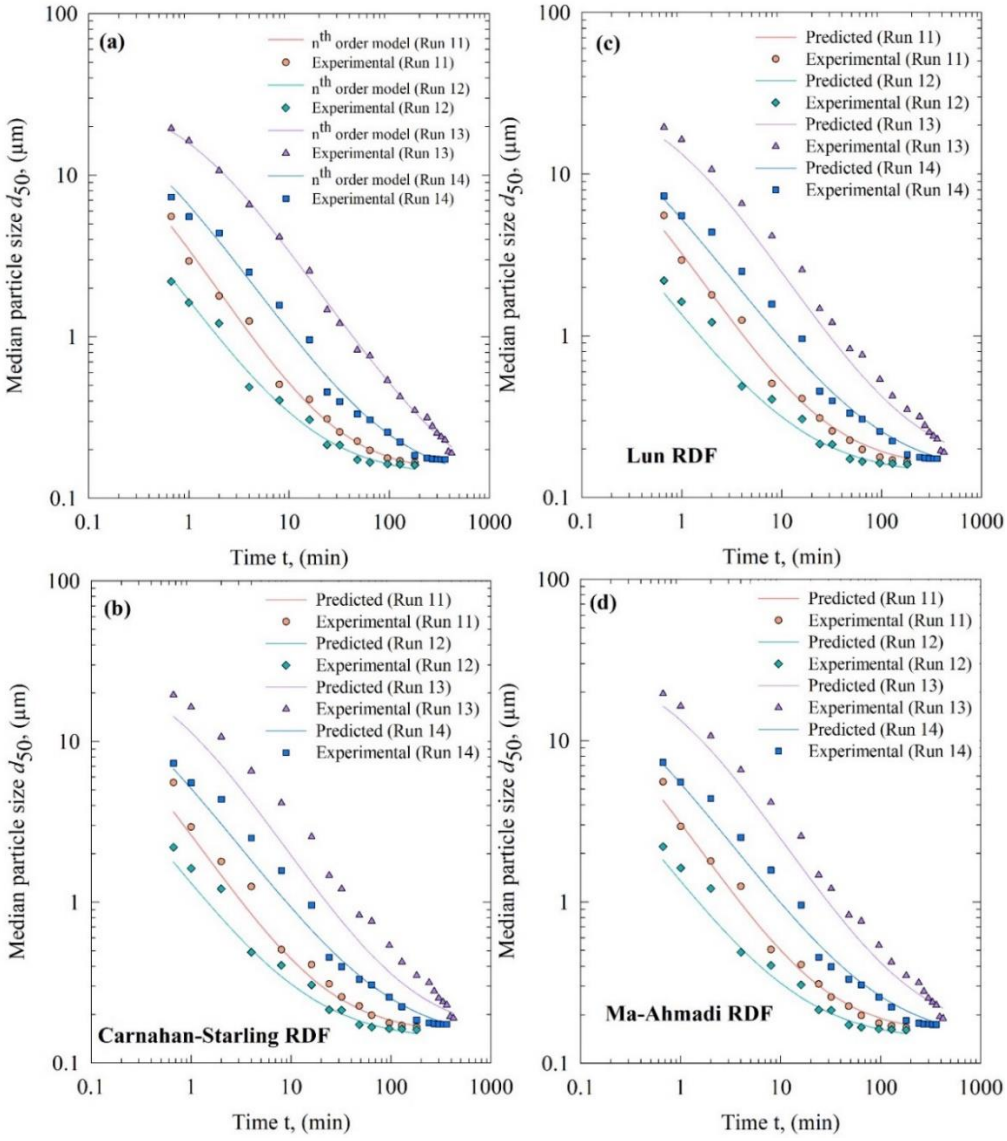

Figure 3.8 Experimentally measured temporal evolution of the median particle size in Runs 11–14 and (a) its direct fitting by the *n*th-order breakage kinetics model and the evolution predicted by the semi-theoretical MLRMs of the microhydrodynamic parameters, which were calculated using (b) the Carnahan–Starling RDF, (c) the Lun RDF, and (d) the Ma–Ahmadi RDF.

Table 3.3 Statistical Summary of the *n*th-order Kinetics Model Fits for Runs 11–14 and Predictions of the Breakage Rate Constant *k* by Various Semi-Theoretical MLRMS and Two Empirical MLRMS

Run	Type of fit and prediction	d_{lim} (μm)	*n* (-)	*k* ($\mu m^{n-1} min^{-1}$)	R^2 (-)	SSR (-)
11	*n*th-order model fit	0.142	2.00	0.264	0.996	0.023
	Prediction with the Starling RDF	0.152	2.04	0.344	0.986	0.083
	Prediction with the Lun RDF	0.152	2.04	0.267	0.995	0.030
	Prediction with the Ahmadi RDF	0.152	2.04	0.284	0.994	0.034
	Empirical (Equation (3.10)) prediction	0.152	2.04	0.092	0.822	1.06
	Empirical (Equation (3.12)) prediction	0.152	2.04	0.531	0.937	0.378
12	*n*th-order model fit	0.136	2.12	0.527	0.996	0.023
	Prediction with the Starling RDF	0.137	2.18	0.678	0.988	0.064
	Prediction with the Lun RDF	0.137	2.18	0.650	0.990	0.053
	Prediction with the Ahmadi RDF	0.137	2.18	0.657	0.990	0.056
	Empirical (Equation (3.10)) prediction	0.137	2.18	–0.573[a]	N/A	N/A
	Empirical (Equation (3.12)) prediction	0.137	2.18	0.818	0.975	0.132
13	*n*th-order model fit	0.093	2.09	0.023	0.999	0.015
	Prediction with the Starling RDF	0.152	2.04	0.049	0.955	0.508
	Prediction with the Lun RDF	0.152	2.04	0.037	0.985	0.157
	Prediction with the Ahmadi RDF	0.152	2.04	0.037	0.985	0.163
	Empirical (Equation (3.10)) prediction	0.152	2.04	0.523	0.294	8.43
	Empirical (Equation (3.12)) prediction	0.152	2.04	–0.339[a]	N/A	N/A
14	*n*th-order model fit	0.125	2.11	0.093	0.993	0.050
	Prediction with the Starling RDF	0.137	2.18	0.110	0.987	0.106
	Prediction with the Lun RDF	0.137	2.18	0.105	0.989	0.092
	Prediction with the Ahmadi RDF	0.137	2.18	0.101	0.990	0.084
	Empirical (Equation (3.10)) prediction	0.137	2.18	–0.142[a]	N/A	N/A
	Empirical (Equation (3.12)) prediction	0.137	2.18	–0.129[a]	N/A	N/A

[a]Physically implausible. The d_{50}–*t* prediction was not generated; therefore, SSR and R^2 were not determined

The best empirical MLRM, Equation (3.10), is a function of the bead loading, the Young's modulus of the beads, and their squares, but disregards the stirrer speed. This is physically implausible because of the significant impact of the stirrer speed on P_w, the MHD parameters, and the breakage kinetics. Interestingly, most of the empirical BMs

identified by the subset selection did not even have any bead properties, e.g., Equation (3.11). This also seems physically implausible because the YSZ beads led to faster breakage than the CPS beads (**Figure 3.1b**). There was no need to illustrate the evolution predicted by Equation (3.11) for Runs 11–14 in **Figure 3.9** because Equation (3.11) cannot even differentiate the impact of YSZ vs. CPS beads. Unlike in **Figure 3.8**, two of the four curves (CPS) would unfortunately not be different from the other two (YSZ), if included in **Figure 3.9**. When the empirical MLRM with all process parameters and at least one bead property is considered, e.g., Equation (3.12), the predictive power of the empirical MLRM was still poor. These findings point out that the empirical MLRMs must have more than 4 terms, possibly including higher-order terms (e.g., cubic terms) as well as more interaction terms (binary as well as ternary interaction terms). However, such an MLRM with more than 4 terms would require a much denser set of experimental data (more process runs) for acceptably low error and statistical significance of the associated coefficients. One should note that many of the best models with only 4 terms (see **Tables B.6–B.9**) have statistically insignificant parameters. Without performing additional experiments, addition of higher-order terms will most likely result in higher errors of the parameter estimates and statistical insignificance of the parameters. All these issues have been circumvented owing to the use of microhydrodynamic parameters as predictors in the semi-theoretical MLRMs.

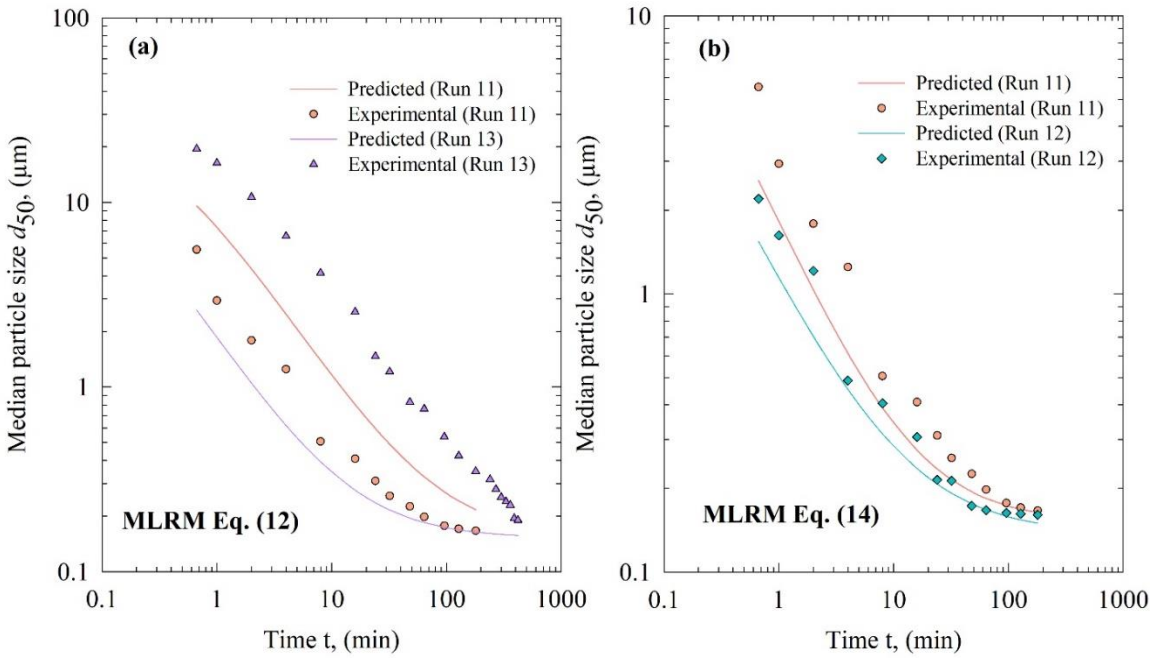

Figure 3.9 Experimentally measured temporal evolution of the median particle size in Runs 11–14 and the evolution predicted by the empirical MLRMs expressed by (a) Equation (3.10) and (b) Equation (3.12). Note that the empirical MLRMs failed to predict a physically plausible *k*, i.e., a positive *k*, for some of the runs; hence, the median size evolution for these runs was not calculated.

3.3 Conclusions

This chapter aimed to investigate the impact of bead packing limit concentration in wet stirred media milling by analyzing the microhydrodynamic parameters calculated with various RDFs and their prediction of the breakage kinetic constant *k*. The Lun RDF and the Ma–Ahmadi RDF, accounting for the bead packing limit concentration, predicted much higher frequency of less forceful bead–bead collisions than the Starling RDF that neglects the packing limit concentration. A subset selection algorithm allowed us to determine the best MLRMs of *k* with the microhydrodynamic parameters (semi-theoretical MLRM) or the process–bead parameters (empirical MLRM) as predictors. The Lun RDF-based MLRM showed the best predictions of the breakage kinetics among the semi-theoretical MLRMs, which outperformed all empirical MLRMs. The use of microhydrodynamic

parameters in the regression models has obviated the need for introducing non-linearity in the prediction of k because the MHD parameters themselves depend on the process parameters and the bead properties in a coupled, nonlinear manner. This is why the microhydrodynamics-based semi-theoretical MLRMs with only 4 terms had much better predictive capability than the purely empirical MLRMs. The current chapter has demonstrated the necessity of using an RDF correlation accounting for the bead packing concentration in the calculations of the MHD parameters. The Lun RDF appears to be the best choice due to its simplicity and the highest predictive power.

CHAPTER 4

ANALYSIS OF HEAT GENERATION DURING THE PRODUCTION OF DRUG NANOSUSPENSIONS IN A WET STIRRED MEDIA MILL

Although heat is generated during the wet stirred media milling of drug suspensions, leading to notable temperature rise, a comprehensive analysis of heat generation during WSMM does not exist. Hence, in this chapter, we investigated the impact of stirrer speed, bead loading, and bead size at three levels on the evolution of suspension temperature at the mill outlet during the milling of fenofibrate. The particle sizes and viscosities of the milled suspensions and power were measured. Our results suggest that stirrer speed had the most significant impact on the temperature increase, followed by bead loading and bead size. Both the time when the temperature reached 22 ^{o}C and the temperature at 5 min of milling were strongly correlated with the power. Assessing the impacts of the process parameters on the temperature rise, cycle time, power, and median particle size holistically, an optimal milling process was identified: 3000 rpm with 50% loading of 200 or 400 μm beads. A power number correlation was established to calculate power at any milling condition which determines the heat generation rate. Overall, this chapter indicated the importance of developing a good understanding of heat generation during nanomilling for development of a robust milling process especially for thermally labile drugs.

4.1 Materials and Methods

4.1.1 Materials

Fenofibrate (Jai Radhe Sales, Ahmedabad, India) was used as a model poorly water-soluble drug with 0.8 mg/L aqueous solubility at room temperature [169]. Its aqueous suspension

with hydroxypropyl cellulose (HPC, L grade, Nisso America Inc, New York, NY, USA) and sodium dodecyl sulfate (SDS, ACS grade, GFS chemicals, Columbus, OH, USA) was used as pre-suspension in all experiments. The milling media were Zirmil Y grade yttrium-stabilized zirconia (YSZ) beads with three different nominal sizes: 200, 400, and 800 µm (Saint Gobain ZirPro, Mountainside, NJ, USA). All suspensions were prepared in deionized water.

4.1.2 Wet stirred media milling and temperature measurements

The pre-suspension formulation was selected as 10% FNB, 8% HPC-L, and 0.05% SDS (all w/w with respect to 200 g of DI water), which is similar to the stable formulation used in our prior studies [149, 150], with a slight increase in the polymer concentration to determine the power more accurately. The pre-suspensions were prepared in a shear mixer (Cat#. 14-503, Fisher Scientific, Pittsburgh, PA, USA) at 300 rpm for 2 h and then stored in a refrigerator at 8 ^{o}C overnight. After storage, they were taken out of the refrigerator and mixed for 30 min prior to milling in a Microcer (Netzsch Fine Particle Size Technology, LLC, Exton, PA, USA) wet stirred media mill. This 30 min mixing aimed to homogenize the pre-suspension as the coarse particles could have settled during the storage. The temperature of the precursor suspensions increased by the time they were transferred to the holding tank of the mill. The setup was cooled with the help of a chiller (Model M1-.25A-11HFX, Advantage Engineering, Greenwood, IN, USA). The coolant (20% v/v glycol–water mixture) follows a loop through the system: it first flows around the cooling jacket of the mill chamber, and then flows around the cooling jacket of the holding tank, finally returning to the chiller (refer to **Figure 4.1**). When the chiller liquid temperature reached ~6 ^{o}C and the suspension temperature at the mill outlet, shortly milloutlet temperature, was

at or below 18 ºC, the milling started.

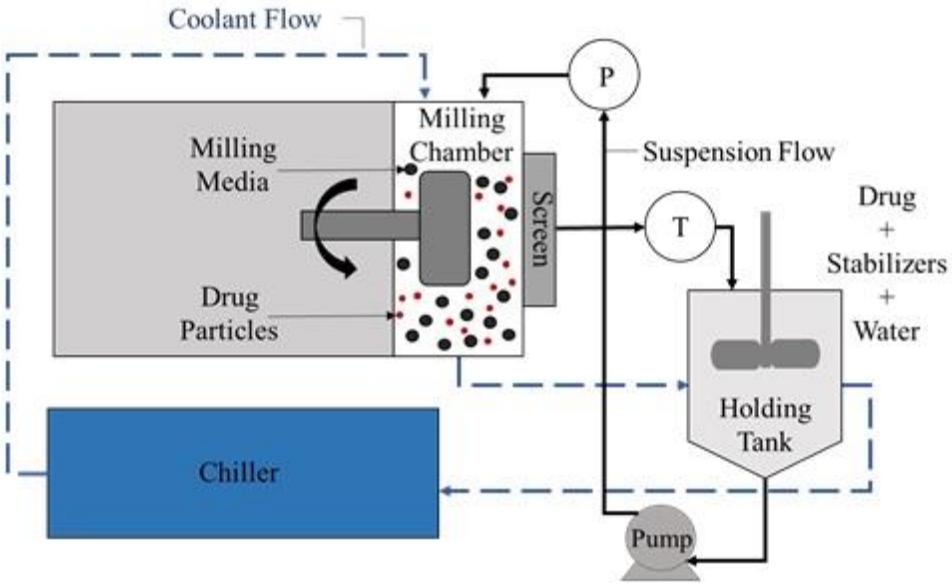

Figure 4.1 Schematic of the recirculation operation mode of wet stirred media milling.

The design of the experiments is as follows: three different stirrer speeds, bead loadings and bead sizes were explored to examine their impact on the timewise evolution of suspension temperature at the mill outlet (**Table 4.1**). The bead loading refers to the ratio of the true volume of the beads over the mill chamber volume V_m = 80 ml (v/v). A peristaltic pump (Cole-Palmer, Master Flex, Vermont Hills, IL, USA) recirculated the suspension between the holding tank and the milling chamber at a volumetric flow rate Q of 126 ml/min. A stainless-steel screen, which has openings half size of the nominal bead size (100, 200, and 400 µm for D_b = 200, 400, and 800 µm, respectively), was used to keep the beads in the milling chamber.

Table 4.1 Process Parameters for the Milling of FNB Suspensions

Run No.	Stirrer Speed, ω (rpm)	Bead Loading, c (-)	Bead size, D_b (μm)
1	2000	0.4	200
2	2000	0.4	400
3	2000	0.4	800
4	2000	0.5	200
5	2000	0.5	400
6	2000	0.5	800
7	2000	0.6	200
8	2000	0.6	400
9	2000	0.6	800
10	3000	0.4	200
11	3000	0.4	400
12	3000	0.4	800
13	3000	0.5	200
14	3000	0.5	400
15	3000	0.5	800
16	3000	0.6	200
17	3000	0.6	400
18	3000	0.6	800
19	4000	0.4	200
20	4000	0.4	400
21	4000	0.4	800
22	4000	0.5	200
23	4000	0.5	400
24	4000	0.5	800
25	4000	0.6	200
26	4000	0.6	400
27	4000	0.6	800

We aimed to keep the mill outlet temperature below 45 ^{o}C, which is the gelation temperature of HPC-L [155]. Moreover, this temperature was close to the processing temperature (40 ^{o}C) used by [159]. Finally, the use of lower temperature than 45 ^{o}C would make the analysis of temperature rise in runs with 4000 rpm more difficult and less accurate. The mill was shut down with continued cooling whenever the outlet temperature reached 45 ^{o}C, which led to multiple intermittent milling/cooling cycles for some highly

energetic milling runs. As the mill outlet temperature was recorded every 30 s (see below) by reading it from the mill screen, we would be able to capture fewer data points if a lower temperature than 45 ^{o}C were used for the mill shutdown for further cooling. This would make the shape of the temperature evolution profile less apparent. The fenofibrate particles in all runs were subjected to a total of 60 min milling; however, the actual cycle time t_c was longer especially when multiple intermittent milling–cooling cycles were implemented. The suspension temperature at the mill outlet and the chiller liquid temperature were recorded every minute (ω=2000 or 3000 rpm) or every 30 s (ω=4000 rpm), to be able to capture the rapid increase when operated at the highest stirrer speed. For the sake of completeness, the evolution of the chiller temperature is presented in **Figures C.1–C.3** (*Appendix C*). The average power supplied by the mill stirrer *P* was determined by dividing the cumulative energy consumption read from the control panel of the mill by the milling time. The milled suspensions were characterized as described in the following section. To demonstrate the reproducibility of the milling and the temperature evolution, Run 15 was replicated.

4.1.3 Characterization techniques

Particle size distributions (PSDs) of the drug suspensions at the end of milling were determined by laser diffraction using LS 13-320 Beckman Coulter instrument (Brea, CA, USA). Before each measurement, a ~1.0 mL suspension sample was diluted with 5.0 ml of the respective stabilizer solution using a vortex mixer (Fisher Scientific Digital Vortex Mixer, Model No: 945415, Pittsburgh, PA) at 1500 rpm for one min. During measurements, polarized intensity differential scattering (PIDS) was maintained between 40% and 50% while the obscuration was maintained below 8%. PSD was provided by the

software, which used the Mie scattering theory. The refractive index of FNB and water was taken as 1.55 and 1.33, respectively. Measurements were repeated four times (n = 4) and the average and standard deviation (SD) of these measurements were reported.

The apparent shear viscosities μ_L of the unmilled suspension and the milled suspensions were measured using R/S plus rheometer (Brookfield Engineering, Middleboro, MS, USA) with a water jacket assembly Lauda Eco (Lauda-Brinkmann LP, Delran, NJ, USA). A CC40 coaxial cylinder with a jacketed setup was used to impart a controlled shear rate on the samples from 0 to 1000 1/s in 60 s. Unless otherwise indicated, the jacket temperature was kept constant at 25 ± 0.5 °C. To illustrate the temperature dependence of the suspension viscosity, the viscosity of the milled suspension (Run 15) was measured at 18, 25, 37, and 45 °C. The raw data were analyzed using the Rheo3000 software and the apparent shear viscosity at the maximum shear rate was taken. The density of the milled suspension was measured by weighing 35 ml of the milled suspension and dividing the mass of the suspension by its volume. Both the viscosity and density measurements were performed thrice (n = 3). Before the measurements, the milled suspension samples were stored to allow for sufficient deaeration. For the apparent shear viscosity, the average and standard deviation (SD) of these measurements were reported. For the density, only the average value was reported for brevity as the standard deviation was negligibly small.

4.2 Results and Discussion

4.2.1 Properties of the drug nanosuspension and general observations about the WSMM process

Prior to milling, the FNB particles had d_{10} of 8.09 µm, d_{50} of 20.3 µm, and d_{90} of 38.9 µm. At the end of 60 min effective milling time, all drug suspensions were milled down to a d_{10} of 0.103–0.212 µm, d_{50} of 0.149–0.400 µm, and d_{90} of 0.223–1.63 µm (**Table 4.2**).

Table 4.2 Particle Size Statistics for the Milled Suspensions

Run no.	d_{10} (µm)	d_{50} (µm)	d_{90} (µm)
1	0.178 ± 0.003	0.314 ± 0.004	0.566 ± 0.014
2	0.190 ± 0.012	0.326 ± 0.011	0.592 ± 0.025
3	0.212 ± 0.008	0.400 ± 0.015	1.63 ± 0.016
4	0.158 ± 0.049	0.263 ± 0.009	0.454 ± 0.015
5	0.140 ± 0.006	0.296 ± 0.053	0.490 ± 0.015
6	0.185 ± 0.002	0.335 ± 0.007	0.661 ± 0.016
7	0.120 ± 0.001	0.204 ± 0.001	0.344 ± 0.002
8	0.123 ± 0.001	0.238 ± 0.002	0.382 ± 0.001
9	0.100 ± 0.011	0.241 ± 0.003	0.468 ± 0.011
10	0.122 ± 0.001	0.199 ± 0.006	0.325 ± 0.025
11	0.113 ± 0.002	0.221 ± 0.023	0.421 ± 0.016
12	0.167 ± 0.014	0.317 ± 0.019	0.642 ± 0.041
13	0.120 ± 0.005	0.174 ± 0.001	0.249 ± 0.001
14	0.121 ± 0.001	0.175 ± 0.001	0.246 ± 0.000
15	0.071 ± 0.002	0.223 ± 0.006	0.446 ± 0.015
16	0.111 ± 0.001	0.162 ± 0.001	0.235 ± 0.000
17	0.112 ± 0.001	0.162 ± 0.000	0.234 ± 0.001
18	0.102 ± 0.008	0.165 ± 0.005	0.258 ± 0.001
19	0.116 ± 0.004	0.172 ± 0.002	0.250 ± 0.001
20	0.111 ± 0.003	0.173 ± 0.002	0.256 ± 0.000
21	0.088 ± 0.005	0.244 ± 0.002	0.490 ± 0.003
22	0.109 ± 0.001	0.159 ± 0.001	0.232 ± 0.001
23	0.111 ± 0.001	0.162 ± 0.000	0.235 ± 0.000
24	0.105 ± 0.001	0.196 ± 0.001	0.384 ± 0.007
25	0.103 ± 0.002	0.149 ± 0.001	0.223 ± 0.001
26	0.106 ± 0.004	0.154 ± 0.003	0.229 ± 0.001
27	0.106 ± 0.007	0.179 ± 0.008	0.329 ± 0.054

[a]The standard deviation refers to multiple measurements by laser diffraction (n = 4). It is not a descriptor of a Gaussian particle size distribution.

Final particle sizes were overall in agreement with the previous findings in the literature [33] in terms of the impact of the stirrer speed, bead loading, and the bead sizes:

smaller drug particles were obtained at the higher stirrer speeds and when a higher bead loading of smaller beads were used. Even though the power consumption was quite different for different milling runs (refer to **Table 4.3**), as expected due to changes in the process parameters, the final median particle sizes d_{50} appeared to stay in a relatively narrow range (**Table 4.2**). For example, if the aim of WSMM is to obtain nanoparticles that have a d_{50} smaller than 0.400 µm, all process parameters used in this chapter could achieve that objective. However, the selection of the process conditions may be limited due to cycle time, power/energy consumption, and associated temperature rise concerns. Regarding a possible crystallinity change due to milling, readers are referred to our extensive characterization studies on a similar formulation of the milled fenofibrate suspension [149, 150], which concluded that fenofibrate remained crystalline, based on XRPD and DSC results.

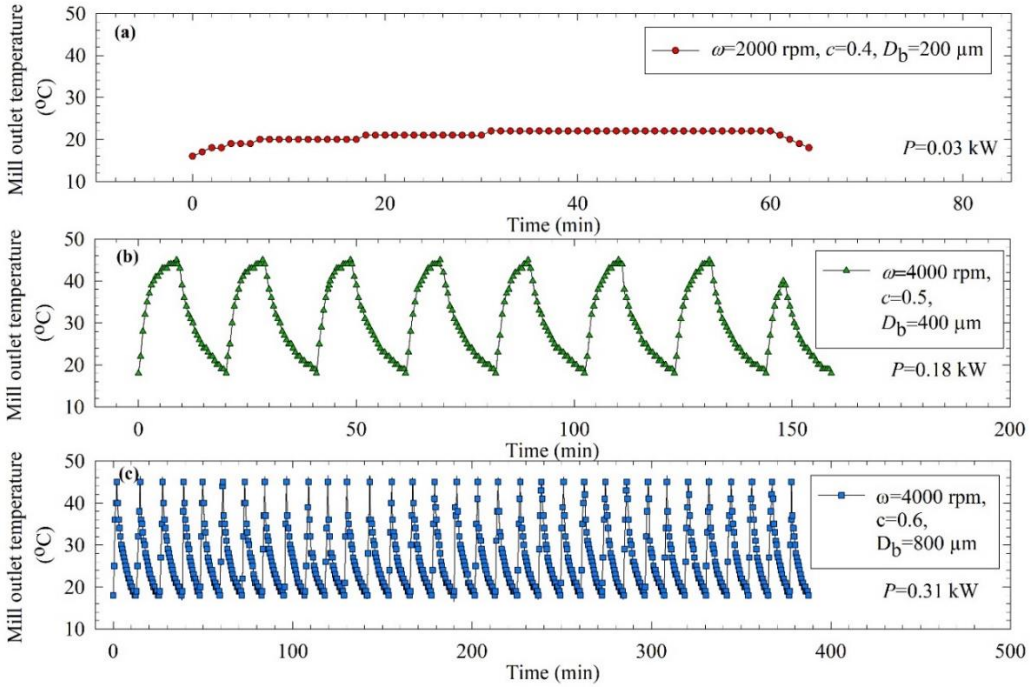

Figure 4.2 Timewise evolution of mill outlet temperature during (a) the lowest energetic run (Run 1) with ω = 2000 rpm, c = 0.4, and D_b = 200 µm, (b) a medium/high energetic run (Run 23) with ω = 4000 rpm, c = 0.5, and D_b = 400 µm, and (c) the highest energetic run (Run 27) with ω = 4000 rpm, c = 0.6, and D_b = 800 µm.

Figure 4.2 illustrates how the suspension temperature at the mill outlet evolved over time for Runs 1, 23, and 27. Note that this temperature is also equal to the temperature of the suspension in the mill chamber as the well-mixedness in the milling chamber has been established as a valid approximation to the residence time distribution in small mills (small length-to-diameter ratio) [87, 93]. **Figure 4.2a** depicts the temperature evolution for the milling run at the lowest energetic level (Run 1), which was operated with the lowest stirrer speed, the lowest bead loading, and the smallest beads. The temperature monotonically increased by 6 °C at the end of 60 min of milling, and the whole operation was completed in one milling–cooling cycle as the temperature did not reach 45°C. The run with the medium/high energetic level (Run 23) caused a temperature increase to 45 °C in around 9 min with a total of 8 intermitting milling-cooling cycles to attain 60 min total milling of the drug. The most energetic level with the highest stirrer speed, bead loading, and the biggest beads (Run 27) caused a jump from 18 °C to 45 °C in around 2 min with a total of 33 cycles. The drug was subjected to milling for 60 min in Runs 1, 23, and 27; however, the cycle time t_c for the milling–cooling cycles was 64, 159, and 388 min, respectively (**Table 4.3**). Although producing relatively fine particles as compared with those of Run 1 (**Table 4.2**), Run 27 is extremely undesirable due to high power consumption, significant/fast heat generation–temperature rise, and long cycle time (**Table 4.3**). These results suggest that at a higher power, the heat generation due to conversion of mechanical shaft work into heat became faster and higher in magnitude, which led to higher temperature and/or more frequent intermittent milling cycles. Hence, the data presented in **Figure 4.2** and **Tables 4.2** and **4.3** for these runs support the hypothesis that the heat

generation rate–temperature rise is largely determined by the power (rate of shaft work applied by the mill stirrer).

Table 4.3 Power Supplied by the Mill Stirrer, Number of Milling Cycles, Cycle Time, Viscosity–Density–Reynolds Number for the Milled Suspension and the Milled Suspension–Bead Mixture, and Power Number.

Run no.	P (kW)	N_{mc} (–)	t_c (min)[a]	μ_L (mPa·s)[b]	ρ_L (kg/m^3)[b]	Re_L (–)[b]	μ_m (mPa.s)[c]	ρ_m (kg/m^3)[c]	Re_m (–)[c]	N_p (–)[c]
1	0.03	1	64	168 ± 1.39	1030	999	1560	3020	316	0.160
2	0.03	1	64	175 ± 1.00	1030	962	1620	3020	304	0.160
3	0.03	1	64	175 ± 0.62	1030	959	1620	3020	303	0.160
4	0.04	1	65	158 ± 0.02	1030	1060	7360	3520	78	0.183
5	0.04	1	66	163 ± 0.21	1030	1030	7610	3520	75	0.183
6	0.05	1	64	166 ± 0.68	1030	1010	7740	3520	74	0.229
7	0.05	1	68	150 ± 1.25	1030	1120	47300	4010	14	0.200
8	0.06	1	65	151 ± 0.48	1030	1120	47600	4010	14	0.240
9	0.06	1	65	149 ± 0.25	1030	1130	47000	4010	14	0.240
10	0.06	1	76	150 ± 1.12	1030	1690	1390	3020	534	0.095
11	0.08	1	75	163 ± 3.66	1030	1540	1510	3020	489	0.126
12	0.08	1	70	165 ± 1.50	1030	1530	1530	3020	484	0.126
13	0.09	1	75	108 ± 1.95	1030	2340	5020	3520	171	0.122
14	0.10	1	76	118 ± 0.25	1030	2140	5500	3520	157	0.135
15	0.10	1	71	120 ± 0.99	1030	2100	5600	3520	154	0.135
16	0.09	1	72	51.3 ± 0.60	1030	4920	16200	4010	61	0.107
17	0.13	1	77	71.5 ± 0.12	1030	3530	22500	4010	44	0.154
18	0.14	1	73	83.1 ± 0.15	1030	3040	26200	4010	37	0.166
19	0.14	2	92	106 ± 0.91	1030	3180	980	3020	1010	0.093
20	0.15	5	136	105 ± 0.51	1030	3210	972	3020	1010	0.100
21	0.15	5	125	138 ± 2.08	1030	2440	1280	3020	772	0.100
22	0.16	4	118	66.3 ± 0.51	1030	5070	3090	3520	371	0.091
23	0.18	8	159	67.5 ± 0.04	1030	4990	3140	3520	365	0.103
24	0.18	9	135	91.8 ± 0.67	1030	3670	4280	3520	269	0.103
25	0.23	10	174	25.7 ± 0.08	1030	13100	8100	4010	162	0.115
26	0.24	13	175	32.8 ± 0.06	1030	10300	10300	4010	127	0.120
27	0.31	33	388	30.7 ± 0.06	1030	10900	9700	4010	135	0.155

[a]Cycle time: 60 min milling and the additional cooling time including the intermittent milling cycles, excluding loading–discharge times.[b]Properties of the milled suspensions.[c]Properties of the milled suspension–bead mixture (calculated) and parameters calculated based on the mixture properties.

Reproducibility of the WSMM process in terms of final milled particle sizes and evolution of the particle size distribution has been well-established in the literature (see e.g., Bilgili and Afolabi, 2012; Li et al., 2017). However, the reproducibility of the temperature evolution has not been established. To demonstrate the reproducibility of the temperature evolution, Run 15 was repeated. **Figure 4.3** demonstrates excellent

reproducibility of the temperature evolution in the replicate Run 15. Also, the temperature dependence of this suspension's viscosity was determined (see Section 4.1).

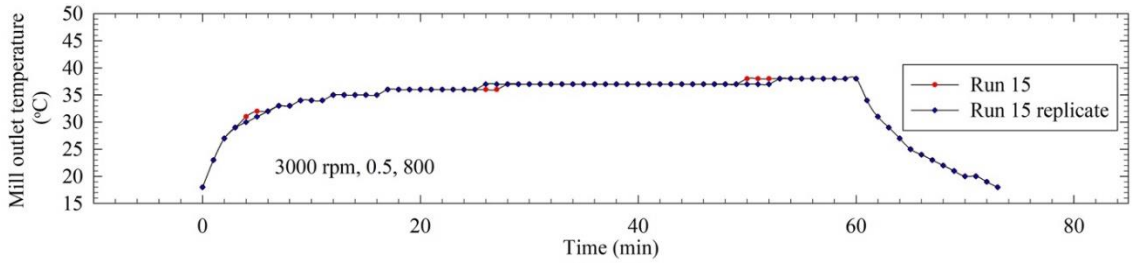

Figure 4.3 Timewise evolution of mill outlet temperature during Run 15 with ω = 3000 rpm, c = 0.5, and D_b = 800 µm, and its replicate experiment.

4.2.2 Impact of stirrer speed on the timewise evolution of suspension temperature at the outlet

Figure 4.4 depicts the impact of stirrer speed for different bead loadings (plotted as subfigures) at a constant bead size of 400 µm (medium value of the experimental design). Readers can find an alternative presentation, looking at the impact of stirrer speed for different bead sizes (plotted as subfigures) at a constant bead loading of 0.5 (center condition of the experimental design) in **Figure C.4**. **Figure 4.4** illustrates a typical temporal evolution curve during the milling: the temperature rose monotonically due to heat generation in the mill albeit at a decreasing rate, and it attained a plateau value clearly at 2000 and 3000 rpm. At 4000 rpm, the increase was steeper; while a plateau temperature was approached, it was not attained. The monotonic increase could be explained by the higher rate of heat generation than that of cooling provided by the chiller liquid and that of the bulk convective cooling provided by the recirculating suspension. Note that the difference between the suspension temperature at the mill outlet and the chiller liquid temperature is the driving force for the overall heat transfer from the milling chamber. Obviously, when the heat generation rate was equal to the heat removal rate, an apparent

steady state was reached. An increase in the stirrer speed led to a higher rate of temperature rise (higher slope) and a higher maximum temperature T_{max} until 45 ºC was reached (**Figure 4.4**). At 4000 rpm, the temperature always reached a T_{max} of 45 °C; hence, multiple intermitting milling–cooling cycles were performed to keep temperature at or below 45 °C until the drug was milled for a total of 60 min.

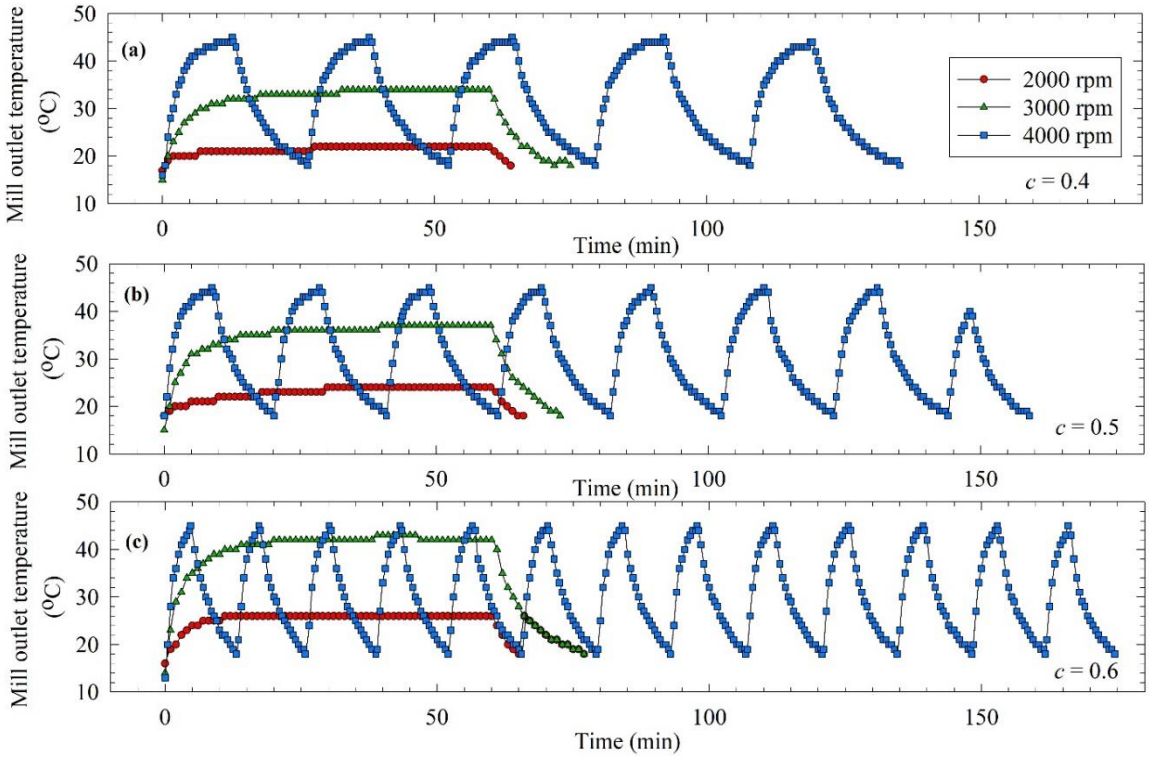

Figure 4.4 Impact of stirrer speed on the timewise evolution of mill outlet temperature for D_b = 400 µm beads at various loadings: (a) c = 0.4 (Runs 2, 11, 20), (b) c = 0.5 (Runs 5, 14, 23), and (c) c = 0.6 (Runs 8, 17, 26).

The decreasing rate of temperature evolution observed in **Figure 4.4** could be ascribed to a decrease in the instantaneous power consumption during the milling, which originates from the reduction of viscosity at the higher temperatures and particle size reduction during the milling [88, 197]. To this end, we measured the unmilled suspension viscosity at 25 ºC as well as the viscosity of Run 15 milled suspension as a function of temperature. The unmilled suspension had an apparent shear viscosity of 198 ± 3.20 mPa·s

at 25 ^{o}C and all milled suspensions had lower apparent shear viscosity at 25 ^{o}C (see **Table 4.3**), which proves that the milled suspension with smaller particles had lower viscosity than the unmilled suspension with coarser particles. Analysis of **Tables 4.2** and **4.3** suggests that the suspensions milled at higher speeds tend to have smaller d_{50} and d_{90} and lower apparent shear viscosity. It is conjectured that higher amount of polymer adsorption onto finer particles generated at the higher stirrer speeds could also play a role in the observed reduction in viscosity. A lower polymer concentration in the bulk suspension upon higher amount of polymer adsorption onto finer particles could result in a lower suspension viscosity than the case when the polymer remains dissolved and smaller amount is adsorbed onto the drug particles with coarser sizes. It is known that a higher polymer concentration in drug nanosuspensions results in higher apparent shear viscosity (see e.g., Bilgili and Afolabi, 2012). Hence, thorough understanding of the impact of particle size on the suspension viscosity warrants a detailed investigation of polymer adsorption onto the drug particles. **Figure 4.5** illustrates that the apparent shear viscosity of the Run 15 milled suspension decreased with increasing temperature. Based on these findings, overall, we confirm that both the size reduction and increase in the suspension temperature during the milling could explain the viscosity reduction and in turn the decrease in instantaneous power and associated heat generation during the milling.

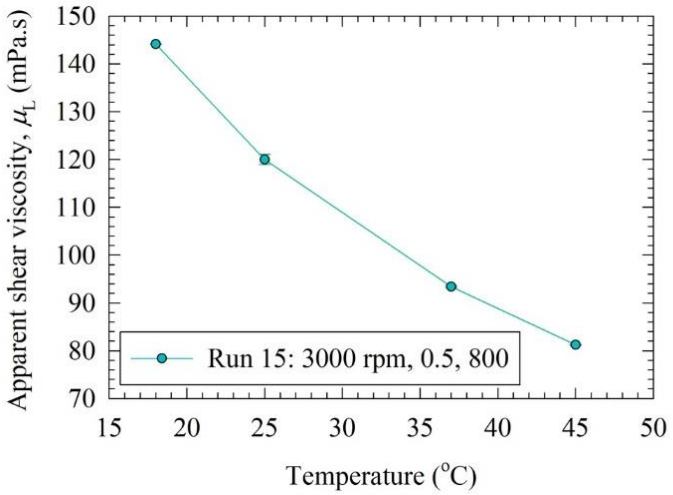

Figure 4.5 The effect of temperature on the apparent shear viscosity of a milled FNB suspension (Run 15).

The comparison of the temperature profiles in **Figures 4.4a, b,** and **c** for the same stirrer speed suggests that at a higher bead loading, the heat generation–temperature rise was faster and the impact of stirrer speed became more remarkable. While the difference between the maximum temperatures caused by 2000 rpm and 3000 rpm in Figure **4.4a** was 12 °C, this difference increased to 16 °C in **Figure 4.4c**. The same conclusion cannot be drawn by comparing 2000 rpm and 4000 rpm or 3000 rpm and 4000 rpm because the maximum temperature was limited to 45 °C in 4000 rpm runs. Therefore, we could compare the number of milling cycles N_{mc} as a more relevant measure (**Table 4.3**). N_{mc} difference between 4000 rpm run and 2000 rpm run in **Figure 4.4a** is 4, and it is 12 in **Figure 4.4c**, signifying the enhanced influence of higher stirrer speed on heat generation at the higher bead loadings.

For an easier and more direct quantitative comparison of the temperature profiles of various runs, we defined some characteristic measures; in fact, two of them were already mentioned in the previous paragraph: maximum temperature T_{max} and number of milling cycles N_{mc}. Note that T_{max} fails to differentiate 4000 rpm runs (as T_{max} = 45 °C); N_{mc} fails

to differentiate 2000 and 3000 rpm runs (as N_{mc} = 1). Therefore, some additional characteristic temperatures and times were defined: $T_{t(5)}$, $T_{t(10)}$, and $T_{t(30)}$ is the suspension temperature at 5, 10, and 30 min milling, respectively. Similarly, $t_{T(22)}$, $t_{T(32)}$, $t_{T(42)}$, and $t_{T(45)}$ is the time when the suspension temperature reached 22, 32, 42, and 45 °C, respectively. All these characteristic measures are reported in **Table C.1** of *Appendix C*. To perform interpolation when needed, MATLAB's pchip function, which is based on piecewise cubic Hermite polynomial interpolation, was used. In line with theoretical expectations for a monotone increasing function $T = T(t)$, the following rank-ordering was observed: $t_{T(22)} < t_{T(32)} < t_{T(42)} < t_{T(45)}$ and $T_{t(5)} < T_{t(10)} < T_{t(30)}$ (**Table C.1**). Among these measures, $t_{T(22)}$ and $T_{t(5)}$ were the most useful for subsequent data analysis and fitting as all runs yielded a $t_{T(22)}$ value and only two runs (Runs 26 and 27) were excluded for $T_{t(5)}$; Runs 26 and 27 reached 45 °C before 5 min.

Figure 4.6 illustrates that $t_{T(22)}$ was lower at the higher stirrer speed due to the faster increase in the temperature. However, since 22 °C was very close to the initial temperature, and the temperature rise was very fast, typically within the first few minutes of the experiments especially at higher stirrer speeds and bead loadings, the discerning power of $t_{T(22)}$ was low at c = 0.6 (**Figure 4.6c**). $T_{t(5)}$ and T_{max} had similar trends: they both increased with increasing stirrer speed. While $T_{t(5)}$ had almost a linear relationship with the stirrer speed, T_{max} had a lower slope from 3000 rpm to 4000 rpm. This could be attributed to the fact that for the 4000 rpm runs, T_{max} was constrained to 45 °C. If those experiments were let run longer, T_{max} would be higher and $T_{t(5)}$ and T_{max} would probably be parallel to each other. For the characteristic times and temperatures of the runs corresponding to **Figure C.4**, readers are referred to **Figure C.5**, which shows the impact of stirrer speed for

different bead sizes (plotted as subfigures) at a constant bead loading of 0.5 in an alternative presentation.

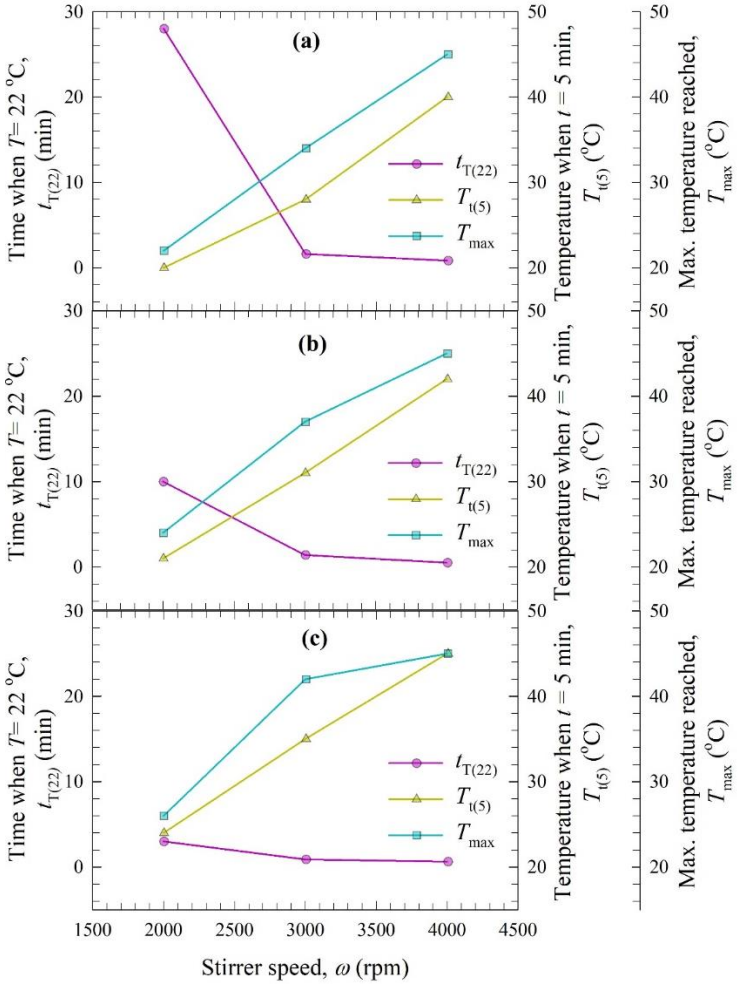

Figure 4.6 Impact of stirrer speed on the characteristic time and temperatures for D_b = 400 μm beads at various loadings: (a) c = 0.4 (Runs 2, 11, 20), (b) c = 0.5 (Runs 5, 14, 23), and (c) c = 0.6 (Runs 8, 17, 26).

4.2.3 Impact of bead loading on the timewise evolution of suspension temperature at the outlet

Figure 4.7 depicts the impact of bead loading for different bead sizes (plotted as subfigures) at a constant stirrer speed of 3000 rpm (at the center of the experimental design). Readers can find an alternative presentation, looking at the impact of bead loading for different stirrer speeds (plotted as subfigures) at a constant bead size of 400 μm

(medium value of the experimental design) in **Figure C.6** (*Appendix C*). An increase in the bead loading while keeping all other parameters constant led to a faster heat dissipation, as signified by the higher slope of the temperature evolution curve and a higher temperature at the same milling time (**Figure 4.7**).

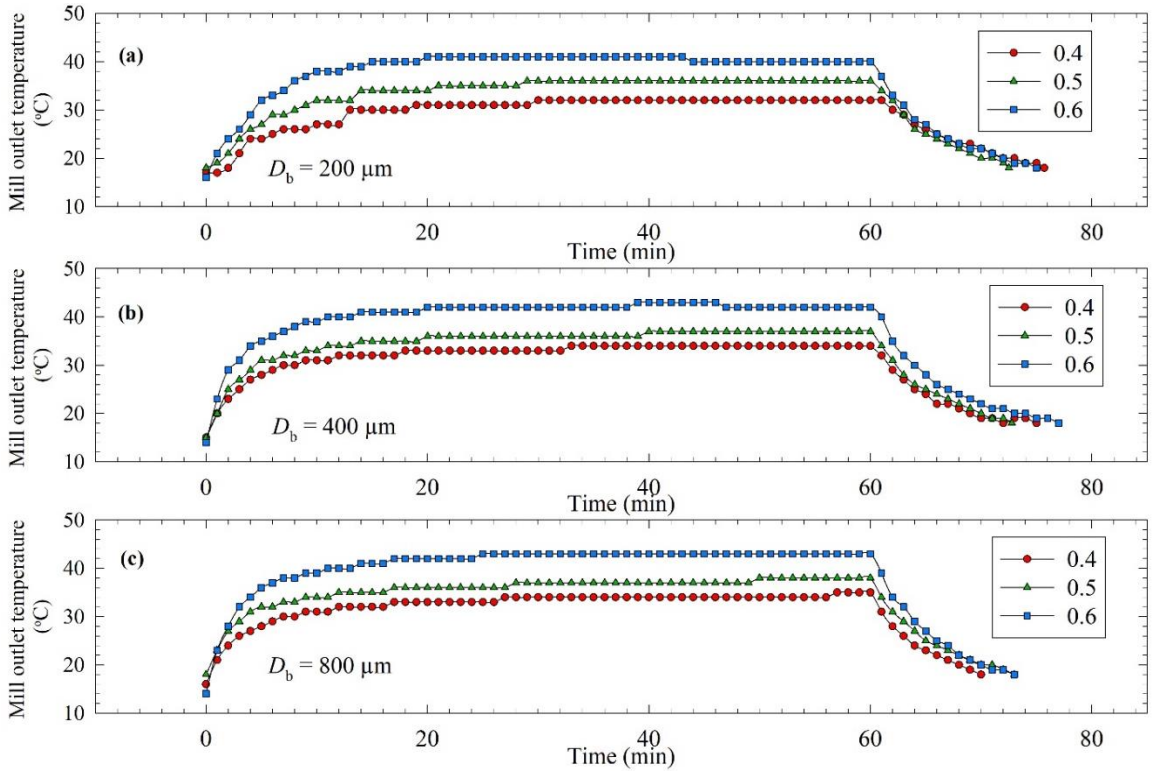

Figure 4.7 Impact of bead loading on the timewise evolution of mill outlet temperature for ω = 3000 rpm and various bead sizes: (a) D_b = 200 µm (Runs 10, 13, 16), (b) D_b = 400 µm (Runs 11, 14, 17), and (c) D_b = 800 µm (Runs 12, 15, 18).

Although the differentiation was not as drastic as it was for the stirrer speed because an increase in bead loading did not cause an increase in N_{mc}, the temperature profiles were clearly separated without any crossover. While the temperature profiles of 0.4 and 0.5 bead loading runs were somewhat close to each other, the temperature profile of the 0.6 bead loading runs were distinctly higher than those of the 0.5 bead loading runs. Both $T_{t(5)}$ and T_{max} increased upon an increase in bead loading, while $t_{T(32)}$ decreased (**Figure 4.8**). Here, we consistently used $t_{T(32)}$ instead of $t_{T(22)}$ because $t_{T(22)}$ could not discern the differences

well when the temperature reading frequency was not sufficient to capture the initial fast increase. The temperature rise was higher when bigger beads were used as can be seen from the upward shifting characteristic temperature curves through **Figure 4.8a** to **4.8c**. **Figures C.6** and **C.7** illustrate that the impact of higher bead loading became more pronounced at the higher stirrer speed. This is most notable from the greater separation of curves at the higher stirrer speeds and the emergence of intermittent milling cycles at 4000 rpm (**Figure C.6c**) vs. 2000 and 3000 rpm (**Figure C.6a** and **b**). This trend was also seen in Section 4.4.2.

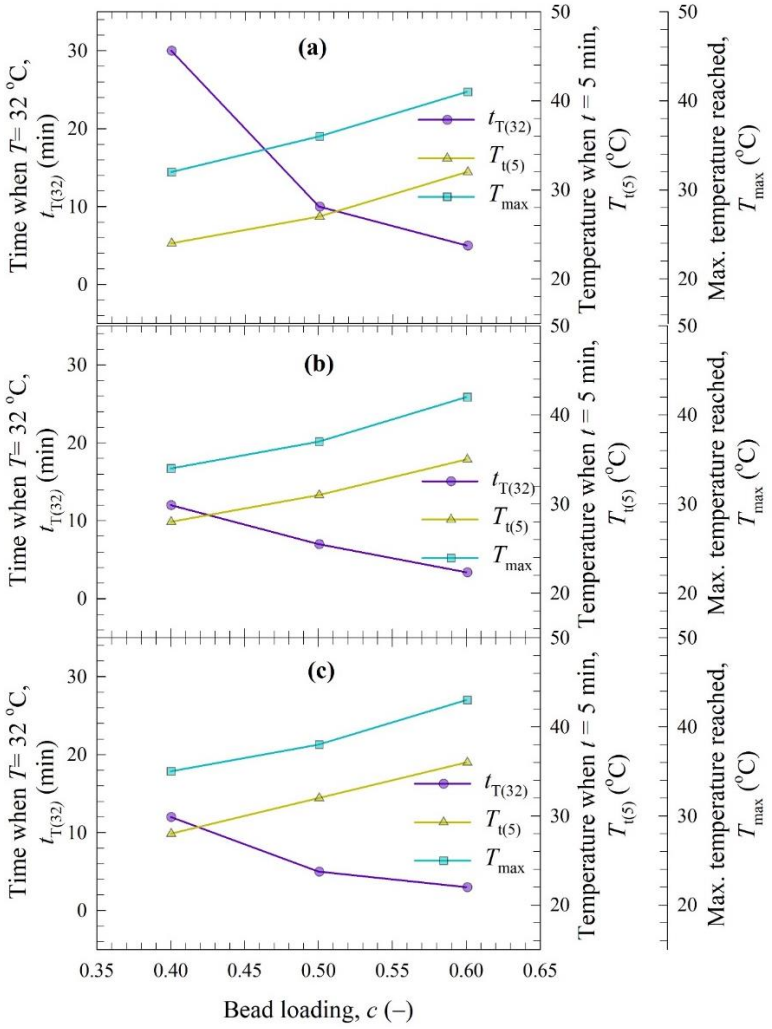

Figure 4.8 Impact of bead loading on the characteristic time and temperatures for ω = 3000 rpm and various bead sizes: (a) D_b = 200 µm (Runs 10, 13, 16), (b) D_b = 400 µm (Runs 11, 14, 17), and (c) D_b = 800 µm (Runs 12, 15, 18).

4.2.4 Impact of bead size on the timewise evolution of suspension temperature at the outlet

Figure 4.9 depicts the impact of bead size for different stirrer speeds (plotted as subfigures) at a constant bead loading of 0.5 (at the center of the experimental design). Readers can find an alternative presentation, looking at the impact of bead size for different bead loadings (plotted as subfigures) at a constant stirrer speed of 3000 rpm (at the center of the experimental design) in **Figure C.8** (*Appendix C*). The impact of the bead size on heat dissipation appears to be the weakest among all process parameters (**Figure 4.9**). At 2000 rpm (**Figure 4.9a**), the temperature profiles were almost identical, and the slopes of the characteristic temperatures were very low (**Figure 4.10**). As expected, $t_{T(22)}$ was the most discriminating parameter due to the slow increase in the temperature. At the higher stirrer speeds, the temperature rise originating from the increasing bead size became more apparent. At 4000 rpm, N_{mc} was higher for the larger beads. In **Figure 4.10c**, $t_{T(45)}$ was used instead of T_{max} because all runs reached 45 °C because it discerned the heat generation differences better. In **Figure C.8**, we could not observe a better differentiation between subfigures unlike **Figure 4.9** suggesting the impact of bead size was weaker when it was analyzed at the higher bead loading (**Figure C.8**) vs. higher stirrer speed (**Figure 4.9**). Supporting this, the slopes of the profiles between 200 and 400 µm were shallower in **Figure C.9** than those in **Figure 4.9**.

Overall, the results presented in Sections 4.2.2–4.2.4 are also in agreement with the hypothesis of the strong correlation between heat dissipation and power, as power values were also the same or very close to each other when different bead sizes were used as opposed to when different stirrer speeds and/or different bead loadings were used (refer to

Table 4.3). Overall, the influence of the process parameters on the heat dissipation can be rank-ordered qualitatively as stirrer speed > bead loading > bead size.

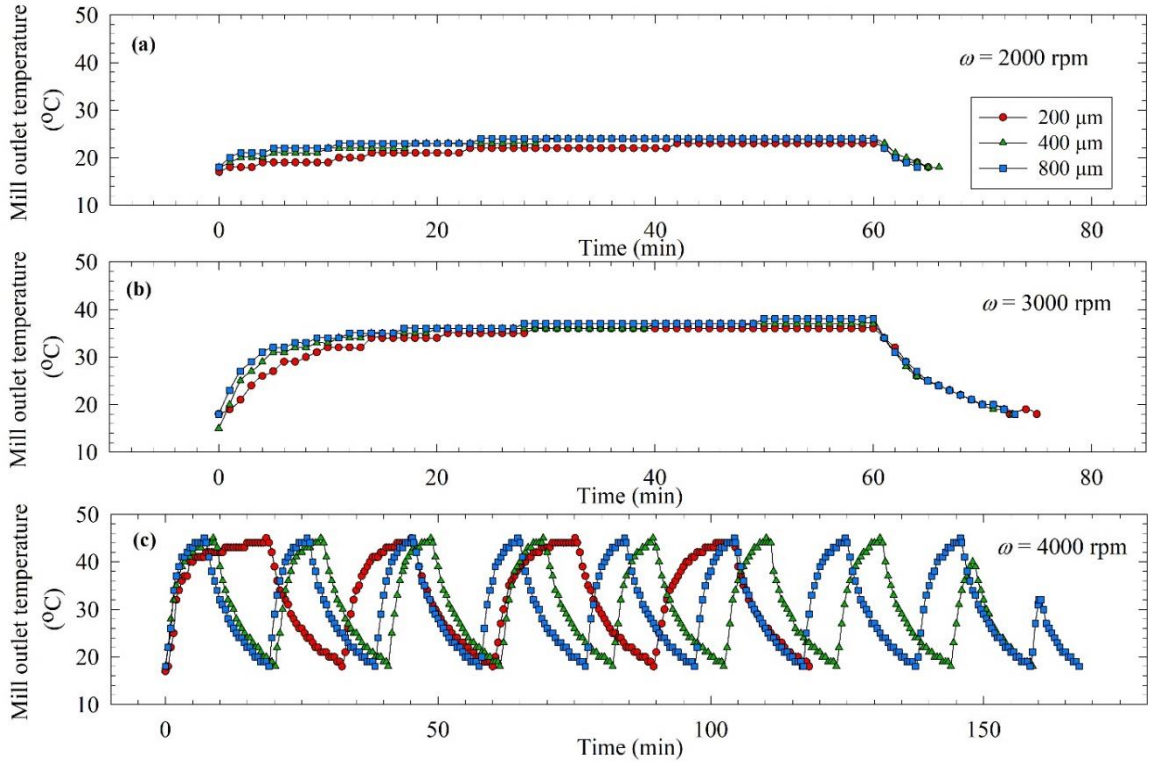

Figure 4.9 Impact of bead size on the timewise evolution of mill outlet temperature for c = 0.5 and various stirrer speeds: (a) ω = 2000 rpm (Runs 4–6), (b) ω = 3000 rpm (Runs 13–15), and (c) ω = 4000 rpm (Runs 22–24).

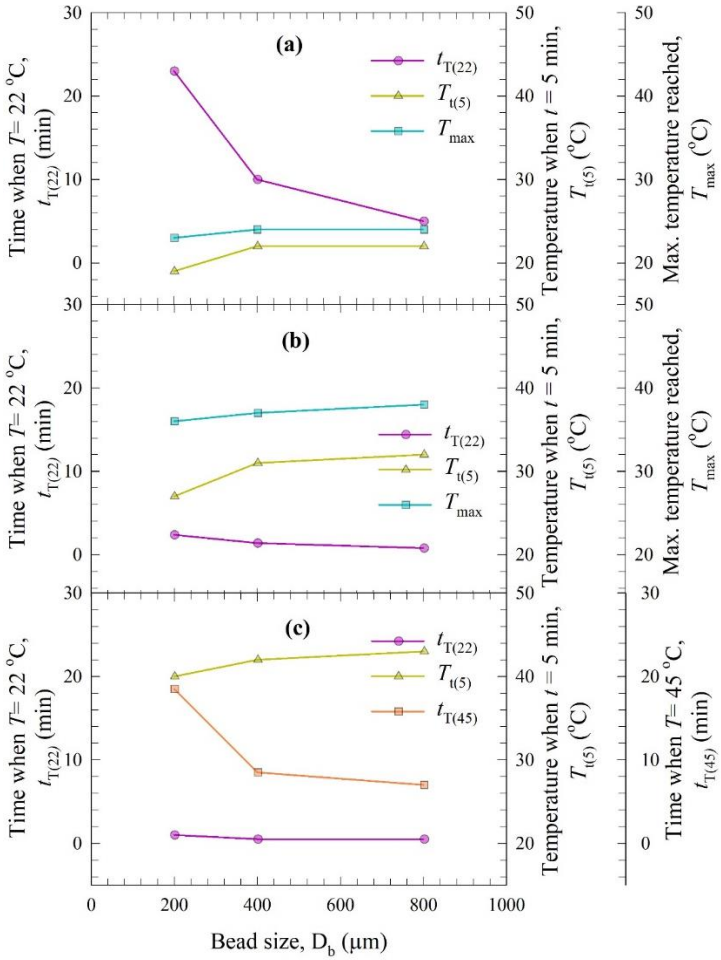

Figure 4.10 Impact of bead size on the characteristic time and temperatures for c = 0.5 and various stirrer speeds: (a) ω = 2000 rpm (Runs 4–6), (b) ω = 3000 rpm (Runs 13–15), and (c) ω = 4000 rpm (Runs 22–24).

4.2.5 Variation of initial mill outlet temperature and evolution of chiller liquid temperature

Due to variations in the temperature of the pre-suspensions during their preparation (refer to Section 4.1.2) and different times it took for the chiller liquid temperature to attain 6 ºC , the initial mill outlet temperature exhibited slight variations, on the order of 1–3 ºC, among most runs, which can be seen from **Figures 4.4, 4.7,** and **4.9**. For example, the *initial* mill outlet temperature for Runs 2, 11, and 20 (**Figure 4.4a**) was 17, 15, and 16 ºC, respectively. Despite its highest initial mill outlet temperature among these runs, Run 2 exhibited the lowest mill outlet temperature during the rest of the milling due to its lowest

power consumption. This finding is not surprising: as the heat generation rate is determined by power consumption and both the heat generation rate and the heat removal rate govern the evolution of the mill outlet temperature during the milling, the slight differences in the initial mill outlet temperatures did not significantly affect the whole temperature profiles comparatively.

Figures C.1–C.3 of the *Appendix C* depict that the temperature of the chiller liquid (coolant), which was pumped into the cooling jacket of the milling chamber, increased as milling progressed. Due to the limited cooling capacity of our chiller and the significant heat generation during the milling, the coolant temperature increased along with the increase in suspension temperature at the mill outlet. As the coolant (20% v/v glycol–water mixture) follows a loop through the system (see **Figure 4.1**), the coolant temperature is intimately linked to the heat generation in the milling chamber and suspension temperature. Unfortunately, such a coupling between the coolant temperature and the heat generation in the mill makes it difficult to analyze the potential impact of the evolving coolant temperature on the suspension temperature. The presence of intermittent milling cycles also complicates this analysis. For example, although Run 26 (4000 rpm) had much higher power consumption and sharper increase of mill outlet temperature than Run 8 (2000 rpm) at c = 0.6 with D_b = 400 µm beads (**Table 4.3**), Run 26 coolant temperature remained flat at 5–6 ^oC whereas Run 8 coolant temperature rose to 13 ^oC (Fig S1(c)). This was ascribed to the 13 intermittent milling cycles with prolonged, additional cooling in Run 26 vs. Run 8 with one cycle of milling–cooling. Overall, a detailed analysis of how this evolution of the coolant temperature affects the process can only be done within the context of an enthalpy balance model for the first milling cycle considering the mill, the holding tank,

and the chiller, which is beyond the scope of this manuscript.

4.2.6 Correlation between the heat generation dynamics and the power consumption

To investigate the hypothesis of a possible correlation between the heat generation dynamics and the power consumption, $t_{T(22)}$ and $T_{t(5)}$ data were fitted by P. Even though these measures were somewhat arbitrary and other measures can be used, $t_{T(22)}$ and $T_{t(5)}$ were available for the majority of the runs (refer to **Table C.1**). Two parameter power-law models were fitted to $t_{T(22)}$ and $T_{t(5)}$ vs. P using SigmaPlot 12.5. All parameters and models were found to be statistically significant with p-value < 0.05. The equations are given below:

$$t_{T(22)} = 0.0018P^{-2.76} \tag{4.1}$$

$$T_{t(5)} = 82.1P^{0.422} \tag{4.2}$$

As expected, an increase in power leads to faster heat generation as signified by the higher temperature at 5 min and faster attainment of 22 ^{o}C (shorter time), which can be seen visually in **Figure 4.11**. Above 0.1 kW, while $t_{T(22)}$ does not change much, $T_{t(5)}$ continues to increase with P remarkably, which makes the relevant milling runs less desirable from a thermal perspective. Equation (4.2) provided a better fit compared to Equation (4.1), which may be due to lack of sensitivity of tT(22) data for some fast heat generation cases, as discussed previously.

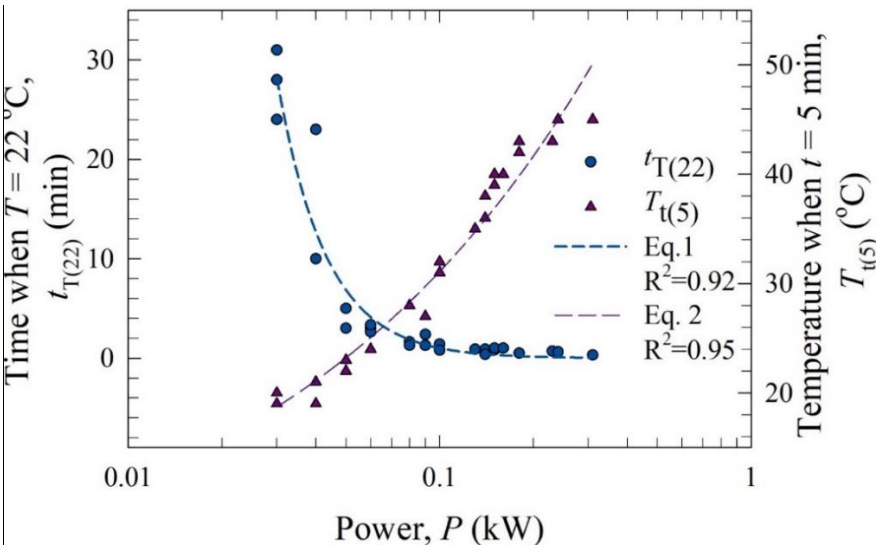

Figure 4.11 Scatter plots and power-law scaling for dependence of characteristic time and temperature on the power required by the mill stirrer.

To establish a quantitative correlation between the temperature rise and the process parameters, the normalized temperature rise was expressed as a power-law function of the normalized process parameters as follows:

$$\frac{T_{t(5)} - T_{\mathrm{ini}}}{T_{\mathrm{ini}}} = 2.16\left(\frac{\omega}{\omega_{\max}}\right)^{2.26}\left(\frac{c}{c_{\mathrm{lim}}}\right)^{0.706}\left(\frac{D_{\mathrm{b}}}{D_{\mathrm{b,max}}}\right)^{0.119} \tag{4.3}$$

where $\omega_{\max}$ is the maximum stirrer speed of our mill (design limit: 4200 rpm), c_{lim} is the packing limit (0.63), and $D_{\mathrm{b,max}}$ is the maximum bead size used (800 μm). It is reasonable to infer from this power-law correlation with R^2 = 0.96 that the process parameters that affect the temperature rise most can be rank-ordered as stirrer speed > bead loading > bead size, which is in line with the temperature profiles in **Figures 4.4, 4.7,** and **4.9**.

4.2.7 Thermal desirability score (TDS) and selection of optimal milling conditions

To guide pharmaceutical scientists and engineers decide if a given set of milling conditions is desirable from a heat generation–temperature rise perspective, a thermal desirability

score TDS was defined below:

$$TDS = 100(N_{\mathrm{mc}}\, T_{\max}/T_{\mathrm{ini}})^{-1/3} \tag{4.4}$$

If the process were isothermal ($T_{\max}/T_{\mathrm{ini}} = 1$ and $N_{\mathrm{mc}} = 1$), *TDS* would be 100, which is practically impossible to achieve due to high heat generation rate during WSMM as compared with the heat removal rate from the jacketed walls of the mill and the holding tank. As the process deviates from isothermality because $T_{\max}/T_{\mathrm{ini}}$ exceeds one and intermittent milling is required at the highest $T_{\max}/T_{\mathrm{ini}}$, the *TDS* decreases. In view of the specific form used for the *TDS* here, roughly speaking, a *TDS* within the range 90–100 would correspond to near-isothermality (excellent) with low temperature rise. A milling process with 80–89, 70–79, and <69 *TDS* may be regarded as good, acceptable, and poor, respectively. We label a *TDS* score <69 poor because it is likely associated with $N_{\mathrm{mc}} > 1$, which also implies a higher cycle time due to multiple intermittent milling–cooling cycles (see **Table 4.3**). It is critical to emphasize that *TDS* is not the sole criterion for process selection (see the discussion below), and its use is dependent on the specific drug formulation and the sensitivity of the drug to temperature. For example, the exponent (1/3) of Equation (4.4) may be increased if the early development data for a drug compound indicates high thermal sensitivity (e.g., thermally labile drugs). Here, the choice of 1/3$^{\mathrm{rd}}$ power is for illustrative purposes. Another caveat to mention is that the values of N_{mc} and any characteristic time–temperature including $T_{\max}$ and T_{ini} obviously depend on the specific milling equipment, chiller capacity, and scale. For example, if one uses a chiller with much higher cooling capacity than the one used in this chapter, the characteristic times $t_{\mathrm{T}(22)}$, $t_{\mathrm{T}(32)}$, $t_{\mathrm{T}(42)}$, and $t_{\mathrm{T}(45)}$ will be higher, and the characteristic temperatures $T_{\mathrm{t}(5)}$, $T_{\mathrm{t}(10)}$, $T_{\mathrm{t}(30)}$, and $T_{\max}$ will be lower. With a decrease in N_{mc}, some runs at 4000 rpm could become

feasible. However, the general trends for the impact of process parameters on the temperature profiles will most likely be similar.

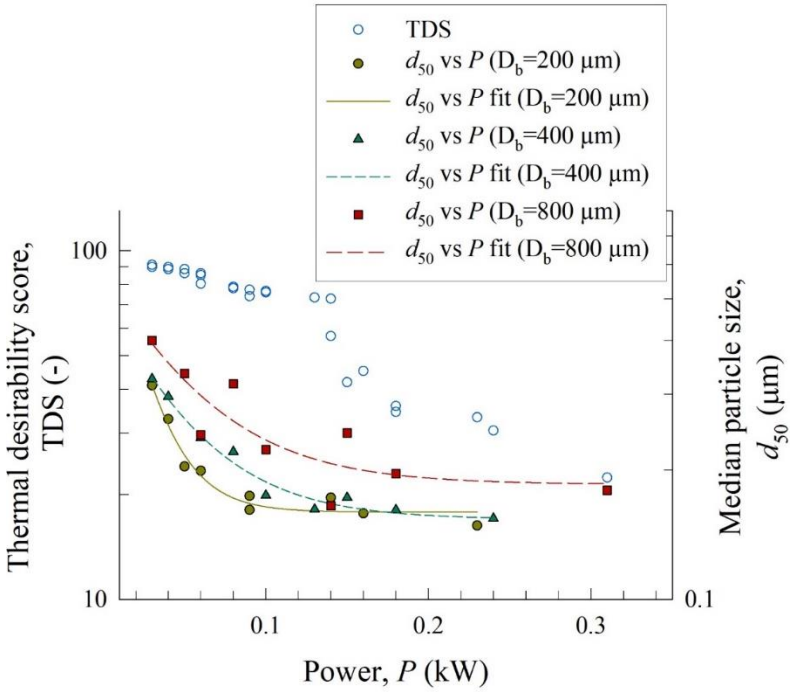

Figure 4.12 Variation of thermal desirability score TDS for the milling process and the median particle size d_{50} of the 60 min milled suspensions (separately shown for different bead sizes used) as a function of the power supplied by the stirrer and their fits by Equations (4.3–4.6).

Figure 4.12 illustrates how *TDS* and final drug median particle size d_{50}, which is another major process selection criteria, vary as a function of the average power supplied *P*. In general, an increase in *P* led to a lower d_{50} (favorable) and lower *TDS* (unfavorable). The power consumption is a relatively rough, bulk measurement that cannot directly explain the microhydrodynamics of bead–bead collisions and it cannot be used to predict the breakage rate [33, 57, 150]. On the other hand, for a given bead size, a higher power consumption is associated with higher values of the microhydrodynamic parameters including the granular temperature of the beads at the higher stirrer speed and higher number of drug particle compressions at the higher bead loading [165]. Hence, it is not

surprising to find lower d_{50} at the higher power consumption. In general, the smaller beads (200 and 400 µm) yielded finer drug particles than 800 µm beads. A plateau median size was approached above 0.1 kW for 200 and 400 µm beads whereas *TDS* deteriorated. An empirical 3-parameter exponential decay function was used to describe the dependence of final median particle size d_{50} for each bead size on P.

$$d_{50(200\ \mu m)} = 0.160 + 0.711\exp(-50.5P) \quad (4.5)$$

$$d_{50(400\ \mu m)} = 0.154 + 0.353\exp(-23.4P) \quad (4.6)$$

$$d_{50(800\ \mu m)} = 0.185 + 0.385\exp(-20.5P) \quad (4.7)$$

R^2 of the fits for Equations (4.5–4.7) are 0.97, 0.98 and 0.80, respectively. Except for Equation (4.7), all models provided a good fit with statistically significant parameters.

Toward the selection of an optimal process, let us take a conservative approach and limit the maximum milling temperature to 37 ^oC as no surface modification and amorphization occurred when temperature was raised from 25 ^oC to 37 ^oC for a fenofibrate nanosuspension stabilized by HPC–SDS [154]. For an intended product specification of d_{10} < 150 nm, d_{50} < 200 nm, and d_{90} < 250 nm, a holistic consideration of *TDS*, power (energy) consumption, and total cycle time (**Table 4.3**) suggests that Run 13 or 14 had the optimal set of milling conditions: 3000 rpm with 50% loading of 200 or 400 µm beads. While having good TDS, Runs 1–12 had too low power that resulted in a relatively a coarse and wide particle size distribution. Despite producing finer particles than those of Runs 1–12, Runs 19–27 had unacceptably high power/energy consumption (≥ 0.14 kW) that entailed multiple intermittent milling cycles with relatively long cycle times, which is signified by *TDS* <57. Although Runs 13, 14, 16, and 17 had acceptable *TDS* and meet the

particle size specifications, only Runs 13 or 14 allow for a maximum allowed temperature of ≤ 37 °C during the milling.

4.2.8 Power consumption correlation as a function of process–suspension properties

As power consumption governs the heat generation during the WSMM, it is important to estimate from a correlation. It is common to correlate the dimensionless power number N_p, a.k.a Newton number,

$$N_p = \frac{P}{D^5 N^3 \rho} \tag{4.8}$$

to the process parameters. Here, N is the stirrer speed and D is the diameter of the mill stirrer. The use of N_p–Reynolds number Re correlation is a common practice in WSMM literature [198]. These correlations can be developed based on the suspension properties for the Re as in [137] or the suspension–bead mixture properties [34, 193]. We have adopted the latter approach and calculated the mixture viscosities μ_m and densities ρ_m as follows [194]:

$$\mu_m = \mu_L[1 + 2.5c + 10c^2 + 0.0019\exp(20c)] \tag{4.9}$$

$$\rho_m = \rho_b c + \rho_L(1 - c) \tag{4.10}$$

$$Re_m = \frac{\rho_m N D^2}{\mu_m} \tag{4.11}$$

Re_m changes mostly with the varying stirrer speed in each run as can be seen in **Table 4.3**. In order to capture the impact of all process parameters, N_p is not only correlated with Re_m but also with the dimensionless numbers of the bead size and bead loading: D_b/D and c/c_{lim}, where c_{lim} (0.63) is the packing limit of the monodispersed spherical beads [147]. A power-law correlation was found by fitting the parameters using Minitab 18 as follows:

$$N_{\mathrm{p}} = 0.89\mathrm{Re}_{\mathrm{m}}^{-0.33}(D_{\mathrm{b}}/D)^{0.105}(c/c_{\mathrm{lim}})^{-1.44} \quad (4.12)$$

As can be seen from **Figure 4.13**, the fit was fairly good with some deviation, which may be due to the size–temperature dependent variation of the suspension viscosity during the milling (refer to **Figure 4.5**) and ensuing change in instantaneous power as well as the limited accuracy of the mixture correlations, expressed by Equations (4.9) and (4.10).

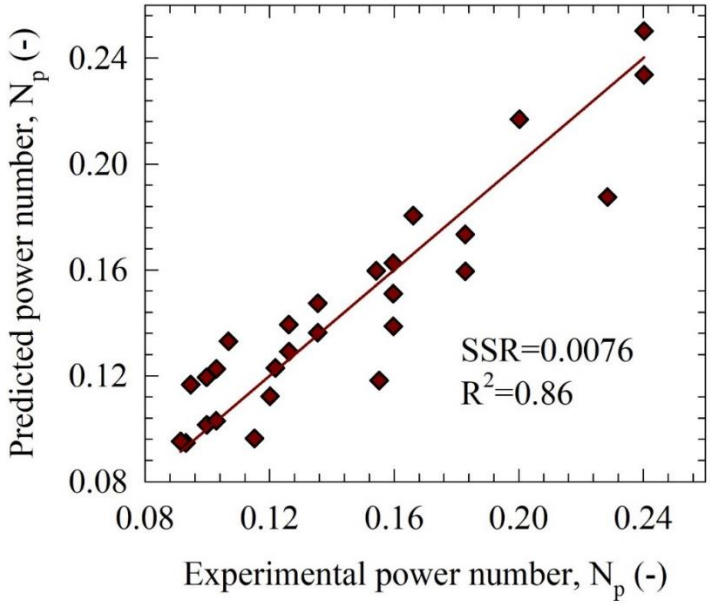

Figure 4.13 Power number N_{p} values that were calculated using experimental properties and its prediction by the power law correlation.

4.3 Conclusions

This chapter has explored the impact of stirrer speed, bead loading, and bead size on the temperature evolution during the WSMM of a drug suspension for the first time in the milling literature. We have demonstrated that the mechanical power converted into heat led to temperature rise. Stirrer speed was found to be the most influential process parameter on the temperature increase, followed by bead loading and bead size. Correlations between characteristic time–temperature of the temperature profile with power consumption were established. The newly defined thermal desirability score, based on deviations from an

ideal isothermal operation, enabled a rough guidance to help optimal process selection. While an increase in power consumption was associated with finer drug particles, it also led to a significant deterioration of the thermal desirability of the milling process. Once maximum temperature allowed and the desirable particles sizes were specified, a milling process with 3000 rpm with 50% loading of 200 or 400 μm beads was identified to be optimal for the production of fenofibrate nanosuspensions upon consideration of thermal desirability score, cycle time, and power/energy consumption holistically. Overall, we have established the importance of examining the heat generation during the WSMM of drug suspensions as an integral part of robust process development–optimization.

CHAPTER 5

AN ENTHALPY-BALANCE MODEL FOR TIMEWISE EVOLUTION OF TEMPERATURE DURING WET STIRRED MEDIA MILLING OF DRUG SUSPENSIONS

This chapter explores the temperature evolution during the production of drug nanosuspensions in a wet stirred media mill using a coupled experimental–enthalpy balance approach. For this aim, milling was performed at three levels of stirrer speed, bead loading, and bead sizes. Temperatures were recorded over time, then simulated using an enthalpy balance model by fitting the fraction of power converted to heat ξ. Moreover, initial and final power, ξ, and temperature profiles at 5 different test runs were predicted by power-law (PL) and machine learning (ML) approaches. Heat generation was higher at the higher stirrer speed and bead loading/size, which was explained by the higher power consumption. Despite its simplicity with a single fitting parameter ξ, the enthalpy balance model fitted the temperature evolution well with root mean squared error (RMSE) of 0.40–2.34 °C. PL and ML approaches provided decent predictions of the temperature profiles in the test runs, with RMSE of 0.93–4.17 and 1.00–2.17 °C, respectively. We established the impact of milling parameters on heat generation–power and demonstrated the simulation–prediction capability of an enthalpy balance model when coupled to the PL–ML approaches.

5.1 Materials and Methods

5.1.1 Materials

BP grade fenofibrate (FNB, BCS Class II) was purchased from Jai Radhe Sales, Ahmedabad, India. L grade hydroxypropyl cellulose (HPC, non-ionic cellulosic polymer)

was donated by Nisso America Inc, New York, NY, USA. ACS grade sodium dodecyl sulfate (SDS, anionic surfactant) was purchased from GFS chemicals, Columbus, OH, USA. Zirmil Y grade Yttrium stabilized zirconia beads (YSZ) with nominal sizes of 100, 200, 400, and 800 µm, were purchased from Saint Gobain ZirPro, Mountainside, NJ, USA.

5.1.2 Wet stirred media milling

About 236 g of pre-suspensions that have 10% FNB, 8% HPC-L, and 0.05% SDS (w/w with respect to 200 g deionized (DI) water) were prepared under constant shear mixing at 300 rpm (Cat#. 14-503, Fisher Scientific, Pittsburgh, PA, USA) for 2 h and were kept under 8 ^{o}C overnight. This stable suspension formulation and process conditions were selected based on (i) our prior studies with fenofibrate [149, 150] and (ii) the rationale that a high polymer concentration could help to ensure sufficiently high power consumption that could be measured accurately. The pre-suspensions were milled by Microcer wet stirred media mill (Netzsch Fine Particle Size Technology, LLC, Exton, PA, USA).

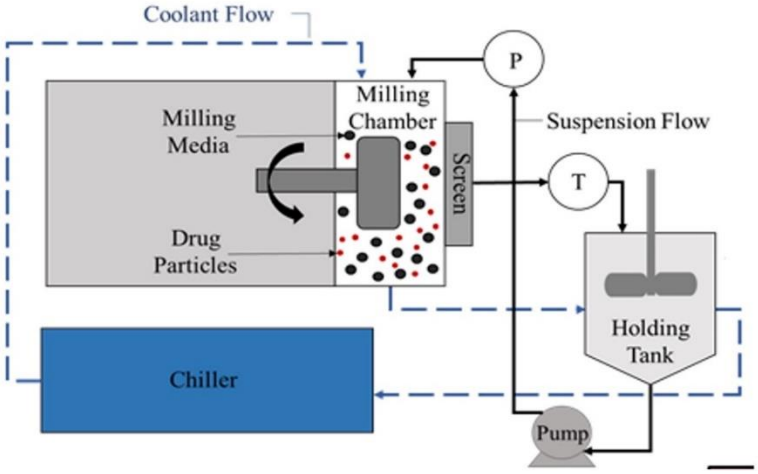

Figure 5.1 Schematic of the wet stirred media mill and the cooling system.

Figure 5.1 presents a schematic of the recirculation operation mode of the mill. The mill has a chamber volume V_m of 80 ml, lined with zirconia, and a zirconia stirrer/shaft.

Suspensions were recirculated between the holding tank and the milling chamber at a volumetric flow rate of 126 mL/min, using a peristaltic pump (Cole-Palmer, Master Flex, Vermont Hills, IL, USA). Stainless-steel screens with nominal opening sizes of 50, 100, 200 and 400 μm were used for 100, 200, 400 and 800 μm nominal-sized beads, respectively, to hold the beads inside the milling chamber. The milling chamber and the holding tank were cooled by a Model M1-.25A-11HFX chiller (Advantage Engineering, Greenwood, IN, USA).

Table 5.1 Process Parameters for the Milling of FNB Suspensions.

Run No.	Stirrer Speed, ω (rpm)	Bead Loading, c (-)	Bead size, D_b (μm)
1[a]	2000	0.4	200
2[a]	2000	0.4	400
3[a]	2000	0.4	800
4[a]	2000	0.5	200
5[a]	2000	0.5	400
6[a]	2000	0.5	800
7[a]	2000	0.6	200
8[a]	2000	0.6	400
9[a]	2000	0.6	800
10[a]	3000	0.4	200
11[a]	3000	0.4	400
12[a]	3000	0.4	800
13[a]	3000	0.5	200
14[a]	3000	0.5	400
15[a]	3000	0.5	800
16[a]	3000	0.6	200
17[a]	3000	0.6	400
18[a]	3000	0.6	800
19[a]	4000	0.4	200
20[a]	4000	0.4	400
21[a]	4000	0.4	800
22[a]	4000	0.5	200
23[a]	4000	0.5	400
24[a]	4000	0.5	800
25[a]	4000	0.6	200
26[a]	4000	0.6	400
27[a]	4000	0.6	800
28[b]	2500	0.45	400
29[b]	2500	0.55	400
30[b]	3500	0.45	400
31[b]	3500	0.55	400
32[b]	4200	0.35	100

[a]Runs that were used in the training set, [b]Runs that were used in the test set.

The milling conditions are presented in **Table 5.1**. The stirrer speed, the bead loading, and the bead size were varied at 3 levels in a full-factorial design of experiments. These 27 runs were used to train our models, and additional 5 runs were performed to test the predictive capability of the developed models. Runs 28–31 correspond to the middle conditions of the training runs and run 32 is in an extrapolated region where the highest stirrer speed (design limit of the mill) and the lowest practical loading of the smallest beads (100 μm) were used.

The milling of the pre-suspension started when the chiller temperature reached ~6 ^{o}C and the mill outlet temperature was below 18 ^{o}C. Both temperatures were recorded at every minute for 2000 rpm and 3000 rpm runs and at every 30 s for 4000 rpm runs. If the mill outlet temperature was below 45 ^{o}C for the whole duration of 60 min milling, the mill was cooled down to 18 ^{o}C (outlet temperature) at the end of 60 min while temperature recording continued. Else, the mill was shut down whenever the temperature reached 45 ^{o}C, and the cooling was continued to attain a mill outlet temperature of 18 ^{o}C. In this second scenario, this intermittent milling–cooling cycle was repeated various times until the suspension was milled for a total of 60 min, and the mill outlet was cooled down to 18 ^{o}C in the end. It is reported that 8% HPC has a gelation temperature of 45 °C despite its high aq. solubility at room temperature, which originates from the aggregation of the polymer chains at or above the gelation temperature [155]. This reversible phenomenon might negatively affect the suspension stability during the milling, which was why the milling was stopped at 45 ^{o}C. Although we have only considered the first cycle in our heat generation–transfer analysis, a sample from 60 min milled suspension was taken for particle size analysis to confirm that drug nanoparticles were produced under all milling

conditions. The instantaneous power at the start (0 min) and end of milling (60 min) was recorded (**Table D.1** of the *Appendix D*). The average power during the whole milling was determined by dividing the cumulative energy consumption, read from the control panel of the mill, by the milling time.

5.1.3 Characterization techniques

The apparent shear viscosities μ_L of the suspensions were measured using R/S plus rheometer (Brookfield Engineering, Middleboro, MS, USA) with a water jacket assembly Lauda Eco (Lauda-Brinkmann LP, Delran, NJ, USA). A CC40 coaxial cylinder with a jacketed setup was used to impart a controlled shear rate on the samples from 0 to 1000 1/s in 60 s. The jacket temperature was kept constant at 25 ± 0.5 °C. The raw data were analyzed using the Rheo3000 software and the apparent shear viscosity at the maximum shear rate (1000 1/s) was used in the calculations as this shear rate emulates the high shear rate in the mill [63]. The density of the suspensions ρ_L was measured by weighing 35 ml of the suspension and dividing the mass of the suspension by its volume. All measurements were repeated thrice and averages were taken. The measured μ_L and ρ_L values can be found in **Table D.1** of the *Appendix D*.

Particle sizes of the milled suspensions were measured by laser diffraction using an LS 13-320 Beckman Coulter instrument (Brea, CA, USA). Polarized intensity differential scattering (PIDS) was kept between 40–50%, and the obscuration was maintained below 8% in all measurements. Mie scattering theory was used by software to compute PSD by taking the refractive indices of FNB and water (1.55 and 1.33, respectively). Prior to each measurement, about 1.0 mL of suspension sample was dispersed into 5.0 mL of the stabilizer solution of the used formulation, using a vortex mixer (Fisher Scientific Digital

Vortex Mixer, Model No: 945415, Pittsburgh, PA, USA) at 1500 rpm for 1 min. Measurements were repeated four times, and the average of these measurements was calculated. The particle size statistics of the 60 min milled suspensions can be found in **Table D.2** of *Appendix D*. Zeta potential of the milled suspension of Run 23 was measured using a zeta potential analyzer thrice (Delsa Nano C, Beckman Coulter, CA, USA).

As-received FNB particles were observed using an Axio Scope.A1 polarized light microscope (PLM) (Carl Zeiss Microscopy GmbH, Göttingen, Germany). Image of milled FNB particles in Runs 23 was taken by a JEOL JSM 7900F field emission scanning electron microscope (SEM) (JEOL USA, Inc., Peabody, MA, USA) operated at 2 kV. About 0.1 mL of the suspension sample was diluted with 10 ml deionized water and centrifuged (Compact II centrifuge, Clay Adams® Brand, Sparks, MD, USA) at 3200 rpm for 10 min to separate the drug particles from the aqueous phase with excess polymer. This dilution–centrifugation procedure was repeated two more times and a droplet from the aliquot of the sample was put on top of a carbon specimen holder and it was placed in a desiccator for overnight drying under vacuum. The dried sample was then sputter coated with gold using BAL-TEC MED020 (BAL-TEC, Balzers, Switzerland) to reduce possible charging during imaging.

5.1.4 Formulation of the enthalpy balance model

Assuming well-mixedness in the holding tank and the milling chamber, with continuous recirculation of the suspension between them, the following macroscopic transient enthalpy balance can be written for the suspension, beads, and stirrer, respectively, in the milling chamber:

$$M_{\mathrm{s,m}} C_{\mathrm{p,s}}\, dT_{\mathrm{s,m}}/dt \tag{5.1}$$
$$= \rho F C_{\mathrm{p,s}} T_{\mathrm{s,ht}} - \rho F C_{\mathrm{p,s}} T_{\mathrm{s,m}} + P\xi + Q_{\mathrm{ch,m}}$$
$$- h_{\mathrm{B,m}} \left(\frac{6M_{\mathrm{b}}}{\rho_{\mathrm{b}} D_{\mathrm{b}}}\right)\left(T_{\mathrm{s,m}} - T_{\mathrm{b}}\right) - h_{\mathrm{B,m}} A_{\mathrm{st,m}}\left(T_{\mathrm{s,m}} - T_{\mathrm{st,m}}\right),$$
$$\text{at } t = 0,\ T_{\mathrm{s,m}}(0) = T_{\mathrm{s,m,0}}$$

$$M_{\mathrm{b}} C_{\mathrm{p,b}}\, dT_{\mathrm{b}}/dt = h_{\mathrm{B,m}} \left(\frac{6M_{\mathrm{b}}}{\rho_{\mathrm{b}} D_{\mathrm{b}}}\right)\left(T_{\mathrm{s,m}} - T_{\mathrm{b}}\right), \text{at } t = 0,\ T_{\mathrm{b}}(0) = T_{\mathrm{b,0}} \tag{5.2}$$

$$M_{\mathrm{st,m}} C_{\mathrm{p,st,m}}\, dT_{\mathrm{st,m}}/dt = h_{\mathrm{B,m}} A_{\mathrm{st,m}}\left(T_{\mathrm{s,m}} - T_{\mathrm{st,m}}\right), \text{at } t = 0,\ T_{\mathrm{st,m}}(0) \tag{5.3}$$
$$= T_{\mathrm{st,m,0}}$$

where subscript m is reserved for the mill chamber (suspension s, beads b, and stirrer st) and subscript ht is reserved for the holding tank (suspension s and stirrer st). Also, M is the mass, C_{p} is the specific heat capacity, T is temperature, t is time, P is power (shaft work done by the stirrer in the milling chamber per unit time), ξ is the fraction of the power P converted into heat, F is the volumetric flow rate of the recirculating suspension (126 ml/min), ρ is the density of the suspension, which was measured as 1.03 g/ml, and Q_{ch} is the rate of heat removal via the jacket of the mill chamber through which the chiller liquid passes. Equations (5.2) and (5.3) describe the heat transfer between the drug suspension and the beads and the stirrer, respectively. Within the temperature range of interest, it is reasonable to assume the constancy of the heat capacities, and all properties measured at 25 °C were taken from the literature. The well-mixedness in the milling chamber has been established as a valid approximation to the residence time distribution in small mills (small length-to-diameter ratio) [87, 93].

A similar enthalpy balance equation can be formulated for the holding tank content as follows:

$$M_{\mathrm{s,ht}}C_{\mathrm{p,s,ht}}\,dT_{\mathrm{s,ht}}/dt = \rho F C_{\mathrm{p,s}}T_{\mathrm{s,m}} - \rho F C_{\mathrm{p,s}}T_{\mathrm{s,ht}} + Q_{\mathrm{ch,ht}} - \mathrm{h_{b,ht}A_{st,ht}}\left(\mathrm{T_{s,ht}} - \mathrm{T_{st,ht}}\right), \text{at } t = 0, \quad T_{\mathrm{s,ht}}(0) = T_{\mathrm{s,ht,0}} \tag{5.4}$$

$$M_{\mathrm{st,ht}}C_{\mathrm{p,st,ht}}\,dT_{\mathrm{st,ht}}/dt = h_{\mathrm{B,ht}}A_{\mathrm{st,ht}}\left(T_{\mathrm{s,ht}} - T_{\mathrm{st,ht}}\right), \quad \text{at } t = 0, \quad T_{\mathrm{st,ht}}(0) = T_{\mathrm{st,ht,0}} \tag{5.5}$$

One should note that there are no beads in the holding tank, but only the drug suspension and the mixing element. Hence, the power input due to stirring in the holding tank was neglected. Cp,s was calculated to be 3.74 J/g°C, by the weighted average of the specific heat capacities of water, FNB, and HPC in the suspension, which were taken as 4.18 J/g°C [199], 1.22 J/g°C [200], and 1.34 J/g°C [201], respectively. $C_{\mathrm{p,b}}$ and $C_{\mathrm{p,st,m}}$ are the specific heat capacities of zirconia beads and the zirconia stirrer element, which were taken as 0.46 J/g°C [202]. $C_{\mathrm{p,st,ht}}$ is the specific heat capacity of the stainless steel stirrer element in the holding tank, which was taken as 0.47 J/g°C [199]. $M_{\mathrm{st,m}}$ and $A_{\mathrm{st,m}}$ were 400 g and 0.0268 m^2, which are constant for all runs; however, as several bead loadings were used in the experiments, the mass of the beads in the mill chamber differed. Therefore, the volume and mass available for the suspension to occupy in the mill chamber varied. All the portion of the suspension that was not in the mill chamber was assumed to be in the holding tank, neglecting the suspension in the recirculation connection tubes (~4% of the total suspension). The height of the stirrer element that is in contact with suspension in the holding tank varied as well. Therefore, M_{b}, $M_{\mathrm{s,m}}$, $M_{\mathrm{st,ht}}$, $M_{\mathrm{s,ht}}$, $A_{\mathrm{st,ht}}$, $h_{\mathrm{B,m}}$, and $h_{\mathrm{B,ht}}$ changed upon changes in the bead loading. Note that Q_{ch} expression was derived in *Appendix D*; $h_{\mathrm{B,m}}$ and $h_{\mathrm{B,ht}}$ are the internal heat transfer coefficients, which were also calculated as described in *Appendix D.*

The chiller liquid (20% glycol–water volumetric mixture) follows a loop through the system: it first flows around the cooling jacket of the mill chamber, and then flows around the cooling jacket of the holding tank, finally returning to the chiller. The heat removal rates from the milling chamber and the holding tank, i.e., $Q_{ch,m,}$ and $Q_{ch,ht}$, respectively, are different. The chiller liquid temperature entering the milling chamber $T_{ch,in}$ was measured and recorded for each sampling time. The chiller liquid temperature exiting the mill chamber $T_{ch,out}$ as well as $Q_{ch,m,}$ and $Q_{ch,ht}$ were determined by performing a separate enthalpy balance for the chiller liquid (refer to *Appendix D*):

$$Q_{\mathrm{ch,m}} = m_{\mathrm{ch}}\, C_{\mathrm{p,ch}}(T_{\mathrm{ch,in}} - T_{\mathrm{s,m}})\left[1 - \exp\left(-UA_{\mathrm{m}}/m_{\mathrm{ch}}C_{\mathrm{p,ch}}\right)\right] \tag{5.6}$$

$$T_{\mathrm{ch,out}} = T_{\mathrm{s,m}} + \left(T_{\mathrm{ch,in}} - T_{\mathrm{s,m}}\right)\exp\left(-UA_{\mathrm{m}}/m_{\mathrm{ch}}C_{\mathrm{p,ch}}\right) \tag{5.7}$$

$$Q_{\mathrm{ch,ht}} = m_{\mathrm{ch}}\, C_{\mathrm{p,ch}}(T_{\mathrm{ch,out}} - T_{\mathrm{s,ht}})\left[1 - \exp\left(-UA_{\mathrm{ht}}/m_{\mathrm{ch}}C_{\mathrm{p,ch}}\right)\right] \tag{5.8}$$

One cautionary note for the readers is that $T_{ch,out}$, $Q_{ch,m,}$ and $Q_{ch,ht}$ are not constants as they depend on $T_{ch,in}$, $T_{s,m}$, and $T_{s,ht}$, which vary with time. Here, m_{ch} is the mass flow rate of the chiller liquid, which was experimentally measured as 830 g/min. $C_{p,ch}$ was found to be 3.97 J/g°C for a weighted average of C_p for the glycol–water mixture. *UA* is the product of the overall heat transfer coefficient and the pertinent heat transfer surface area, which were calculated for the mill chamber and the holding tank separately, as described in *Appendix D*.

The parameters required to solve the set of five ordinary differential equations (odes), Equations (5.1–5.5), were entered as input in a MATLAB (R2020b) code. Some of these parameters are presented in **Table 5.2**. Only the initial and final instantaneous power consumption, P_0 and P_f, were recorded, and a drop in power consumption was experimentally observed. Hence, instead of using the average power consumption, this

variation in P during milling was expressed by utilizing P_0 and P_f values and assuming the simplest mathematical form, a linear drop of power consumption over the milling time during the first milling cycle t_f: $P = P_0+(P_f - P_0)t/t_f$. As we want to develop a simple mathematical model for easy industrial use, we have not sought for detailed experimental measurements of power and more complicated mathematical expressions in this first attempt for a heat generation–transfer analysis of WSMM. Equations (5.1–5.8) were then solved via the ode solver, ode15s, and fitted to experimentally recorded mill outlet temperatures to estimate the only unknown parameter, i.e., ξ, in Runs 1–27 by using a nonlinear optimizer, fmincon [203]. The optimizer minimizes the objective function of ξ, i.e., the root mean squared errors (RMSE) between the measured and simulated $T_{s,m}$ during milling. For fmincon, the absolute error tolerance (AbsTol) and relative error tolerance (RelTol) were set at 10^{-3}. ξ was constrained between 0 and 1 to have physically meaningful fits. For ode15s, AbsTol=10^{-6} and RelTol= 10^{-4} were set with a maximum step size of 0.1 min.

We also simulated the temperature evolution in time for Runs 28–32 in the test set to assess the predictive capability of the model. To this end, the power consumption and ξ for these five test runs were predicted by a power-law (PL) correlation and machine learning (ML) algorithms based on the training on the first 27 runs. Several ML algorithms were trained to predict P_0, P_f, and ξ based on ω, c, and D_b with sklearn package of Python 3 [204] using the computational platform Google Colab. Then, the enthalpy balance model with these predicted P_0, P_f, and ξ was used to simulate the temperature profile, which was compared to the measured profile. The MSE and mean absolute errors (MAE) of various

ML algorithms are presented in **Table D.4** in *Appendix D*, along with the power-law correlations.

5.2 Results and Discussion

5.2.1 General experimental observations and trends

All experimental runs led to formation of fenofibrate nanosuspensions with median sizes d_{50} below 400 nm and 90% passing sizes below ~700 nm, except for Run 3 with low power consumption and the largest beads (800 µm) (refer to **Table D.2** of *Appendix D*). The as-received FNB particles had d_{10} of 8.09 µm, d_{50} (median size) of 20.3 µm, and d_{90} of 38.9 µm; so, WSMM achieved a size reduction ratio of 50–140 based on the median size values in **Table D.3**. **Figure 5.2** allows visualization of this drastic particle size reduction and conversion of as-received, micron-sized FNB particles into nanoparticles. These findings overall confirm that the selection of the formulation and milling parameters was appropriate for producing drug nanosuspensions within 60 min. As we focus on the heat generation–transfer analysis of WSMM in this work, the readers are referred to earlier work [149, 150, 165] for a comprehensive study of other important aspects such as breakage kinetics, short-term storage stability, and crystallinity of the wet-milled FNB suspensions. It suffices to state, based on these XRD, DSC, and SEM studies of the milled FNB particles, that the WSMM did not alter the crystallinity of FNB (refer to **Figure D.1** of the *Appendix D*). As all milled aq. FNB suspensions had identical composition (10% FNB, 8% HPC-L, and 0.05% SDS), we measured the zeta potential of a representative nanosuspension (Run 23). The zeta potential was measured to be –0.01 mV, i.e., almost 0. This result may suggest that in the presence of a neutral adsorbing polymer (HPC) at a very high concentration as compared with the anionic surfactant at 0.05% (well below critical micelle concentration),

the physical stability was mainly afforded by HPC through the steric effects. Presence of HPC could have masked the electrostatic charge provided by SDS [205].

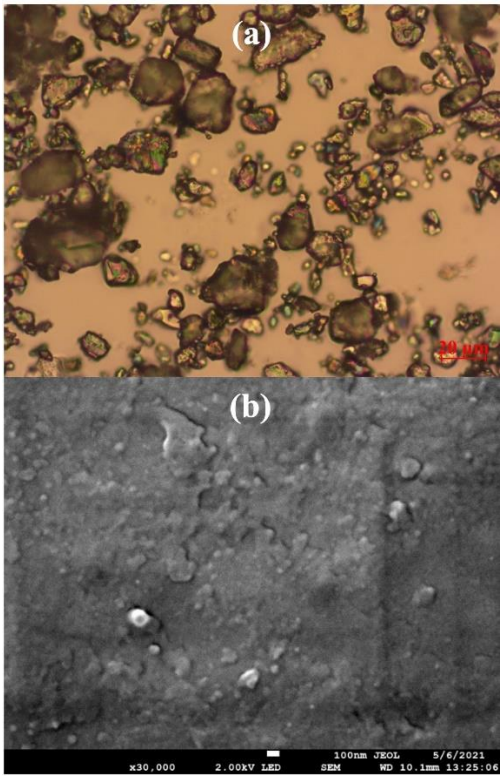

Figure 5.2 (a) Polarized light microscope image of as-received FNB particles (Scale bar: 20 µm) and (b) SEM image of the milled FNB particles in Run 23 (Scale bar: 100 nm).

When the stirrer speed was either 2000 or 3000 rpm, the maximum value of the suspension temperature at the mill outlet $T_{s,m}$ (henceforth referred to as mill outlet temperature or temperature) was less than 45 ^{o}C. Consequently, 60 min milling was completed in one cycle; whereas, at 4000 rpm, multiple intermittent milling cycles were required (**Table D.2** of *Appendix D*). The number of the intermittent cycles increased from 2 up to 33 upon an increase in bead loading and bead size at 4000 rpm. This finding suggests a smaller feasible design space from an operational perspective as milling at 4000 rpm causes a significant temperature rise. An increase in any of the three milling parameters led to higher power P exerted by the stirrer, which in turn was converted into

heat via various dissipation mechanisms. We hypothesize that the power P (shaft work done by the stirrer of the mill) or heat generation rate $P\xi$ is the driving force (source term in the enthalpy balance model) for the temperature rise. **Figure 5.3** illustrates that there exists a strong correlation between temperature rise T_{rise} at 6 min and average P or $P\xi$ (Runs 1–25). The fitting was performed using the nonlinear regression function of Minitab v.21.1. The empirical Gompertz growth model described the T_{rise} as a sole function of P and $P\xi$ separately with excellent goodness-of-fit (R^2 = 0.99), and the detailed fit statistics are presented in **Table D.3** of *Appendix D*. The empirical power-law model, which is commonly used in chemical engineering correlations, was used to describe the same data via the stirrer speed ω, bead loading c, and bead size D_{b}

$$T_{\text{rise}} = 41.4(\omega/\omega_{\text{max}})^{2.23}(c/c_{\text{lim}})^{0.912}(D_{\text{b}}/D_{\text{b,max}})^{0.160} \quad (6.9)$$

The milling parameters were normalized by the maximum design speed of the stirrer ω_{max} = 4200 rpm, the packing limit of the monodispersed spherical beads c_{lim} = 0.63 [147], and the maximum bead size $D_{\text{b,max}}$ = 800 μm used here. The fit quality of this power-law model was reasonable (R^2 = 0.92, RMSE = 2.7 °C). Equation (5.9) indicates that the most remarkable positive impact on T_{rise} arose from the stirrer speed, while the bead loading had a linear impact, and the impact of bead size was much weaker. The empirical models presented in **Figure 5.3** and in Equation (5.9) were also physically plausible in the limit $P \rightarrow 0$ and $P\xi \rightarrow 0$ as they predict negligibly small (<0.1 °C) or 0 temperature rise.

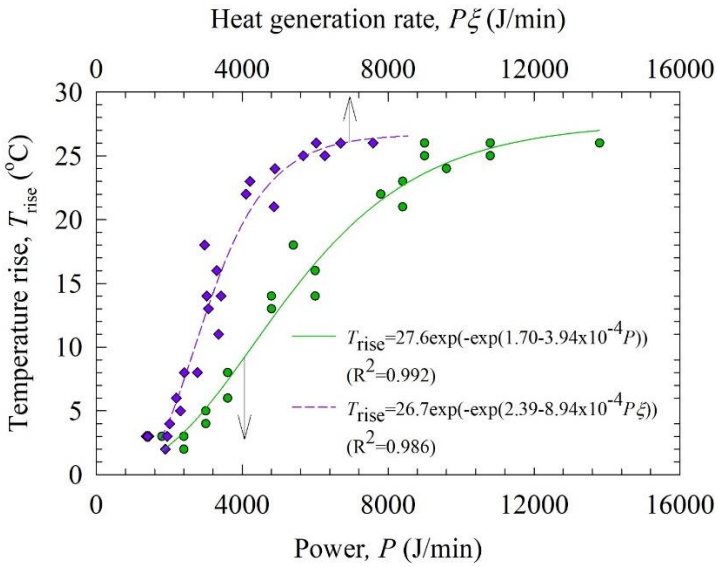

Figure 5.3 Temperature rise at 6 min of milling vs. average power consumption and average heat generation rate (Runs 1–25).

Although its choice is somewhat arbitrary, 6 min was selected because T_{rise} was notable experimentally for most runs while only two runs (Runs 26 and 27) out of 27 were excluded. Note that Runs 26 and 27 were in the cooling phase at 6 min. Any sampling time above 13 min would have to exclude 7 or more runs out of 27 runs. As our purpose was to illustrate the impact of P, $P\xi$, and milling parameters, we were content with the selection of 6 min, especially considering that a more rigorous and thorough analysis was performed within the context of the enthalpy balance model.

5.2.2 Temperature evolution during the WSMM and its fitting by the enthalpy balance model

The measured outlet temperatures during the milling phase were plotted along with the simulated temperatures that were obtained via the enthalpy balance model fits to ξ for 0.4, 0.5, and 0.6 bead loadings (see **Figures 5.4, 5.5,** and **5.6**, respectively). Note that the suspension temperature at the mill outlet is also equal to the suspension temperature in the mill $T_{s,m}$ due to the well-mixedness assumption. Let us first analyze the experimental data.

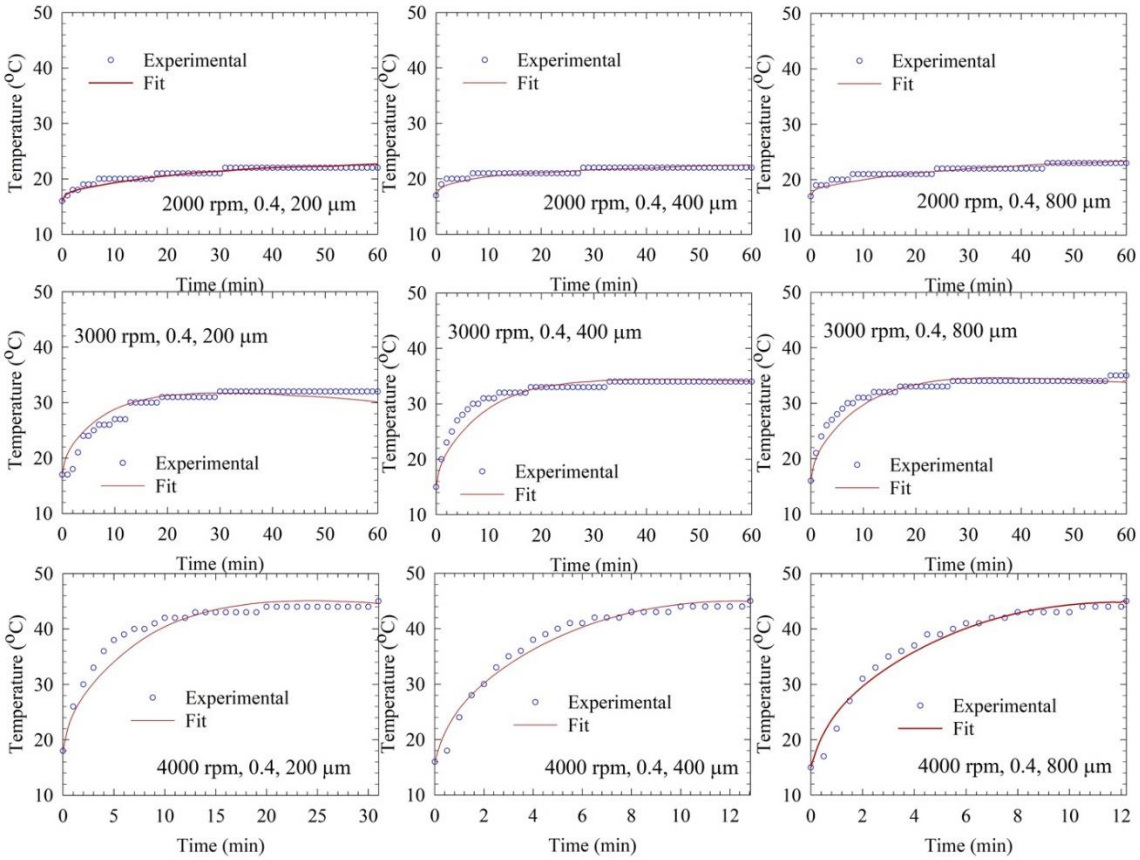

Figure 5.4 Temporal evolution of the mill outlet temperature measured experimentally and simulated–fitted via the enthalpy balance model for various stirrer speeds (increasing from top to bottom) and bead sizes (increasing from left to right) when the bead loading was 0.4. Training set: Runs 1–3, 10–12, and 19–21.

The temperature monotonically increased with time albeit at a decreasing rate, attaining or tending toward a plateau. The temperature measurement has an uncertainty of ±0.5 ºC. Because of this, when the heat generation rate was relatively low (2000 and 3000 rpm vs. 4000 rpm runs), experimentally measured temperature profiles belonging to 2000 and 3000 rpm exhibited several discrete step-like increase. In addition, the increase in chiller temperature during the milling might have contributed to this type of profile. In **Figures 5.4-5.6**, the impact of bead size can be seen in each row, and the impact of stirrer speed can be seen in each column. To see the impact of bead loading, the corresponding subfigures of **Figures 5.4-5.6** should be compared. Overall, stirrer speed had the most

significant impact on temperature rise: 4000 rpm milling caused the temperature to reach 45 °C, which is the maximum allowed temperature, in all conditions in less than 60 min; therefore, during the first intermittent milling cycle, 4000 rpm experiments run shorter compared to all other experiments. Bead loading was the second important process parameter for the temperature rise, while the bead size had the least impact. The difference of maximum temperatures between 200 μm and 800 μm beads in most of the 2000 and 3000 rpm runs was about 1 °C; only for c = 0.6 (Runs 16–18), the difference was as high as 9 °C. At 4000 rpm and constant bead loading, larger beads reduced the time to reach 45 °C. Regardless, the impact of bead size was not as significant as that of the stirrer speed and the bead loading. As will be explained in the discussion, the power required to stir beads with larger nominal sizes was either the same or slightly higher. Overall, the qualitative analysis of the temperature profiles in **Figures 5.4-5.6** agrees with the empirical model of T_{rise} (Equation (5.9)) as a function of the milling parameters.

Despite its simplicity with only one fitting parameter, i.e., ζ, the enthalpy balance model could fit the experimental temperature evolution well, with RMSE between 0.40–2.34 °C in Runs 1–27. Except for a few runs at 3000 rpm and 0.5–0.6 bead loading, the model captured salient features and experimental trends regarding the temperature rise during the milling, as illustrated in **Figures 5.4-5.6**: (i) a monotonic increase of temperature during the milling, (ii) a monotonic decreasing rate of temperature rise during the milling, (iii) an approach to or attainment of a plateau temperature, (iv) attainment of maximum temperature of 45 °C only at 4000 rpm, thus corroborating the need for multiple intermittent milling cycles, (v) earlier attainment of this maximum temperature at the higher loading of

larger beads, and finally (vi) relative impact ranking on temperature rise: stirrer speed > bead loading > bead size.

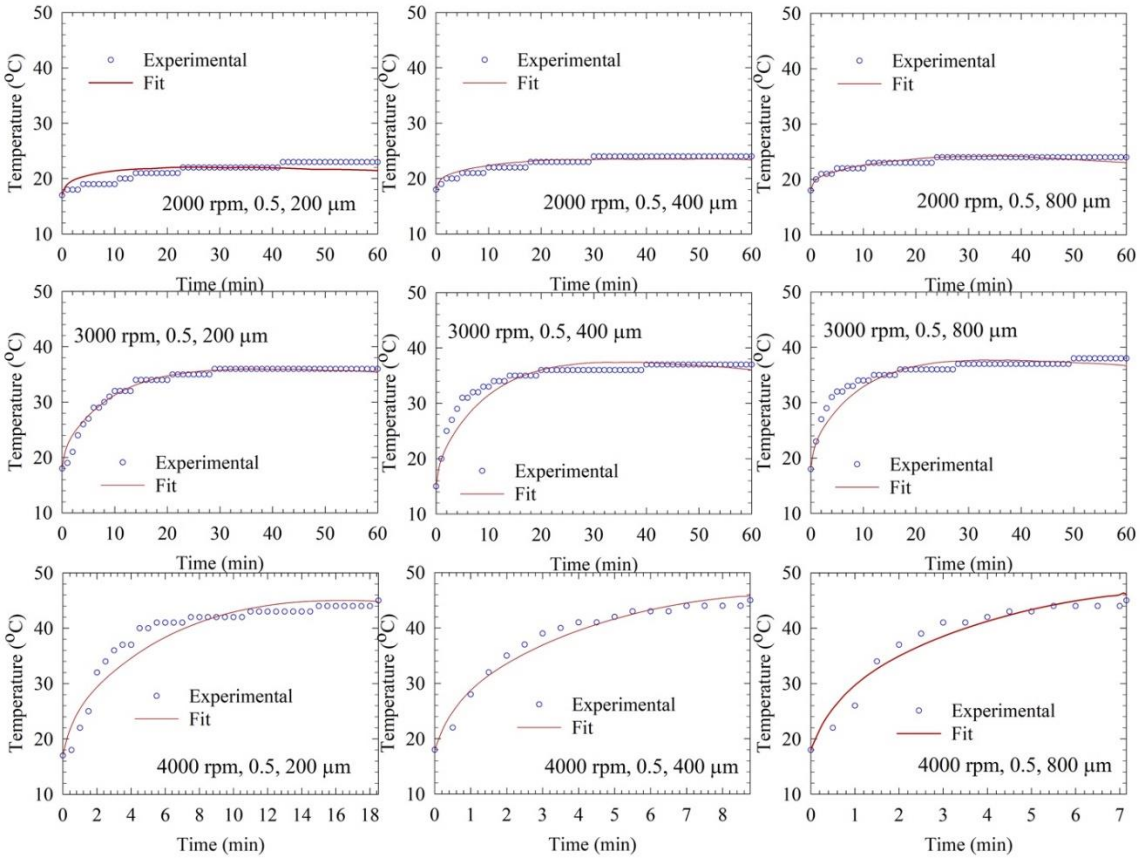

Figure 5.5 Temporal evolution of the mill outlet temperature measured experimentally and simulated–fitted via the enthalpy balance model for various stirrer speeds (increasing from top to bottom) and bead sizes (increasing from left to right) when the bead loading was 0.5. Training set: Runs 4–6, 13–15, and 22–24.

Although the suspension temperature in the holding tank was not measured, our model also simulated its evolution (see **Figure D.2** as an illustration in *Appendix D*). The suspension temperature in the holding tank was always lower (about 2–14 °C) than the suspension temperature at the mill outlet, and its rise was slower as compared with that in the milling chamber. Hence, the choice of examining the mill outlet temperature experimentally and computationally in this chapter is a conservative approach from a process development perspective. In addition, the bead and stirrer temperatures for selected

runs are depicted in **Figure D.2**. The temperature of the suspension, the beads, and the stirrer in the milling chamber were almost identical, signifying a thermal equilibrium in the mill chamber content (bead–drug suspension–stirrer). This finding is not surprising considering the high stirrer speeds (2000–4000 rpm) in the mill chamber. However, we caution the readers that the length scale of the heat transfer also plays a role in reaching thermal equilibrium; hence, thermal equilibrium may not be achieved in pilot or commercial scale mills. The temperature in the holding tank also increases, albeit at a decreasing rate, due to recirculating suspension between the mill chamber and the holding tank. However, that temperature rise is lower in extent and slower due to negligible heat generation due to relatively small shaft work associated with mixing in holding tank.

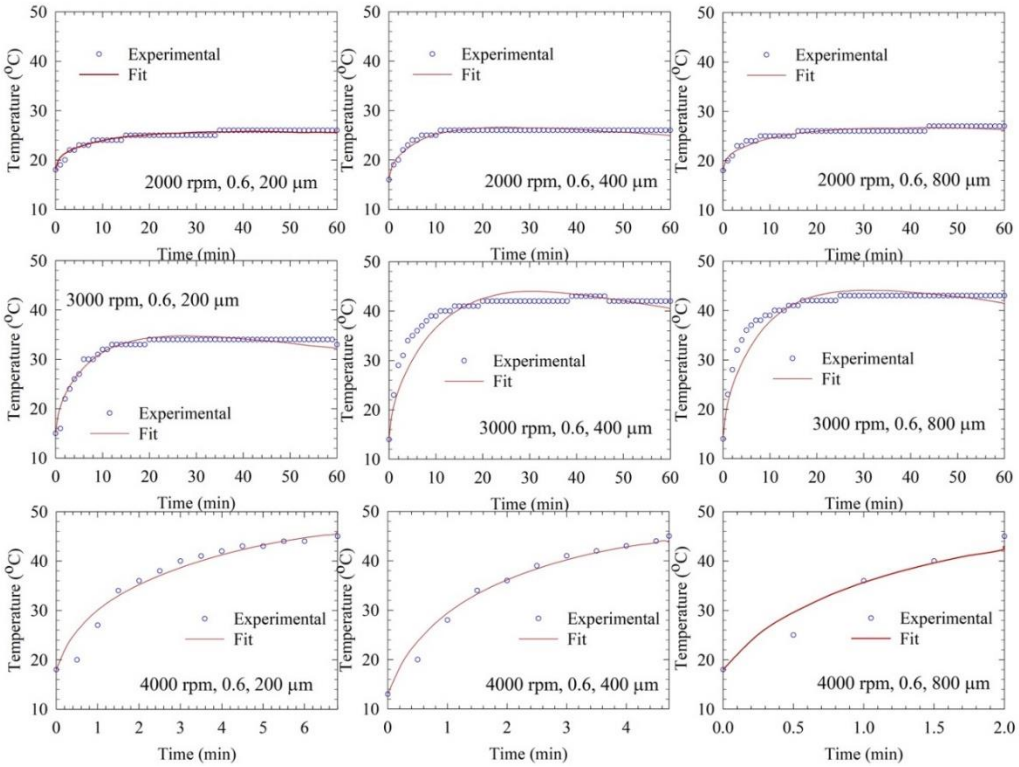

Figure 5.6 Temporal evolution of the mill outlet temperature measured experimentally and simulated–fitted via the enthalpy balance model for various stirrer speeds (increasing from top to bottom) and bead sizes (increasing from left to right) when the bead loading was 0.6. Training set: Runs 7–9, 16–18, and 25–27.

The above dynamic trends can be explained as follows: Equation (5.1) suggests a competition between heat generation rate $P\xi$ and heat removal rate Q_{ch}. As the suspension temperature in the mill and the holding tank increased, the driving force for external cooling and therefore Q_{ch} increased (refer to Equations 5.6 and 5.8). Moreover, as can be seen from **Table D.1** of *Appendix D,* except for Runs 1–3, a notable drop in power consumption from P_0 to P_f was observed, which could be explained by a decrease in suspension viscosity upon reduction in particle size (see e.g., [88]) and an increase in temperature [197] during the milling. Indeed, the unmilled FNB suspension had an apparent shear viscosity of 198 ± 3.20 mPa·s and the milled FNB suspensions had lower apparent shear viscosity (see **Table D.1**). Moreover, **Figure D.3** corroborates the theoretically expected decrease of apparent shear viscosity upon an increase in temperature up to 45 ^{o}C. As the power consumption is a positive source term and Q_{ch} is a negative source term in Equation (5.1) and that the former decreases during the milling while the latter increases, the net heat generation–removal rate decreases in time, which mostly explains the general dynamic trends during the milling. Note that a "bulk cooling effect" in the mill also arises from the recirculating suspension, as explained by the first two terms on the r.h.s. of Equation (5.1) and $T_{s,ht} < T_{s,m}$. In view of the monotonic increase in suspension temperature in the holding tank, albeit more slowly as compared with the suspension temperature in the mill (**Figure D.2**), this effect remains somewhat invariant during the milling due to constancy of the temperature difference $T_{s,ht} - T_{s,m}$ (after an initial rise). So, at least for the specific scale of the mill/chiller used, we assert that the observed general trends mostly originate from the competition between decreasing $P\xi$ and increasing Q_{ch} during the milling.

Let us discuss some of the quantitative deviations observed in **Figures 5.4–5.6**. The average RMSE for 2000, 3000, and 4000 rpm runs is 0.54, 1.24, and 1.67 ^{o}C, respectively. In some runs at 3000 rpm, the simulated temperature profile exhibited a maximum followed by about 1 ^{o}C drop (c = 0.5) and 2–4 ^{o}C drop (c = 0.6). This suggests that after some time, the heat generation rate became lower than the heat removal rate. One explanation could be related to the assumption of linear decrease of power consumption in time. While this assumption was simple and allowed for a good fit, it is likely that the decrease in power consumption may have a non-linear pattern (not examined in this chapter). It is also worth-mentioning that the assumptions made in the model development, e.g., constant thermo-physical properties and the specific correlations used for the overall and internal/external heat transfer coefficients could partly explain the observed deviations. For example, for a given set of fixed milling parameters, i.e., stirrer speed, bead loading, and bead size, the suspension viscosity decreases with time (see e.g., the experimental data in [88]) due to increase in temperature and/or decrease in particle size during milling. When we mention particle size effect on viscosity, we should also consider the mechanism: we speculate that higher amount of polymer adsorption onto finer particles generated at the higher stirrer speeds and/or bead loading could account for the observed reduction in viscosity. A lower polymer concentration in the bulk suspension upon higher amount of polymer adsorption onto finer particles could result in a lower suspension viscosity than the case when the polymer remains dissolved and smaller amount is adsorbed onto the drug particles with coarser sizes. A more elaborate model could consider such evolution of viscosity as well as variation of power consumption during the whole milling time, not just initially and at the end of milling (for the power). Since measuring timewise evolution of

viscosity at multiple milling time points and temperatures for 27 experimental runs is a laborious task, it was not performed in this first attempt to model the temperature rise during the WSMM process, especially considering the success of the rather simple one-parameter model with a linear drop of power in time.

Table 5.2 Properties Used in the Enthalpy Balance Model as well as the Fitted ξ Parameter Statistics

Run no.	M_b (g)	$M_{s,m}$ (g)	$M_{st,ht}$ (g)	$M_{s,ht}$ (g)	$h_{B,m}$ (J/min °Cm^2)	$h_{B,ht}$ (J/min °Cm^2)	UA_m (J/min °C)	UA_{ht} (J/min°C)	ξ (-)	RMSE (°C)
1	192	49.44	10.29	186.1	211492	5299	63.31	69.34	0.76	0.41
2	192	49.44	10.29	186.1	211492	5299	63.31	69.34	0.80	0.40
3	192	49.44	10.29	186.1	211492	5299	63.31	69.34	0.78	0.47
4	240	41.20	10.15	194.3	142703	5807	71.53	67.03	0.79	1.17
5	240	41.20	10.15	194.3	142703	5807	71.53	67.03	0.81	0.59
6	240	41.20	10.15	194.3	142703	5807	71.53	67.03	0.67	0.42
7	288	32.96	10.00	202.5	86097	6384	80.85	62.78	0.77	0.44
8	288	32.96	10.00	202.5	86097	6384	80.85	62.78	0.67	0.49
9	288	32.96	10.00	202.5	86097	6384	80.85	62.78	0.61	0.49
10	192	49.44	10.29	186.1	277133	5299	63.31	70.54	0.77	1.30
11	192	49.44	10.29	186.1	277133	5299	63.31	70.54	0.63	1.14
12	192	49.44	10.29	186.1	277133	5299	63.31	70.54	0.64	0.99
13	240	41.20	10.15	194.3	186993	5807	71.53	68.70	0.62	0.69
14	240	41.20	10.15	194.3	186993	5807	71.53	68.70	0.55	1.39
15	240	41.20	10.15	194.3	186993	5807	71.53	68.70	0.57	1.15
16	288	32.96	10.00	202.5	112818	6384	80.85	65.25	0.55	0.92
17	288	32.96	10.00	202.5	112818	6384	80.85	65.25	0.57	2.00
18	288	32.96	10.00	202.5	112818	6384	80.85	65.25	0.54	1.62
19	192	49.44	10.29	186.1	335723	5299	63.31	71.23	0.58	1.66
20	192	49.44	10.29	186.1	335723	5299	63.31	71.23	0.63	1.23
21	192	49.44	10.29	186.1	335723	5299	63.31	71.23	0.67	1.38
22	240	41.20	10.15	194.3	226526	5807	71.53	69.67	0.51	2.09
23	240	41.20	10.15	194.3	226526	5807	71.53	69.67	0.58	1.28
24	240	41.20	10.15	194.3	226526	5807	71.53	69.67	0.62	1.81
25	288	32.96	10.00	202.5	136670	6384	80.85	66.72	0.55	1.83
26	288	32.96	10.00	202.5	136670	6384	80.85	66.72	0.61	1.37
27	288	32.96	10.00	202.5	136670	6384	80.85	66.72	0.63	2.34
28	192	49.44	10.29	186.1	211492	5299	63.31	69.34	0.72	0.51
29	192	49.44	10.29	186.1	211492	5299	63.31	69.34	0.62	0.59
30	192	49.44	10.29	186.1	211492	5299	63.31	69.34	0.53	1.56
31	240	41.20	10.15	194.3	142703	5807	71.53	67.03	0.58	1.01
32	240	41.20	10.15	194.3	142703	5807	71.53	67.03	0.56	1.13

The fitted fraction of power converted to heat ξ varied between 0.51–0.81 with an overall mean ± standard deviation of 0.65 ± 0.09 (**Table 5.2**). Relatively high ξ values confirm the well-established notion in the WSMM literature that a small fraction of power

applied is spent on (drug) particle deformation–breakage and most of it dissipates as heat [34, 162]. In fact, some of the shaft work is spent on generating new surfaces (surface energy), sound, and elastic part of bead–bead and bead–wall collisions. We must mention the caveat that as the model is too simplistic with a multitude of assumptions, the ξ values may not reflect the actual fraction of power converted to heat as ξ is, by and large, a fitting parameter affected by the accuracy of the experimental measurements and the assumptions made in the model development. Predicting ξ based on bead–particle–bead and bead–particle–wall collisions in the bead–drug suspension mixture and their impact on energy spectra is extremely difficult, if not impossible; such an approach does not exist in the open literature. Hence, explaining variation of ξ on fundamental grounds appears to be elusive. On the other hand, microhydrodynamic analysis of bead–bead collisions [34, 57, 150] has provided some insights into mechanisms of energy dissipation arising from both the liquid–beads viscous friction and lubrication, partially inelastic bead–bead collisions, and shearing of the equivalent liquid (milled drug suspension). However, no connection has been made between the heat generation rate and the energy dissipation rates within the context of the microhydrodynamic model yet.

5.2.3 Predictive capability of the model: temperature profiles in test runs

Most of the required input parameters for the enthalpy balance model were either measured or calculated. Once the initial and final power values were measured, one could run the optimizer to fit ξ, as we have done in this chapter for Runs 1–27 (training set). To be able to predict the temperature profile for any new set of milling conditions, e.g., Runs 28–32 (test set), one should first predict P_0, P_f, and ξ. In other words, one should be able to predict the temperature profiles without performing any new experiments (Runs 28–32). To this

end, power-law (PL) correlations and machine learning (ML) algorithms were implemented following their training on the Runs 1–27 data. P_0 and P_f were correlated with the milling parameters through power number N_p, which is a commonly used dimensionless number in mixing studies and WSMM [34, 137].

$$N_p = P/(D^5 N^3 \rho_{mix}) \tag{6.10}$$

where N is the stirrer speed (1/s) and D is the diameter of the stirrer element (0.07 m). $N_{p,0}$ and $N_{p,f}$ were calculated based on P_0 and P_f. In this analysis, the mixture N_p was calculated using the density and viscosity of the milled suspension–bead mixture (see Equation (D.16) of *Appendix D*). In order to capture the impact of all process parameters, $N_{p,0}$ and $N_{p,f}$ were correlated with the stirrer speed, the bead size, and the bead loading after putting them into non-dimensional forms: ω/ω_{max}, D_b/D, and c/c_{lim}. The following power-law correlations were found by fitting the parameters using Minitab 21.1, with the fit statistics for P_0 and P_f shown in **Table D.4** of *Appendix D*.

$$N_{p,0} = 0.33(\omega/\omega_{max})^{-0.81}(c/c_{lim})^{0.77}(D_b/D)^{0.14} \tag{5.11}$$

$$N_{p,f} = 0.26(\omega/\omega_{max})^{-1.2}(c/c_{lim})^{0.55}(D_b/D)^{0.18} \tag{5.12}$$

We also sought for power-law correlations of ξ with P0, stirrer speed, bead loading, and bead size in different combinations and the best prediction was found when ξ was correlated to P_0 as follows:

$$\xi = 2.68P_0^{-0.16} \tag{5.13}$$

where the fitting statistics for the test and training sets can be seen in **Table D.4**. An alternative fitting of N_p using the mixture Reynolds number Re_m is presented in "Power Number Correlation with Reynolds Number and Process Parameters" of *Appendix D*. Equation (D.6) illustrates P scales with $\mu_m^{0.33}$ (weak dependence) and $N^{2.67}$ (strong, close

to cubic dependence). This explains why the power consumption and thus the temperature rise were higher at the higher stirrer speed despite the lower viscosity at higher stirrer speed.

Table 5.3 Experimentally Measured–Fitted and Predicted P_0, P_f, and ξ Values as well as the RMSE Of The Simulated Temperature Profiles

Run no.	Direct fit approach[a]				PL prediction[b]				ML prediction[b]			
	P_0 J/min	P_f J/min	ξ (-)	RMSE ℃	P_0 J/min	P_f J/min	ξ (-)	RMSE ℃	P_0 J/min	P_f J/min	ξ (-)	RMSE ℃
28	4200	3600	0.72	0.514	4530	3785	0.69	0.927	4440	3600	0.72	1.02
29	6000	4800	0.62	0.592	6093	4873	0.66	1.02	5760	4440	0.68	0.999
30	9600	7200	0.53	1.56	9475	6996	0.62	2.22	9720	6960	0.60	2.17
31	11400	9600	0.58	1.01	12744	9007	0.59	1.17	12480	8640	0.57	1.29
32	9600	7800	0.56	1.13	8157	5620	0.63	4.17	9480	6720	0.62	1.63

[a]P_0 and P_f were measured; ξ was estimated by fitting the simulated temperature from the enthalpy balance model to the experimentally measured temperature. RMSE was calculated comparing the simulated and experimental temperature profiles. [b]P_0, P_f, and ξ were all predicted via the empirical power-law (PL) model and the machine learning (ML) approach. RMSE was calculated comparing the simulated and experimental temperature profiles.

The predicted P0, Pf, and ξ values for Runs 28–32 by PL and ML approaches are reported in **Table 5.3** and the respective predictions of the temperature profiles are illustrated in **Figure 5.7. Table 5.3** and **Figure 5.7** also present a "Direct fit" approach wherein P0 and Pf were experimentally determined, and ξ was obtained from direct fitting to the experimental temperature profiles. In the PL approach, P0, Pf. and ξ were predicted by Equations (5.10–5.13). Among all machine learning (ML) algorithms, k-nearest neighborhood (KNN) algorithm with k = 5 was selected because it provided the lowest MSE and MAE in predicting P0, Pf. and ξ in the test runs, Runs 28–32 (refer to **Table D.4** in *Appendix D*). The differences between the predicted P0 and Pf values using the PL and

ML approaches and the experimental P0 and Pf values did not follow a particular trend (**Table 5.3**) and most of them were statistically insignificant. On the other hand, the predicted ξ values by both approaches tend to be higher than those obtained by direct fitting to the experimental data; but some values are similar or slightly lower.

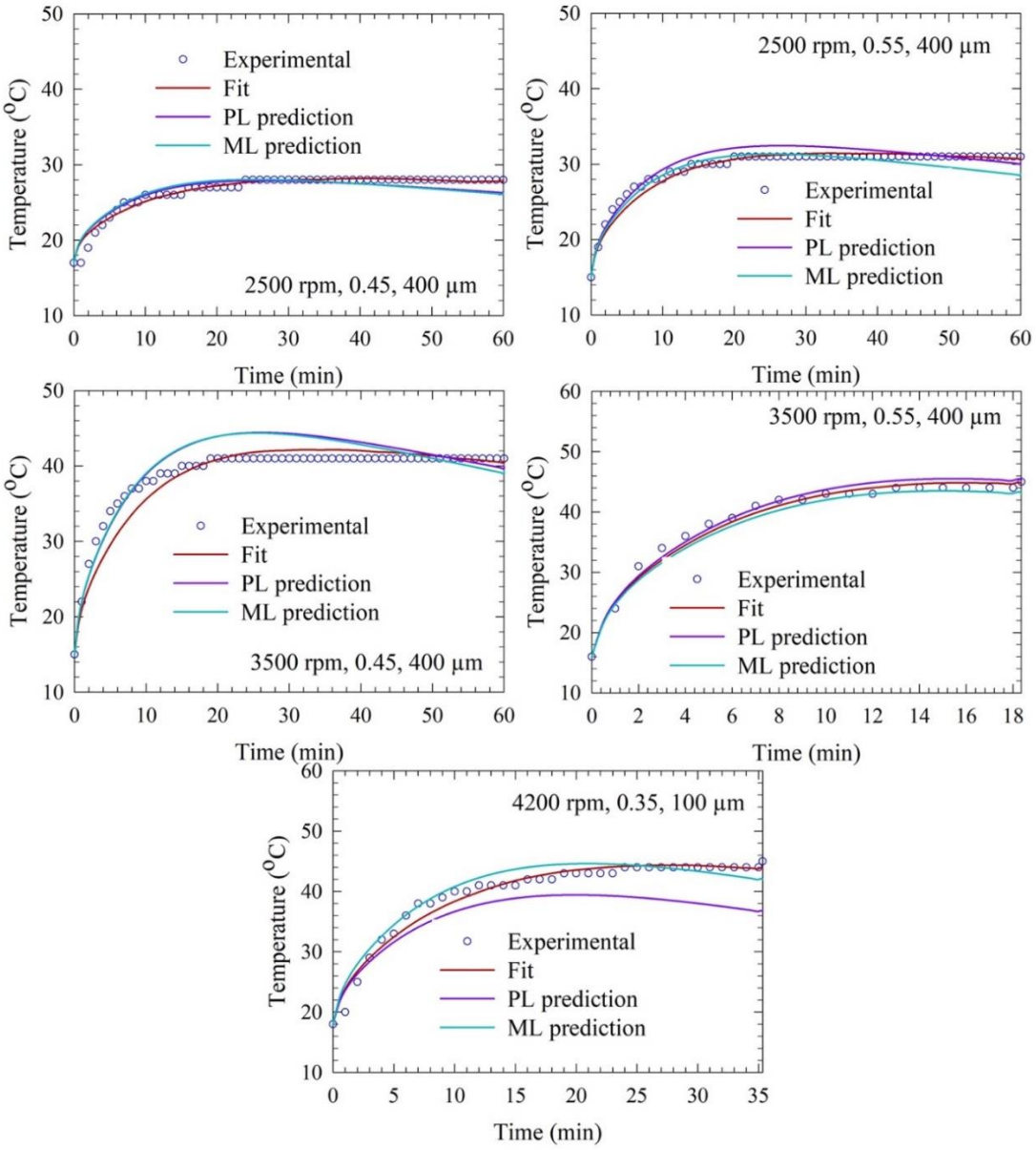

Figure 5.7 Temporal evolution of the mill outlet temperature measured experimentally, simulated–fitted via the enthalpy balance model, and simulated using P_0, P_f, and ξ, which were predicted via the empirical power-law (PL) model and the machine learning (ML) model with the KNN algorithm. Test Set: Runs 28–32.

Predicted P0, Pf, and ξ were entered in MATLAB and simulations were performed with the enthalpy balance model to generate the temperature profiles presented in **Figure 5.7**. The predicted profiles were close to the experimental data points visually; the predictions for Runs 28, 29, and 31 were almost as good as the direct fits, as also signified by RMSE values in **Table 5.3**. For Run 30, the model predictions showed a clear maximum, which was ~3 °C higher than the experimentally measured highest temperature. After 5 min, PL prediction for Run 32 underpredicted the temperature, with a ~7 °C maximum difference from the experiment; whereas the ML prediction was reasonably accurate. The average RMSEs for all five test runs were calculated as 1.90 and 1.42 ^{o}C for the PL approach and ML approach. Overall, these results demonstrate that the enthalpy balance model with the PL and ML approaches has a decent predictive capability. Even though both PL and ML approaches can be used to obtain predictions, the ML approach performed slightly better based on the smaller MSE and MAE of the P and ξ predictions (**Table D.4**) and smaller RMSE of the predicted temperature profiles (**Table 5.3**).

5.3 Conclusions

This chapter has presented the first systematic and comprehensive exploration of the temperature evolution, heat generation, and heat transfer aspects of the wet stirred media milling of a drug suspension. Analysis of the experimental results and the simulations performed with the enthalpy balance model has pointed out that the shaft work done per unit time (mechanical power consumption) by the mill stirrer is the sole source of the temperature rise, and the milling parameters impacted the temperature rise in the order: stirrer speed > bead loading > bead size. The present chapter has also demonstrated that the enthalpy balance model, along with the power-law fitting and machine learning

approaches, can be used to predict the timewise evolution of temperature profiles in various milling conditions. It is hoped that the presented simple modeling framework will be used by pharmaceutical engineers/formulators in process design and optimization especially when they are confronted with developing a thermolabile drug nanosuspension via the WSMM process.

CHAPTER 6

PREDICTING THE TEMPERATURE EVOLUTION DURING NANOMILLING OF DRUG SUSPENSIONS VIA A SEMI-THEORETICAL LUMPED-PARAMETER MODEL

Chapter 5 has provided a comprehensive enthalpy balance model (EBM) for the simulation of timewise evolution of temperature during the wet stirred media milling process. Chapter 6 aims to establish both descriptive and predictive capabilities of a semi-theoretical lumped parameter model (LPM) for temperature evolution. In the experiments, the mill was operated at various stirrer speeds, bead loadings, and bead sizes, while the temperature evolution at the mill outlet was recorded. The LPM was formulated and fitted to the experimental temperature profiles in the training runs, and its parameters, i.e., the apparent heat generation rate Q_{gen} and the apparent overall heat transfer coefficient times surface area UA, were estimated. For the test runs, these parameters were predicted as a function of the process parameters via a power law (PL) model and machine learning (ML) model. The LPM augmented with the PL and ML models was used to predict the temperature evolution in the test runs. The LPM predictions were also compared with those of an enthalpy balance model (EBM) developed in Chapter 6. The LPM had a fitting capability with root-mean-squared error (RMSE) smaller than 0.9 ℃, and a prediction capability, when augmented with the PL and ML models, with RMSEs smaller than 4.1 and 2.1 ℃, respectively. Overall, the LPM augmented with the PL model had both good descriptive and predictive capability, whereas the one with the ML model has comparable predictive capability. Despite being simple with two parameters and obviating the need for sophisticated numerical techniques for its solution, the semi-theoretical LPM generally

predict the temperature evolution similarly or slightly better than the EBM, warranting its use by pharmaceutical engineers for the modeling of the nanomilling process.

6.1 Materials and Methods

6.1.1 Materials

A BCS Class II API, fenofibrate (FNB), was used as a model poorly water-soluble drug, which was purchased from Jai Radhe Sales (BP grade, Ahmedabad, India). Hydroxypropyl cellulose (HPC) was used for stabilizing the drug suspension as a non-ionic polymer, which was generously donated by Nisso America Inc. (L grade, NY, USA). Besides, an anionic surfactant, sodium dodecyl sulfate (SDS), was used for wettability enhancement, and it was purchased from GFS chemicals (ACS grade, OH, USA).

6.1.2 Wet stirred media milling

The suspension formulation was the same for all runs where the w/v % of the ingredients was 10% FNB, 8% HPC-L, and 0.05% SDS with respect to 200 ml of deionized water. Based on our prior studies, this formulation is known to be physically stable during milling and storage [149, 165]. A pre-suspension was prepared by adding the powders to deionized water gradually under constant mixing with a shear stirrer (Cat#. 14-503, Fisher Scientific, PA, USA) operating at 300 rpm for 2 h. The theoretical batch size was fixed for all processing runs: 236 g. Pre-suspensions were stored at 8 ℃ overnight prior to milling, to let it settle and get rid of the foaming that occurred during shear mixing. On the milling days, suspensions were stirred on a magnetic stirrer until they equilibrated close to room temperature.

A Microcer wet stirred media mill (Netzsch Fine Particle Size Technology, LLC, PA, USA) was used for milling the pre-suspensions. It has an 80 ml chamber volume lined with zirconia, a zirconia shaft, and stainless steel screens whose openings are of half the size of the yttrium stabilized zirconia beads (YSZ, Saint Gobain ZirPro, NJ, USA). A Cole-Palmer peristaltic pump (Master Flex, 9 IL, USA) recirculated the suspension between the holding tank and mill chamber at a 126 ml/min flow rate, which was kept the same for all processing runs. The milling conditions are shown in **Table 6.1**, where 27 experiments were used as training runs and 5 additional runs were used for testing the model prediction capability. Stirred speed, bead loading, and bead size were varied at 3 levels for the training runs.

Despite the use of a chiller with an initial temperature of 6.1 ℃, the temperature rise during the process was inevitable due to heat generation as the drug suspension with the beads was stirred. Milling was started when the chiller temperature reached 6.1 ℃, and the mill outlet temperature was equal to or below 18 ℃. Even though keeping the initial temperatures for both the chiller and the mill outlet the same would be a better approach, only the initial chiller temperature could be kept the same; the initial temperature at the mill outlet varied in a narrow range (13–18 ^{o}C) due to variation in the ambient temperature, the pre-suspension temperature, and operator practice. During experiments, mill outlet temperature was recorded every minute (Runs 1–17) or every 30 s (Runs 18–27). The effective milling time was the same for all runs (60 mins), whereas the operating time was variable (60–380 min) due to intermitting milling to prevent temperature exceeding the gelation temperature of the polymer (45 ^{o}C) [155]. In an intermittent milling cycle, the mill was shut down while cooling continued, and whenever the mill outlet temperature reached

18 °C, the milling continued. Note that we considered only the first milling cycle in the simulations. The average power consumption P was calculated by dividing the total energy consumption read in the mill panel by the effective milling time.

Table 6.1 Process Parameters for the Milling of FNB Suspensions

Run No.	Stirrer Speed, ω (rpm)	Bead Loading, c (-)	Bead Size, D_b (μm)
1[1]	2000	0.4	200
2[1]	2000	0.4	400
3[1]	2000	0.4	800
4[1]	2000	0.5	200
5[1]	2000	0.5	400
6[1]	2000	0.5	800
7[1]	2000	0.6	200
8[1]	2000	0.6	400
9[1]	2000	0.6	800
10[1]	3000	0.4	200
11[1]	3000	0.4	400
12[1]	3000	0.4	800
13[1]	3000	0.5	200
14[1]	3000	0.5	400
15[1]	3000	0.5	800
16[1]	3000	0.6	200
17[1]	3000	0.6	400
18[1]	3000	0.6	800
19[1]	4000	0.4	200
20[1]	4000	0.4	400
21[1]	4000	0.4	800
22[1]	4000	0.5	200
23[1]	4000	0.5	400
24[1]	4000	0.5	800
25[1]	4000	0.6	200
26[1]	4000	0.6	400
27[1]	4000	0.6	800
28[2]	2500	0.45	400
29[2]	2500	0.55	400
30[2]	3500	0.45	400
31[2]	3500	0.55	400
32[2]	4000	0.35	100

[1]Runs that were used in the training set, [2]Runs that were used in the test set.

6.1.3 Formulation of the lumped-parameter model (LPM)

During the milling of drug suspensions, heat is generated because of the conversion of mechanical energy input by the stirrer of the mill. The heat generated is removed by a coolant passing through the jacket of the milling chamber. Ignoring the enthalpic effects associated with the suspension recirculation between the holding tank and the milling chamber, we can come up with a simple, low-fidelity model that retains the essential elements of the heat generation–transfer. The difference between the heat generation rate and heat removal rate will cause the internal energy build-up in the mill as milling continues and temperature in the mill rises. These aspects are captured by the following semi-theoretical lumped-parameter model:

$$mC_{\mathrm{p}}\frac{dT}{dt} = Q_{\mathrm{gen}} - UA(T - T_{\mathrm{ch}}) \tag{6.1}$$

where t is milling time, m is the mass in the mill chamber, C_{p} is the specific heat capacity, T is the temperature at the mill outlet, Q_{gen} is the apparent heat generation rate during milling, UA is the apparent overall heat transfer coefficient times surface area, and T_{ch} is the chiller temperature. Strictly speaking, Equation (6.1) represents a transient enthalpy balance for a perfectly mixed batch process. The perfect mixing implies that the mill outlet temperature is equal to the temperature of the suspension in the mill chamber. The well-mixedness in the milling chamber has been established as a valid approximation to the residence time distribution in small mills (small length-to-diameter ratio) [87]. Hence, for a recirculation mill operating with *a fixed batch size and recirculation rate*, Q_{gen} and UA may only represent the heat generation rate and overall heat transfer coefficient times surface area, in some approximate, apparent, and statistical manner because they are obtained by fitting to experimental data directly. While UA can be estimated based on heat

transfer correlations for the internal and external convective heat transfer coefficients [166], such correlations are approximate, and none exists for the specific stirrer–mill chamber geometry. We also assumed time-invariant, constant Q_{gen}, C_p, UA, and T_{ch} (6.1 °C.).

Upon separating the variables in Equation (6.1), integrating both sides, and imposing the initial condition, i.e., $t = 0, T = T_0$, the following equation for the time-wise evolution of mill outlet temperature (shortly temperature hereafter) was obtained:

$$T = T(t) = \left(T_{ch} + \frac{Q_{gen}}{UA}\right) + \left(T_0 - T_{ch} - \frac{Q_{gen}}{UA}\right) \exp\left(-\frac{UA}{mC_p}t\right) \quad (6.2)$$

Here, m and C_p were determined considering the materials in the mill chamber: the beads (zirconia, C_p = 0.46 J/g°C [202]), the suspension (10% FNB with respect to water, C_p = 3.93 J/g°C), and the stirrer element (zirconia, C_p = 0.46 J/g°C). While the stirrer element mass was constant, the bead and suspension mass varied when bead loading was changed in various runs (refer to **Table 6.1**). The C_p was calculated as the weighted average of the C_p of individual materials and the mC_p was found to be 465.6, 455.2, 444.8, 460.4, 450.0, and 470.9 J/°C for 0.4, 0.5, 0.6, 0.45, 0.55, and 0.35 bead loadings respectively.

6.1.4 Fits by the LPM and predictions by the LPM augmented with the PL and ML models

By fitting Equation (6.2) to the experimental T vs. t data in SigmaPlot 12, Q_{gen} and UA were estimated. Then, these parameters were mathematically expressed as a function of the process parameters for the 27 training runs and predicted as a function of the process parameters for the five test runs using a power law (PL) model and a machine learning (ML) model. Minitab was used for the PL predictions, whereas Google Colab was used for the ML predictions. Among the several applied machine learning approaches using Google

Colab, as shown in **Table E.1** of *Appendix E*, k-nearest neighborhood (KNN) with $k = 5$ was selected due to its low mean squared error (MSE) and mean absolute error (MAE) compared to other methods for the test runs. Therefore, ML refers to KNN (k = 5) for the rest of this study.

6.2 Results and Discussions

6.2.1 Properties of the milled suspensions and particles

As the scope of this study is the simulation of temperature rise during WSMM via a lumped-parameter model, readers are referred to previous investigations for full characterization of particle sizes, viscosity, crystallinity, and morphology of the particles after milling [166, 206]. Here, it suffices to summarize the key findings. All runs yielded nanoparticles upon 60 min milling, where the median particle sizes varied between 149–400 nm. The HPC–SDS combination successfully stabilized the drug nanoparticles by mitigating their aggregation during milling and storage. The nanoparticles were visible in SEM, confirming the laser diffraction results. XRD results of the nanoparticles showed the characteristic peaks of as-received FNB, indicating the crystal structure of the FNB was largely preserved during the milling.

6.2.2 Fitted LPM parameters and the origin of temperature rise during the milling

The data on the timewise evolution of the mill outlet temperature was fitted by the LPM, as represented by Equation (6.2) for each training run (Runs 1–27). The fitted parameters are presented in **Table 6.2** along with the root-mean-squared error (RMSE). The RMSE values ranged between 0.15–0.90 ^{o}C. Such low RMSE values suggest that the LPM has excellent fitting or descriptive capability of the temperature profiles despite having only

two parameters. **Figure 6.1** demonstrates that the apparent heat generation rate Q_{gen} is linearly and strongly correlated with the average mechanical power consumption P (R^2 = 0.97). The value of the constant slope of the linear correlation in **Figure 6.1** indicates that about 64% of the power consumption (rate of shaft work) dissipates as heat. This is not surprising at all: only a small fraction of the mechanical energy spent on mixing the suspension–bead mixture is used to deform the particles [34]. Most is converted into heat through dissipative processes such as viscous losses, inelastic bead–bead and bead–wall collisions, etc. [62]. Some of the shaft work is also spent on generating new particle surfaces (surface energy), sound, and elastic bead–bead and bead–wall collisions [33].

Table 6.2 Fitted Parameters of the LPM and Associated Statistics for the Training Runs

Run No: Identifier	Q_{gen} (J/min)	UA (J/min°C)	RMSE (°C)
1: 2000 0.4 200	755.2	47.79	0.40
2: 2000 0.4 400	1616	103.5	0.46
3: 2000 0.4 800	787.4	48.08	0.56
4: 2000 0.5 200	441.4	25.82	0.32
5: 2000 0.5 400	720.8	40.18	0.33
6: 2000 0.5 800	1296	72.88	0.39
7: 2000 0.6 200	1343	68.63	0.44
8: 2000 0.6 400	2625	131.9	0.15
9: 2000 0.6 800	1822	89.95	0.50
10: 3000 0.4 200	1402	53.92	0.55
11: 3000 0.4 400	2938	107.0	0.57
12: 3000 0.4 800	2798	101.0	0.66
13: 3000 0.5 200	1837	61.49	0.40
14: 3000 0.5 400	3243	107.3	0.72
15: 3000 0.5 800	3307	107.4	0.83
16: 3000 0.6 200	2624	94.08	0.43
17: 3000 0.6 400	4598	128.2	0.76
18: 3000 0.6 800	4542	124.4	0.80
19: 4000 0.4 200	5075	135.1	0.42
20: 4000 0.4 400	6266	162.7	0.41
21: 4000 0.4 800	6245	162.5	0.51
22: 4000 0.5 200	6116	162.7	0.90
23: 4000 0.5 400	8490	220.0	0.30
24: 4000 0.5 800	9359	238.1	0.60
25: 4000 0.6 200	8383	208.9	0.62
26: 4000 0.6 400	10600	261.7	0.28
27: 4000 0.6 800	10740	171.9	0.34

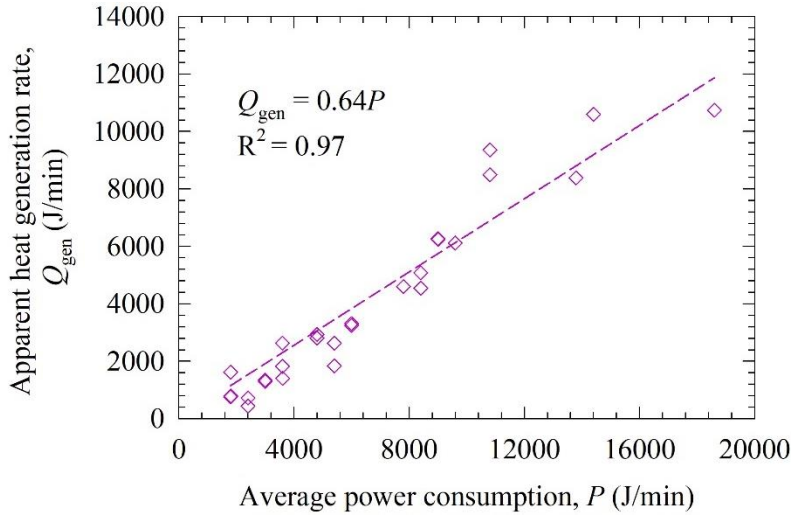

Figure 6.1 Correlation between apparent heat generation rate Q_{gen} and power consumption P.

Before we delve into the experimental temperature profiles and their fitting by the LPM, let us quickly assess how the temperature rise T_{rise} in the mill at 6 min was affected by the apparent heat generation rate Q_{gen} parameter of the LPM. Based on Equation (6.1), we expect that Q_{gen} is the driving force for the temperature rise, which was illustrated in **Figure 6.2**. Overall, the temperature rise was more pronounced for higher Q_{gen} or higher P, in view of **Figure 6.1**. The Gompertz growth function in Equation (6.3) fitted the temperature rise well (R^2 = 0.95). For Q_{gen} = 0, it predicts a negligibly small temperature rise (~0.7 ^{o}C).

$$T_{\text{rise}} = 26.67 \exp[-\exp(1.30 - 6.02 \times 10^{-4} Q_{\text{gen}})] \tag{6.3}$$

It is worth mentioning the caveat that the LPM is too simplistic with a multitude of assumptions; therefore, the Q_{gen} values do not reflect the actual heat generation rate; by and large, Q_{gen} is a fitting parameter affected by the accuracy of the experimental measurements and the assumptions made in the model development. On the other hand, **Figures 6.1** and **6.2** and the correlations therein strongly associate Q_{gen} with the underlying physics of the conversion of shaft work (power consumption) into heat and ensuing temperature rise. The

upshot of these findings is that the LPM differs from a purely empirical model. The latter would fit temperature evolution as a function of time with parameters that have no connection to the physics of the heat generation–transfer phenomena.

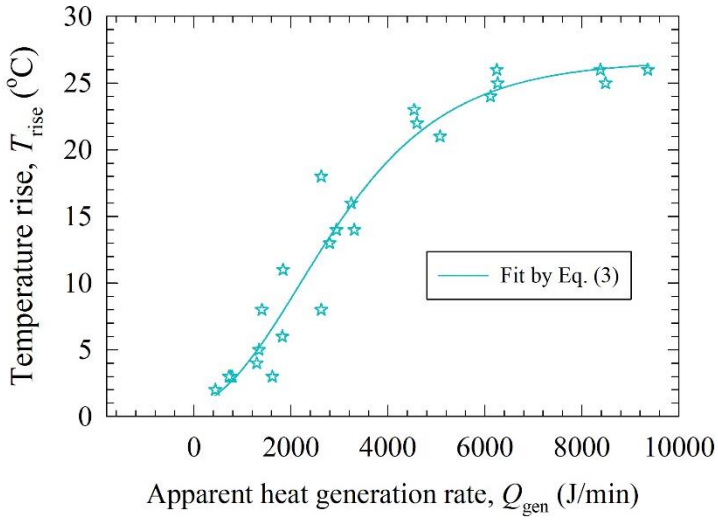

Figure 6.2 Temperature rise at 6 min as a function of the apparent heat generation rate (Runs 1–25).

6.2.3 LPM-fitted temperature profiles and LPM–PL/LPM-ML predictions in the training runs

Figures 6.3–6.5 depict the experimental time-wise evolution of the temperature profiles at various bead loadings and sizes for stirrer speeds of 2000, 3000, and 4000 rpm, respectively, and their direct fitting by the LPM. In agreement with the low RMSE values (**Table 6.2**), the fitted profiles visually corroborate that the LPM has excellent fitting capability despite its simplicity. A cursory look at the experimental temperature profiles suggests that the mill outlet temperature rose during the milling due to the conversion of the shaft work into heat and ensuing heat generation. While the temperature rise was monotonic, the temperature attained a steady-state value for 2000 and 3000 rpm runs. The heat generation was so high at 4000 rpm that the mill was shut down earlier than 60 min and many intermittent milling cycles were conducted. In all profiles, the slope of the

temperature profile decreased during the milling. Guner et al. [206] attributed the decreasing rate of temperature rise to a decrease in the instantaneous power consumption during the milling, which originates from the reduction of viscosity at the higher temperatures and particle size reduction during the milling [88, 197]. **Figures 6.3–6.5** also imply that a higher stirrer speed led to higher heat generation rate; stirrer speed is the dominant process parameter, whereas the impact of the bead size is the weakest.

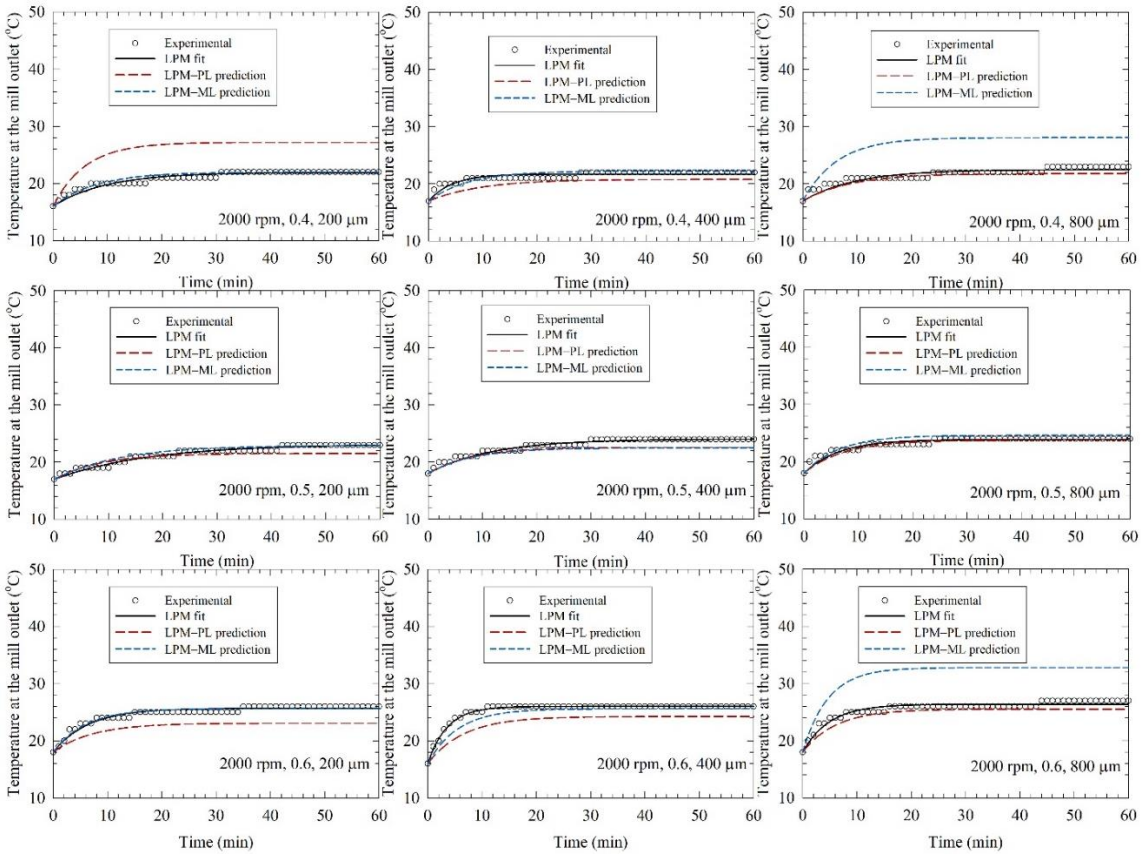

Figure 6.3 Experimental temperature profiles, direct fits by the lumped parameter model (LPM), and predictions by the LPM coupled with a power law (PL) model and a machine learning (ML) model. Left-to-right: increasing bead size, top-to-bottom: increasing bead loading, stirrer speed: 2000 rpm.

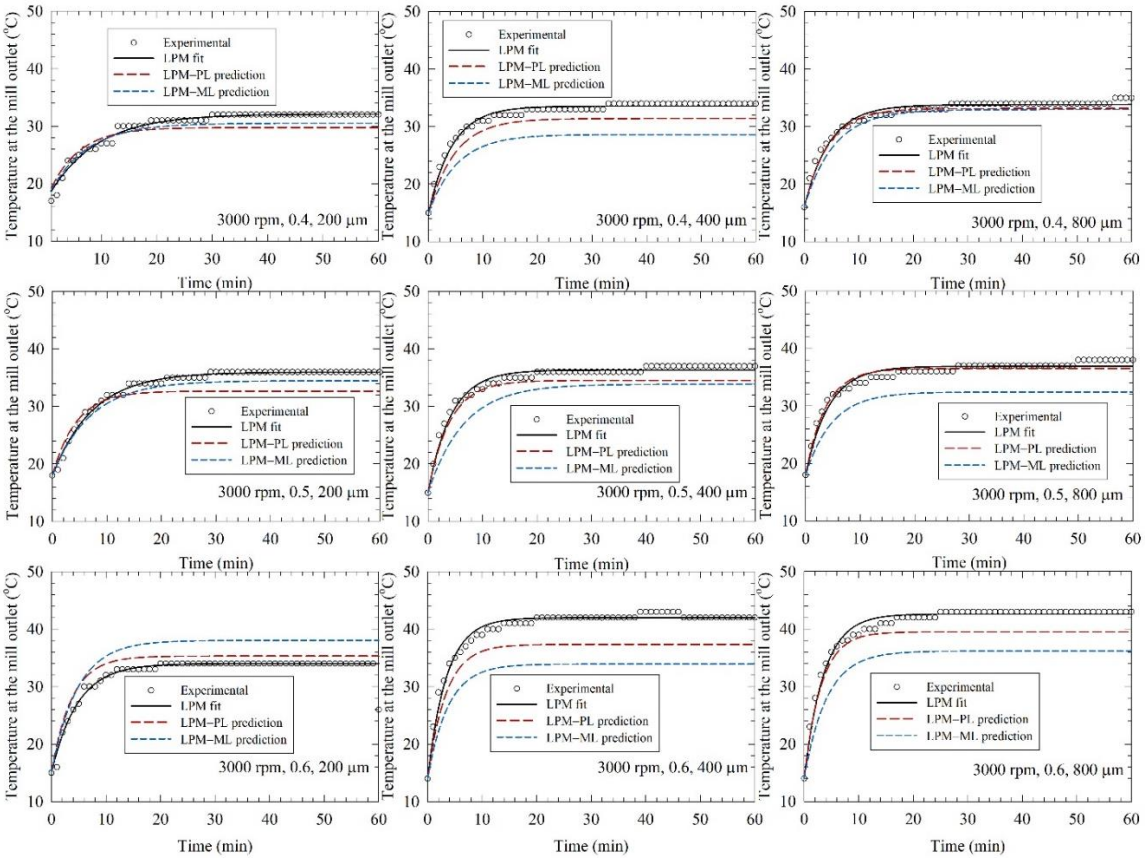

Figure 6.4 Experimental temperature profiles, direct fits by the lumped parameter model (LPM), and predictions by the LPM coupled with a power law (PL) model and a machine learning (ML) model. Left-to-right: increasing bead size, top-to-bottom: increasing bead loading, stirrer speed: 3000 rpm.

To quantify the impact of the process parameters, motivated by our earlier work [166], a power-law (PL) model and machine learning (ML) model were trained using the directly fitted values of Q_{gen} and UA in Runs 1–27, which were conducted at various stirrer speeds ω, bead loadings c, and the bead sizes D_{b}. For the PL model training, Minitab was used, and Equations (6.4) and (6.5) were obtained via fitting.

$$Q_{\text{gen}} = 6.56 \times 10^{-8} \omega^{3.02} c^{1.29} D_{\text{b}}^{0.22} \tag{6.4}$$

$$UA = 1.32 \times 10^{-4} \omega^{1.68} c^{0.77} D_{\text{b}}^{0.12} \tag{6.5}$$

Equations (6.4) and (6.5) signify through their exponents that the stirrer speed and the bead loading had the most significant impact on Q_{gen} and UA, whereas the bead size

impact was much weaker. The relative impact of these parameters can be rank-ordered as follows: stirrer speed > bead loading >> bead size. It is well-known that an increase in the stirrer speed and bead loading increases the power consumption in a wet stirred media mill [34, 137], which in turn leads to higher Q_{gen}. Similarly, it is well-known that an increase in stirrer speed and bead loading also leads to an increase in the internal convective heat transfer coefficient in the mill chamber, which could lead to a higher *UA* [207, 208].

Augmenting the PL model, Equations (6.4) and (6.5), and the ML model (KNN) with the LPM, we predicted the temperature profiles and compared them with the experimental profiles as well as the profiles generated by direct fitting with the LPM alone (see **Figures 6.3–6.5**). The associated mean squared error (MSE) and mean absolute error (MAE) are reported in **Table E.1** of *Appendix E.* The predictions by the LPM–PL and the LPM–ML deviated from the experimental data more than the direct fits by the LPM alone, which is intuitively expected. These deviations can be reduced by expanding the number of training runs through additional experiments at other stirred speeds and bead loadings. Both the LPM–PL and the LPM–ML predicted the profiles very well in many runs (e.g., Run 2, 12, 21). The LPM–PL predictions were generally closer to the experimental profiles than the LPM–ML predictions, with a few notable exceptions for each stirrer speed. The maximum deviation between the LPM–PL prediction and the experimental data ranged from 1.5 to 6.5 ^{o}C, with a mean and standard deviation of 3.1 ± 1.3 ^{o}C. Overall, the LPM captured successfully some salient qualitative patterns of the temperature profiles: (i) the monotonic temperature increase with a decreasing rate, (ii) attainment or approach to a steady-state temperature, (iii) the drastic decrease of time to reach 45 ^{o}C at 4000 rpm, and (iv) the relative impact of the process parameters.

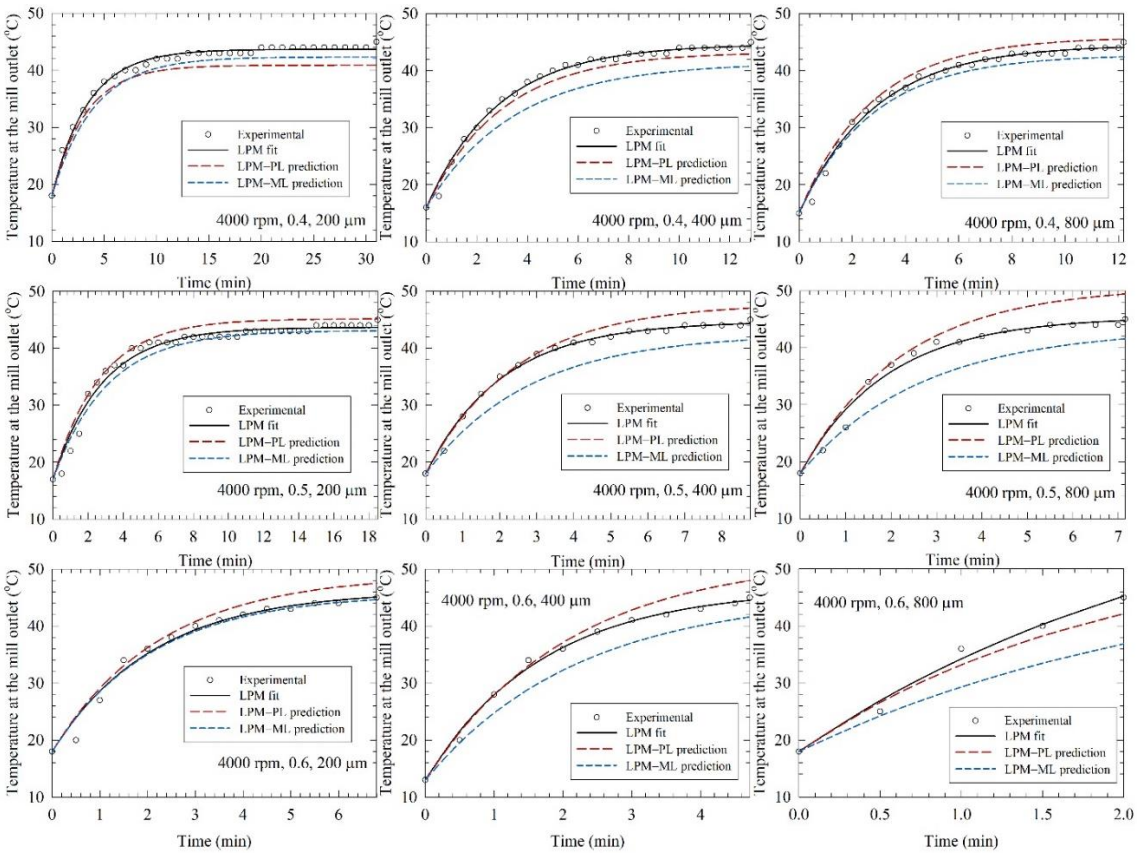

Figure 6.5 Experimental temperature profiles, direct fits by the lumped parameter model (LPM), and predictions by the LPM coupled with a power law (PL) model and a machine learning (ML) model. Left-to-right: increasing bead size, top-to-bottom: increasing bead loading, stirrer speed: 4000 rpm.

6.2.4 Comparative analysis of LPM and EBM fits and their predictions for the test runs

We reserved Runs 28–32 data for testing the simple LPM in comparison to the more elaborate EBM. We first fitted the LPM and the EBM to the experimental temperature profiles directly and estimated Q_{gen} and UA (see the RMSE in **Table 6.3**) and illustrated the fitted profiles in **Figure 6.6**. The EBM data were retrieved from Guner et al. [166] for comparison. **Figure 6.6** and **Table 6.3** data suggest that the LPM fitted the experimental temperature profiles slightly better than the EBM. The average ± standard deviation of the RMSEs are 0.50 ± 0.12 °C for the LPM and 0.96 ± 0.43 °C for the EBM, where LPM has

a lower deviation from the experimental data and is more consistent, according to the lower standard deviation.

Table 6.3 Parameters of the LPM Estimated by Direct Fitting as well as Predicted Using the PL and ML Models Coupled to the LPM along with the Associated Statistics

Runs	Direct fitting				PL prediction				ML prediction			
	Q_{gen} (J/min)	*UA* (J/min°C)	LPM RMSE (°C)	EBM RMSE (°C)[1]	Q_{gen} (J/min)	*UA* (J/min°C)	LPM RMSE (°C)	EBM RMSE (°C)[1]	Q_{gen} (J/min)	*UA* (J/min °C)	LPM RMSE (°C)	EBM RMSE (°C)[1]
2500 0.45 400	1481	68	0.35	0.51	1634	78	0.74	0.93	1792	77	1.51	1.02
2500 0.55 400	2495	101	0.42	0.59	2118	91	1.49	1.02	2506	95	1.44	1.00
3500 0.45 400	4084	118	0.50	1.56	4519	137	1.56	2.22	4555	132	0.59	2.17
2500 0.55 400	5567	147	0.56	1.01	5856	160	1.02	1.17	5911	162	1.19	1.29
4200 0.35 100	3185	84	0.66	1.13	4180	129	4.13	4.17	4359	124	2.08	1.63

[1]RMSE data were taken from Guner et al. 2022 [166] for comparison with the LPM.

The LPM–PL and LPM–ML model predictions are compared with the EBM-PL and the EBM–ML predictions, which were retrieved from Guner et al. [166], in **Figures 6.7** and **6.8**. While all LPM predictions approached an asymptote as the experimental data did, the EBM predictions tended to have a maximum temperature (**Figure 6.7**). Besides, there are better and worse prediction examples when the LPM and EBM predictions are compared. The average ± standard deviation of the RMSEs are 1.57 ± 0.99 °C for all LPM predictions and 1.66 ± 1.00 °C for all EBM predictions. Overall, the LPM is better for predictions but based on the average RMSEs, the difference is not as drastic as it is when the RMSEs associated with direct fitting is compared.

The average ± standard deviation of the RMSEs are 1.79 ± 1.35 °C and 1.36 ± 0.54 °C, respectively, for the LPM–PL and LPM–ML predictions. The LPM–PL exhibited better

or similar predictive capability for most of the test runs as can be seen from **Figure 6.8**, which represents the comparative RMSEs visually. However, the LPM–PL prediction for Run 32 was notably bad. A similarly bad prediction was made by the EBM–PL for the same run. Interestingly, despite its larger deviations for the training runs, when augmented with either the LPM or the EBM, the prediction with the ML model had much lower RMSE than that with the PL model for Run 32. The process conditions of this run were purposefully chosen to be outside the domain of the training runs to test the models under extreme cases. They are not likely used in a lab or industrial setting due to unrealistically low bead loading and very small bead sizes. In general, small beads like 100 μm are more difficult to handle compared with 300–600 μm beads during the operations. Nonetheless, these findings suggest that either the EBM or the LPM should be used with caution outside the domain of the training runs.

6.2.5 The LPM and the EBM comparison and the limitations of the LPM

The full EBM developed by Guner et al. [166] is a comprehensive model of the heat generation–transfer in WSMM that considers recirculation and batch size as well as the cooling rate provided by the jackets of the milling chamber and the holding tank. It entails using the values of power consumption, physico-chemical properties of the fluid and the beads, and the dimensions of the mill setup, which were needed for the calculation of the U and A_m. The EBM is so versatile that it can be used to investigate the impacts of different coolant types and flow rates as well as the material of construction of the mill on the cooling rate and temperature evolution. Despite all these capabilities and higher fidelity to the actual milling process, its use entails more time, effort, and accurate numerical methods for the simulations/parameter estimation. Moreover, one must obtain appropriate data and

correlations for the physical–thermal–heat transfer properties. The EBM consists of five ordinary differential equations (ODEs) with the fraction of power converted into heat ξ as the sole parameter. The estimation of ξ entails using a sophisticated optimizer coupled to the ODE solver. Hence, for facile modeling of the temperature profiles, improved process understanding into the impact of the process parameters, and effective control and optimization of the WSMM process, development of simple, low-fidelity models like the LPM is warranted.

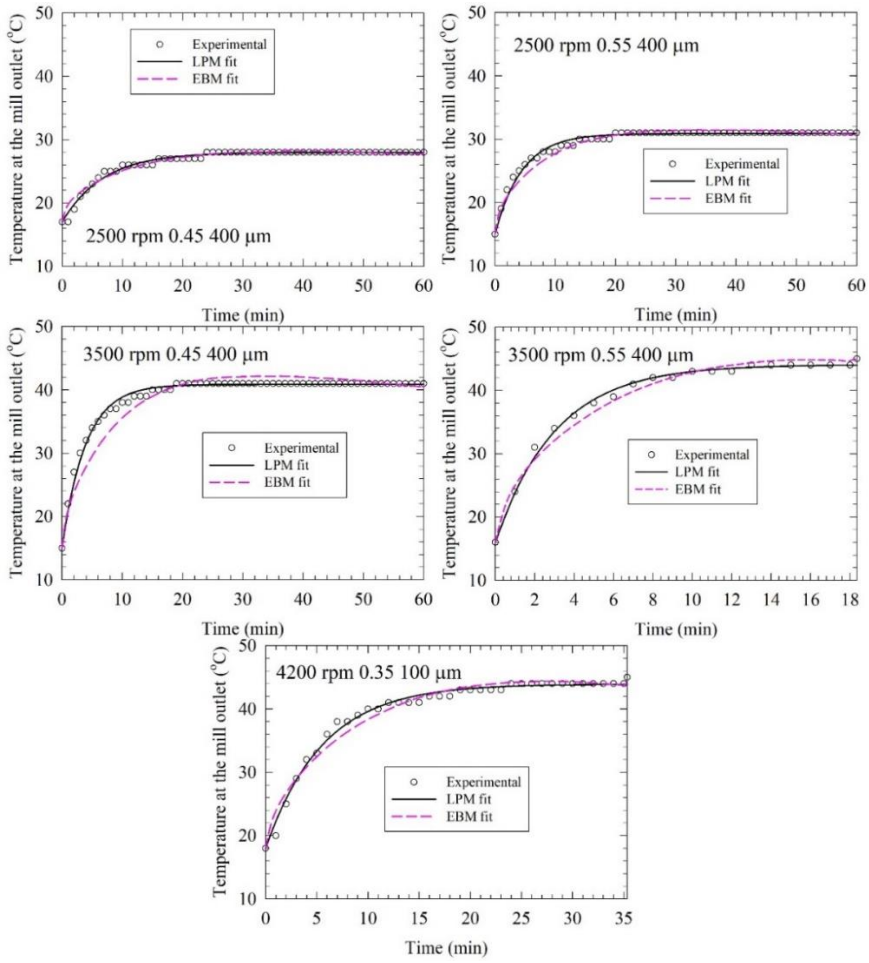

Figure 6.6 Direct fitting of the experimental temperature profiles via the lumped parameter model (LPM) and the enthalpy balance model (EBM) for the test runs (Runs 28–32).
Source for EBM fits: [166]

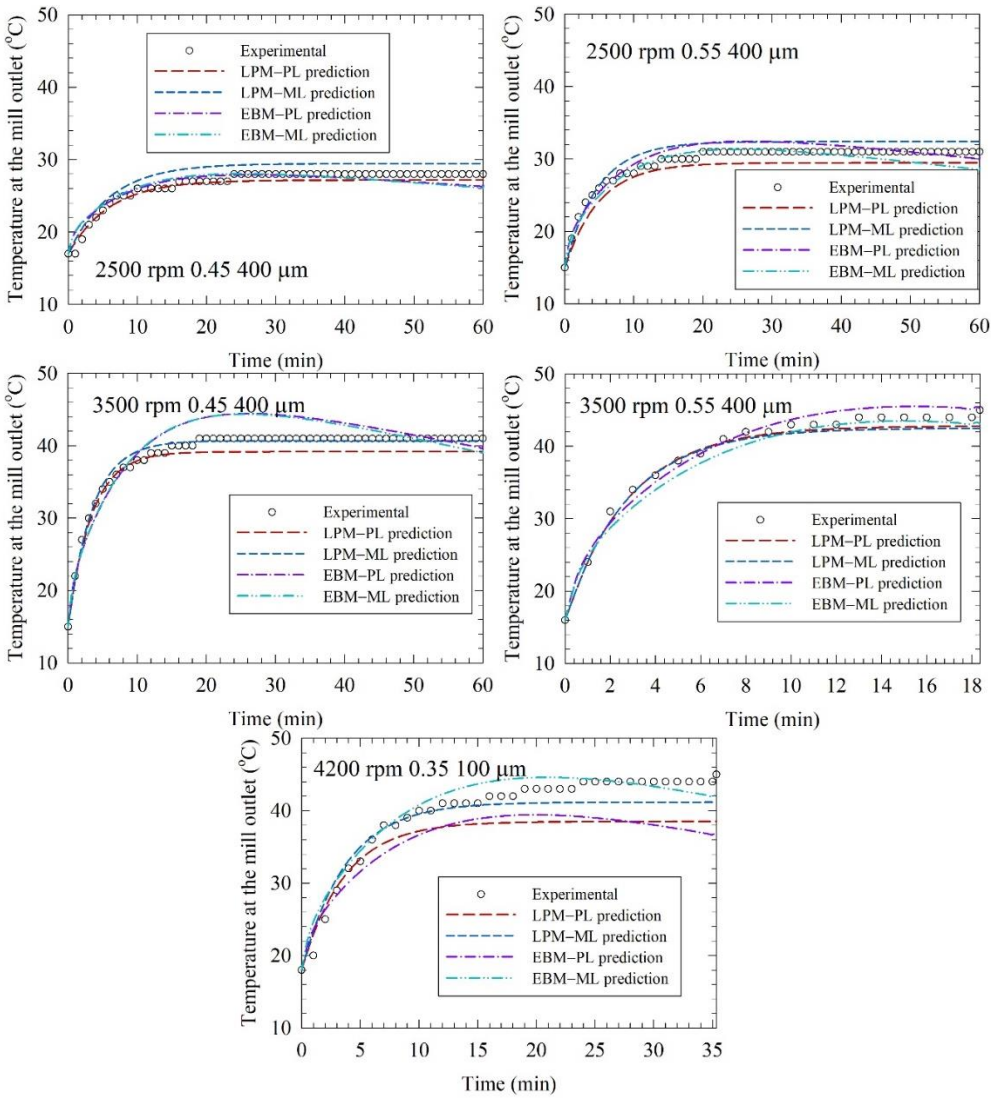

Figure 6.7 Predictions by power law (PL) and machine learning (ML) models coupled with the lumped parameter model (LPM) and the enthalpy balance model (EBM) for the test runs (Runs 28–32).
Source for EBM predictions: [166]

In contrast to the EBM, the LPM is a simple semi-theoretical model, with two adjustable parameters, which was developed based on various assumptions mentioned in Section 2.2.2. Hence, it has a closed-form analytical solution and can be easily used without much effort and time, while obviating the need for sophisticated ODE solvers/optimizers. The main limitation of the LPM is that it is only valid for a given mill set-up with constant batch size and recirculation rate. This aspect may not be critical because, to the best

knowledge of the authors, these parameters are usually kept invariant while the impacts of the stirrer speed, the bead loading, the bead size, and milling time have been investigated in most WSMM process studies (see e.g., the reviews [10, 17]). Another limitation of the LPM is that while it can predict the temperature of the suspension in the milling chamber, it does not provide any information about the temperatures of the suspension in the holding tank, temperatures of the beads, the stirrer of the mill chamber, and the stirrer of the holding tank. Contrarily, the EBM predicted the lower temperature of the suspension in the holding tank than that in the milling chamber and establishment of thermal equilibrium among the suspension, the stirrer element, and the beads owing to fast convective heat transfer and relatively small size of the beads and the mill stirrer [166].

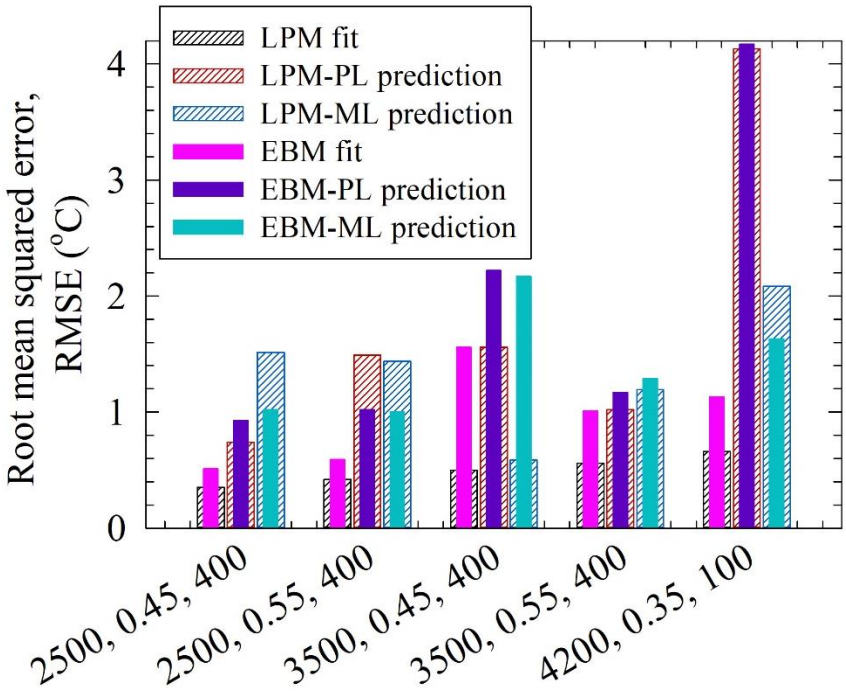

Figure 6.8 Comparison of the root-mean-squared errors of the direct fits and the predictions made by the power law (PL) and machine learning (ML) models coupled with the lumped parameter model (LPM) and the enthalpy balance model (EBM).
Source for EBM RMSEs: [166]

Despite its simplicity, when augmented with the PL and the ML models, the LPM predictions of the temperature profiles in the test runs were better than or similar to the

EBM predictions (refer to **Figures 6.7** and **6.8**). Moreover, the LPM predicts a monotone decreasing temperature profile with a steady-state temperature approached for sufficiently long milling, which is in excellent qualitative agreement with the profiles in **Figures 6.3–6.7**. In fact, Equation (2) clearly shows that in the limit $t \rightarrow \infty$, the temperature reaches a steady-state temperature of $T_{ch} + Q_{gen}/UA$. Although the EBM has higher fidelity to the real WSMM operation, its predictions could be worse, and some predictions exhibited a maximum and ensuing drop in temperature instead of a monotonic approach to a steady-state in the temperature profiles (**Figure 6.7**). In general, the temperature drop from the maximum is within a couple of degrees Celsius, and this error was acceptable. Note that even the EBM has its own assumptions and sources of modeling errors; refer to Guner et al. [166] for a detailed discussion of the modeling errors. For example, in the UA_m calculations, the mixture correlations for the physical properties and the internal/external convective heat transfer coefficients have some errors. The LPM is free of that source of modeling error because *UA* was used as a fitting parameter; therefore, having two fitting parameters, as opposed to the one fitting parameter of the EBM, enhanced its fitting and prediction capability.

The main drawback of the LPM is that it does not consider the enthalpic effects associated with the recirculation of the drug suspension and the thermal inertia effects associated with the batch volume of the suspension in the holding tank. Precisely because of this simplification, the LPM is referred to as a *semi-theoretical model* here, which considers some physical aspects of the process in some time-average, approximate, and statistical sense. Its Q_{gen} and *UA* are fitting parameters that are not equal to the true heat generation rate and the product of the overall heat transfer coefficient and the heat transfer

surface area. In fact, the actual heat generation rate and even the overall heat transfer coefficient vary with time and temperature [166, 206]. However, as established in this study, Q_{gen} is strongly and positively correlated with the power consumption and is the driver for temperature rise, while the *UA* correlation with the process parameters revealed a similar qualitative dependence of the convective heat transfer coefficients on the process parameters in their correlations (refer to such correlations in [33]).

The LPM's treatment of the recirculation operation as an equivalent batch operation seems unreasonable for the modeling of temperature profiles on purely theoretical grounds. Being aware of this limitation, we accept resulting modeling error for the sake of simplicity as LPM is intended to be a low-fidelity model for industrial use. Also, it is worth-mentioning that a similar approach has already been adopted for the modeling of the evolution of the median particle size and even the whole particle size distribution during the recirculation operation of the WSMM by multiple research groups (e.g., [57, 96, 97]).

6.3 Conclusions

This study has developed and implemented a semi-theoretical, lumped-parameter model (LPM) as an alternative to the recently developed enthalpy balance model (EBM) for simulating and predicting the temperature evolution during the nanomilling of drug suspensions. It has two fitting parameters which make it more flexible compared to enthalpy balance model; therefore, it provides better fitting results. While the apparent heat generation rate and the apparent heat transfer coefficient multiplied by the heat transfer surface area are not equal to the actual values, they could be predicted by process conditions via the machine learning (ML) and the power-law (PL) approaches. The fittings and predictions of the LPM were found to be slightly better than those of the EBM. Overall,

our experimental and modeling results suggest that the LPM has excellent descriptive/fitting capability besides its reasonably good predictive capability. Coupled with its simplicity that obviates the need for using a sophisticated coupled optimizer–ODE solver, it could be selected for facile modeling of the WSMM process. Hence, we provide pharmaceutical engineering literature with two different models, the LPM and the EBM, which can be used on a fit-for-purpose basis. If a quick analysis and modeling of the temperature profiles are needed without significant effort/time, then the LPM is advantageous and should be used. The LPM can also be used for process control easily. However, if the aim is to intensify and optimize the process that entails a detailed and deep understanding of the impact of the recirculation rate, batch size, cooling type/capacity, and material of construction, then the EBM must be used. In that case, power consumption, physico-chemical and thermal properties of the suspensions and the beads as well as reliable correlations for the convective heat transfer coefficient must be obtained from the literature and/or determined experimentally.

CHAPTER 7

USE OF BEAD MIXTURES AS A NOVEL PROCESS OPTIMIZATION APPROACH TO NANOMILLING OF DRUG SUSPENSIONS

Chapters 2–6 have presented an experimental and theoretical analyses of the impacts of the process parameters on the breakage kinetics–cycle time, power consumption, and heat generation–temperature rise. The results suggest that by modulating the process parameters such as stirrer speed, bead loading, bead size–material, etc., one can optimize the WSMM process. This chapter, on the other hand, evaluates the feasibility of cross-linked polystyrene (CPS)–yttrium-stabilized zirconia (YSZ) bead mixtures as a novel optimization approach for fast, effective production of drug nanosuspensions during WSMM. Aqueous suspensions of 10% fenofibrate (FNB, drug), 7.5% HPC-L, and 0.05% SDS were wet-milled at 3000–4000 rpm and 35%–50% volumetric loading of CPS:YSZ bead mixtures (CPS:YSZ 0:1–1:0 v:v). Laser diffraction, SEM, viscometry, DSC, and XRPD were used for characterization. An *n*th-order model described the breakage kinetics, while a microhydrodynamic model allowed us to gain insights into the impact of bead materials. CPS beads achieved the lowest specific power consumption, whereas YSZ beads led to the fastest breakage. Breakage followed second-order kinetics. Optimum conditions were identified as 3000 rpm and 50% loading of 0.5:0.5 v/v CPS:YSZ mixture from energy–cycle time–heat dissipation perspectives. The microhydrodynamic model suggests that YSZ beads experienced more energetic/forceful collisions with smaller contact area as compared with CPS beads owing to the higher density–elastic modulus of the former. The work presented in this chapter demonstrated the feasibility of CPS–YSZ bead mixtures and

rationalized its optimal use in WSMM through their modulation of breakage kinetics, energy utilization, and heat dissipation.

7.1 Materials and Methods

7.1.1 Materials

Fenofibrate (FNB, BP grade), which is a BCS Class II drug, was purchased from Jai Radhe Sales (Ahmedabad, India). The aqueous solubility of FNB is 0.8 mg/L at room temperature [169]. Two stabilizers were used: a non-ionic cellulosic polymer (HPC: hydroxypropyl cellulose, L grade, Nisso America Inc, New York, NY, USA) and an anionic surfactant (SDS: sodium dodecyl sulfate, ACS grade, GFS chemicals, Columbus, OH, USA). Zirmil Y grade YSZ beads and HCC grade CPS beads, both with a nominal size of 400 µm, were purchased from Saint Gobain ZirPro (Mountainside, NJ, USA) and Norstone Inc. (Bridgeport, PA, USA), respectively. The density of the YSZ beads and the CPS beads are 6000 kg/m^3 and 1040 kg/m^3.

7.1.2 Wet stirred media milling

The stabilizer types and their concentrations were selected based on detailed stability studies of FNB suspensions performed by our group [46, 47, 54]. About 235 g pre-suspensions that have 10% FNB, 7.5% HPC-L, and 0.05% SDS with respect to 200 g deionized (DI) water were prepared under constant shear mixing at 300 rpm (Cat#. 14-503, Fisher Scientific, Pittsburgh, PA, USA) for 2 h and were kept under 8 ^{o}C overnight. The rationale for this formulation selection was as follows: not only did this formulation ensure physical stability, but also it built up sufficiently high suspension viscosity, which in turn led to accurate measurement of the power consumption and accurate calculation of the

microhydrodynamic parameters. The pre-suspensions were milled by Microcer wet stirred media mill (Netzsch Fine Particle Size Technology, LLC, Exton, PA, USA) for 180 min under the conditions presented in **Table 7.1.** The low–high values of the stirrer speed and the bead loading (volume fraction in the mill chamber) were set based on earlier studies [57, 90] along with the objective of approaching a limiting particle size within 180 min and the design constraint of the mill (4200 rpm). The percent volume ratio of CPS:YSZ in the bead mixtures were varied between 100:0−0:100. The mill has a chamber volume V_m of 80 ml, lined with zirconia, and a zirconia shaft. Suspensions were recirculated between the holding tank and the milling chamber at a volumetric flow rate of 126 mL/min, using a peristaltic pump (Cole-Palmer, Master Flex, Vermont Hills, IL, USA). A 200 μm nominal sized stainless-steel screen was used to hold the beads inside the milling chamber. The temperature of the milling chamber and the holding tank was kept below 35 ^{o}C by using a chiller (Model M1-.25A-11HFX, Advantage Engineering, Greenwood, IN, USA). Due to limitation of our water-cooled chiller, *additional* intermittent cooling during which the mill was stopped while cooling continued was adopted from [63, 90, 161] when the temperature reached 35 ^{o}C in Runs 9–20. At the end of milling experiments with bead mixtures, the beads were transferred to a separation funnel with an aqueous 2.1 M salt (magnesium sulfate) solution. The beads were easily separated due to their stark density differences in the salt solution. The CPS beads floated and YSZ beads sank, which were collected at the bottom of the separation funnel. The separated beads were washed with copious DI water and dried for reuse.

Table 7.1 Process Parameters and the Volume Percentage of CPS and YSZ Beads (CPS:YSZ) in The Bead Mixtures Used for the Milling of FNB Suspensions

Run No.	Stirrer Speed, ω (rpm)	Bead Loading, c (-)	CPS:YSZ (%:%)
1	3000	0.35	100:0
2	3000	0.35	75:25
3	3000	0.35	50:50
4	3000	0.35	25:75
5	3000	0.35	0:100
6	3000	0.50	100:0
7	3000	0.50	75:25
8	3000	0.50	50:50
9	3000	0.50	25:75
10	3000	0.50	0:100
11	4000	0.35	100:0
12	4000	0.35	75:25
13	4000	0.35	50:50
14	4000	0.35	25:75
15	4000	0.35	0:100
16	4000	0.50	100:0
17	4000	0.50	75:25
18	4000	0.50	50:50
19	4000	0.50	25:75
20	4000	0.50	0:100

Samples were taken from the outlet of the mill at certain time intervals (2^s, s = 0, 1, 2,...7) with the additional sampling at 20 s, 40 s, 24 min, 48 min, 96 min, and 180 min. The final sample was taken from the holding tank, and all samples were immediately characterized via laser diffraction. Nanosuspensions were stored in a refrigerator at 8 ^oC for 7 days for short-term stability testing. Before the characterization experiments, the refrigerated nanosuspensions were mixed and allowed to reach thermal equilibrium with the room temperature.

The average power consumption P during the milling was determined by dividing

the cumulative energy consumption read from the control panel of the mill by the milling time. The average stirrer power per unit volume P_w was calculated via $P_w = P/V_m$. The power consumption during the stirring of the suspension in the absence of the beads ε_{ht} was determined similarly. The power consumption, when there was no material in the mill (no-load), was also measured and subtracted during the calculation of P_w and ε_{ht}.

7.1.3 Characterization techniques

Particle size distribution (PSD) of the FNB suspensions at various milling times and after their storage was determined by laser diffraction using LS 13-320 Beckman Coulter instrument (Brea, CA, USA). The polarized intensity differential scattering was maintained between 40% and 50% while the obscuration was maintained below 8%. PSD was computed by the software using the Mie scattering theory. Refractive indices of 1.55 and 1.33 were used for FNB and water (measurement medium), respectively. Before each measurement, a ~1.0 mL suspension sample was dispersed into 5.0 mL of the stabilizer solution using a vortex mixer (Fisher Scientific Digital Vortex Mixer, Model No: 945415, Pittsburgh, PA) at 1500 rpm for one minute. Measurements were repeated four times and the mean ± standard deviation (SD) was reported. The sizes of the milling beads were measured via laser diffraction in dry dispersion mode (Helos/Rodos, Sympatec, NJ, USA). The measured median sizes of the beads were used in the microhydrodynamic calculations.

Images of 180 min milled FNB particles in Runs 1 and Run 20 were taken by a JEOL JSM 7900F field emission scanning electron microscope (SEM) (JEOL USA, Inc., Peabody, MA, USA) operated at 2 kV. About 0.1 mL of the suspension sample was diluted with 10 ml deionized water and centrifuged (Compact II centrifuge, Clay Adams® Brand, Sparks, MD, USA) at 3200 rpm for 10 min to separate the drug particles from the aqueous

phase with excess polymer. This dilution–centrifugation procedure was repeated two more times where 8 ml of the aliquot was decanted and replaced with fresh deionized water. After the third step, a droplet from the aliquot of the sample was put on top of a carbon specimen holder and it was placed in a desiccator for overnight drying under vacuum. The dried samples were then sputter coated with gold using BAL-TEC MED020 (BAL-TEC, Balzers, Switzerland) to reduce possible charging during imaging. As-received FNB particles as well as the YSZ and CPS beads that were separated from the bead mixture at the end of Run 19 were observed using an Axio Scope.A1 polarized light microscope (PLM) (Carl Zeiss Microscopy GmbH, Göttingen, Germany).

The crystallinity of the as-received drug as well as that of the drug in the unmilled physical mixture of FNB–HPC–SDS that has the same formulation as the milled suspensions, and overnight dried, milled suspensions (Runs 1 and 20) were examined using XRPD (PANalytical, Westborough, MA, USA), provided with Cu K_α radiation (λ = 1.5406 Å). The samples were scanned for 2θ ranging from 5^o to 40^o at a scan rate of 0.165 s^{-1}. A Mettler–Toledo polymer analyzer DSC (Model: DSC 3) (Columbus, OH, USA) was used to obtain the peak melting temperature T_m and fusion enthalpy ΔH_f of as-received FNB as well as FNB particles in the physical mixture and after milling (Run 1 and Run 20). Nanosuspension samples were dried and weighed before being placed in a sealed perforated aluminum pan of 40 µL and loaded into the DSC. All samples were heated at a rate of 5 °C/min with a temperature range of 25–150 °C. Nitrogen was used at a flow rate of 60 mL/min. Data analysis was performed using STARe V16.20 software provided by Mettler–Toledo.

The apparent shear viscosities μ_L of the milled suspensions were measured using R/S plus rheometer (Brookfield Engineering, Middleboro, MS, USA) with a water jacket assembly Lauda Eco (Lauda-Brinkmann LP, Delran, NJ, USA). A CC40 coaxial cylinder with a jacketed setup was used to impart a controlled shear rate on the samples from 0 to 1000 1/s in 60 s. The jacket temperature was kept constant at 25 ± 0.5 °C. The raw data were analyzed using the Rheo3000 software and the apparent shear viscosity at the maximum shear rate (1000 1/s) was used in the microhydrodynamic model as this shear rate emulates the high shear rate in the mill [63]. The density of the milled suspension was measured by weighing 35 ml of the milled suspension and dividing the mass of the suspension by its volume.

7.1.4 Analysis of breakage kinetics and energy utilization

For a well-stabilized suspension, the median particle size d_{50} usually decreases over time t until a limiting size d_{lim} is reached [46]. In general, the breakage rate can be described by a differential equation of the form: $dd_{50} = -k(d_{50} - d_{lim})^n$, where k is a breakage rate constant k and n is the kinetic exponent. The solution of this first-order differential equation by separation of variables leads to the following nth-order breakage kinetic model:

$$d_{50}(t) = d_{lim} + \{[d_{50}(0) - d_{lim}]^{1-n} - (1-n)kt\}^{\frac{1}{1-n}} \quad (7.1)$$

in which $d_{50}(0)$ is the initial median size. Marquardt-Levenberg algorithm was used to fit Equation (7.1) to d_{50}–t data, except 20 s (less than one mean residence time), and d_{lim}, k, and n were estimated. The following constraint was imposed during the parameter estimation: $d_{lim} < d_{50}$ (180 min) [90].

In addition to k, two other kinetic measures were used: t_{d50} and t_{d90}, similar to [33, 90]: t_{d50} is the time required for the drug particles to reach a d_{50} of 0.25 µm and t_{d90} is the

time for d_{90} to reach 0.5 μm. While any d_{50} and d_{90} lower than 1 μm can be selected for t_{d50} and t_{d90} for the kinetic analysis, a targeted particle size can also be selected based on intended delivery route, specific pharmaceutical application, and drug formulation. MATLAB's pchip function, which is based on piecewise cubic Hermite polynomial interpolation, was used to calculate t_{d50} and t_{d90}. The specific energy consumption by the mill at t_{d50} and t_{d90} was calculated as follows:

$$E_{td50} = \frac{P_w V_m t_{d50}}{m_D} \quad \text{and} \quad E_{td90} = \frac{P_w V_m t_{d90}}{m_D} \tag{7.2}$$

where m_D is the total mass of the drug in the suspension, V_m is the milling chamber volume. Normalized t_{d50}, E_{td50}, and P_w were defined in Equation (7.3) and a merit score for process optimality was defined and calculated for each run (Equation (7.4)).

$$\overline{t_{d50}} = \frac{t_{d50}}{t_{d50,\max} - t_{d50,\min}}, \quad \overline{E_{td50}} = \frac{E_{td50}}{E_{td50,\max} - E_{td50,\min}}, \text{and } \overline{P_w} = \frac{P_w}{P_{w,\max} - P_{w,\min}} \tag{7.3}$$

$$\text{Merit score} = \frac{1}{w_1 \mathrm{H}(\overline{P_w} - 0.407) + w_2 \overline{E_{td50}} + w_3 \overline{t_{d50}}} \tag{7.4}$$

where max and min refer to maximum and minimum values, w_1, w_2, and w_3 are the weighting coefficients [0–1], H is the Heaviside unit step function, and 0.407 is the normalized P_w value above which the mill was shut down for intermittent cooling once or multiple times (Runs 9–20). Microhydrodynamic model has been utilized as described in Sections 1.4.2 and 2.2.5.

7.2 Results and Discussion

7.2.1 Wet media milling and properties of FNB particles

Table 7.2 presents the characteristic particle size statistics d_{10}, d_{50}, and d_{90} of the FNB suspensions after 180 min milling and 7-day storage. The median sizes of all 20 milled suspensions varied in a narrow range from 0.156–0.185 μm (**Table 7.2**). Considering that as-received FNB particles had d_{10} = 3.82 μm, d_{50} = 27.6 μm, and d_{90} = 55.5 μm, the laser diffraction results signify drastic FNB particle size reduction during the WSMM. The PLM image of the as-received FNB particles and SEM images of the milled particles in Runs 1 and 20 are presented in **Figure 7.1.** The as-received particles with sizes from a few microns to ~50 μm having various shapes such as rounded, angular, and irregular (**Figure 7.1a**) underwent drastic size reduction and formed drug nanoparticles after milling even at the least energetic milling conditions in Run 1 (**Figure 7.1b**) and most energetic conditions in Run 20 (**Figure 7.1c**), corroborating the laser diffraction results. Despite the multiple dilution–centrifugation steps for the SEM sample preparation, adsorbed HPC on FNB surfaces and excess HPC partially covered and even encapsulated some of the FNB particles in the SEM images, somewhat lowering the image quality (**Figure 7.1b,c**). As can be seen from the PLM images (**Figure 7.2a,b**), both the CPS and YSZ beads were intact even after the most aggressive milling process for CPS (Run 19) at ω = 4000 rpm and c = 0.50 when the softer CPS beads were hit by the harder YSZ beads with 1:3 CPS:YSZ volume ratio for 180 min. The median sizes of the CPS beads and the YSZ beads were measured as 444 μm and 405 μm, respectively, via laser diffraction (see **Figure 7.2c** for the volumetric density distributions). For runs that utilized bead mixtures, the bead mixture

separation into CPS beads and YSZ beads for subsequent use was facile. Except the intermittent cooling (Runs 9–20), there was no processability issue.

Table 7.2 Particle Size Statistics of the FNB Suspensions After Milling and 7-Day Storage

Run No.	Particle Sizes After Milling (μm)			Particle Sizes After 7-Day Storage (μm)		
	d_{10} ± SD[a]	d_{50} ± SD[a]	d_{90} ± SD[a]	d_{10} ± SD[a]	d_{50} ± SD[a]	d_{90} ± SD[a]
1	0.118 ± 0.001	0.185 ± 0.001	0.271 ± 0.004	0.118 ± 0.003	0.186 ± 0.002	0.273 ± 0.001
2	0.116 ± 0.001	0.179 ± 0.001	0.267 ± 0.007	0.112 ± 0.001	0.185 ± 0.007	0.267 ± 0.001
3	0.110 ± 0.000	0.168 ± 0.000	0.247 ± 0.000	0.110 ± 0.003	0.168 ± 0.002	0.247 ± 0.000
4	0.115 ± 0.001	0.169 ± 0.001	0.242 ± 0.001	0.113 ± 0.003	0.170 ± 0.002	0.247 ± 0.000
5	0.114 ± 0.001	0.167 ± 0.001	0.244 ± 0.001	0.110 ± 0.001	0.170 ± 0.004	0.245 ± 0.000
6	0.119 ± 0.001	0.165 ± 0.001	0.227 ± 0.001	0.118 ± 0.000	0.163 ± 0.001	0.227 ± 0.000
7	0.117 ± 0.002	0.163 ± 0.001	0.226 ± 0.001	0.116 ± 0.001	0.162 ± 0.001	0.228 ± 0.001
8	0.116 ± 0.001	0.162 ± 0.001	0.224 ± 0.001	0.114 ± 0.001	0.160 ± 0.001	0.226 ± 0.000
9	0.115 ± 0.001	0.157 ± 0.001	0.218 ± 0.001	0.113 ± 0.001	0.158 ± 0.001	0.221 ± 0.000
10	0.117 ± 0.003	0.159 ± 0.001	0.213 ± 0.000	0.115 ± 0.001	0.157 ± 0.001	0.215 ± 0.001
11	0.114 ± 0.001	0.174 ± 0.001	0.251 ± 0.000	0.114 ± 0.001	0.174 ± 0.001	0.250 ± 0.001
12	0.117 ± 0.002	0.166 ± 0.001	0.233 ± 0.001	0.115 ± 0.002	0.166 ± 0.002	0.234 ± 0.001
13	0.117 ± 0.001	0.164 ± 0.001	0.229 ± 0.001	0.114 ± 0.001	0.162 ± 0.001	0.230 ± 0.000
14	0.116 ± 0.001	0.164 ± 0.000	0.228 ± 0.000	0.111 ± 0.001	0.160 ± 0.001	0.230 ± 0.001
15	0.115 ± 0.001	0.161 ± 0.001	0.225 ± 0.000	0.115 ± 0.001	0.161 ± 0.001	0.226 ± 0.001
16	0.123 ± 0.004	0.164 ± 0.001	0.212 ± 0.005	0.119 ± 0.001	0.158 ± 0.001	0.212 ± 0.001
17	0.123 ± 0.006	0.162 ± 0.001	0.208 ± 0.001	0.122 ± 0.001	0.159 ± 0.001	0.210 ± 0.001
18	0.125 ± 0.001	0.159 ± 0.000	0.208 ± 0.001	0.120 ± 0.000	0.156 ± 0.000	0.209 ± 0.000
19	0.121 ± 0.001	0.156 ± 0.001	0.209 ± 0.000	0.114 ± 0.001	0.151 ± 0.001	0.211 ± 0.000
20	0.124 ± 0.001	0.157 ± 0.001	0.208 ± 0.001	0.119 ± 0.003	0.154 ± 0.002	0.209 ± 0.001

[a]Standard deviation (SD) of the particle size statistic based on four size measurements.

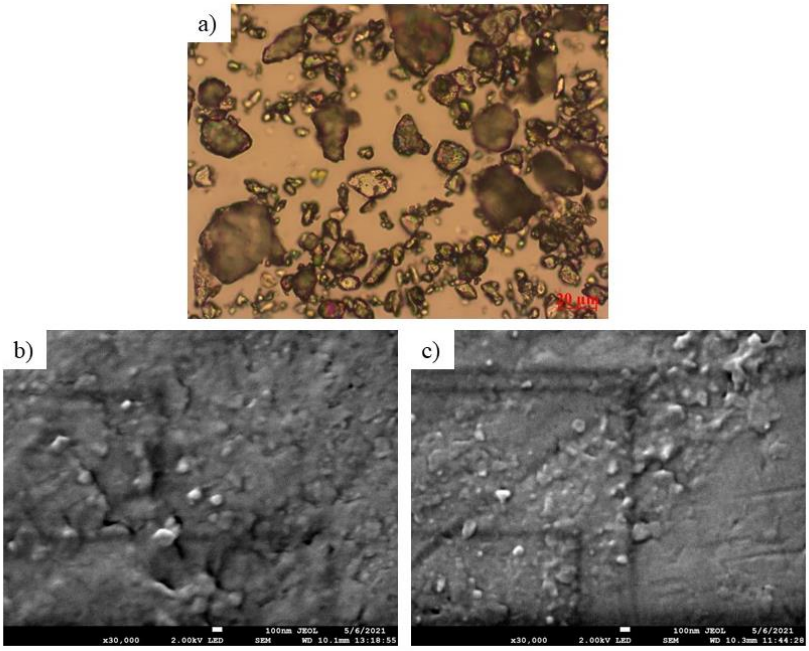

Figure 7.1 (a) PLM image of as-received FNB particles, (b) SEM image of 180 min milled FNB particles in Run 1 (×30,000 magnification, scale bar: 100 nm), and (c) SEM image of 180 min milled FNB particles in Run 20 (×30,000 magnification, scale bar: 100 nm). Run 1 refers to milling at ω = 3000 rpm, c = 0.35, and CPS:YSZ = 100:0; Run 20 refers to milling at ω = 4000 rpm, c = 0.5, and CPS:YSZ = 0:100.

After the storage of the nanosuspensions for 7 days, the particle sizes did not increase notably due to either aggregation or Ostwald ripening, signifying their good short-term stability (see **Table 7.2**). **Figure F.1** (*Appendix F*) depicts the apparent shear viscosity μ vs. shear rate γ profiles of the milled suspensions, while **Table F.1** (*Appendix F*) presents the estimated parameters of the power–law viscosity model: $\mu = \mu_0 \gamma^{q-1}$. The viscosity profiles displayed slight pseudoplasticity (shear-thinning), tending to near-Newtonian behavior (exponent $q \cong 0.9$–1). Stable, wet-milled suspensions of itraconazole [209] and griseofulvin [205] were obtained when stabilized by HPC–SDS, and such suspensions had similar q values. In those studies, the unstable suspensions with low HPC concentration and/or without SDS had large drug aggregates which exhibited strong pseudoplasticity (q as low as 0.1–0.3). Overall, the orthogonal measurements via laser diffraction and

viscometry suggest that the 10% FNB formulation with 7.5% HPC and 0.05% SDS led to stable suspensions at all processing conditions and that the milling dynamics were largely dominated by breakage rather than aggregation. These findings are not surprising as the combined use of cellulosic polymer–anionic surfactant provided physical stability for many drug nanosuspensions owing to the electrosteric stabilization and wettability enhancement [10, 46, 47, 54, 205].

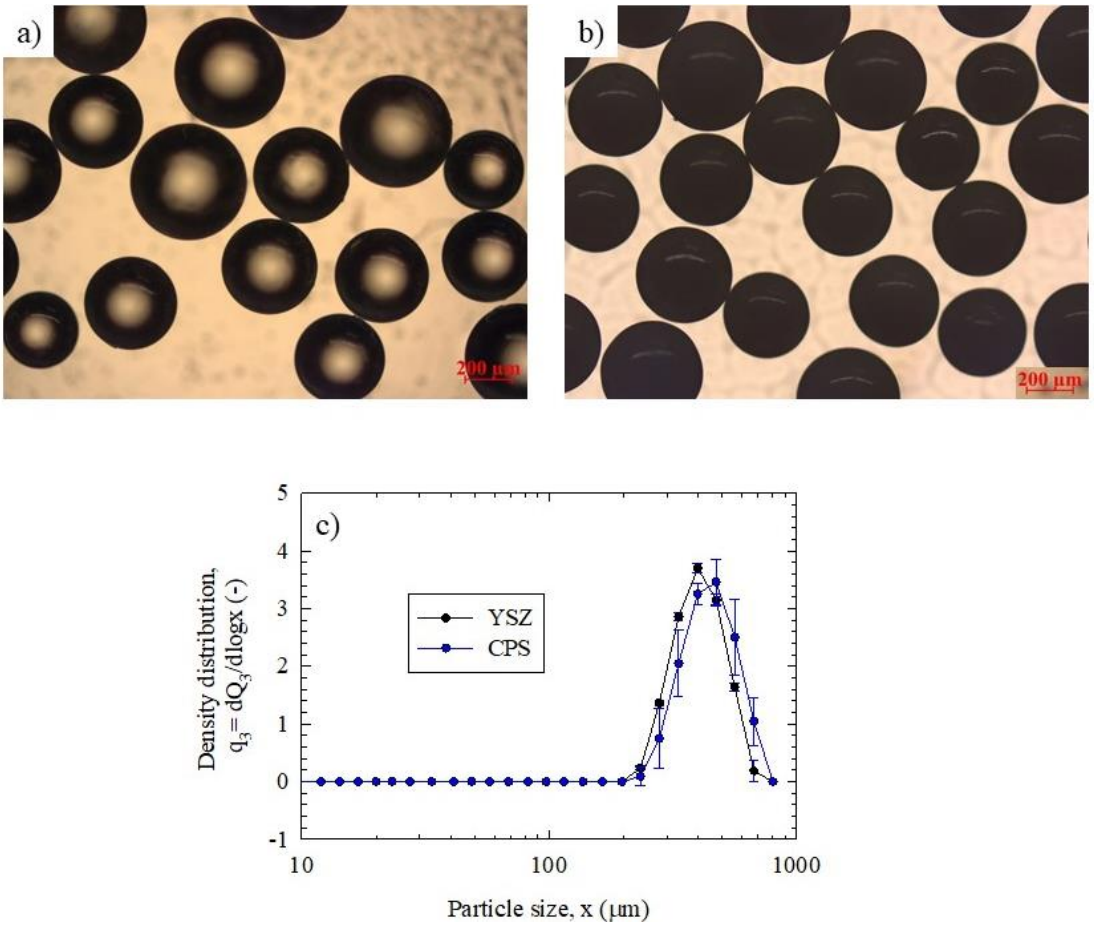

Figure 7.2 Microscopic images of (a) CPS beads and (b) YSZ beads as well as their (c) their size distributions after Run 19. Run 19 refers to milling at ω = 4000 rpm, c = 0.5, and CPS:YSZ = 25:75. Q_3 refers to cumulative volume fraction, while q_3 refers to volume density distribution.

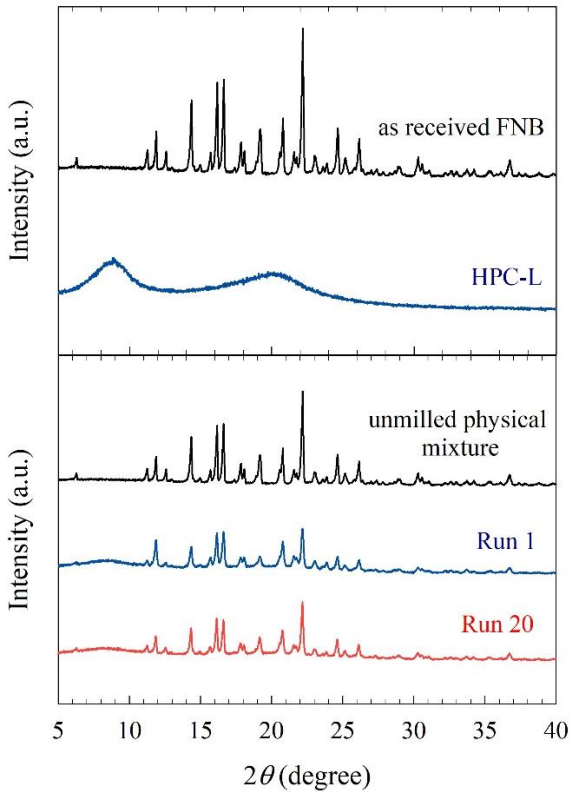

Figure 7.3 XRPD diffractograms of as-received FNB, HPC-L, unmilled physical mixture, and dried nanosuspensions prepared in Runs 1 and 20. Run 1 refers to milling at ω = 3000 rpm, c = 0.35, and CPS:YSZ = 100:0; Run 20 refers to milling at ω = 4000 rpm, c = 0.5, and CPS:YSZ = 0:100.

WSMM may alter the crystalline nature of the drug. Hence, XRPD diffractograms of the dried–milled suspensions from the least energetic run (Run 1 with the lowest P_w) and the most energetic run (Run 20 with the highest P_w) were compared with those of the unmilled physical mixture of the same formulation and as-received FNB and HPC (**Figure 7.3**). SDS was not analyzed as its concentration was very low in the formulation. The shortened characteristic peaks of FNB for the physical mixture and the milled samples can be attributed to the dilution and surface coverage of FNB particles by HPC [210]. Moreover, the milled samples have slightly shorter peaks compared to the physical mixture, which can be due to either a better coverage of drug particles by the polymer or defect formation during milling [89]. DSC traces (**Figure 7.4**) exhibited endotherms

associated with the fusion of FNB in the physical mixture and dried FNB nanosuspensions, whereas a halo was observed for the amorphous HPC. The fusion enthalpy decreased proportional to the presence of HPC in the physical mixture. The FNB in dried nanosuspensions had slightly smaller ΔH_f and 2–3 °C T_m reduction as compared with FNB in the physical mixture. The presence of smaller crystals (nanocrystals) in the suspensions and defect formation could largely account for this small reduction. Overall, both the XRPD and DSC results suggest that the crystalline nature of FNB was largely preserved after milling while formation of defects and a small fraction of amorphous FNB cannot be totally ruled out.

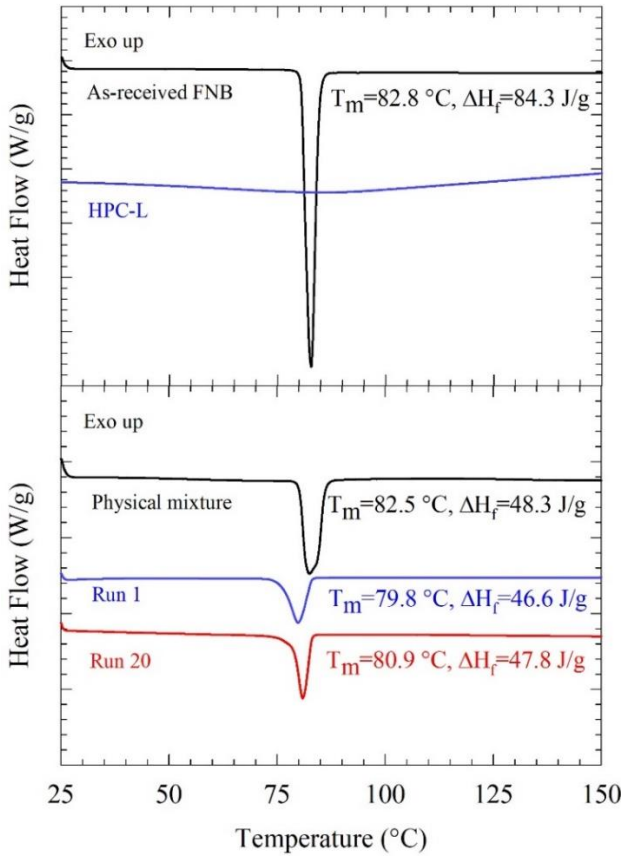

Figure 7.4 DSC traces, with fusion enthalpy ΔH_f and peak melting point temperature T_m, of as-received FNB, HPC-L, unmilled physical mixture, and dried nanosuspensions prepared in Runs 1 and 20. Run 1 refers to milling at ω = 3000 rpm, c = 0.35, and CPS:YSZ = 100:0; Run 20 refers to milling at ω = 4000 rpm, c = 0.5, and CPS:YSZ = 0:100.

7.2.2 Breakage kinetics and microhydrodynamic analysis

The temporal evolution of d_{50} and d_{90} during the WSMM as a function of YSZ loading (volume fraction in the CPS–YSZ bead mixture) c_{YSZ} was depicted in **Figure 7.5a,b** for low–high values ω and c. For the sake of completeness, the evolution of d_{10} is illustrated in **Figure F.2** (*Appendix F*) as d_{10} data have not been used in the analysis of breakage kinetics and assessment of the extent of breakage [61, 211]. While **Figure 7.5** presents the direct impact of YSZ loading in the CPS:YSZ mixtures, the same data are also illustrated in an alternative way to depict the impact of the stirrer speed ω and the bead loading c directly (**Figure F.3**, *Appendix F*).

Before delving into a detailed analysis of breakage kinetics and impact of bead mixtures, it is important to recognize the salient features of the temporal evolution depicted in **Figure 7.5.** Both d_{50} and d_{90} decreased monotonically in all experiments, which indicates breakage was the dominant mechanism as opposed to aggregation during the time scale of the milling, again owing to the good stabilization provided by the HPC–SDS combination. For all runs except the ones with ω = 3000 rpm–c = 0.35, d_{50} approached or almost attained a limiting median size d_{lim}, which is also known as the apparent "grinding limit" [65, 130], within 180 min. One can see from **Figure 7.5** and **Figure F.3** that the time to approach this limit got shorter at higher ω and c. Reproducibility of the WSMM process has been well-established (see the reviews [10, 17] and the references cited therein). Here, the whole preparation–milling for Runs 4 and Run 14 was repeated. As expected, the time-wise evolution of d_{10}, d_{50}, and d_{90} was almost identical in the repeated runs; and negligibly small deviations were within experimental accuracy of the size measurements (**Figure F.4**, *Appendix F*).

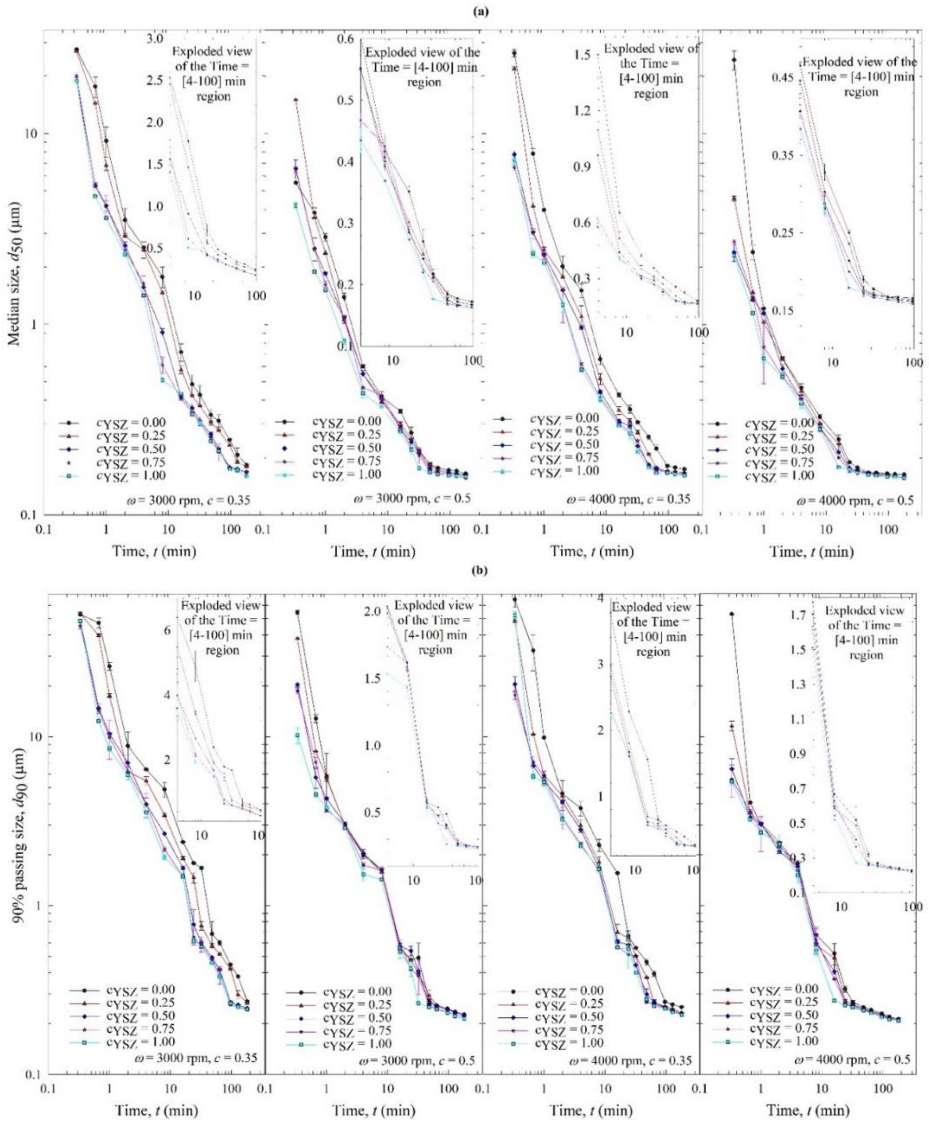

Figure 7.5 Effects of YSZ loading (volume fraction in the CPS-YSZ bead mixture) cYSZ on the time-wise evolution of (a) d_{50} and (b) d_{90} for various stirrer speed ω, bead loading c.

One way to assess the overall impact of the bead mixtures and process parameters on the breakage kinetics *qualitatively* is to compare particle sizes at various time points on the d_{50} temporal evolution curve. For example, at any given time, a higher bead loading c resulted in smaller particles when the stirrer speed ω was kept constant; and at constant c, higher ω did the same (**Figure F.3**, *Appendix F*). Doing this for the curves in **Figure 7.5a**, with a focus on the inset, reveals that YSZ beads led to faster breakage than the CPS beads

and that the CPS:YSZ bead mixtures generally exhibited evolution curves in between of those of CPS alone and YSZ alone. However, this analysis does not consider all points simultaneously, and the visual discrimination becomes difficult in the nano-size domain; the best discrimination between the performances of the mixtures could be made within the first 20 min of milling. Hence, a *quantitative* analysis of the breakage kinetics was performed using the *n*th-order kinetic model (Equation (7.1)) and the characteristic time measures like t_{d50} and t_{d90}: lower t_{d50}–t_{d90} and higher k both suggest faster breakage. The *n*th-order kinetic model fitted the data well: $R^2 \geq 0.99$, and both the model and its three parameters n, d_{lim}, and k were statistically significant: p-value < 0.05 (**Table F.2**, *Appendix F*). The d_{lim} values were lower than d_{50} values at 180 min, which gives credence to the model, and they varied from 0.118–0.161 μm for all 20 runs (0.143±0.011 μm with 7.7% RSD). Surprisingly, the overall breakage kinetics was almost second-order, i.e., $n \cong 2$ (2.03±0.086 with 4% RSD). Hence, the breakage rate constant k is an excellent quantitative parameter that can be used for comparing the kinetics in different runs. A cursory look at the k, t_{d50}, and t_{d90} values in **Figure 7.6** suggests that the three kinetic measures reveal similar trends in terms of the impact of c_{YSZ}, ω, and c and that they agree reasonably with the qualitative assessment based on the temporal evolution curves discussed above. In general, an increase in c_{YSZ}, ω, and c led to faster breakage: higher k and lower t_{d50} and t_{d90}. However, since the differences between the kinetics with different bead mixtures were not drastic, the increase in the YSZ concentration did not provide a monotonic decrease in t_{d50} and t_{d90} in a few cases which could be due to the experimental error in the particle size measurements but k is not affected by these experimental errors as much, suggesting monotonic increase with YSZ concentration since it considers all particle size data. **Figure**

7.6a,c illustrates that when the total bead loading was low (c = 0.35), the impact of YSZ fraction in the mixture did not have a drastic impact on the kinetic measures for $c_{YSZ} \geq 0.5$ compared to $c_{YSZ} < 0.5$ according to the t_{d50}-t_{d90} curves. Especially at low bead loadings, CPS beads caused some clogging and addition of small concentrations of YSZ beads helped with this issue and increased the initial breakage rate more. However, at c_{YSZ} = 0.50 there were no clogging and increasing c_{YSZ} further just provided faster breakage kinetics since there was no practical clogging issue anymore and this caused the decreasing slope of t_{d50}-t_{d90} curves. Although the absolute values of t_{d50} and t_{d90} varied less upon changes in c_{YSZ} at c = 0.50, the relative changes were still notable. For example, t_{d50} and t_{d90} decreased by 29% and 27% (**Figure 7.6b**) and 48% and 50% (**Figure 7.6d**), respectively, when c_{YSZ} was varied from 0 to 1.

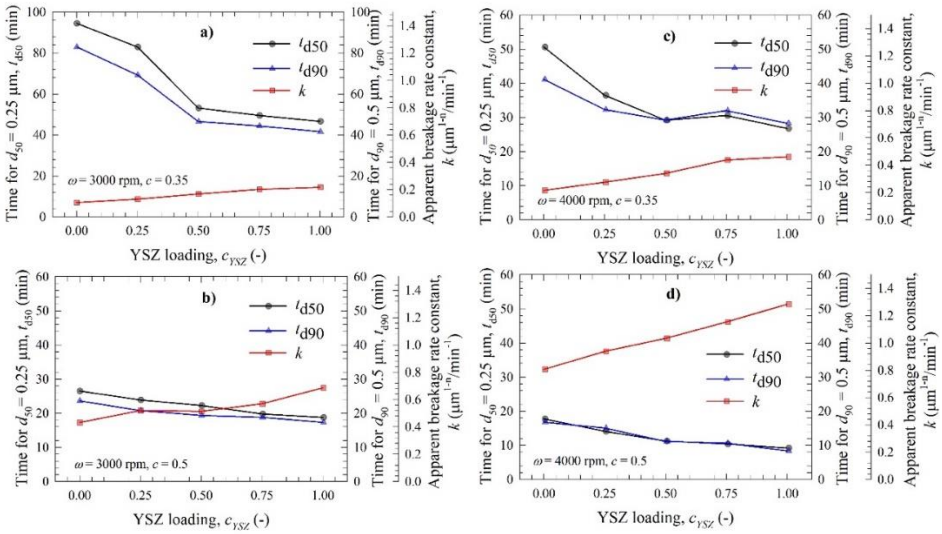

Figure 7.6 Effects of YSZ loading (volume fraction in the CPS–YSZ bead mixture) c_{YSZ} on characteristic milling times t_{d50}, t_{d90}, and apparent breakage rate constant k, during the milling of FNB particles at various stirrer speeds ω and bead loadings c.

As the current microhydrodynamic theory is restricted to beads of one material type (CPS or YSZ, but not both), we consider here non-mixture runs with c_{YSZ} = 0 (CPS) and c_{YSZ} = 1 (YSZ) to gain fundamental insights into the distinct breakage kinetics associated

with CPS and YSZ. **Figure 7.7** presents the impact of bead material on t_{d50} at two stirrer speeds ω and beads loadings c. **Figure 7.8** presents the calculated parameters of the microhydrodynamic model (actual data available in **Table F.3**, *Appendix F*). All microhydrodynamic parameters were higher at the higher speed (**Figure 7.8**), which physically explains the lower t_{d50} in **Figure 7.7** in terms of more frequent and energetic/forceful bead–bead collisions. On the other hand, an increase in c caused two major counteracting changes: the drug particles were compressed more frequently (higher a) between beads that fluctuate more frequently (higher ν) due to higher g_0 and reduced inter-bead distance. On the other hand, the beads moved slower (lower u_b) with lower fluctuating kinetic energy (lower θ), leading to less energetical/forceful collisions (lower maximum contact pressure σ_b^{max} with lower α_b). As the first favorable change was dominant over the second less favorable change, perhaps attributable to the drastic change in a as compared with the other relatively smaller changes, overall, breakage occurred faster at higher c (see **Figure 7.7**). These findings are in line with our previous study on the WSMM of griseofulvin [90].

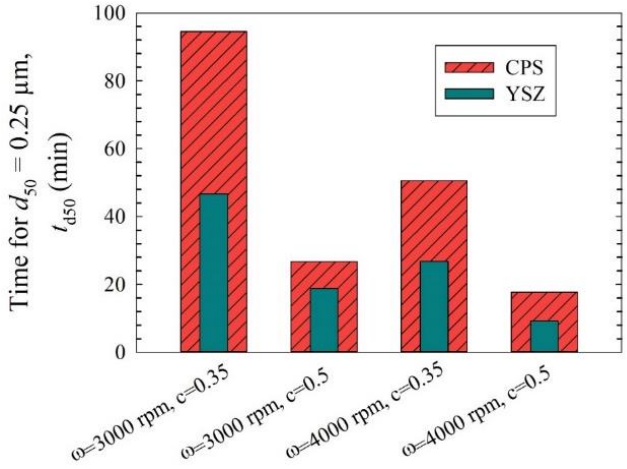

Figure 7.7 Milling time required to attain a median drug particle size d_{50} of 0.25 µm in the milling runs with CPS beads alone and YSZ beads alone (Runs 1, 5, 6, 10, 11, 15, 16, and 20).

The YSZ beads were associated with higher values of all microhydrodynamic parameters, except the radius of the contact circle α_b and a, than the CPS beads (**Figure 7.8**). Due to their higher density and associated higher power consumption, the YSZ beads engaged in more energetic/forceful collisions (higher σ_b^{max}), leading to a higher energy dissipation rate associated with the deformation of the drug particles (higher $\Pi\sigma_y$). Surprisingly, albeit having higher θ and ν, YSZ beads resulted in similar a to CPS beads at 3000 rpm and slightly higher a than CPS beads at 4000 rpm. The larger α_b, which stems from the lower modulus of elasticity of CPS, as well as lower θ and ν of CPS beads counteracted each other, ultimately leading to these close values of a. However, as most other parameters were higher for the YSZ beads, it is not surprising to see that the YSZ beads led to faster drug particle breakage than the CPS beads (**Figure 7.7**). Based on these microhydrodynamic considerations of the CPS and YSZ beads, even without having a new microhydrodynamic theory for the mixtures, one could argue that the bead mixtures would not be more favorable than the YSZ beads from a breakage kinetics (cycle time) perspective alone.

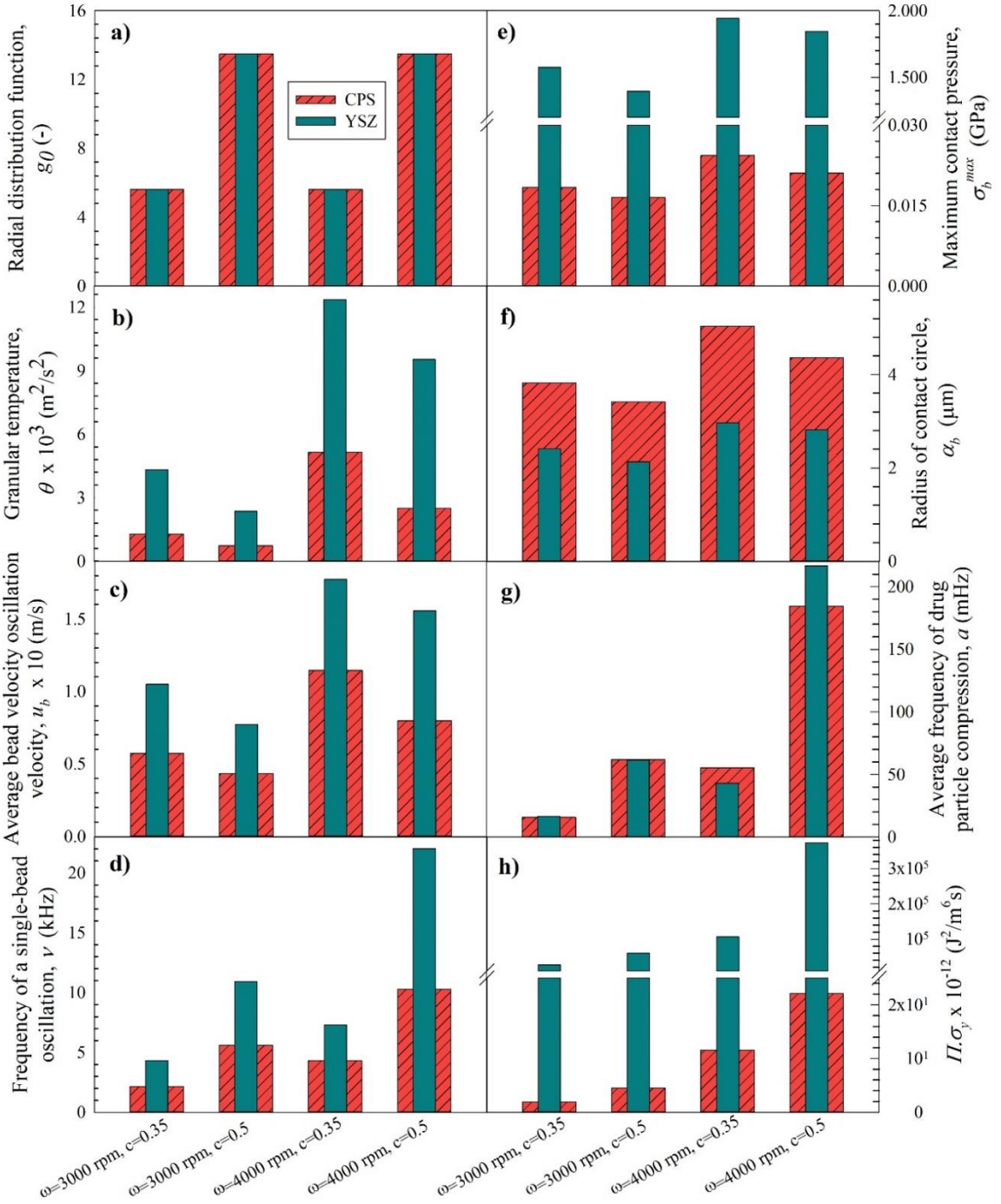

Figure 7.8 Effects of the stirrer speed ω and the bead loading c on (a) radial distribution function at contact g_0, (b) granular temperature θ, (c) average bead oscillation velocity u_b, (d) frequency of a single-bead oscillation ν, (e) maximum contact pressure σ_b^{max}, (f) radius of contact circle α_b, (g) average frequency of drug particle compression a, and (h) the pseudo energy dissipation rate $\Pi\sigma_y$ for milling runs with CPS beads alone and YSZ beads alone (Runs 1, 5, 6, 10, 11, 15, 16, and 20).

7.2.3 Power–specific energy consumption and heat dissipation related issues

Interestingly, in pharmaceutical WSMM literature, an analysis of power–specific energy consumption, as well as heat transfer aspects, are sorely missing. **Figure 7.9** depicts the change in average power consumption per unit volume P_w and specific energy consumption to reach a median size of 0.25 µm, i.e., E_{td50} as a function of the YSZ loading in the bead mixtures c_{YSZ} at various ω–c. Clear trends are illustrated by **Figure 7.9a**: P_w increased with higher c_{YSZ}, ω, and c; maximum values were observed for the YSZ beads. The higher P_w can be explained by the higher density ρ_m and viscosity μ_m of the bead–milled drug suspension mixture (see **Table F.1**, *Appendix F*), which were calculated using the following equations [194]:

$$\mu_m = \mu_L[1 + 2.5c + 10c^2 + 0.0019\exp(20c)] \quad (7.5)$$

$$\rho_m = [\rho_{YSZ}c_{YSZ} + \rho_{CPS}(1 - c_{YSZ})]c + \rho_L(1 - c) \quad (7.6)$$

As can be seen from Equations (7.5–7.6), an increase in the total bead concentration c causes an increase in both ρ_m and μ_m. An increase in the volume fraction of the denser beads c_{YSZ} ($\rho_{YSZ} > \rho_{CPS}$) results in an increase in ρ_m. Besides, an increase in the stirrer speed is known to increase the power consumption [137]. The non-linear trends of P_w with c_{YSZ} can be explained by the low precision readings of the values from the mill screen, and also by the small variation in the suspension viscosity from run to run, due to measurement errors of powder weights and liquid volumes while preparing the suspension.

Interestingly, E_{td50} exhibited a more complex, non-monotonic response in contrast with P_w (**Figure 7.9b**). The difference originates from the contradicting trends effect of t_{d50} and P_w on E_{td50}; breakage kinetics accounts for the difference. As can be seen from **Figure 7.9b** (data in **Table F.4**, *Appendix F*), while E_{td50} and E_{td90}, in general, were higher at the

higher ω at constant c; they were lower with the higher c at constant ω. Even though P_w was higher at the higher c (constant ω), the breakage was faster too (lower t_{d50}–t_{d90} and higher k); hence, E_{td50} and E_{td90} were lower. The lowest E_{td50} and E_{td90} occurred when milling was performed with the CPS beads at ω = 3000 rpm and c =0.50 (**Figure 7.9b**). On the other hand, the lowest P_w was achieved when milling was performed with the CPS beads at ω = 3000 rpm and c =0.35 (**Figure 7.9a**).

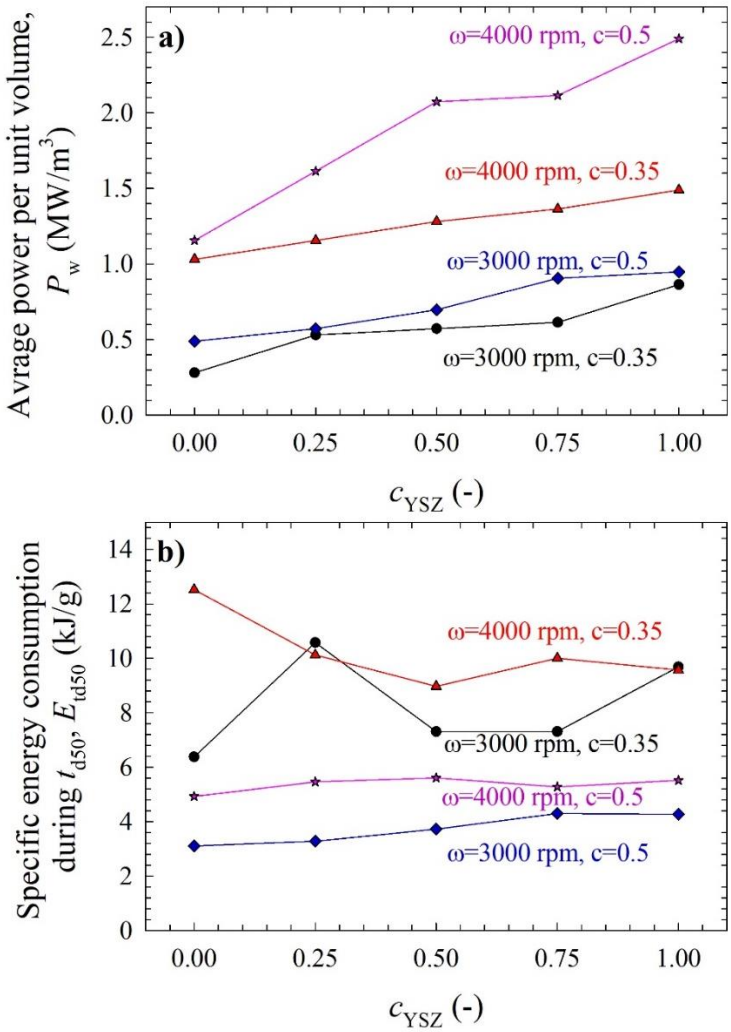

Figure 7.9 Effects of YSZ loading (volume fraction in the CPS–YSZ bead mixture) c_{YSZ}, the stirrer speed ω, and the bead loading c on (a) the average stirrer power per unit volume P_w and (b) the specific energy consumption during t_{d50}, E_{td50}.

E_{td50} or E_{td90} can be used to determine the electric utility costs required for milling the drug particles to the desired target size, while P_w appears to affect the heat dissipation and associated cooling load/cost. While costs associated with milling and cooling could be important in manufacturing–operations, they are not necessarily the most important aspects. In this chapter, although we did not perform a heat transfer analysis, it was clear that P_w was positively correlated with the temperature rise and frequency of intermittent cooling events during the milling. The mill was shut down for intermittent cooling due to limited cooling capacity of our water-cooled chiller and the milling chamber wall's ceramic lining as opposed to a stainless-steel lining. No intermittent cooling was needed for Runs 1–8 for which P_w was less than 0.9 MW/m^3 (**Table F.1**, *Appendix F*). Intermittent cooling was applied once during Runs 9–11. The milling was interrupted only a few times in Runs 12–17. It is possible that a chiller with much higher cooling capacity might have obviated the need for intermittent cooling for these runs. Unfortunately, the intermittent cooling was applied periodically (mill shutdown every ~8–10 min) for Runs 18–20, which is clearly an operational failure mode. The P_w profiles in **Figure 7.9a** and these intermittent cooling episodes overall imply that the YSZ beads are less favorable than the CPS beads when low heat dissipation/temperature rise is desired during the milling.

7.2.4 Various process optimality criteria and associated merit scores

The upshot of the analysis above is that CPS beads are superior to YSZ beads when lower P_w and avoidance of heat dissipation related shutdowns are desired, which is contrary to what fast breakage/low cycle time would demand (YSZ beads alone). This implies that a CPS–YSZ bead mixture, as opposed to CPS or YSZ beads alone, is expected to yield an optimal process. Here, we consider several process optimality criteria to gain insights into

the selection of bead mixtures and WSMM process conditions. In general, selecting an optimal WSMM process is a complex, multi-faceted task, requiring consideration of various factors including the properties of the drug formulation and the targeted particle size as well as costs, cycle time, absence of out-of-specification events, etc. If the physical or chemical stability of a drug suspension is extremely susceptible to temperature [53, 153] or temperature rise during the milling, then a process which does not lead to high P_w should be designed with a high-capacity chiller. A process with 35–50% CPS beads loading running at 3000 rpm may be a good candidate. However, we will not consider details of such extreme scenarios here.

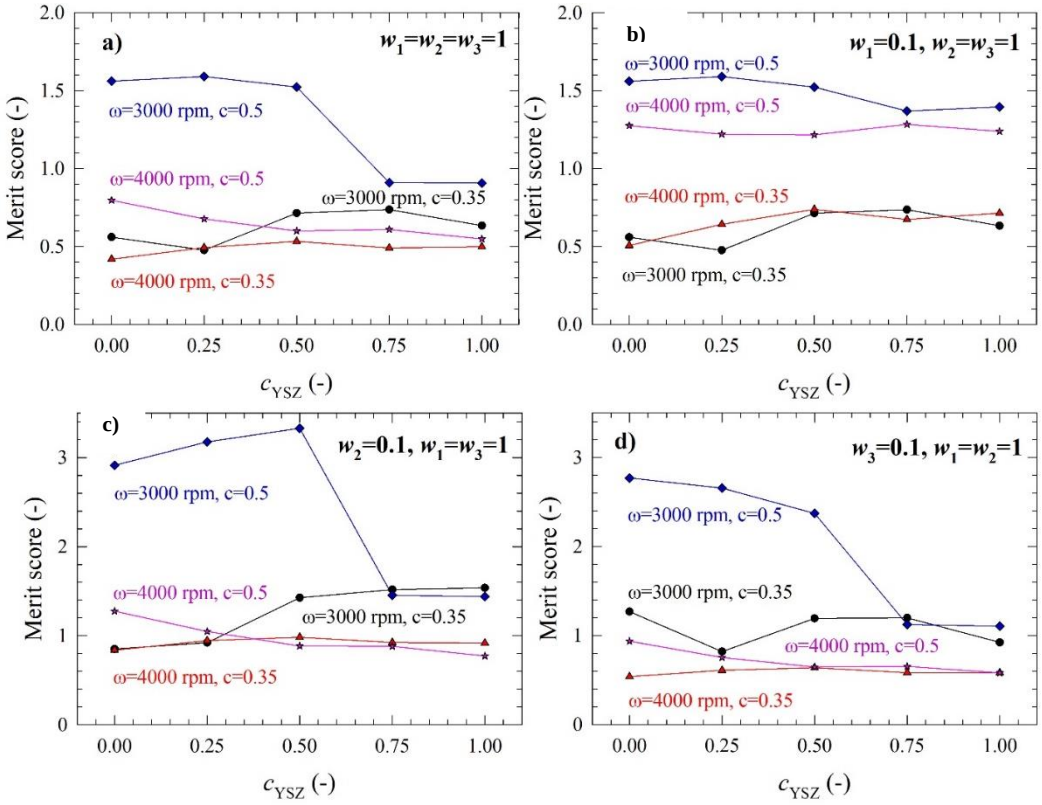

Figure 7.10 Effects of YSZ loading (volume fraction in the CPS–YSZ bead mixture) c_{YSZ}, the stirrer speed ω, and the bead loading c on the merit score for various weights: (a) $w_1 = w_2 = w_3 = 1$, (b) $w_1 = 0.1$, $w_2 = w_3 = 1$, (c) $w_2 = 0.1$, $w_1 = w_3 = 1$, and d) $w_3 = 0.1$, $w_1 = w_2 = 1$.

In general, an ideal WSMM process should produce a targeted drug particle size at the shortest cycle time with the lowest energy expenditure without serious heat dissipation–temperature rise/control issues. Hence, we defined a merit score, Equation (7.4), to guide our optimal process selection. We considered three major factors: heat dissipation related issues, energy expenditure (cost), and cycle time, and created four different scenarios with different values of the weighting coefficients w1, w2, and w3 in the merit score calculation. A higher merit score indicates that the operating parameters and bead mixtures selected are more desirable within the context of specific process optimization criteria considered. **Figures 7.10a, b, c**, and **d**, respectively, correspond to a base-case scenario wherein all three factors contribute to the merit score equally (w1 = w2 = w3 = 1), a scenario wherein heat dissipation related process shutdowns as related to P_w are partly mitigated by a high-capacity chiller (reduced w_1, $w_1 = 0.1$), a scenario wherein energy expenditure is considered less significant compared to cycle time and temperature related process shutdowns (most likely scenario in pharmaceutical industry as compared with other industries, reduced w_2: $w_2 = 0.1$), and a scenario wherein milling cycle time is considered less important than other two factors (reduced w_3, $w_3 = 0.1$). Based on the merit scores, a decision tree for the selection of optimal bead mixtures was developed and presented in **Figure 7.11**.

As can be seen from **Figures 7.10** and **7.11**, in many scenarios, bead mixtures as opposed to single type of beads should be selected for optimal performance.

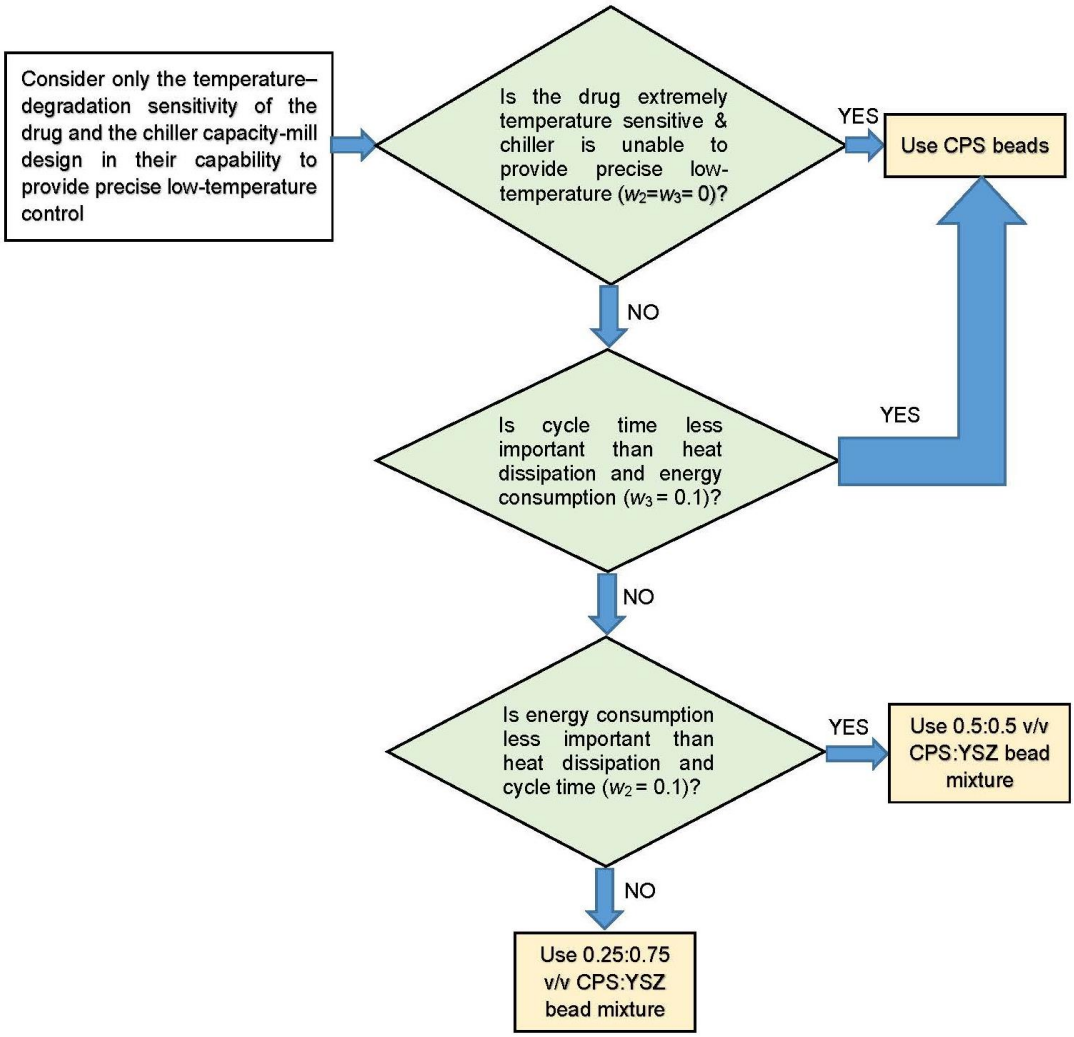

Figure 7.11 A decision tree for the selection of bead mixtures constructed based on merit scores for various scenarios. Unless otherwise indicated, the weighting coefficients used in the merit score calculations are $w_1 = w_2 = w_3 = 1$.

7.3 Conclusions

In wet media milling of FNB, the YSZ beads were more favorable than the CPS beads when faster breakage and shorter milling cycle time were desired, whereas the CPS beads were superior to the YSZ beads in terms of reduced power consumption and reduced likelihood of process shutdowns stemming from high heat dissipation and temperature rise. The microhydrodynamic model attributed the faster breakage with the YSZ beads compared to the CPS beads to their more frequent, energetic/forceful collisions than those

of CPS beads owing to the higher density–elastic modulus of the YSZ beads. Mixtures of two different bead types, YSZ and CPS, achieved optimal wet stirred media milling (WSMM) when three factors, i.e., specific energy consumption (cost), milling cycle time (breakage kinetics), and heat dissipation related process shutdowns were simultaneously considered. In 9 out of 16 total cases examined (4 different processes with various ω–c in 4 different scenarios), a bead mixture had the highest merit score as compared to CPS or YSZ beads alone. A decision tree was developed based on various scenarios with different relative importance of the three factors. CPS alone is optimal when cycle time is considered less significant than the other two factors or when a drug with extreme sensitivity to temperature rise during the milling is considered. Obviously, these scenarios are rather unlikely. In the most likely pharmaceutical manufacturing scenario wherein specific energy consumption is less significant than the other two factors, 0.5:0.5 v/v CPS:YSZ is optimal. When all factors are equally important or the heat dissipation originated shutdowns are considered less significant, the 0.25:0.75 CPS:YSZ bead mixture is optimal. Stable fenofibrate nanosuspensions were prepared under all processing conditions; yet, the overall optimal process conditions were found to be 3000 rpm and 50% loading of 0.5:0.5 v/v CPS:YSZ.

CHAPTER 8

DO MIXTURES OF BEADS WITH DIFFERENT SIZES IMPROVE WET STIRRED MEDIA MILLING OF DRUG SUSPENSIONS?

The aim of this study is to investigate the impacts of bead sizes and their mixtures under various stirrer speeds and bead loadings on breakage kinetics, the number of milling cycles applied to prevent overheating, and power consumption during the nanomilling of drug (griseofulvin) suspensions. To this end, narrowly sized zirconia beads with 100, 200, and 400 μm nominal sizes and their half-and-half binary mixtures were investigated at two stirrer speeds and two bead loadings. Particle size evolution was measured during the 3 h milling experiments using laser diffraction, and the number of milling cycles were recorded along with the power consumption. An *n*th-order breakage model was fitted to the experimental median particle size evolution, and various microhydrodynamic parameters were calculated. In general, the beads and bead mixtures with smaller median sizes tend to achieve faster breakage. While the microhydrodynamic model highlighted counteracting effects of bead size, it has limited applicability to the bead mixtures. For additional test runs performed, the kinetics model augmented with a decision tree model using process parameters outperformed that augmented with an elastic-net regression model using the microhydrodynamic parameters. Based on a proposed process merit score, the use of bead mixtures did not lead to notable process improvement; 100 μm beads outperformed bead mixtures and coarser beads in terms of fast breakage, low power consumption, and low intermittent milling cycles, albeit the clogging issue prevalent especially at the lowest energetic conditions.

8.1 Materials and Methods

8.1.1 Materials

BP/EP grade micronized griseofulvin (GF) was purchased from Letco Medical (Decatur, AL, USA). GF is a BCS Class II drug and has a solubility of 14.2 mg/L at 37 °C [212]. Hydroxypropyl cellulose (HPC, L grade, Nisso America Inc, New York, NY, USA) was used as a non-ionic polymeric stabilizer, and sodium dodecyl sulfate (SDS, ACS grade, GFS chemicals, Columbus, OH, USA) was used as an anionic surfactant. Zirmil Y grade yttrium-stabilized zirconia (YSZ) beads (Saint Gobain ZirPro, Mountainside, NJ, USA) with 6000 kg/m^3 density and 100, 200 and 400 µm nominal sizes were used. Their actual median sizes were 112, 194, and 403 µm, respectively, as measured by a laser diffraction particle size analyzer in the dry mode of dispersion (Helos/Rodos, Sympatec, NJ, USA). As can be seen from **Table 8.1**, these beads had a relatively narrow distribution with span values well below 1. In this Chapter, we refer to these beads received from the supplier as narrowly-sized beads to distinguish them from their binary mixtures which had wider distributions. The actual median sizes were used in microhydrodynamic calculations.

Table 8.1 Characteristic Sizes d_{10}, d_{50}, and d_{90} of the As-received Beads and Their Spans

Nominal size (µm)	d_{10} (µm)	d_{50} (µm)	d_{90} (µm)	Span[a]
100	87	112	145	0.524
200	140	194	263	0.633
400	293	405	560	0.659

[a]span $= (d_{90} - d_{10})/d_{50}$.

8.1.2 Experimental methods

A suspension of GF, HPC-L, and SDS was prepared using a shear mixer (Cat.# 14-503, Fisher Scientific, Pittsburgh, PA, USA) at 300 rpm for 2 h. The formulation was selected

as 10% GF, 7.5% HPC-L, and 0.05% SDS based on our prior investigations [90, 150]. The pre-suspensions were stored overnight at 8 °C after preparation and before milling. Microcer wet stirred media mill (Netzsch Fine Particle Size Technology, LLC, Exton, PA, USA) was operated for 3 h with the parameters presented in **Table 8.2**, where the stirrer speed ω, bead loading c, and the mass fraction of the beads with 100, 200, and 400 μm nominal bead sizes, i.e., (x_{100}–x_{200}–x_{400}), were varied.

Table 8.2 Process Conditions Used for Milling Including the Mass % of 100–200–400 μm Beads

Run no.	Stirrer speed (rpm)	Bead loading (-)	x_{100} (%)[a]	x_{200} (%)[a]	x_{400} (%)[a]
1	3000	0.35	100	0	0
2	3000	0.35	50	50	0
3	3000	0.35	0	100	0
4	3000	0.35	50	0	50
5	3000	0.35	0	50	50
6	3000	0.35	0	0	100
7	3000	0.50	100	0	0
8	3000	0.50	50	50	0
9	3000	0.50	0	100	0
10	3000	0.50	50	0	50
11	3000	0.50	0	50	50
12	3000	0.50	0	0	100
13	4000	0.35	100	0	0
14	4000	0.35	50	50	0
15	4000	0.35	0	100	0
16	4000	0.35	50	0	50
17	4000	0.35	0	50	50
18	4000	0.35	0	0	100
19	4000	0.50	100	0	0
20	4000	0.50	50	50	0
21	4000	0.50	0	100	0
22	4000	0.50	50	0	50
23	4000	0.50	0	50	50
24	4000	0.50	0	0	100
T1[b]	3500	0.43	100	0	0
T2[b]	3500	0.43	0	100	0
T3[b]	3500	0.43	0	0	100
T4[b]	2500	0.30	33	33	33

[a]Mass percentage. [b]Test runs that were used to evaluate the prediction capability of the models.

The bead loading was calculated as the ratio of the true volume of the beads over the mill chamber volume V_m = 80 ml (*v/v*), which is filled by the recirculating drug suspension. A

peristaltic pump (Cole-Palmer, Master Flex, Vermont Hills, IL, USA) recirculated the suspension between the holding tank and the milling chamber at a volumetric flow rate Q of 126 ml/min. Stainless-steel screen that has half size of the smallest nominal bead size used in the mixtures was used to keep the beads in the milling chamber. The setup was cooled with the help of a chiller (Model M1-.25A-11HFX, Advantage Engineering, Greenwood, IN, USA) to keep the temperature under control; additional intermitting milling cycles were applied when/if the temperature reached 35 ^{o}C [149, 150]. The number of milling cycles were recorded during the experiments, which was also used in the process merit score calculation. The average power consumption P was determined by dividing the cumulative energy consumption read from the control panel of the mill by the milling time. The average stirrer power per unit volume P_w was calculated for all runs by $P_w = P/V_m$. The power consumption during the stirring of the suspension in the absence of the beads ε_{ht} was found by the same method. The power consumption when there was no material in the mill (no-load) was obtained and subtracted during the calculation of P_w and ε_{ht}.

Particle size distribution (PSD) of the drug suspensions at various milling times was determined by laser diffraction using LS 13-320 Beckman Coulter instrument (Brea, CA, USA). The samples were taken from the mill outlet, where the temperature was measured, at certain time intervals (2^s, s = 0, 1, 2,...7) with the addition of 40 s, 24 min, 48 min, 96 min, 128 min and 180 mins. The final sample was taken from the holding tank and all samples were measured with laser diffraction [89]. Before each measurement, a ~2.0 mL suspension sample was diluted with 5.0 mL of the respective stabilizer solution using a vortex mixer (Fisher Scientific Digital Vortex Mixer, Model No: 945415, Pittsburgh, PA) at 1500 rpm for a min. During measurements, polarized intensity differential scattering

(PIDS) was maintained between 40% and 50% while the obscuration was maintained below 8%. PSD was provided by the software which used the Mie scattering theory. The refractive indices of GF and water were taken as 1.65 and 1.33, respectively. Measurements were repeated four times and the average and standard deviation (SD) of these measurements were determined.

The apparent shear viscosities μ_L of the milled suspensions were measured using R/S plus rheometer (Brookfield Engineering, Middleboro, MS, USA) with a water jacket assembly Lauda Eco (Lauda-Brinkmann LP, Delran, NJ, USA). A CC40 coaxial cylinder with a jacketed setup was used to impart a controlled shear rate on the samples from 0 to 1000 1/s in 60 s. The jacket temperature was kept constant at 25 ± 0.5 °C. The raw data were analyzed using the Rheo3000 software and the apparent shear viscosity at the maximum shear rate was taken. The density of the milled suspension was measured by weighing 35 ml of the milled suspension and dividing the mass of the suspension by its volume. The measurements were performed thrice and the average value was reported.

8.1.3 Modeling methods

Microhydrodynamic model with Lun RDF has been utilized here, as described in previous chapters. Since a different drug was used here, Young modulus of the drug particles and Poisson's ratio of the drug particles were taken from ref. [139] as 11.5 GPa and 0.3. And the volume fraction of the drug particles in the suspension was calculated as 0.061.

The following *n*th-order breakage kinetics model derived by Guner et al. [150] were used to fit the experimental median particle sizes:

$$d_{50}(t) = d_{\lim} + \left[\left(d_{50,0} - d_{\lim}\right)^{1-n} - (1-n)kt\right]^{1/(1-n)} \tag{8.1}$$

wherein $d_{50,0}$ is the initial median size, d_{lim} is the limiting median size, and k is the breakage rate constant. Marquardt–Levenberg optimization algorithm in Sigmaplot (Version 12.5) was used to fit the log-transformed experimental median sizes at various time points by Equation (8.1), and d_{lim}, n, and k were estimated. In the fitting, a constraint was placed on the limiting particle size, which should be smaller than the final median particle size [90].

A relationship between the estimated parameters of the nth-order model (k, n, d_{lim}) and the calculated microhydrodynamic parameters (σ_b^{max}, α_b, a, and $\Pi\sigma_y$) and process parameters (ω, c, x_{100}-x_{200}-x_{400}) were sought using machine learning algorithms. Google Colab was used for this analysis, where sklearn package of Python was utilized. Most of the models used were capable of doing regression for all responses at the same time and provided the total of root mean squared errors of all responses. On the other hand, gradient boosting was not suitable for doing regression to multiple responses, so MultiOutputRegressor command which consists of fitting one regression per response was used and total RMSE was reported as well. For the model selection, the models are calibrated using the training set which consists of 24 experiments with full factorial DOE and they were tested using four test runs where the first three were operated at the average conditions of the design space with individual bead sizes and the last test run is in the extrapolated region where a lower stirrer speed and bead loading was used with 1/3rd mixture of all bead sizes. Leave-one-out cross validation was used in the training set to gain an overall idea about the prediction capability of the models and RMSEs were reported. Finally, the models were selected as the ones that give the lowest test RMSE. Please note that experimental data (power and viscosity) were used to estimate the microhydrodynamic parameters, which are the predictors in the test set for

microhydrodynamic-based prediction.

In order to rank-order the performance of the WSMM process with different milling conditions and assess the impact of bead mixtures vs. nominal single-sized beads, a merit score was defined similarly to refs. [90, 149]. In the merit score, normalized values of inversed breakage rate constant $1/k$ (as a rough measure of cycle time), the power P, and number of intermittent milling cycles N_{mc} were used as follows:

$$\overline{1/k} = (1/k - 1/k_{\min})/(1/k_{\max} - 1/k_{\min}) \tag{8.2}$$

$$\bar{P} = (P - P_{\min})/(P_{\max} - P_{\min}) \tag{8.3}$$

$$\overline{N_{mc}} = (N_{mc} - N_{mc,\min})/(N_{mc,\max} - N_{mc,\min}) \tag{8.4}$$

$$Merit\ Score = \frac{100}{10^{(\overline{1/k} + \bar{P} + \overline{N_{mc}})/3}} \tag{8.5}$$

8.2 Results and Discussion

8.2.1 Breakage kinetics and power consumption

Figure 8.1 shows the time-wise evolution of the median particle size where each subfigure is for a stirrer speed–bead loading pair and each curve in each subfigure is for a different bead size (narrowly-sized beads and binary bead mixtures). The percentages of the three narrowly-sized beads in the bead mixture are given in the legend. Just for the sake of representation, the nominal bead sizes and their averages are indicated in the figures and the text, while the actual median bead sizes from the laser diffraction (refer to Table 8.1) were used for the microhydrodynamic calculations. In this context, the average sizes in the bead mixtures were calculated as 100, 150, 200, 250, 300, 400 μm for the 100–0–0, 50–50–0, 0–100–0, 50–0–50, 0–50–50, and 0–0–100 mass fractions of the 100, 200, and

400μm narrowly-sized beads, respectively, which are shown from top to bottom in legends.

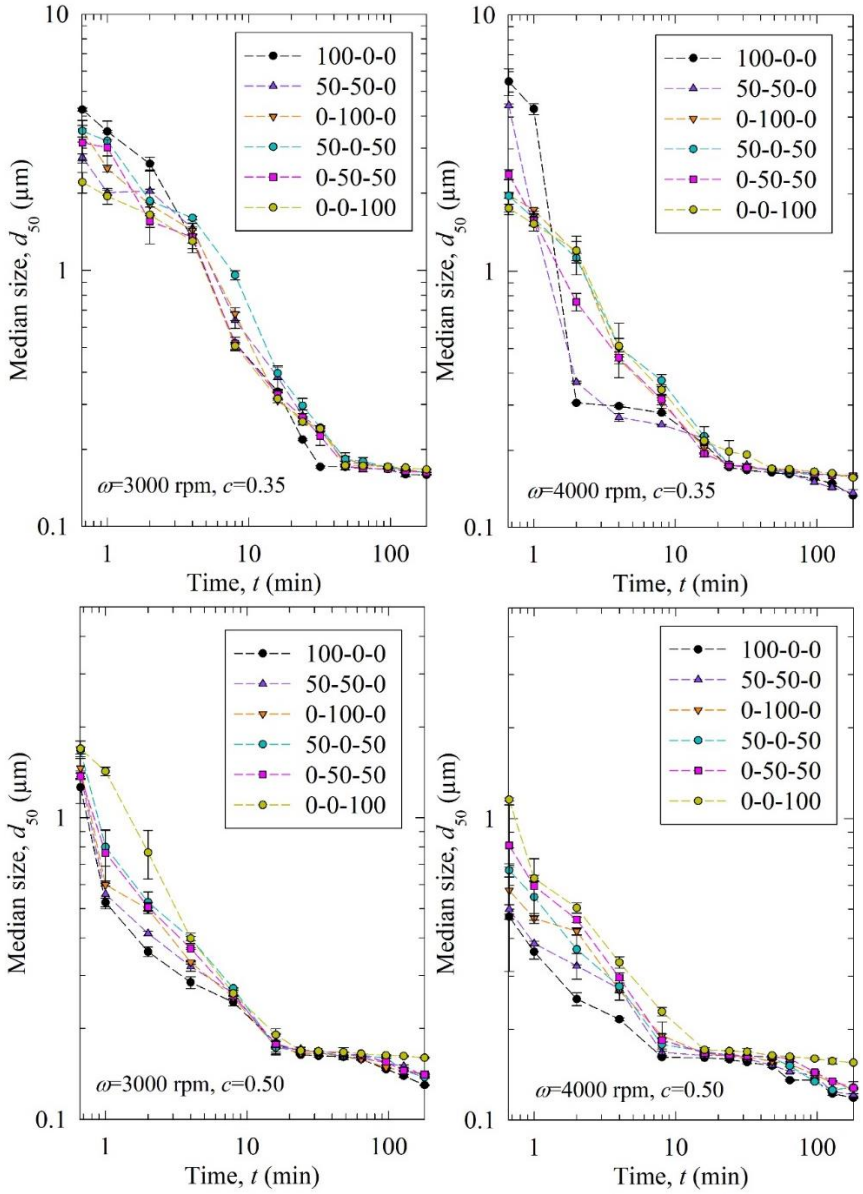

Figure 8.1 Timewise evolution of the median drug particle size d_{50} during 180 min of milling with various mass fractions of 100–200–400 μm beads at different stirrer speeds ω–bead loadings c.

The feed GF particles had the characteristics sizes of d_{10} = 4.30 μm, d_{50} = 11.4 μm, and d_{90} = 23.5 μm, while the GF particles had a median size below 200 nm upon 3 h milling at all process conditions studied, signifying the drastic size reduction during the WSMM process. A general observation from **Figure 8.1** is that the decrease in the median size of

the drug particles was monotonic and the median size approached a limiting particle size in all process conditions. As the stirrer speed and the bead loading increased, the apparent breakage rate increased as indicated by the smaller median size after a certain milling time.

When the breakage rates of different bead sizes and their mixtures are compared, we note that usually the smaller the beads, the more rapid the breakage. While the separation of the profiles is not as clear at the lowest energetic condition (Runs 1–6: 3000 rpm, 0.35), the profiles are more distinguishable at the higher energetic conditions. The reason for that is at the low stirrer speed and bead loading, the small beads (100 μm) could not nip the coarse drug particles initially present effectively, which caused an operational problem, i.e., clogging of the mill screen. Regardless, upon further milling, drug particles became smaller; 100 μm beads caught up quickly and provided even faster breakage towards the end of 3 h milling, as compared with coarser beads (400 μm). For other stirrer speed bead–loading combinations, especially at 0.5 bead loading cases, and as the average bead size increased, a slower breakage was observed throughout the milling. There is no evidence for a synergistic effect of the combination of beads with different sizes in binary mixtures on the breakage kinetics when the binary bead mixtures were compared to narrowly-sized beads with nominal sizes of 100, 200, and 400 μm. The profiles of the median size evolution of the bead mixtures approximately fell within the profiles of individual bead sizes. This finding is in agreement with previous studies on wet and dry stirred media milling [167, 168]. No clogging was observed for the 200 and 400 μm beads under any process conditions. The binary mixtures of 100 μm beads with 200 or 400 μm beads and the narrowly-sized 100 μm beads at the higher energetic conditions exhibited a less severe clogging issue (shorter duration) as compared with the narrowly-sized 100 μm

beads in Run 1.

As the profiles of the median size evolution are close to each other, the differences may be hard to discern between the 6 curves for the different bead sizes/mixtures. Therefore, we fitted the *n*th-order breakage model and compared the breakage rate constants. The fitted parameters and statistics are presented in **Table 8.3**. Overall, the fits were successful with the average adjusted R^2 of 0.97, and only one run had it below 0.90: 0.87 in Run 13. The average and standard deviation of d_{lim} were found to be 0.125 ± 0.026. The average *n* was found to be ~2 similar to previous studies [149, 150], but with a higher standard deviation of 0.36. The difference might be due to the usage of different bead sizes/mixtures and drug in this study. Besides, usage of bead mixtures could be causing a different order of breakage kinetics from two because coarser beads could be more effective in breaking only the coarse drug particles initially present (typically about >10 µm), whereas small beads are more effective for breaking all particles below 5 µm, especially those in the colloidal size domain. This argument is based on the notion of an optimal bead size:feed particle size ratio of 20:1, recommended for WSMM of hard materials like quartz [213], as well as the median sizes of the feed GF particles and the narrowly-sized beads.

Figure 8.2 presents the impact of process conditions on the breakage rate constant *k* and a characteristic time for the median size to reach 0.2 µm t_{d50}. A higher *k* value and a lower t_{d50} value is an indication of faster breakage and they trends are usually opposite to each other.

Table 8.3 Statistics of the *n*th-order Breakage Model Fits

Run identifier	k (μm^{1-n}/min)	n (-)	d_{lim} (μm)	R^2	Adj R^2	SSR
3000 0.35 100-0-0	0.292	1.62	0.148	0.992	0.991	0.066
3000 0.35 50-50-0	0.191	2.25	0.083	0.965	0.958	0.263
3000 0.35 0-100-0	0.214	2.07	0.107	0.978	0.974	0.167
3000 0.35 50-0-50	0.116	2.26	0.048	0.960	0.953	0.310
3000 0.35 0-50-50	0.248	2.01	0.117	0.976	0.972	0.183
3000 0.35 0-0-100	0.210	2.37	0.076	0.954	0.946	0.343
3000 0.50 100-0-0	1.54	1.89	0.130	0.969	0.964	0.189
3000 0.50 50-50-0	1.46	1.91	0.139	0.968	0.962	0.184
3000 0.50 0-100-0	1.39	1.92	0.142	0.973	0.968	0.158
3000 0.50 50-0-50	1.18	2.01	0.138	0.980	0.976	0.123
3000 0.50 0-50-50	1.28	1.99	0.141	0.990	0.988	0.062
3000 0.50 0-0-100	0.85	1.85	0.150	0.996	0.995	0.027
4000 0.35 100-0-0	1.22	1.18	0.133	0.890	0.870	0.777
4000 0.35 50-50-0	1.17	1.27	0.136	0.938	0.927	0.427
4000 0.35 0-100-0	0.571	1.88	0.140	0.981	0.977	0.149
4000 0.35 50-0-50	0.511	2.01	0.130	0.986	0.983	0.109
4000 0.35 0-50-50	0.808	1.76	0.156	0.997	0.997	0.018
4000 0.35 0-0-100	0.497	2.10	0.127	0.976	0.971	0.181
4000 0.50 100-0-0	5.10	2.46	0.119	0.996	0.995	0.014
4000 0.50 50-50-0	4.65	2.71	0.113	0.995	0.994	0.018
4000 0.50 0-100-0	3.08	2.64	0.114	0.994	0.992	0.025
4000 0.50 50-0-50	2.42	2.28	0.126	0.997	0.996	0.013
4000 0.50 0-50-50	1.87	2.23	0.128	0.995	0.994	0.024
4000 0.50 0-0-100	1.53	1.92	0.153	0.990	0.989	0.063

While there are some deviations from the general trends for 0.35 bead loading cases, in general, the data presented in **Figure 8.2** and **Table 8.3** suggest that (i) higher k and lower t_{d50} occurred at the higher stirrer speed and/or higher bead loading, (ii) k decreased and t_{d50} increased when the average size of the beads was increased, and (iii) the stirrer speed and the bead loading had a stronger impact on the breakage kinetics than the bead size. The slopes were the steepest for 4000 rpm, 0.5 bead loading case, where the k for the smallest beads was 3.3 fold of the k of the largest beads. The 100 μm beads alone outperformed coarser beads and the bead mixtures in terms of faster kinetics although

clogging of the screen during the initial phase of the milling was noted with these beads.

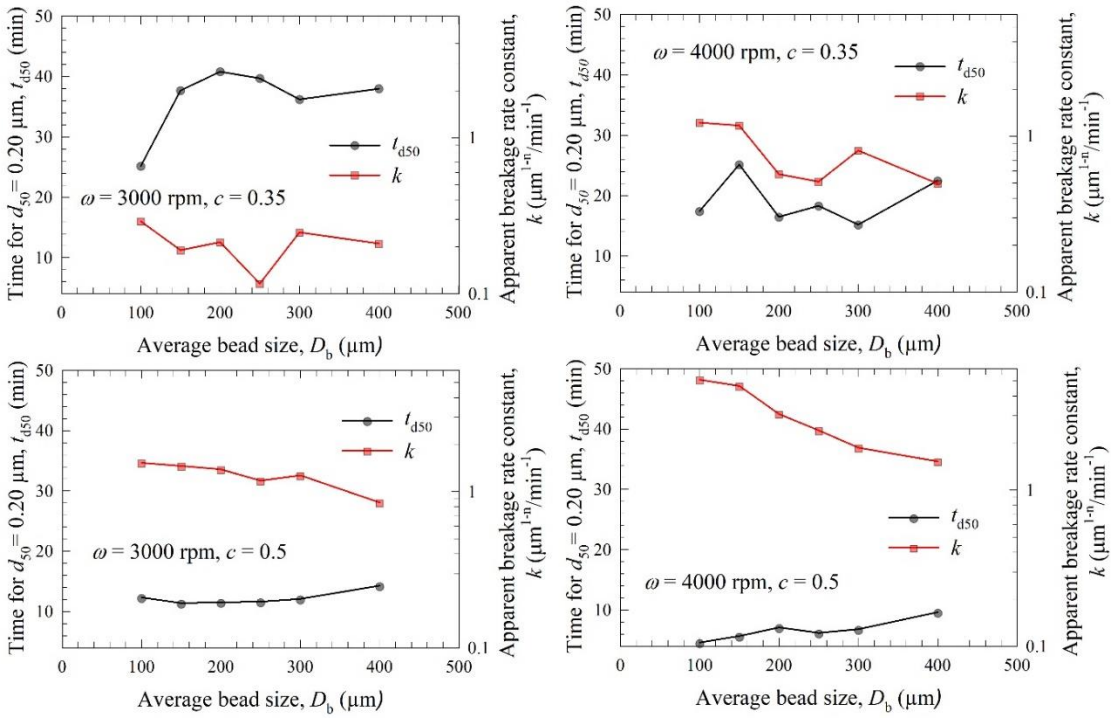

Figure 8.2 Impact of the average bead size on the breakage rate constant k and the time needed for the median particle size to reach 0.20 µm t_{d50} for various stirrer speeds ω–bead loadings c. Average bead sizes of 150, 250, and 300 µm correspond to 50%–50% w/w mixtures of 100–200 µm, 100–400, and 200–400 µm beads, respectively.

The impact of process conditions on the power consumption during milling and the apparent shear viscosity of the milled suspensions is illustrated in **Figure 8.3**. While the values are significantly different in each subfigure, the curves are rather flat showing the bead size impact is not as influential as the stirrer speed and the bead loading. Still, coarser beads (200 and 400 µm) require more power to operate, which makes smaller beads even more advantageous if power consumption is a concern. This increase in the power with increasing stirrer speed, bead loading, and bead size was also reflected in the number of milling cycles N_{mc} as can be seen in **Table G.2** in the *Appendix G*. Numerous cycles had to be applied especially at 4000 rpm runs, which were more frequent compared to prior heat transfer study [166], due to prolonged milling time and lower value of maximum

temperature allowed in this study: 45 °C in [166] vs. 35 °C here.

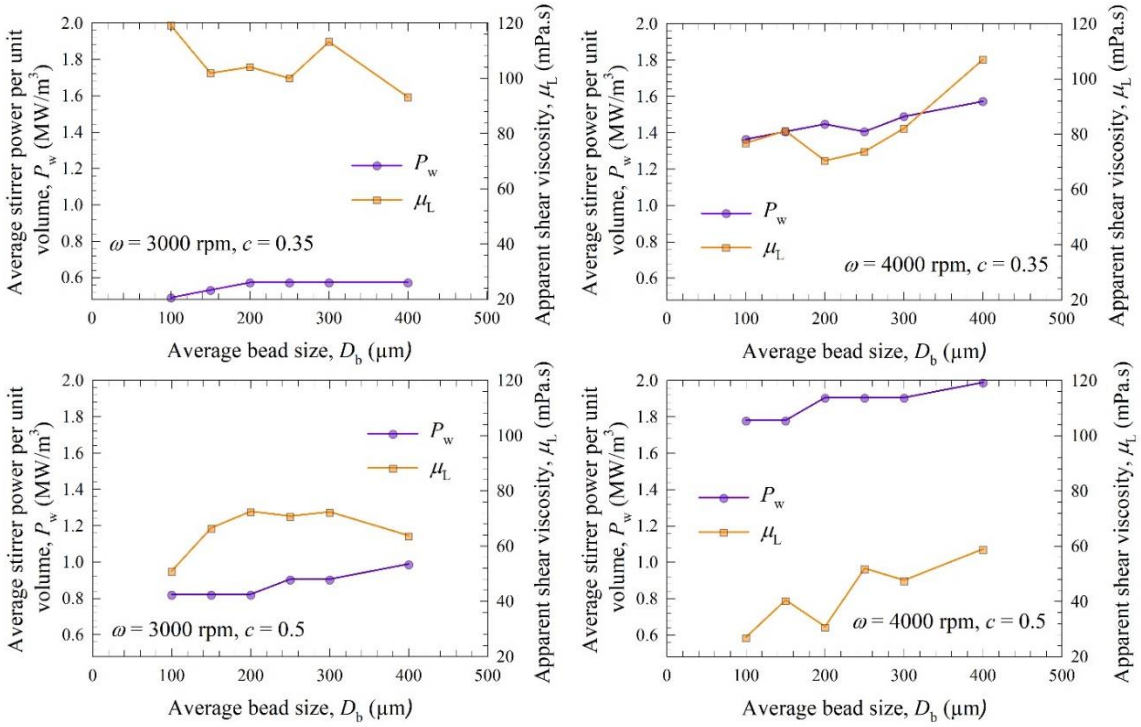

Figure 8.3 Impact of the average bead size on the average power consumption and the apparent shear viscosity of the milled suspension for each ω–c pair. Average bead sizes of 150, 250, and 300 μm correspond to 50%–50% w/w mixtures of 100–200 μm, 100–400, and 200–400 μm beads, respectively.

These findings are not surprising as Guner et al. [166, 206] established that heat generation and ensuing temperature rise during the WSMM is positively and strongly correlated with the power consumption. Shutting down a mill for cooling without milling (N_{mc} > 1) is undesirable for pilot and commercial scale operations. However, this intermittent milling is unavoidable if one ones to keep the temperature under control in small scale milling equipment at highly energetic processing conditions expolored here. The main reason for this is the inadequate bulk convective cooling provided by the recirculating suspension as the thermal inertia of the suspension batch placed in the holding tank of a small-scale mill is orders of magnitude smaller than that in the pilot–commercial scale equipment. Of course, relatively low cooling capacity of the particular chiller of our

mill could partly contribute to the need for intermittent milling. **Figure 8.3** also shows that similar to power, viscosity of the milled suspensions was lower when smaller beads were used. Besides, it decreased with higher bead loading and stirrer speed, as the smaller drug particles in the suspensions led to lower viscosity [88].

8.2.2 Microhydrodynamic basis of the impact of the processing conditions

The microhydrodynamic model was formulated with the major assumption that the beads are spherical and monodispersed. [34, 132]. Although the as-received beads with nominal sizes of 100, 200, and 400 μm have a relatively narrow distribution (refer to **Table 8.1**), the bead mixtures automatically have much wider distributions due to 50%–50% combination of the respective bead sizes. Hence, the microhydrodynamic model is expected to be more accurate for the narrowly-sized beads than for the bead mixtures. To correlate the breakage rate to the microhydrodynamic parameters for the case of bead mixtures, the average of the median bead sizes of the relevant narrowly-sized beads in the 50%–50% binary mixtures were used in the calculations, as a crude first approximation. All microhydrodynamic parameters are reported in **Table G.1** in *Appendix G*.

Figures 8.4–8.7 show the change in each microhydrodynamic parameter with increasing average bead size, where each figure is for a given stirrer speed–bead loading pair. Since the assumption of the usage of a single average bead size for the bead mixtures is not validated yet, runs with bead mixtures are shown separately in the figures. The microhydrodynamic trends for the impacts of bead size are very similar to those observed in Li et al. [33]. On one hand, the fluctuating motion of the smaller beads was less vigorous, as signified by the lower granular temperature θ (see also **Table G.1** in *Appendix G*). This effect can be explained by the lower applied power P_w (see **Figure 8.3**) and the higher bead

number concentration. The slower fluctuating motion of the smaller beads was also reflected in the lower average bead oscillation velocity u_b, which led to the development of a lower maximum contact pressure σ_b^{max}, i.e., lower stress intensity. Up to this point, one may argue that the drug particle breakage would be slower with the use of smaller beads as the aforementioned changes in the microhydrodynamic parameters do not favor particle breakage. On the other hand, while the frequency of bead oscillations v is somewhat similar for 3000 rpm runs (**Figures 8.4** and **8.5**), it increased when smaller beads were used, at 4000 rpm runs (**Figures 8.6** and **8.7**). Moreover, while the average frequency of drug particle compressions a is similar for all bead sizes in the lowest energetic case (**Figure 8.4**), it was higher for the smaller beads in the 3000 rpm 0.5 bead loading case (**Figure 8.5**) and the difference became more pronounced at 4000 rpm runs. This effect of the smaller beads, especially on a, favors faster breakage. In addition, the radius of contact circle was greater for the bigger beads. The pseudo energy dissipation rate was higher for the bigger beads, except for the highest energetic condition (**Figure 8.7**) as a result of contrary trends in stress intensity (σ_b^{max})–stress frequency (a). Overall, these microhydrodynamic parameters suggest that smaller beads lead to more frequent bead–bead collisions with lower stress intensity, and a seems to be the most impactful microhydrodynamic parameter on the observed breakage kinetics as it indicates smaller beads are advantageous for faster breakage. It can also explain why the difference in the performance of the different bead sizes is very small in the 3000 rpm 0.35 run (refer to **Figures 8.1** and **8.2**) because a values are very close to each other. It should be noted that for soft, brittle materials like most drugs, the stress frequency as signified by a is expected to be more important than the stress intensity as signified by σ_b^{max} provided the stress

intensity is sufficiently high.

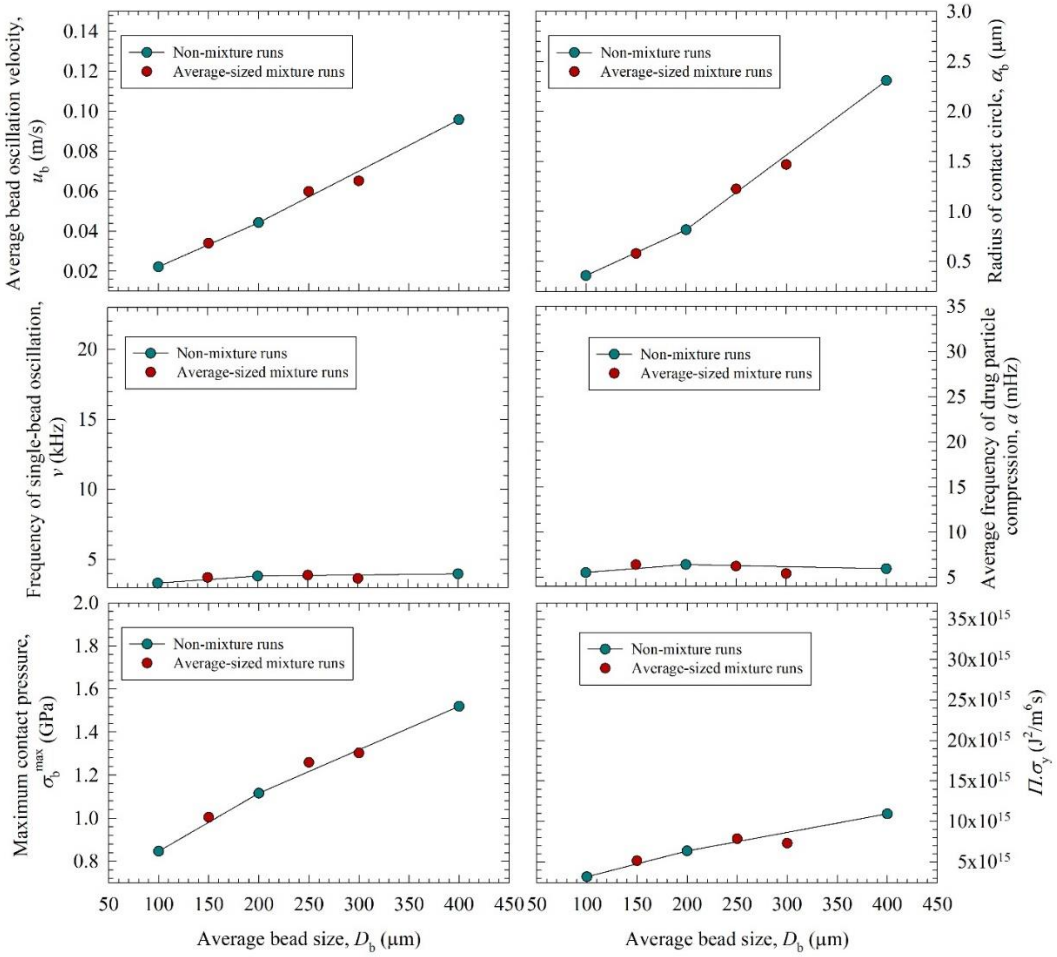

Figure 8.4 Impact of average bead size on the microhydrodynamic parameters when the stirrer speed was 3000 rpm, and the bead loading was 0.35. Average bead sizes of 150, 250, and 300 μm correspond to 50%–50% w/w mixtures of 100–200 μm, 100–400, and 200–400 μm beads, respectively.

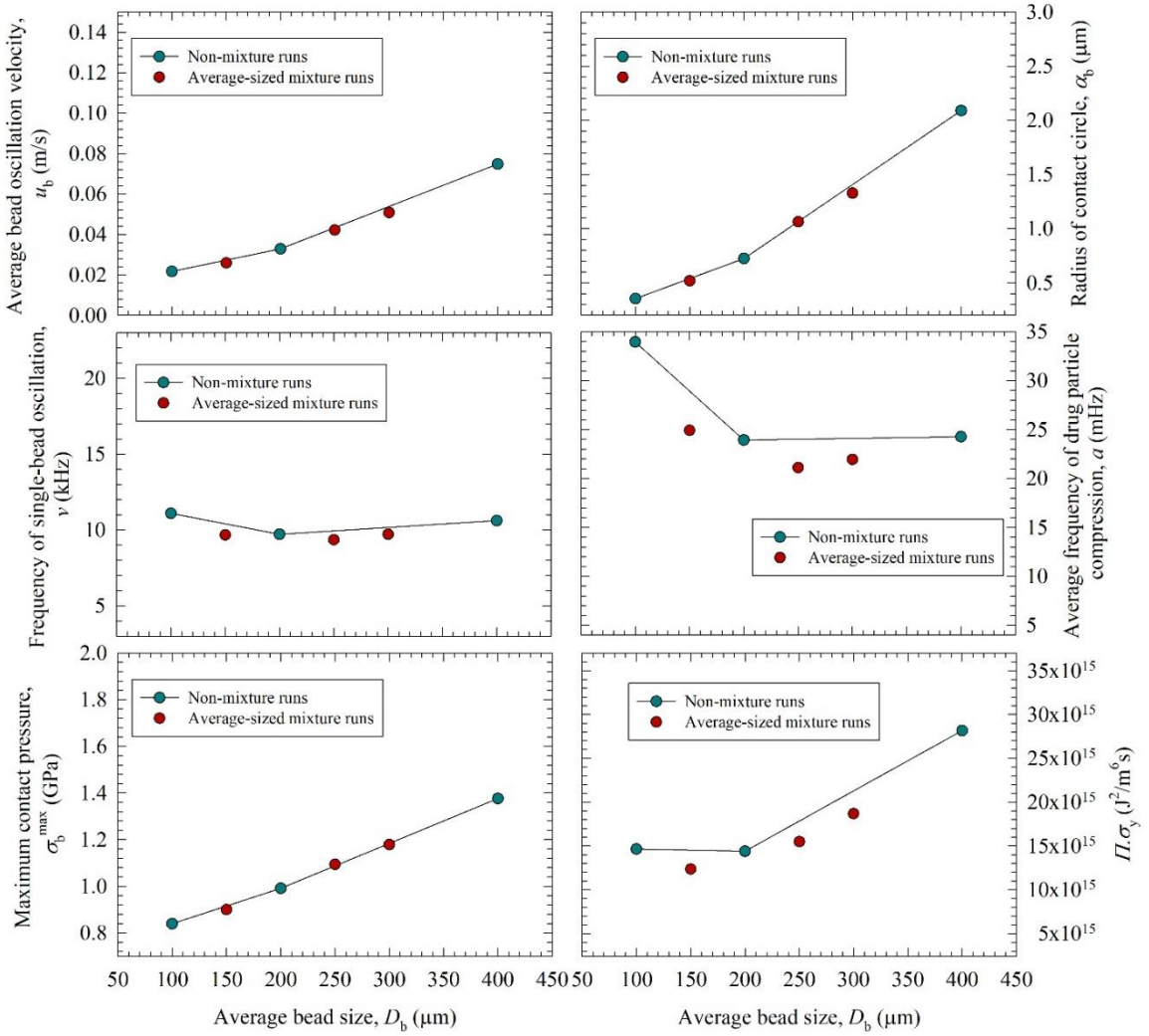

Figure 8.5 Impact of average bead size on the microhydrodynamic parameters when the stirrer speed was 3000 rpm, and the bead loading was 0.50. Average bead sizes of 150, 250, and 300 μm correspond to 50%–50% w/w mixtures of 100–200 μm, 100–400, and 200–400 μm beads, respectively.

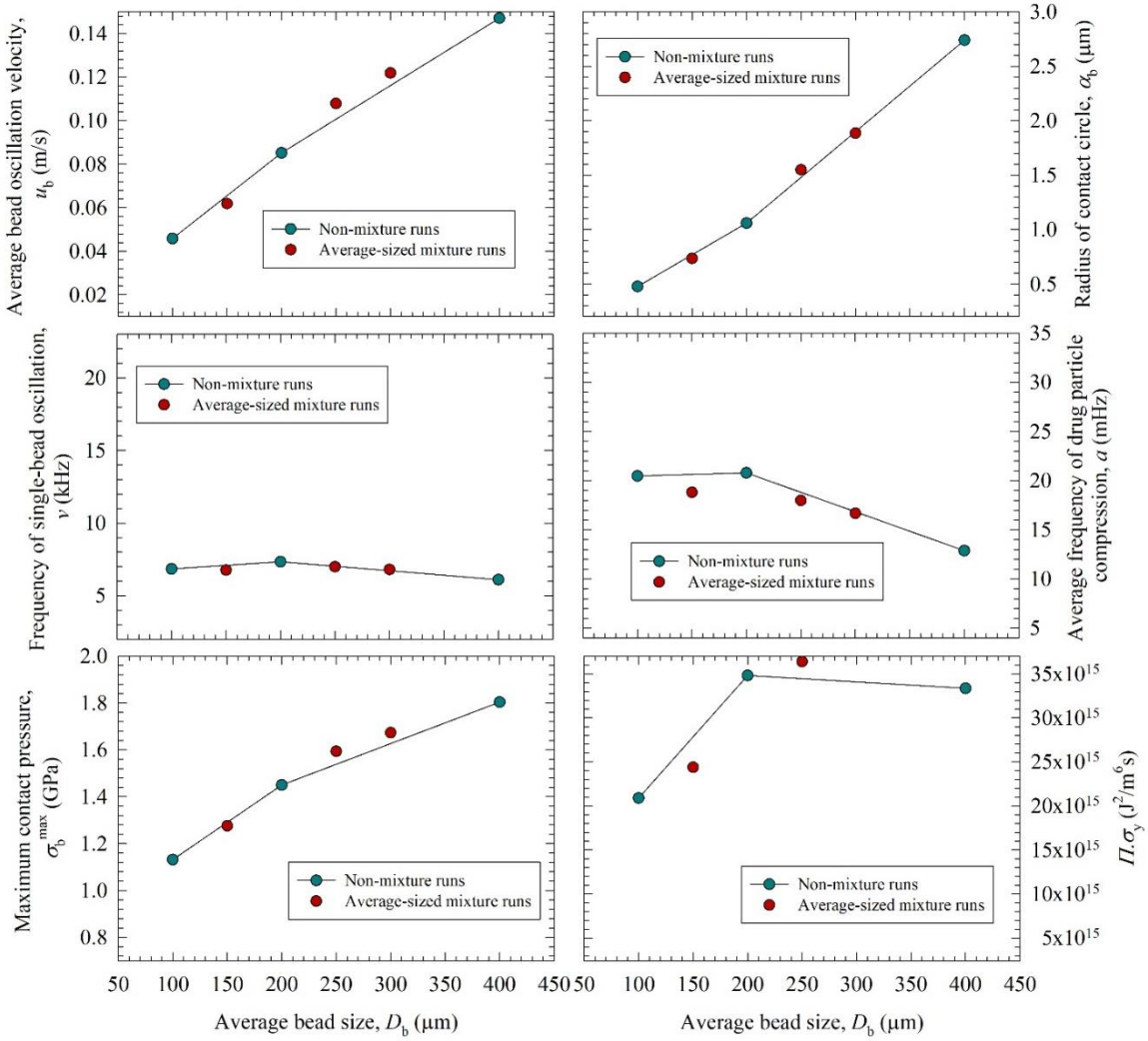

Figure 8.6 Impact of average bead size on the microhydrodynamic parameters when the stirrer speed was 4000 rpm, and the bead loading was 0.35. Average bead sizes of 150, 250, and 300 μm correspond to 50%–50% w/w mixtures of 100–200 μm, 100–400, and 200–400 μm beads, respectively.

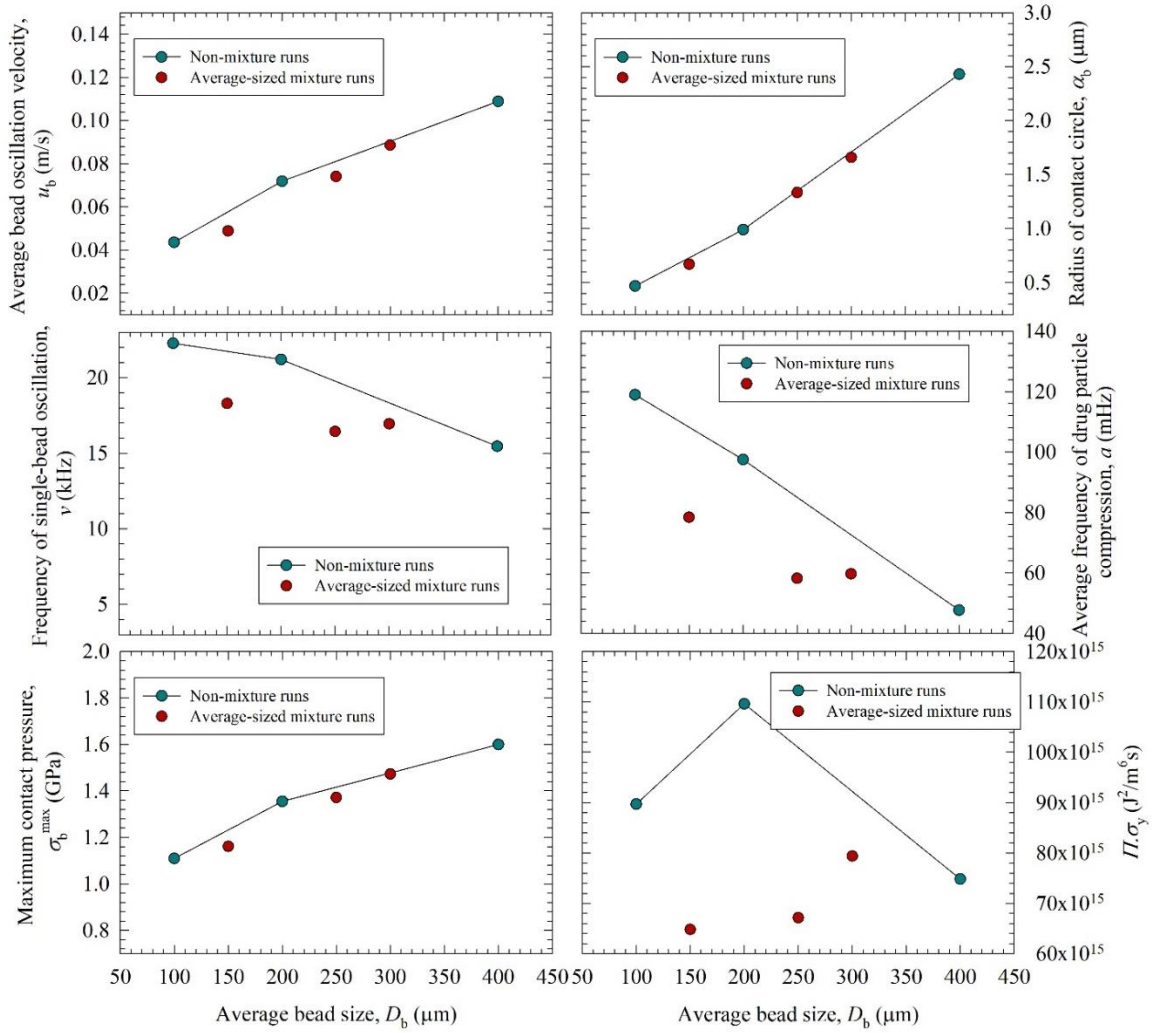

Figure 8.7 Impact of average bead size on the microhydrodynamic parameters when the stirrer speed was 4000 rpm, and the bead loading was 0.50. Average bead sizes of 150, 250, and 300 μm correspond to 50%–50% w/w mixtures of 100–200 μm, 100–400, and 200–400 μm beads, respectively.

When the microhydrodynamic parameters of non-mixture runs (narrowly-sized beads) and bead mixture runs are compared, those of the bead mixtures usually fell around the trendlines of the narrowly-sized beads. However, significant deviations from the trendlines were observed for a and $\Pi\cdot\sigma_y$ at the higher energetic runs (**Figures 8.5–8.7**). This is partly due to nonlinearity of a and $\Pi\cdot\sigma_y$ trends with bead sizes, where a was shown to have an exponential decay-like relationship with bead size in ref. [63]. Most importantly, these deviations originate from the oversimplification of treating the bead mixture as an

equivalent monodispersed bead with the calculated average bead size. In the microhydrodynamic model, there is no distinction between different types of collisions of beads with different sizes and associated radial distribution functions at contact. The radial distribution function at contact was assumed to be a function of bead concentration alone for monodispersed spheres, but not the bead sizes. It is also possible that beads with different sizes have different granular temperatures [214]. Unfortunately, the existing microhydrodynamic model does not treat mixtures of different bead sizes. New, expanded microhydrodynamic models must consider different bead sizes for accurate prediction of the bead mixtures. In the literature for two-phase gas–solid flows, mixtures of different particle sizes have been considered for polydisperse powders, and different values of the radial distribution function at contact g_0 were determined [214, 215]. For example, in the context of a binary mixture of fine–coarse particles, different g_0 expressions have been formulated for the various types of particle collisions, i.e., fine–coarse, fine–fine, and coarse–coarse. Such approaches must be adopted in advancing the microhydrodynamic model for bead mixtures.

8.2.3 Breakage kinetics predictions

The fitted parameters of *n*th-order model, i.e., k, n and d_{lim}, were predicted using i) the following microhydrodynamic parameters: maximum bead contact pressure $\sigma_b^{\max}$, radius of contact circle α_b, average frequency of drug particle compressions a, and pseudo energy dissipation rate for the drug particles $\Pi\sigma_y$ and ii) the following process parameters: stirrer speed ω, bead loading c, and mass fraction of the bead sizes in the mixture x_{100}–x_{200}–x_{400}. Several machine learning approaches were examined to find the best model (refer to **Table G.3** in *Appendix G*). For the training data set, leave one out cross validation RMSE values

were small and close for some of the approaches, indicating those models are not overfitting and safe to be used. Among those models, the one with smallest test RMSE was selected; elastic-net regression and decision tree when microhydrodynamic parameters and process parameters were used as predictors, respectively. The predicted parameters and RMSE of the predicted median particle sizes were reported in **Table 8.4**, and the predicted evolution of the median particle size is illustrated in **Figure 8.8**.

Table 8.4 *n*th-order Model Parameters for the Test Runs Obtained via Direct Fit, and Predicted with MHD Parameters via Elastic-Net Regression, and Predicted with Process Parameters via Decision Tree

Run Identifier	Model	k ($\mu m^{1-n}/min$)	n (-)	d_{lim} (μm)	RMSE (μm)
3500 0.43 100-0-0	Direct fit	1.45	1.78	0.144	0.623
	Microhydrodynamic prediction	1.17	1.91	0.125	0.604
	Empirical prediction	1.54	1.89	0.130	0.668
3500 0.43 0-100-0	Direct fit	1.28	1.88	0.144	0.049
	Microhydrodynamic prediction	0.953	1.92	0.125	0.092
	Empirical prediction	1.39	1.92	0.142	0.081
3500 0.43 0-0-100	Direct fit	0.814	2.07	0.144	0.066
	Microhydrodynamic prediction	0.612	2.01	0.125	0.183
	Empirical prediction	0.854	1.85	0.150	0.120
2500 0.30 33-33-33	Direct fit[a]	0.282	2.01	0.214	0.027
	Microhydrodynamic prediction[a]	0.606	1.88	0.125	0.144
	Empirical prediction[a]	0.191	2.25	0.083	0.072

[a]Data between 0.66-16 min were excluded due to clogging issue.

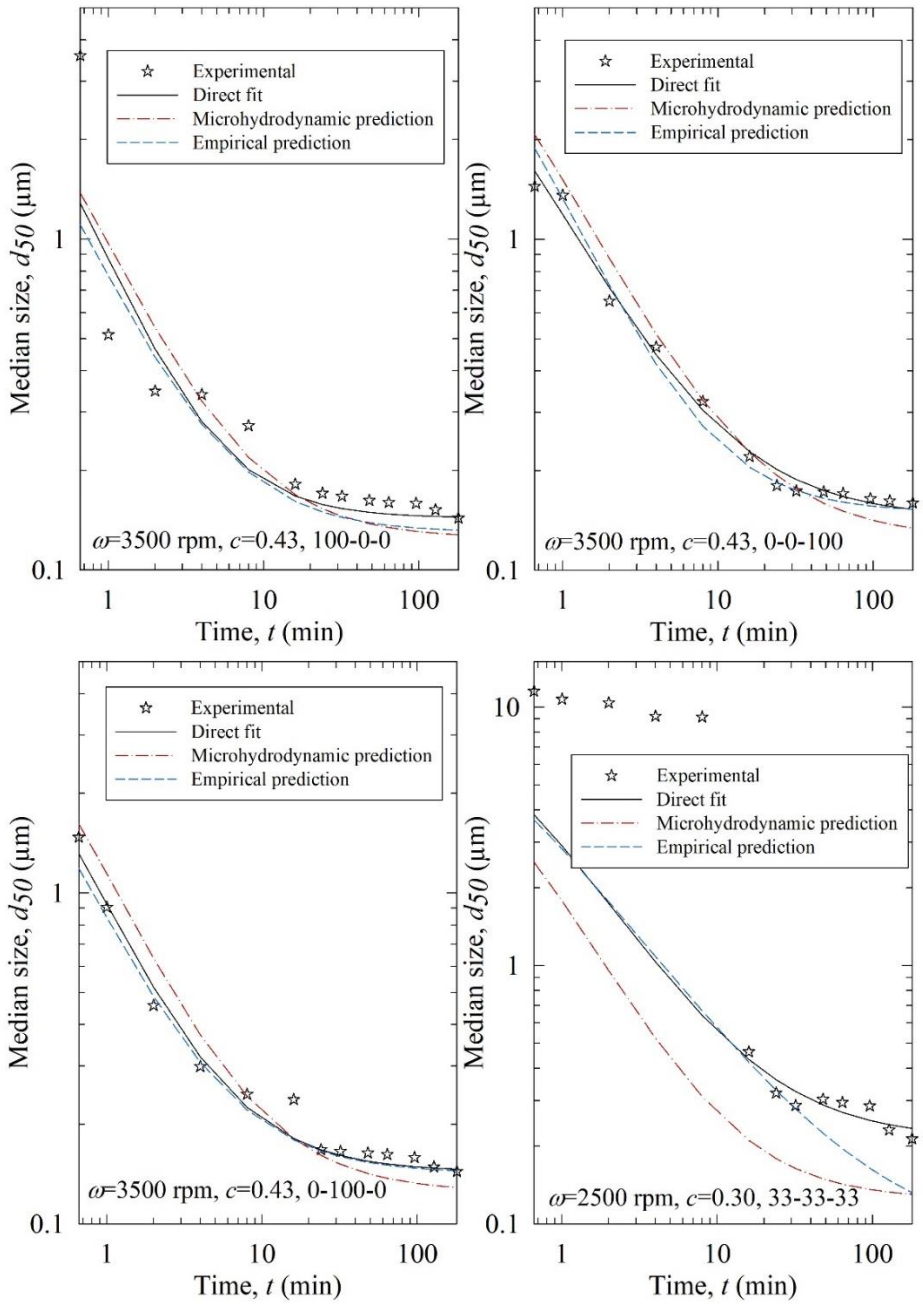

Figure 8.8 Experimental time-wise evolution of the median particle size for the test runs, their direct fit by the *n*th-order breakage kinetics model, their prediction by the *n*th-order breakage kinetics model augmented with elastic-net regression using the microhydrodynamic parameters, and their empirical prediction by the *n*th-order breakage kinetics model augmented with a decision tree using the process parameters.

According to the RMSEs in **Table 8.4** and the predicted profiles in **Figure 8.8**, the process parameter-based predictions were superior to the microhydrodynamic parameter-

based predictions. Except for the 3500, 0.43, 100-0-0 run (Run T1), the process parameter-based predictions agreed well with the experimental data. The poor performance of the microhydrodynamic parameter-based approach originates from the inability of the microhydrodynamic model to treat poly-dispersed beads, especially bead mixtures, accurately. The microhydrodynamic model treats bead mixtures as equivalent monodispersed spheres with average bead size of the constituent beads. Although the beads are almost spherical [149] and narrowly-sized (refer to **Table 8.1**), they are not monodispersed. As the microhydrodynamic model is limited to monodisperse beads, its predictions were not successful. Indeed, when the bead size was fixed and no bead mixture was used in an earlier study for the milling of another drug, the microhydrodynamic parameter-based predictions were superior to the process parameter-based predictions [150]. Here, process parameter-based predictions were reasonably good, even for the extrapolated test run (Run T4: 2500, 0.30, 33-33-33). This extrapolated test run had severe clogging problem because it was operated at a very low energetic condition, which does not represent a typical WSMM operation, and the milling data from 0–16 min was not considered in the fitting/prediction.

8.2.4 Identification of the optimal process–bead sizes based on merit scores

To assess the impact of the process parameters and bead sizes, merit scores were calculated and presented in **Table G.2** in *Appendix G*. Per Equation (5), the merit score factors in cycle time through $1/k$, power P, and the extent of heat generation–temperature rise through the number of intermittent milling cycles N_{mc}. In general, higher $1/k$, P, and N_{mc} are not desirable, as signified by their negative impact on the merit score. **Figures 8.9 and 8.10** depict the variation of the process merit scores when N_{mc} was considered or disregarded,

respectively, in the calculation along with the power P and the inverse of the breakage rate constant $1/k$.

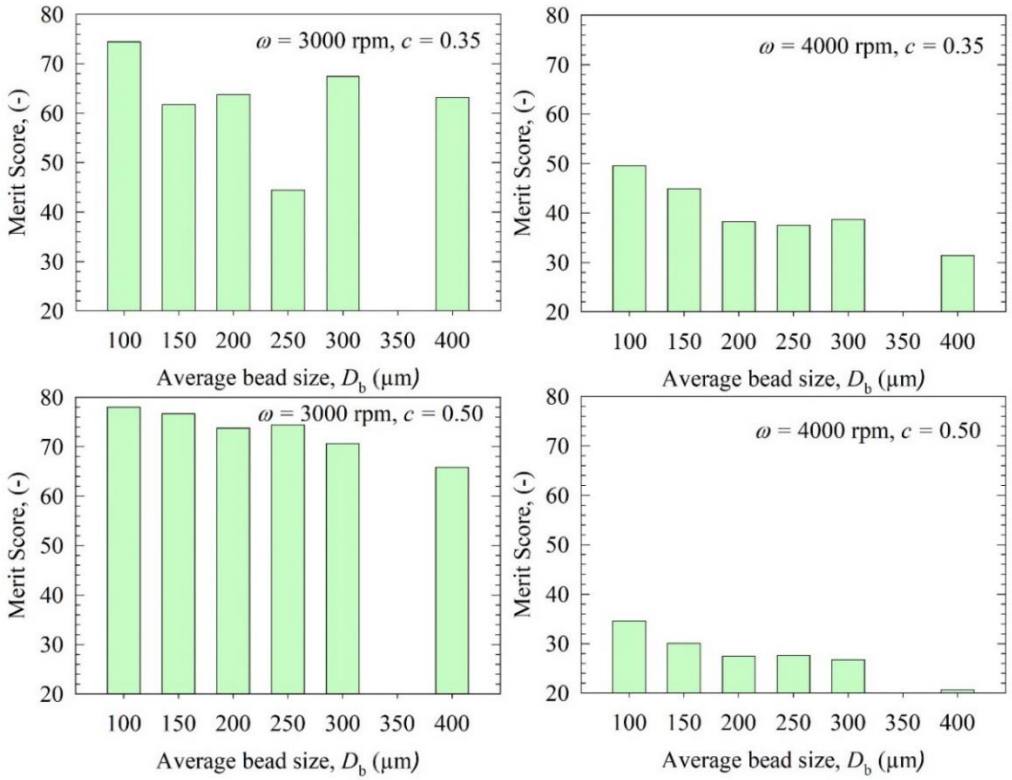

Figure 8.9 Impact of bead size mixtures on the merit score (based on the breakage rate constant, the power, and the number of intermittent milling cycles) for each ω–c pair. Average bead sizes of 150, 250, and 300 μm correspond to 50%–50% w/w mixtures of 100–200 μm, 100–400, and 200–400 μm beads, respectively.

A cursory look at **Figure 8.9** immediately reveals that an increase in stirrer speed from 3000 to 4000 rpm led to a remarkable decrease in the merit score at both bead loadings due to a simultaneous increase in both P and N_{mc}. Note that N_{mc} relates to strict temperature control and prevention of temperatures exceeding the maximum temperature allowed (35 ^{o}C). For non-pharmaceutical products that are not temperature-sensitive, consideration of N_{mc} is not warranted as higher maximum temperatures are allowed. For such a scenario, N_{mc} was disregarded; the merit scores were lower when the stirrer speed was increased from 3000 to 4000 rpm; but, the change was less drastic (**Figure 8.10**).

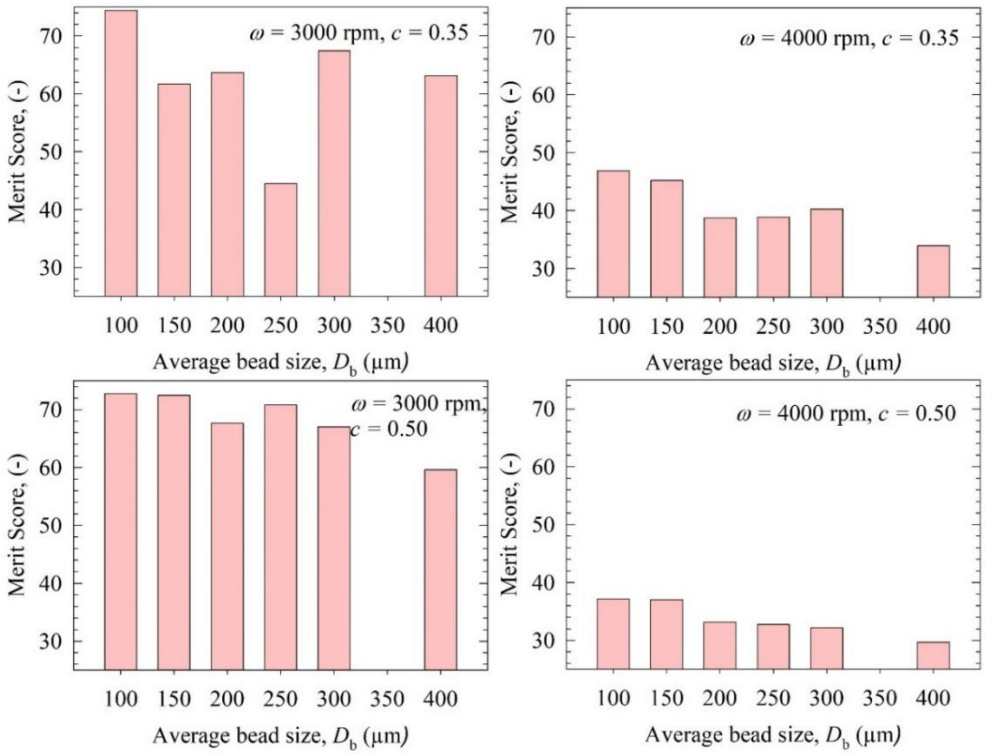

Figure 8.10 Impact of bead size mixtures on the merit score (based on the breakage rate constant and the power) for each ω–c pair. Average bead sizes of 150, 250, and 300 μm correspond to 50%–50% w/w mixtures of 100–200 μm, 100–400, and 200–400 μm beads, respectively.

Both **Figures 8.9 and 8.10** illustrate that there exist an optimal set of process conditions: ω = 3000 rpm and c = 0.50. At these optimal conditions, the merit scores were less sensitive to the average bead sizes. In general, narrowly sized 100 μm beads alone (not in a binary mixture) are more advantageous as they provide a higher merit score in terms of power consumption, breakage kinetics, and heat generation. Based on merit score ranking, except for the lowest energy case, 50–50–0 binary mixture of the beads is the second best, while the narrowly-sized 400 μm beads alone were the worst. The ranking of other beads/bead mixtures were different for different ω–c pairs. As the breakage kinetics results did not follow a clear pattern in terms of bead size impact for the lowest–energy case (ω = 3000 rpm and c = 0.35) due to clogging issues, it is understandable why its

associated merit scores did not follow a general trend in **Figures 8.9 and 8.10**.

8.2.5 Overall assessment and additional considerations

Guner et al. [149] established that a judicious combination of crosslinked polystyrene and yttrium-stabilized zirconia beads in mixtures led to highest merit scores and significant process improvement. Unlike the mixtures of beads with different materials of construction, mixtures of beads with widely different sizes did not bring any advantage because the smallest beads (100 µm) themselves have all of the benefits related to the process considerations. However, it is worth mentioning that there are some challenges with these small beads, which may make the second-best performer (50–50 mixture of the 100–200 µm) more appealing: handling of the 100 µm beads is harder during the bead loading/cleaning steps than that of the coarser beads. Clogging of the mill screen was observed with the 100 µm beads and its binary mixtures during the first 8–16 min of the respective runs, and we managed to prevent a process shut-down by changing the flow direction of the pump to reverse and reverse-back the flow of the suspension multiple times until the drug particle size became small enough not to cause further clogging during prolonged milling. Obviously, this practice is not desirable in an industrial setting. The clogging issue became less notable and of shorter duration for the mixtures of the 100 µm beads with the 200 and 400 µm beads, although it was not eliminated. Therefore, when 100 µm beads are to be used in an industrial scale operation, pre-milling of the drug particles, e.g., by a rotor-stator mill, could be the surest solution to this clogging problem. Alternatively, drug particles could be added to the holding tank of the mill gradually over a period of ~16 min to reduce particle concentration in the milling chamber during the initial phase of the milling where clogging occurred. Along with this approach, the

suspension flow rate could be ramped up from 0–126 ml/min slowly over the first 8–16 min, which will also help to reduce clogging. In this study with the small-scale mill, multiple flow reversals during the initial phase of milling helped to reduce clogging issue, and these other methods were not employed.

The upshot of our results is that there is no notable advantage to using either bead mixtures or coarser beads alone (200 and 400 μm) except for some ease of handling during the manufacturing operations with the coarser beads and lower price of the coarser beads. This latter advantage of the coarser beads has been highlighted by Patel et al. [15] for justifying the use of bead mixtures containing fine–coarse beads. **Table G.2** in *Appendix G* shows the bead prices calculated for each run and it is inversely proportional to the average bead sizes. However, this simplistic cost analysis misses several important points. First, small beads wear at a lower rate and extent than coarse beads [63]; thus, they have a longer operational lifetime before discarding than the coarse beads. Hence, during the manufacturing, the coarse beads would necessitate more frequent replenishment than the small beads. Moreover, small beads are preferable from a wear–product contamination perspective, which is important to pharmaceutical products. Second, when in a bead mixture, the small beads are nipped between the coarse beads, which may increase the wear rate of the smaller beads, and this aspect needs further investigation. In fact, we purposefully limited the size ratio between the coarsest beads to the smallest beads to 4:1. The use of coarser beads, e.g., 800 μm beads, could have caused a higher extent of damage to the smaller beads and is purposefully excluded.

8.3 Conclusions

In this study, we have explored the impacts of bead size and use of bead mixtures on the

breakage kinetics, the power consumption, and the number of intermittent milling cycles. The breakage kinetics were predicted reasonably well by the *n*th-order kinetic model augmented with decision trees using the process conditions. In general, 3000 rpm and a volumetric bead concentration of 50% along with the smallest beads (100 µm alone) had the highest process merit score, and the bead mixtures did not provide any synergistic improvement. The microhydrodynamic analysis attributed the fastest breakage with the 100 µm beads to the high frequency of drug particle compressions between the beads. However, serious deviations from the microhydrodynamic trends were observed when the model was applied to the bead mixtures especially at the higher energetic conditions. Hence, this study also highlighted the need for the development of a new microhydrodynamic model which considers poly-dispersed beads. We conclude that while 200 and 400 µm beads may have some operational ease of handling and lower cost, a more detailed analysis suggested these advantages are overrated. Considering lower media wear associated with the 100 µm beads as compared with the 200 and 400 µm beads, the driver for utilization of small beads gets even stronger for pharmaceutical applications where product contamination must be mimimized. The pre-milling of the drug suspension in a rotor-stator mill is expected to eliminate any clogging issue associated with the 100 µm beads during the initial phase of milling, which is only notable at the low stirrer speed and the bead loading conditions. Other practical approaches such as gradual addition of the drug powder into the stabilizer solution and ramping-up the suspension flow rate during this phase could also alleviate this practical operational issue with the 100 µm beads. These practical aspects will be considered in a future study.

CHAPTER 9

CONCLUSIONS AND FUTURE WORK

9.1 Conclusions

The upshot of our review of the publications on the modeling of WSMM presented in Chapter 1 is that (i) more widespread use of mechanistic modeling is warranted as most modeling efforts in pharmaceutical nanomilling have been dedicated to empirical, statistically-based models, (ii) none of the models could simulate all aspects of the WSMM process, and (iii) each modeling approach is typically good at analyzing a certain aspect of the process, and has various pros/cons. Chapter 1 also discussed that the MHD model is superior to the SI–SN model due to its simplicity and capability of accounting for microhydrodynamics without long and computationally expensive CFD simulations. As it allows natural coupling with CFD EE model through the "granular temperature" and provides a path to the development of a PBM with mechanistic breakage kernels, coupled models involving MHD, are expected to yield a more detailed process understanding at a reasonable computational cost. To this end, in this dissertation, we have decided to use and improve/advance the MHD model in the modeling of WSMM and developed a combined kinetic–microhydrodynamic modeling approach noting that there is no PBM with accurate mechanistic kernels for WSMM in the literature. Hence, instead of using PBM, we experimentally tracked the evolution of the average kinetic behavior during WSMM, i.e., the timewise evolution of the median size of the milled suspensions and developed new empirical kinetic models to describe the breakage kinetics and relate the kinetic parameters to the MHD model (Chapters 2 and 3). It is expected that such coupled kinetic–

microhydrodynamic models will stimulate development of mechanistic breakage kernels through coupled PBM–MHD in the future.

Chapter 2 showed us that although first order breakage kinetic model has been widely used in the literature, *n*th-order model ($n \cong 2$) had a better fitting capability to the timewise evolution of the median particle size during milling when all data points, including early measurements, were considered. Unlike the purely empirical correlation between the breakage rate constant and the process parameters, the kinetic–microhydrodynamic correlation was proved to have a great prediction competence for both center point experiments and extrapolated experiments, which were outside the range of the DOE used for the model calibration. Chapter 3 investigated how microhydrodynamic parameters were affected when the packing limit of the beads was taken into account. The results showed that MHD parameters could explain the experimental breakage kinetics better when Lun and Ma-Ahmadi radial distribution functions at contact were used instead of Carnahan-Starling, in which the packing concentration limit was disregarded. This impressive outcome proved the worthiness of this physically driven model. Besides providing us with significant insights, such models can be used for process development, optimization, and intensification as a complementary tools to experiments.

Chapters 4–6 presented the first comprehensive studies on the combined experimental–theoretical analyses of heat generation–transfer during WSMM. Chapter 4 revealed a drastic temperature rise during the milling which was affected by stirrer speed, bead loading, and bead size. An increase in any one of these variables led to a higher temperature rise while their impact was ranked ordered in the following manner: stirrer speed > bead loading >> bead size. Chapter 5 formulated an enthalpy balance model (EBM)

to successfully simulate the temperature evolution during milling considering all related heat transfer properties of the system by only one fitting parameter, which could be predicted via process conditions. Chapter 6 derived a lumped parameter model (LPM) as an alternative approach, which was more flexible with 2 fitting parameters. Since the overall heat transfer coefficient was not calculated but fitted, the need for correlations and properties to calculate it was eliminated and it did not require the power consumption information, unlike the EBM. In other words, the LPM had some advantages compared to the EBM since it required less information and provided good estimations of the temperature profile. However, both mechanistic models like the EBM and semi-theoretical models like the LPM have usage areas as one could provide more insight about the process and the other could be more practical.

Chapter 7 used CPS–YSZ bead mixtures for the first time in the milling literature and concluded that while CPS beads were more energy efficient and YSZ beads led to faster breakage of the drug particles, their mixtures could optimize the process holistically, especially when heat dissipation was considered. This work also enabled us to design a decision tree for the judicious selection of various bead mixtures for specific considerations in the pharmaceutical industry. Finally, small beads were found to be superior to other bead sizes and their mixtures in terms of cycle time, heat dissipation, and power consumption with some handling and cost drawbacks (Chapter 8). MHD analysis of the bead size mixtures was done based on the average bead size in the mixtures. While this approach could be considered as over-simplification, it provided some insights into the role of bead size in particle breakage.

Overall, this dissertation has attempted to resolve major process challenges facing the WSMM process: relatively slow and inefficient process, high heat dissipation, high energy consumption, etc. using combined experimental and theoretical approaches with the modified microhydrodynamic model. For the first time in literature, heat generation–transfer aspects of the process have been investigated. The EBM and LPM models have provided significant insights into the evolution of temperature during milling. This dissertation has established that the process can be effectively optimized via three distinctly different approaches: (i) optimize the stirrer speed and bead loading for a given bead size–material of construction, (ii) optimize the composition of bead mixtures with different bead materials at a fixed set of stirrer speed–bead loading, and (iii) simultaneous optimization of bead mixture composition at various stirrer speed–bead loadings. Unfortunately, mixtures of beads with different sizes do not provide sufficient optimization flexibility. From a modeling perspective, the microhydrodynamically and enthalpy-driven mechanistic or phenomenological models as well as various correlations developed in this dissertation will help engineers to simulate and predict the impact of various parameters and identify optimal processing conditions along with failure modes.

9.2 Future Work

In Chapter 2, excellent descriptive (fitting) capability of the *n*th-order kinetic model as well as the good predictive capability of the kinetic–microhydrodynamic correlation has been established. Not only do these models provide mechanistic process understanding of the bead–bead collisions and capture frequency of the drug particles in the mill, but they also enable engineers to predict the evolution of the median particle size for a multitude of stirrer speed–bead loading–bead type combinations. This could save effort, time and

materials as well as allow engineers to identify failure modes and optimal processing conditions and bead type. However, the current kinetic–microhydrodynamic correlation is not independently predictive as the power consumption data needed for Runs 9–12 were still obtained from the experiments. To obviate the need for measuring the power consumption P_w without too many additional experiments, one can use the P_w values obtained from the DOE (Runs 1–8) and develop a general correlation for P_w as a function of the dimensionless Euler number Eu, Reynolds number Re, and Froude number Fr for a specific mill and such a correlation can be used for predicting P_w [137]. Alternatively, P_w can be estimated by a relatively inexpensive Eulerian–Eulerian simulation, with Kinetic Theory of Granular Flow (KTGF) for the beads phase (see e.g., [102]), of the torque required to rotate the stirrer of the mill via computational fluid dynamics (CFD), and the approach can be validated using the existing data from Runs 1–8. Such simulations will also allow a thorough understanding of the recirculation effects. As discussed in Section 2.2.7, the impact of recirculation on the particle size can be analyzed using a PBM for the mill–holding tank. Clearly, there is a strong need for a mechanistic PBM that incorporates the microhydrodynamic parameters in its specific breakage rate, which is analogous to k here. Hence, the current chapter and the establishment of the k correlation with the three microhydrodynamic parameters motivate the development of a mechanistic PBM. Development of such a mechanistic PBM will allow for predicting the temporal evolution of the whole particle size distribution, rather than the median size alone. In addition, the kinetic–microhydrodynamic model informs future mechanistic PBM–MHD coupled models in terms of how specific breakage rate kernels of PBM can be formulated in terms

of most relevant microhydrodynamic parameters, i.e., of which the average frequency of drug particle compressions between the beads turns out to be the most important parameter.

For developing a further understanding of the temperature increase during milling, the impact of polymer–surfactant concentration on the viscosity of the suspensions and heat generation should be investigated as well. Also, to develop a more fundamental understanding of the variation of the fraction of power converted into heat at various milling conditions, various energy dissipation mechanisms at the bead–bead collision scale should be evaluated within the context of a microhydrodynamic model. Since temperature rise has been a recently addressed challenge, it needs attention for investigating its other various aspects, for example, the impact of other process parameters such as different bead material, flow rate, drug loading, and their modeling. Besides, it should be studied at different scales and our hypothesis is the temperature increase would be lower at larger scales due to the cooling effect of the recirculated suspension from the holding tank. The EBM model could be improved by deriving more realistic correlations for calculating the overall heat transfer coefficient. Also, instead of empirical correlations, a mechanistic estimate for the fraction of power converted to heat could be sought.

The successful use of bead mixtures will pave the way to develop robust, optimal WSMM processes while providing unprecedented flexibility in process design and optimization. Future work can focus on the examination of the impact of bead mixtures on media wear and contamination. Besides, there is a need for developing MHD analysis for bead mixtures of both different materials and different sizes, which could be a subject of a future study.

APPENDIX A

SUPPLEMENTARY DATA FOR CHAPTER 2

This appendix contains supplementary tables and codes related to the breakage kinetics models and microhydrodynamic correlations, which was studied in Chapter 2.

Table A.1 Average Stirrer Power per Unit Volume P_w, Apparent Shear Viscosity μ_L and Density ρ_L of the Milled Drug Suspensions as well as the Calculated Microhydrodynamic Parameters for the Wet Milling Experiments

Run no.	P_w (W/m^3)	μ_L ($mPa{\cdot}s$)[a]	ρ_L (kg/m^3)	$\theta\times10^3$ (m^2/s^2)	u_b (m/s)	v (kHz)	σ_b^{max} (GPa)	α_b (μm)	a (mHz)	$\Pi\sigma_y$ (J^2/m^6s)
1	2.81×10^5	160	1030	1.28	0.06	2.15	1.84×10^{-2}	3.82	15.9	1.90×10^{12}
2	8.65×10^5	119	1030	4.32	0.10	4.32	1.58	2.41	16.7	2.73×10^{16}
3	4.90×10^5	118	1030	0.74	0.04	5.60	1.65×10^{-2}	3.42	61.7	4.55×10^{12}
4	9.48×10^5	57.4	1030	2.35	0.08	10.9	1.40	2.13	61.5	6.05×10^{16}
5	1.03×10^6	144	1020	5.15	0.11	4.31	2.43×10^{-2}	5.04	55.5	1.16×10^{13}
6	1.49×10^6	67.4	1030	12.4	0.18	7.31	1.94	2.97	43.9	1.07×10^{17}
7	1.16×10^6	81.0	1030	2.50	0.08	10.3	2.11×10^{-2}	4.37	185	2.22×10^{13}
8	2.49×10^6	32.5	1030	9.53	0.16	22.0	1.85	2.82	217	3.73×10^{17}
9	5.31×10^5	113	1030	1.77	0.07	4.44	1.97×10^{-2}	4.07	51.2	6.17×10^{12}
10	1.45×10^6	57.6	1030	7.29	0.14	9.86	1.75	2.67	64.5	1.15×10^{17}
11	1.15×10^5	174	1030	0.78	0.04	1.15	1.67×10^{-2}	3.46	5.50	5.83×10^{11}
12	5.31×10^5	123	1030	4.08	0.10	2.88	1.56	2.38	8.57	1.48×10^{16}

[a]Taken at the shear rate γ of 1000 1/s.

Table A.2 Statistics of the Estimated MLRM Coefficients, Including the Intercept, Correlating the Breakage Rate Constant K of the nth-order Kinetic Model to the Microhydrodynamic Parameters

Fit	Parameter			Model			
	Symbol[a]	Coefficient[b]	p value	R^2	Adj R^2	SSR	p value
First-order MLRM, BM_2	**Intercept** ($\mu m^{(n-1)}min^{-1}$)	1.44×10^{-1}	1.76×10^{-1}	0.828	0.799	0.182	1.72×10^{-3}
	a (mHz)	4.65×10^{-3}	1.72×10^{-3}				
First-order MLRM, BM_3	Intercept ($\mu m^{(n-1)}min^{-1}$)	6.15×10^{-1}	3.65×10^{-3}	0.963	0.948	0.039	2.61×10^{-4}
	α_b (μm)	-1.44×10^{-1}	7.80×10^{-3}				
	a (mHz)	4.85×10^{-3}	1.08×10^{-4}				
First-order MLRM, BM_4	**Intercept** ($\mu m^{(n-1)}min^{-1}$)	5.49×10^{-1}	1.96×10^{-2}	0.969	0.945	0.033	1.82×10^{-3}
	$\boldsymbol{\alpha_b}$ (μm)	-1.23×10^{-1}	4.76×10^{-2}				
	a (mHz)	4.43×10^{-3}	2.79×10^{-3}				
	$\boldsymbol{\Pi\sigma_y}$ ($\times10^{-16}$ J^2/m^6s)	3.66×10^{-3}	4.46×10^{-1}				
First-order MLRM, BM_5	**Intercept** ($\mu m^{(n-1)}min^{-1}$)	5.43×10^{-1}	1.53×10^{-1}	0.969	0.927	0.033	1.36×10^{-2}
	$\boldsymbol{\sigma_b^{max}}$ (GPa)	1.37×10^{-3}	9.82×10^{-1}				
	$\boldsymbol{\alpha_b}$ (μm)	-1.21×10^{-1}	1.72×10^{-1}				
	$\boldsymbol{a}$ (mHz)	4.44×10^{-3}	1.28×10^{-2}				
	$\boldsymbol{\Pi\sigma_y}$ ($\times10^{-16}$ J^2/m^6s)	3.55×10^{-3}	6.24×10^{-1}				
Second-order MLRM, BM_4	**Intercept** ($\mu m^{(n-1)}min^{-1}$)	5.50×10^{-1}	1.00×10^{-2}	0.975	0.956	0.026	1.16×10^{-3}
	α_b (μm)	-1.56×10^{-1}	8.26×10^{-3}				
	$\boldsymbol{a}$ (mHz)	8.05×10^{-3}	2.64×10^{-2}				
	$\boldsymbol{a^2}$ (mHz^2)	-1.35×10^{-5}	2.39×10^{-1}				
Second-order MLRM, BM_5	**Intercept** ($\mu m^{(n-1)}min^{-1}$)	3.65×10^{-1}	1.98×10^{-2}	0.995	0.989	0.005	8.36×10^{-4}
	α_b (μm)	-1.16×10^{-1}	9.76×10^{-3}				
	a (mHz)	9.23×10^{-3}	4.92×10^{-3}				
	$\boldsymbol{\Pi\sigma_y}$ ($\times10^{-16}$ J^2/m^6s)	7.85×10^{-3}	3.85×10^{-2}				
	$\boldsymbol{a^2}$ (mHz^2)	$-2.28\text{x}10^{-2}$	2.70×10^{-2}				
MLRM with interaction terms, BM_4	**Intercept** ($\mu m^{(n-1)}min^{-1}$)	7.11×10^{-2}	1.37×10^{-1}	0.987	0.978	0.013	2.3×10^{-4}
	a (mHz)	1.63×10^{-2}	1.68×10^{-3}				
	$\alpha_b a$ (μm.mHz)	-2.81×10^{-3}	3.91×10^{-3}				
	$\boldsymbol{a\Pi\sigma_y}$ ($\times10^{-16}$ mHz J^2/m^6s^2)	-7.35×10^{-5}	2.98×10^{-2}				
MLRM with interaction terms, BM_5	**Intercept** ($\mu m^{(n-1)}min^{-1}$)	4.26×10^{-2}	6.40×10^{-2}	0.999	0.997	0.001	1.06×10^{-4}
	a (mHz)	1.25×10^{-2}	1.32×10^{-3}				
	$\boldsymbol{\sigma_b^{max} a}$ (GPa.mHz)	2.18×10^{-3}	1.33×10^{-2}				
	$\alpha_b a$ (μm.mHz)	-1.91×10^{-3}	4.16×10^{-3}				
	$a\Pi\sigma_y$ ($\times10^{-16}$mHz J^2/m^6s^2)	-1.45×10^{-4}	2.70×10^{-3}				

[a]Statistically insignificant (p value > 0.01) parameters are **bolded**. $\Pi\sigma_y$ is treated as a single parameter as σ_y is a constant. [b]The coefficients have the units that make the MLRM equation dimensionally homogeneous.

A.1 Sample MATLAB Code for the Microhydrodynamic Calculations

Main.m

```
global Pw     % Power applied to the stirrer per unit volume, W/(m^3)
global Db     % Milling bead diameter, m
global c      % solids volumetric concentration
global g0     % radial distribution function at contact
global k      % restitution coefficient for bead-bead collisions
global Rdiss0 % dissipation coefficient taking into account squeezing the liquid film
global ub     % average particle oscillation velocity, m/s
global v      % frequency of the single bead oscillation, 1/s
global Em     % non-dimensional particle-particle gap thickness at which the lubrication force stops
continous increase and becomes a constant
global visliq  % dynamic viscosity of the equivalent liquid to be measured from viscometer, kg/ms
global dliq  % density of the equivalent liquid, kg/(m^3)
global dbeads  % density of the media beads, kg/(m^3)
global K       % empirical correlation coefficient for correction for large Reynolds numbers
global Eht       % granular energy balance for a well-mixed slurry in the mill
global Rb  %m radius of bead
global etab %Poisson ratio of the bead
global Yb  %Young modulus of the bead
global Rp  %radius of the particle
global eps  %volume fraction of the drug in the suspension
global Ystar %reduced elastic modulus of the beads
global Yp   %Young modulus of the particle
global etap  %Poisson ratio of the particle
global gamma
global clim  %maximum bead concentration

y0=[1e-6]; % case with 1 unknown, 1 equation, the initial guess was gotten from Eskin's paper at 3200rpm

% Solver based on medium scale Gauss-Newton optimization with quadcubic line search
% Do NOT change the solver parameters below:
options=optimset('Diagnostics','on','Display','iter','Largescale','off','TolX',[1e-6],'TolFun',[1e-10],...
'MaxIter',[2e4],'MaxFunEvals',[2e4],'TolCon',[1e-10],'DiffMaxChange',[1e-8],'DiffMinChange',[1e-10]);
[y,fval,exitflag,output]=fsolve(@Equationset,y0,options);

% y(1) is equal to the granular temperature theta
ub=sqrt((8/pi)*y(1)); %m/s
V=((24*c*g0)/Db)*sqrt(y(1)/pi); %Hz
v=V/1000 ; %KHz
Fbn=1.96*(Yb/(1-etab^2))^(2/5)*(dbeads^(3/5))*(Rb^2)*(y(1)^(3/5));
Alphab=(0.75*(1-etab^2)/Yb*Rb*Fbn)^(1/3); %m
alphab=Alphab*10^6 ; %micrometer
sigmabmax=3*Fbn/(2*pi*(Alphab)^2)/10^9; %GPa
p=0.97*c/(1-c)*((dbeads*(1-etab^2)/Yb)^(2/5))*(y(1)^(2/5))*Rp/Rb;
A=p*V; %Hz
a=A*1000; %mHz
pisigmaA=2.23*(c^2)*2*g0/((pi^(5/2))*eps);
pisigmaB=(Yb/(1-etab^2))^(18/15);
pisigmaC=((Ystar/Yp)^gamma);
pisigmaD=(dbeads^(4/5))/Rb^2*(y(1)^(13/10));
pisigma=2.23*(c^2)*2*g0/((pi^(5/2))*eps)*((Yb/(1-
etab^2))^(18/15))*((Ystar/Yp)^gamma)*(dbeads^(4/5))*Rp/Rb^2*(y(1)^(13/10)); %(J2/m6.s)
granulartemperature=y; %m2/s2
```

```
% END OF MAIN PROGRAM %
g0
granulartemperature %m2/s2
ub %m/s
v %KHz
sigmabmax %GPa
alphab %(micrometer)
a %mHz
pisigma %J2/m6.s)
format shortg
Result=[g0; y(1); ub; v; sigmabmax; alphab; a; pisigma]
```

Equationset.m

```
global Pw     % Power applied to the stirrer per unit volume, W/(m^3)
global Db     % Milling bead diameter, m
global c      % solids volumetric concentration
global g0     % radial distribution function at contact
global k      % restitution coefficient for bead-bead collisions
global Rdiss0 % dissipation coefficient taking into account squeezing the liquid film
global ub     % average particle oscillation velocity, m/s
global v      % frequency of the single bead oscillation, 1/s
global Em     % non-dimensional particle-particle gap thickness at which  the lubrication force stops
continuous increase and becomes a constant
global visliq  % dynamic viscosity of the equivalent liquid to be measured from viscometer, kg/ms
global dliq  % density of the equivalent liquid, kg/(m^3)
global dbeads  % density of the media beads, kg/(m^3)
global K       % empirical correlation coefficient for correction for large Reynolds numbers
global Eht       % granular energy balance for a well-mixed slurry in the mill
global Rb   %m radius pf bead
global etab  %Poisson ratio of the bead
global Yb   %Young modulus of the bead
global Rp   %radius of the particle 0min
global eps   %volume fraction of the drug in the suspension
global Ystar  %reduced elastic modulus of the beads
global Yp   %Young modulus of the particle
global etap  %Poisson ratio of the particle
global gamma
global clim %maximum bead concentration
Pw=822916.6667; % please get from data % Power applied to the stirrer per unit volume, W/(m^3)
Eht=0; % please get from data % granular energy balance for a well-mixed slurry in the mill
%other parameters
c= 0.55;% please get from data %  solids volumetric concentration i.e (50 ml bead powder *void
fraction)/total volume of chamber
k= 0.76; % particle-particle restitution coef. ref. Tatsumi see coefficient of restitution paper 0.76 for YSZ,
0.9 for CPS
Em=0.003;   % non-dimesnional particle-particle gap thickness
visliq=0.048390987;%kg/(m·s) Please measure for each sample
dliq= 1026; %kg/(m^3) Please measure for each sample
dbeads=6000;%kg/(m^3)% measured
Db= 0.000405; %m please include the diameter of the bead with different sizes.
Rb= Db/2; %m radius of the bead
etab=0.2; %poisson ratio of the bead  (0.2 for YSZ 0.33 for CPS)
Yb=200*10^9; %Pa Young modulus of the bead (200 GPa for YSZ, 1.5 GPa for CPS)
Rp=13.723*10^-6; %0 min (m)radius of the particle
eps=0.07444882; %volume fraction of the drug in the suspension
```

```
Ystar=((1-etab^2)/Yb+(1-etap^2)/Yp)^(-1); %reduced elastic modulus of the beads
Yp=8.93*10^9; %Pa Young modulus of the particle
etap=0.3; %Poisson ratio of the particle
gamma=1/3;
clim=0.63;
% calculate the emprical correlation coefficient
K=(0.096+0.142*c^0.212)/((1-c)^4.454);

%Calculate the radial distribution function at contact
g0=(1-(c/clim)^(1/3))^-1

% Dissipation Coefficient
Rdiss0=1+3*((0.5*c)^0.5)+(135/64)*c*log(c)+11.26*c*(1-5.1*c+16.57*(c^2)-21.77*(c^3))-
log(Em)*g0*c;
Re=Db*dliq*(y(1)^0.5)/visliq;

Rdiss=Rdiss0+Re*K;
nb=6*c/(pi*(Db^3));
epsvis= 9*pi*visliq*Db*nb*y(1)*Rdiss;
epscoll=(12/(Db*sqrt(pi)))*(1-(k^2))*(c^2)*dbeads*g0*(y(1)^1.5);
func(1)=Pw-epsvis-epscoll-Eht;
```

A.2 R Code for the Subset Selection Algorithm

```
for (i in c(1:4)) {
  print(paste("running variable", i))
  bestAdjR=0
  bestRSS=Inf
  regnames=combn(colnames(data[,!(names(data) %in% c('k'))]),i)
  for (j in c(1:length(regnames[1,]))) {
    model=paste0("k~",paste("0",paste(regnames[,j],collapse="+"),sep = "+"))
    #model=paste0("k~",paste(regnames[,j],collapse="+"))
    fit=lm(as.formula(model),data = data)
    adjR=summary(fit)$adj.r.squared
    RSS=anova(fit)["Residuals", "Sum Sq"]
    R2=summary(fit)$r.squared
    Pvalue=summary(fit)$coefficients[,4]
    Pmodel=lmp(fit)
    if (adjR>=bestAdjR) {
      bestAdjR=adjR
      bestRSS=RSS
      bestModel=model
      bestR2=R2
      bestcoef=coef(fit)
      bestPvalue=Pvalue
      bestfit=fit
      bestPmodel=Pmodel
    }

  }
```

```
  print("best model")
  print("best coef")
  print(formatC(bestcoef, format="e", digits = 2))
  print("best Pvalue")
  print(formatC(bestPvalue, format="e", digits = 2))
  print("Best R2")
  print(bestR2)
  print("adj r")
  print(bestAdjR)
  print("bestRSS")
  print(bestRSS)
  print("bestPmodel")
  print(formatC(bestPmodel, format="e", digits = 2))

}
```

APPENDIX B

SUPPLEMENTARY DATA FOR CHAPTER 3

This appendix contains the subset selection algorithm and supportive tables and figures related to the bead packing limit concentration study as described in Chapter 3.

B.1 Details of the Subset Selection Algorithm

Algorithm 1: Subset Selection with LOOCV

Input: Data Set: $(x_i^1, x_i^2, \dots, x_i^T; y_i)_{i=1}^I$

For each $j = 1, 2, \dots, J$:

  For each z $\in$ {combination $\binom{T}{j}$ of predictors}

    For each $i = 1, 2, \dots, I$:

      (a) Set training set: $(x_r^z; y_r)\ \forall\ r = 1,2, \dots, i-1, i+1, \dots, I$

      (b) Set test set: $(x_i^z; y_i)$

      (c) Fit the model using training set

      (d) Calculate the squared error e_i^2 using test set and fitted model

    (a) Set $SSR_z = \sum_{i=1}^{I} e_i^2$

  (a) Set the best model BM_j as the one with the lowest SSR_z

Select overall best models (BMs) among $BM_1, BM_2, \dots, BM_j$ as the one(s) that have lowest SSR and all predictors have a statistically significant relationship (p value ≤ 0.01) with the response.

Subset selection algorithms are used to find a subset of predictors that are most related to the response variable. For each number of predictors, all subsets of features with a fixed number of predictors are considered for model fitting, and the best model is selected among

them using a criterion such as SSR or adjusted R^2. In this chapter, we modified the subset selection algorithm presented in ref. [182]. Cross-validation techniques have been commonly used to estimate the predictive power of trained models in a realistic setting [216]. Our choice of sampling technique is known as leave-one-out cross-validation (LOOCV), which works well in datasets with small sample sizes [217]. Algorithm 1 presents the subset selection with LOOCV. Our dataset was divided into two parts: training sets and test sets. In this resampling paradigm, the test set consisted of only one observation (milling run), whereas the training set included all the remaining observations. The model was fitted with the samples in the training set and error was calculated using the sample in the test set. This process was repeated the number of times as the number of observations until each observation was used as the test set only once. The performance of the model was evaluated by summing the errors for each fitted model using the single observation in the test. LOOCV is less biased compared to other cross-validation techniques such as validation set approach and k-fold cross-validation [182]. A disadvantage of LOOCV is the high computational cost of the model fitting. Our subset selection algorithm with LOOCV did not have this disadvantage; fitting the MLRM was very fast as the sample size was not too large.

In the implementation of the subset selection algorithm, we set J = 4 as the maximum number of features (independent variables) for our experiments. Then, for each number of features considered, we generated a combination $\binom{T}{j}$ of features. This set is {{1},{2},{3},{4}} when j = 1, {{1,2},{1,3},{1,4},{2,3},{2,4},{3,4}} when j = 2, {{1,2,3},{1,2,4},{1,3,4},…} when j = 3, and similarly for the case T = 4. In the same way, feature sets were generated for the cases when T = 8 and T = 10. We iterated through these

subsets to calculate the LOOCV error. For each observation, we assigned the training set to be all observations, except one, and the test set to be the remaining observation. I = 10 is the set for the subset selection algorithm. We fitted a model with a selected subset of features using the training set and calculated squared error using the test set. The squared errors were summed to calculate the SSR for a certain feature set. Then, an MLRM model was selected using the lowest SSR as the best model (BM) for a certain number of features considered. Finally, overall BM was selected as the model with the lowest SSR.

B.2 Supportive Tables and Figures

Table B.1 The Average Stirrer Power per Unit Volume P_w, the Apparent Shear Viscosity μ_L and the Density ρ_L of the Milled Drug Suspensions (Measured In Runs 1–14), as well as the Viscosity μ_M and the Density ρ_M of the Bead–Milled Drug Suspensions (Estimated)

Run No.	P_w (W/m^3)	μ_L (mPa·s)[a]	ρ_L (kg/m^3)	μ_m (mPa·s)[b]	ρ_m (kg/m^3)[c]
1	2.81×10^5	160	1030	829	1030
2	8.65×10^5	119	1030	616	2770
3	4.90×10^5	118	1030	5520	1040
4	9.48×10^5	57.4	1030	2680	3520
5	1.03×10^6	144	1020	748	1030
6	1.49×10^6	67.4	1030	349	2770
7	1.16×10^6	81.0	1030	3780	1030
8	2.49×10^6	32.5	1030	1520	3520
9	1.11×10^6	76.5	1030	24100	1040
10	2.16×10^6	16.9	1030	5330	4010
11	5.31×10^5	113	1030	1490	1030
12	1.45×10^6	57.6	1030	761	3140
13	1.15×10^5	174	1030	586	1030
14	5.31×10^5	123	1030	414	2510

[a]Taken at the shear rate γ of 1000 1/s. [b]$\mu_m = \mu_L[1 + 2.5c + 10c^2 + 0.0019\,exp(20c)]$ [c]$\rho_m = \rho_b c + \rho_L(1 - c)$

Table B.2 Microhydrodynamic Parameters Calculated Using the Carnahan–Starling RDF

Run No.	g_0 (-)	θ (m^2/s^2)	u_b (m/s)	ν (kHz)	σ_b^{max} (GPa)	α_b (μm)	a (mHz)	$\Pi\sigma_y$ (J^2/m^{6}s)
1	3.00	2.04×10^{-3}	7.20×10^{-2}	1.45	2.02×10^{-2}	4.19	12.9	1.85×10^{12}
2	3.00	6.77×10^{-3}	1.31×10^{-1}	2.89	1.72	2.63	13.4	2.61×10^{16}
3	6.00	1.57×10^{-3}	6.32×10^{-2}	3.63	1.92×10^{-2}	3.98	53.9	5.38×10^{12}
4	6.00	4.70×10^{-3}	1.09×10^{-1}	6.88	1.60	2.45	51.1	6.63×10^{16}
5	3.00	8.08×10^{-3}	1.43×10^{-1}	2.88	2.66×10^{-2}	5.52	44.5	1.11×10^{13}
6	3.00	1.86×10^{-2}	2.18×10^{-1}	4.80	2.11	3.22	33.3	9.74×10^{16}
7	6.00	5.10×10^{-3}	1.14×10^{-1}	6.53	2.43×10^{-2}	5.03	156	2.49×10^{13}
8	6.00	1.67×10^{-2}	2.06×10^{-1}	12.9	2.06	3.15	159	3.43×10^{17}
9	10.9	2.29×10^{-3}	7.63×10^{-2}	9.58	2.07×10^{-2}	4.29	248	2.30×10^{13}
10	10.9	9.16×10^{-3}	1.53×10^{-1}	21.0	1.83	2.80	305	4.14×10^{17}
11	4.14	3.08×10^{-3}	8.86×10^{-2}	2.98	2.20×10^{-2}	4.55	42.9	6.44×10^{12}
12	4.14	1.20×10^{-2}	1.75×10^{-1}	6.44	1.93	2.95	51.4	1.12×10^{17}
13	2.46	1.16×10^{-3}	5.43×10^{-2}	0.76	1.81×10^{-2}	3.74	4.25	5.26×10^{11}
14	2.46	6.08×10^{-3}	1.24×10^{-1}	1.91	1.69	2.58	6.67	1.35×10^{16}

Table B.3 Microhydrodynamic Parameters Calculated Using the Lun RDF

Run No.	g_0 (-)	θ (m^2/s^2)	u_b (m/s)	ν (kHz)	σ_b^{max} (GPa)	α_b (μm)	a (mHz)	$\Pi\sigma_y$ (J^2/m^6s)
1	5.62	1.28×10^{-3}	5.72×10^{-2}	2.15	1.84×10^{-2}	3.82	15.9	1.90×10^{12}
2	5.62	4.32×10^{-3}	1.05×10^{-1}	4.32	1.58	2.41	16.7	2.73×10^{16}
3	13.5	7.41×10^{-4}	4.34×10^{-2}	5.60	1.65×10^{-2}	3.42	61.7	4.55×10^{12}
4	13.5	2.35×10^{-3}	7.74×10^{-2}	10.9	1.40	2.13	61.5	6.05×10^{16}
5	5.62	5.15×10^{-3}	1.15×10^{-1}	4.31	2.43×10^{-2}	5.04	55.5	1.16×10^{13}
6	5.62	1.24×10^{-2}	1.77×10^{-1}	7.31	1.94	2.97	43.0	1.07×10^{17}
7	13.5	2.50×10^{-3}	7.98×10^{-2}	10.3	2.11×10^{-2}	4.37	184	2.22×10^{13}
8	13.5	9.53×10^{-3}	1.56×10^{-1}	22.0	1.85	2.82	217	3.73×10^{17}
9	62.0	4.12×10^{-4}	3.24×10^{-2}	23.0	1.47×10^{-2}	3.04	301	1.40×10^{13}
10	62.0	2.65×10^{-3}	8.22×10^{-2}	64.0	1.43	2.18	567	4.68×10^{17}
11	8.13	1.77×10^{-3}	6.72×10^{-2}	4.44	1.97×10^{-2}	4.07	51.2	6.16×10^{12}
12	8.13	7.30×10^{-3}	1.36×10^{-1}	9.87	1.75	2.67	64.5	1.15×10^{17}
13	4.53	7.66×10^{-4}	4.42×10^{-2}	1.14	1.66×10^{-2}	3.44	5.4	5.67×10^{11}
14	4.53	4.08×10^{-3}	1.02×10^{-1}	2.88	1.56	2.38	8.6	1.48×10^{16}

Table B.4 Microhydrodynamic Parameters Calculated Using the Ma–Ahmadi RDF

Run No.	g_0 (-)	θ (m^2/s^2)	u_b (m/s)	ν (kHz)	σ_b^{max} (GPa)	α_b (μm)	a (mHz)	$\Pi\sigma_y$ (J^2/m^6s)
1	5.18	1.37×10^{-3}	5.90×10^{-2}	2.05	1.87×10^{-2}	3.87	15.5	1.91×10^{12}
2	5.18	4.60×10^{-3}	1.08×10^{-1}	4.12	1.60	2.44	16.3	2.73×10^{16}
3	13.7	7.31×10^{-4}	4.31×10^{-2}	5.64	1.65×10^{-2}	3.41	61.8	4.54×10^{12}
4	13.7	2.32×10^{-3}	7.69×10^{-2}	11.0	1.39	2.12	61.7	6.04×10^{16}
5	5.18	5.48×10^{-3}	1.18×10^{-1}	4.10	2.47×10^{-2}	5.11	54.1	1.16×10^{13}
6	5.18	1.31×10^{-2}	1.83×10^{-1}	6.94	1.97	3.00	41.8	1.06×10^{17}
7	13.7	2.47×10^{-3}	7.93×10^{-2}	10.4	2.10×10^{-2}	4.35	185	2.21×10^{13}
8	13.7	9.43×10^{-3}	1.55×10^{-1}	22.2	1.84	2.81	218	3.73×10^{17}
9	48.6	5.26×10^{-4}	3.66×10^{-2}	20.4	1.54×10^{-2}	3.20	294	1.51×10^{13}
10	48.6	3.28×10^{-3}	9.14×10^{-2}	55.8	1.49	2.28	538	4.84×10^{17}
11	8.06	1.79×10^{-3}	6.74×10^{-2}	4.41	1.97×10^{-2}	4.08	51.1	6.17×10^{12}
12	8.06	7.35×10^{-3}	1.37×10^{-1}	9.82	1.75	2.68	64.4	1.15×10^{17}
13	3.92	8.50×10^{-4}	4.65×10^{-2}	1.04	1.70×10^{-2}	3.52	5.1	5.62×10^{11}
14	3.92	4.51×10^{-3}	1.07×10^{-1}	2.62	1.59	2.43	8.1	1.46×10^{16}

Table B.5 Statistical Summary of Parameter Estimation (Runs 1–10) Using the *n*th-order Kinetic Model

Run	Parameter	Value	p value (-)_	R^2 (-)	Adj. R^2 (-)	SSR (-)
1	d_{lim} (µm)	0.161	0.0015	0.989	0.987	0.077
	k (µm^{n-1}min^{-1})	0.105	0.0002			
	n (-)	1.86	<0.0001			
2	d_{lim} (µm)	0.132	<0.0001	0.995	0.994	0.029
	k (µm^{n-1}min^{-1})	0.217	<0.0001			
	n (-)	2.06	<0.0001			
3	d_{lim} (µm)	0.158	<0.0001	0.996	0.996	0.022
	k (µm^{n-1}min^{-1})	0.432	<0.0001			
	n (-)	1.90	<0.0001			
4	d_{lim} (µm)	0.142	<0.0001	0.997	0.997	0.013
	k (µm^{n-1}min^{-1})	0.686	<0.0001			
	n (-)	2.08	<0.0001			
5	d_{lim} (µm)	0.152	<0.0001	0.995	0.994	0.030
	k (µm^{n-1}min^{-1})	0.215	<0.0001			
	n (-)	1.95	<0.0001			
6	d_{lim} (µm)	0.137	<0.0001	0.997	0.997	0.016
	k (µm^{n-1}min^{-1})	0.461	<0.0001			
	n (-)	2.10	<0.0001			
7	d_{lim} (µm)	0.154	<0.0001	0.996	0.995	0.023
	k (µm^{n-1}min^{-1})	0.806	<0.0001			
	n (-)	1.96	<0.0001			
8	d_{lim} (µm)	0.143	<0.0001	0.998	0.998	0.009
	k (µm^{n-1}min^{-1})	1.28	<0.0001			
	n (-)	2.12	<0.0001			
9	d_{lim} (µm)	0.134	<0.0001	0.995	0.994	0.021
	k (µm^{n-1}min^{-1})	2.41	<0.0001			
	n (-)	2.52	<0.0001			
10	d_{lim} (µm)	0.129	<0.0001	0.996	0.995	0.018
	k (µm^{n-1}min^{-1})	2.74	<0.0001			
	n (-)	2.56	<0.0001			

Table B.6 Statistical Summary of the Estimated MLRM Coefficients Correlating the Breakage Rate Constant *k* to the Micro-Hydrodynamic Parameters Calculated with the Carnahan–Starling RDF

Approach	Best Model	Parameter			Model			
		Symbol[a]	Coefficient[b]	p value	R^2	Adj. R^2	SSR[c]	p value
First order-MLRM	BM_1	a (mHz)	8.67×10^{-3}	4.16×10^{-8}	0.969	0.966	0.679	4.16×10^{-8}
	BM_2	**α_b (μm)**	-1.90×10^{-2}	5.25×10^{-1}	0.971	0.963	0.704	7.29×10^{-7}
		a (mHz)	9.03×10^{-3}	2.17×10^{-6}				
	BM_3	**σ_b^{max} (GPa)**	8.78×10^{-2}	2.51×10^{-1}	0.976	0.966	0.847	4.85×10^{-6}
		α_b (μm)	-2.77×10^{-2}	3.63×10^{-1}				
		a (mHz)	8.75×10^{-3}	8.53×10^{-6}				
	BM_4	**σ_b^{max} (GPa)**	1.81×10^{-1}	1.48×10^{-1}	0.980	0.967	1.124	3.07×10^{-5}
		α_b (μm)	-4.80×10^{-2}	2.02×10^{-1}				
		a (mHz)	9.65×10^{-3}	1.27×10^{-4}				
		$\Pi\sigma_y$ ($\times10^{-16}$ J^2/m^6s)	-1.13×10^{-2}	3.11×10^{-1}				
Second order-MLRM	BM_1	a (mHz)	8.67×10^{-3}	4.16×10^{-8}	0.969	0.966	0.679	4.16×10^{-8}
	BM_2	a (mHz)	9.17×10^{-3}	6.56×10^{-7}	0.974	0.967	0.656	4.70×10^{-7}
		α_b^2 (μm^2)	-6.80×10^{-3}	2.68×10^{-1}				
	BM_3	**α_b (μm)**	1.56×10^{-1}	1.14×10^{-1}	0.982	0.974	0.661	1.76×10^{-6}
		a (mHz)	8.58×10^{-3}	3.90×10^{-6}				
		α_b^2 (μm^2)	-3.83×10^{-2}	7.27×10^{-2}				
	BM_4	**a (mHz)**	3.32×10^{-3}	9.94×10^{-2}	0.990	0.983	0.845	4.35×10^{-6}
		$\Pi\sigma_y$ ($\times10^{-16}$ J^2/m^6s)	6.48×10^{-2}	2.25×10^{-2}				
		a^2 (mHz^2)	2.35×10^{-5}	1.81×10^{-2}				
		$\Pi\sigma_y^2$($\times10^{-32}$ $J^4/m^{12}s^2$)	-1.81×10^{-3}	2.28×10^{-2}				
MLRM with interaction	BM_1	a (mHz)	8.67×10^{-3}	4.16×10^{-8}	0.969	0.966	0.679	4.16×10^{-8}
	BM_2	**α_b (μm)**	-1.90×10^{-2}	5.25×10^{-1}	0.971	0.963	0.704	7.29×10^{-7}
		a (mHz)	9.03×10^{-3}	2.17×10^{-6}				
	BM_3	a (mHz)	2.80×10^{-2}	5.31×10^{-5}	0.995	0.993	0.446	1.81×10^{-8}
		$\alpha_b a$ (μm.mHz)	-4.39×10^{-3}	4.90×10^{-4}				
		$a\Pi\sigma_y$ ($\times10^{-16}$ mHz·J^2/m^6s)	-1.67×10^{-4}	1.04×10^{-3}				
	BM_4	a (mHz)	1.32×10^{-2}	7.50×10^{-6}	0.995	0.992	0.332	3.89×10^{-7}
		$\sigma_b^{max}\alpha_b$ (GPa·μm)	4.44×10^{-2}	2.97×10^{-2}				
		$\sigma_b^{max}\Pi\sigma_y$ ($\times10^{-16}$ GPa·J^2/m^6s)	1.38×10^{2}	1.64×10^{-3}				
		$\alpha_b\Pi\sigma_y$ ($\times10^{-16}$ μm·J^2/m^6s)	-9.05×10^{1}	1.64×10^{-3}				

[a]Statistically insignificant (p value > 0.01) parameters are **bolded** and the best model was indicated by red color. $\Pi\sigma_y$ is treated as a single parameter as σ_y is a constant; [b]The coefficients have the units that make the MLRM equation dimensionally homogeneous; [c]The unit of SSR is $\mu m^{2n-2}min^{-2}$.

Table B.7 Statistical Summary of the Estimated MLRM Coefficients Correlating the Breakage Rate Constant k to the Micro-Hydrodynamic Parameters Calculated with the Lun RDF

Approach	Best Model	Parameter			Model			
		Symbol[a]	Coefficient[b]	p value	R^2	Adj. R^2	SSR	p value
First-order MLRM	BM_1	a (mHz)	5.55×10^{-3}	7.70×10^{-7}	0.941	0.935	2.355	7.70×10^{-7}
	BM_2	**σ_b^{max} (GPa)**	6.90×10^{-2}	5.46×10^{-1}	0.944	0.930	2.536	9.86×10^{-6}
		a (mHz)	5.36×10^{-3}	1.32×10^{-5}				
	BM_3	**σ_b^{max} (GPa)**	2.27×10^{-1}	9.66×10^{-2}				
		a (mHz)	6.46×10^{-3}	3.84×10^{-5}	0.966	0.951	2.437	1.72×10^{-5}
		$\Pi\sigma_y$ ($\times10^{-16}$ J^2/m^6s)	-2.20×10^{-2}	7.32×10^{-2}				
	BM_4	**σ_b^{max} (GPa)**	2.67×10^{-1}	1.34×10^{-1}				
		α_b (μm)	-1.96×10^{-2}	6.71×10^{-1}	0.967	0.945	3.164	1.43×10^{-4}
		a (mHz)	6.73×10^{-3}	4.40×10^{-4}				
		$\Pi\sigma_y$ ($\times10^{-16}$ J^2/m^6s)	-2.50×10^{-2}	1.03×10^{-1}				
Second-order MLRM	BM_1	a (mHz)	5.55×10^{-3}	7.70×10^{-7}	0.941	0.935	2.355	7.70×10^{-7}
	BM_2	a (mHz)	5.37×10^{-3}	1.00×10^{-5}				
		σ_b^{max2} (GPa^2)	4.10×10^{-2}	5.25×10^{-1}	0.944	0.930	2.465	9.66×10^{-6}
	BM_3	a (mHz)	6.81×10^{-3}	1.24×10^{-5}				
		$\Pi\sigma_y$ ($\times10^{-16}$ J^2/m^6s)	4.49×10^{-2}	6.49×10^{-2}	0.975	0.965	1.601	5.46×10^{-6}
		$\Pi\sigma_y^2$($\times10^{-32}$ $J^4/m^{12}s^2$)	-1.44×10^{-3}	2.65×10^{-2}				
	BM_4	a (mHz)	6.86×10^{-3}	5.31×10^{-5}				
		$\Pi\sigma_y$ ($\times10^{-16}$ J^2/m^6s)	7.34×10^{-2}	3.10×10^{-1}	0.976	0.960	1.733	5.34×10^{-5}
		σ_b^{max2} (GPa^2)	-6.99×10^{-2}	6.64×10^{-1}				
		$\Pi\sigma_y^2$($\times10^{-32}$ $J^4/m^{12}s^2$)	-2.01×10^{-3}	1.91×10^{-1}				
MLRM with interaction terms	BM_1	$\alpha_b a$ (μm·mHz)	2.07×10^{-3}	4.02×10^{-6}	0.915	0.906	2.041	4.02×10^{-6}
	BM_2	a (mHz)	7.15×10^{-3}	5.13×10^{-6}				
		$a\Pi\sigma_y$ ($\times10^{-16}$ mHz·J^2/m^6s)	-4.80×10^{-5}	2.31×10^{-2}	0.970	0.963	1.479	7.76×10^{-7}
	BM_3	a (mHz)	6.98×10^{-3}	1.37×10^{-5}				
		σ_b^{max} α_b (GPa·μm)	3.76×10^{-2}	2.29×10^{-1}	0.976	0.966	1.461	4.78×10^{-6}
		$a\Pi\sigma_y$ ($\times10^{-16}$ mHz J^2/m^6s)	-5.06×10^{-5}	1.82×10^{-2}				
	BM_4	a (mHz)	1.61×10^{-2}	2.22×10^{-8}				
		$\Pi\sigma_y$ ($\times10^{-16}$ J^2/m^6s)	1.58×10^{-2}	1.49×10^{-5}	1.000	0.999	0.034	1.35×10^{-10}
		$\alpha_b a$ (μm·mHz)	-2.65×10^{-3}	6.11×10^{-7}				
		$a\Pi\sigma_y$ ($\times10^{-16}$ mHz·J^2/m^6s^2)	-1.45×10^{-4}	7.60×10^{-8}				

[a]Statistically insignificant (p value > 0.01) parameters are **bolded** and the best model was indicated by red color. $\Pi\sigma_y$ is treated as a single parameter as σ_y is a constant; [b]The coefficients have the units that make the MLRM equation dimensionally homogeneous; [c]The unit of SSR is $\mu m^{2n-2}min^{-2}$.

Table B.8 Statistical Summary of the Estimated MLRM Coefficients Correlating the Breakage Rate Constant k to the Micro-Hydrodynamic Parameters Calculated with the Ma–Ahmadi RDF

Approach	Best Model	Parameter			Model			
		Symbol[a]	Coefficient[b]	p value	R^2	Adj. R^2	SSR	p value
First order-MLRM	BM_1	a (mHz)	5.77×10^{-3}	5.54×10^{-7}	0.945	0.939	1.963	5.54×10^{-7}
	BM_2	**a (mHz)**	6.01×10^{-2}	5.85×10^{-1}				
		$\Pi\sigma_y$ ($\times10^{-16}$ J^2/m^6s)	5.59×10^{-3}	1.06×10^{-5}	0.947	0.934	2.181	7.64×10^{-6}
	BM_3	**σ_b^{max} (GPa)**	2.10×10^{-1}	1.03×10^{-1}				
		a (mHz)	6.71×10^{-3}	2.99×10^{-5}				
		$\Pi\sigma_y$ ($\times10^{-16}$ J^2/m^6s)	-2.10×10^{-2}	6.89×10^{-2}	0.968	0.955	2.033	1.30×10^{-5}
	BM_4	**σ_b^{max} (GPa)**	2.64×10^{-1}	1.17×10^{-1}				
		α_b (μm)	-2.71×10^{-2}	5.44×10^{-1}				
		a (mHz)	7.12×10^{-3}	3.40×10^{-4}				
		$\Pi\sigma_y$ ($\times10^{-16}$ J^2/m^6s)	-2.53×10^{-2}	8.35×10^{-2}	0.970	0.951	2.502	1.02×10^{-4}
Second order-MLRM	BM_1	a (mHz)	5.77×10^{-3}	5.54×10^{-7}	0.945	0.939	1.963	5.54×10^{-7}
	BM_2	a (mHz)	6.98×10^{-3}	1.41×10^{-5}				
		$\Pi\sigma_y^2$($\times10^{-32}$ $J^4/m^{12}s^2$)	-3.62×10^{-4}	9.06×10^{-2}	0.963	0.953	2.113	1.96×10^{-6}
	BM_3	a (mHz)	7.03×10^{-3}	1.27×10^{-5}				
		$\Pi\sigma_y$ ($\times10^{-16}$ J^2/m^6s)	3.71×10^{-2}	9.87×10^{-2}				
		$\Pi\sigma_y^2$($\times10^{-32}$ $J^4/m^{12}s^2$)	-1.20×10^{-3}	3.80×10^{-2}	0.975	0.965	1.377	5.42×10^{-6}
	BM_4	a (mHz)	7.78×10^{-3}	5.09×10^{-5}				
		$\Pi\sigma_y$ ($\times10^{-16}$ J^2/m^6s)	4.83×10^{-2}	4.50×10^{-2}				
		α_b^2 (μm^2)	-1.14×10^{-2}	1.68×10^{-1}				
		$\Pi\sigma_y^2$($\times10^{-32}$ $J^4/m^{12}s^2$)	-1.58×10^{-3}	1.83×10^{-2}	0.983	0.971	1.297	2.11×10^{-5}
MLRM with interaction	BM_1	a (mHz)	5.77×10^{-3}	5.54×10^{-7}	0.945	0.939	1.963	5.54×10^{-7}
	BM_2	a (mHz)	7.23×10^{-3}	5.92×10^{-6}				
		$a\Pi\sigma_y$ ($\times10^{-16}$ mHz·J^2/m^6s)	-4.33×10^{-5}	3.69×10^{-2}	0.969	0.962	1.398	8.87×10^{-7}
	BM_3	a (mHz)	1.76×10^{-2}	2.28×10^{-5}				
		$\alpha_b a$ (μm·mHz)	-2.93×10^{-3}	5.86×10^{-4}				
		$a\Pi\sigma_y$ ($\times10^{-16}$ mHz·J^2/m^6s)	-1.18×10^{-4}	8.94×10^{-5}	0.995	0.993	0.822	2.21×10^{-8}
	BM_4	a (mHz)	1.79×10^{-2}	5.61×10^{-7}				
		$\Pi\sigma_y$ ($\times10^{-16}$ J^2/m^6s)	1.12×10^{-2}	1.85×10^{-3}				
		$\alpha_b a$ (μm·mHz)	-3.05×10^{-3}	1.02×10^{-5}				
		$a\Pi\sigma_y$ ($\times10^{-16}$ mHz·J^2/m^6s^2)	-1.42×10^{-4}	2.15×10^{-6}	0.999	0.998	0.146	2.94×10^{-9}

[a]Statistically insignificant (p value > 0.01) parameters are **bolded** and the best model was indicated by red color. $\Pi\sigma_y$ is treated as a single parameter as σ_y is a constant; [b]The coefficients have the units that make the MLRM equation dimensionally homogeneous; [c]The unit of SSR is $\mu m^{2n-2}min^{-2}$.

Table B.9 Statistical Summary of the Estimated Empirical MLRM Coefficients Correlating the Breakage Rate Constant *k* to the Process Parameters–Bead Properties

Approach	Best Model	Parameter			Model			
		Symbol[a]	Coefficient[b]	p value	R^2	Adj. R^2	SSR	p value
First-order MLRM	BM_1	c (-)	2.28	1.46×10^{-3}	0.694	0.660	6.723	1.46×10^{-3}
	BM_2	**ω (rpm)**	-4.62×10^{-4}	9.88×10^{-2}	0.787	0.733	5.685	2.07×10^{-3}
		c (-)	5.65	1.61×10^{-2}				
	BM_3	c (-)	7.87	2.12×10^{-3}				
		ρ_b (kg/m^3)	-2.82×10^{-3}	9.43×10^{-3}	0.890	0.844	3.777	9.68×10^{-4}
		Y_b (GPa)	7.19×10^{-2}	9.42×10^{-3}				
	BM_4	**ω (rpm)**	3.31×10^{-4}	4.00×10^{-1}				
		c (-)	7.87	3.41×10^{-3}				
		ρ_b (kg/m^3)	-3.97×10^{-3}	3.87×10^{-2}	0.904	0.839	4.181	3.32×10^{-3}
		Y_b (GPa)	1.01×10^{-1}	3.76×10^{-2}				
Second-order MLRM	BM_1	c^2 (-)	4.88	1.33×10^{-4}	0.817	0.797	4.281	1.33×10^{-4}
	BM_2	**c (-)**	-4.84	1.43×10^{-2}	0.918	0.897	2.153	4.61×10^{-5}
		c^2 (-)	1.43×10^{1}	1.62×10^{-3}				
	BM_3	**ω (rpm)**	4.70×10^{-4}	9.56×10^{-2}				
		c (-)	-1.22×10^{1}	1.96×10^{-2}	0.946	0.923	1.780	8.28×10^{-5}
		c^2 (-)	2.21×10^{1}	2.63×10^{-3}				
	BM_4	c (-)	-4.41×10^{1}	3.49×10^{-3}				
		Y_b (GPa)	5.82	6.42×10^{-3}				
		c^2 (-)	5.63×10^{1}	1.51×10^{-3}	0.982	0.970	0.715	2.35×10^{-5}
		Y_b^2 (GPa^2)	-2.89×10^{-2}	6.43×10^{-3}				
MLRM with interaction terms	BM_1	ωc (rpm)	6.54×10^{-4}	1.16×10^{-3}	0.708	0.676	6.397	1.16×10^{-3}
	BM_2	ω (rpm)	-7.60×10^{-4}	6.11×10^{-3}				
		ωc (rpm)	2.24×10^{-3}	9.22×10^{-4}	0.892	0.865	2.897	1.36×10^{-4}
	BM_3	ω (rpm)	-8.01×10^{-4}	6.74×10^{-3}				
		ωc (rpm)	2.24×10^{-3}	1.42×10^{-3}	0.905	0.864	3.402	5.97×10^{-4}
		ωY_b (rpm·GPa)	4.14×10^{-7}	3.66×10^{-1}				
	BM_4	**ωc (rpm)**	2.29×10^{-3}	1.50×10^{-2}				
		$\omega\rho_b$ (rpm·kg/m^3)	-8.17×10^{-7}	2.62×10^{-2}				
		ωY_b (rpm·GPa)	2.10×10^{-5}	3.99×10^{-2}				
		$c\rho_b$ (kg/m^3)	-5.21×10^{-5}	9.16×10^{-1}	0.905	0.842	5.060	3.19×10^{-3}

[a]Statistically insignificant (p value > 0.01) parameters are **bolded** and the best model was indicated by red color; [b]The coefficients have the units that make the MLRM equation dimensionally homogeneous; [c]The unit of SSR is $\mu m^{2n-2}min^{-2}$.

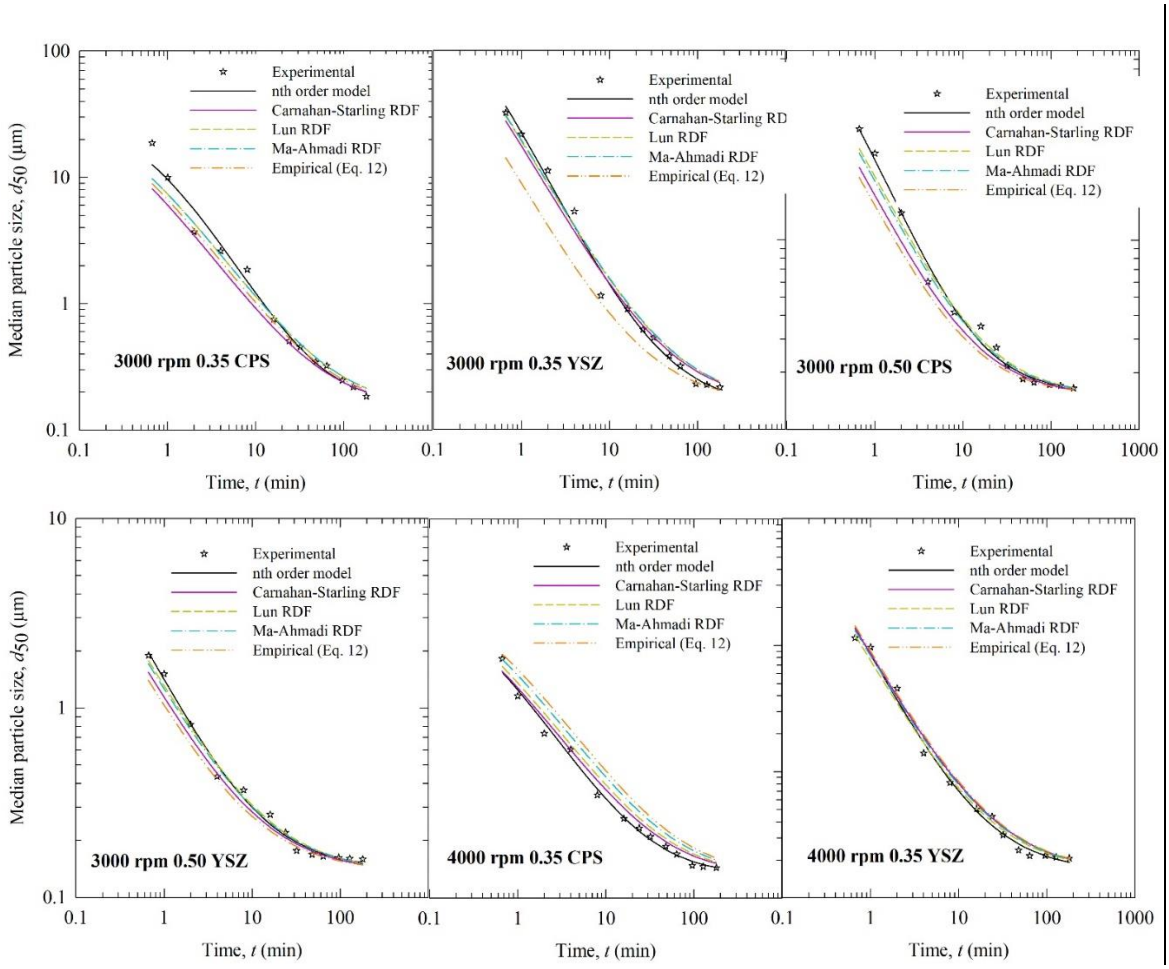

Figure B.1 Timewise evolution of the median particle size: experimental data, *n*th-order kinetics model fit, and predictions by Equations (6.7–6.10) with averaged d_{lim} and n values for each bead material (Runs 1–6).

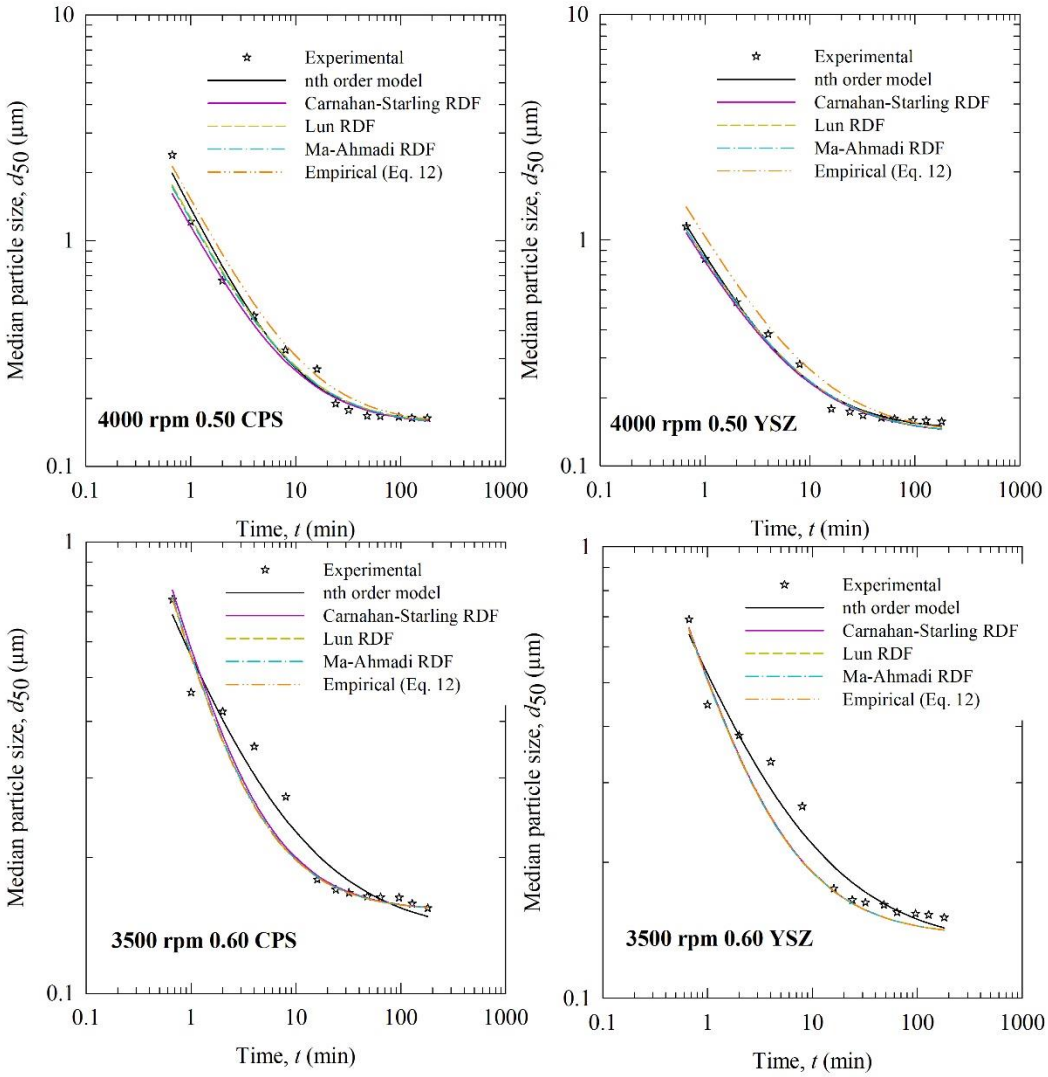

Figure B.2 Timewise evolution of the median particle size: experimental data, *n*th-order kinetics model fit, and predictions by Equations (6.7–6.10) with averaged d_{lim} and n values for each bead material (Runs 7–10).

APPENDIX C

SUPPLEMENTARY DATA FOR CHAPTER 4

This appendix contains supportive tables and figures about the thermal analysis of wet stirred media milling as referred in Chapter 4.

Table C.1 Characteristic Temperatures and Times for Each Milling Run

Run No.	$t_{T(22)}$ (min) [b]	$t_{T(32)}$ (min) [b]	$t_{T(42)}$ (min)[b]	$t_{T(45)}$ (min)[b]	$T_{t(5)}$ (°C)[c]	$T_{t(10)}$ (°C)[c]	$T_{t(30)}$ (°C)[c]	T_{max} (°C)[c]	N_m [c]	TDS (-)
1	31	N/A	N/A	N/A	19	20	21	22	1	91.0
2	28	N/A	N/A	N/A	20	21	22	22	1	91.0
3	24	N/A	N/A	N/A	20	21	22	23	1	89.7
4	23	N/A	N/A	N/A	19	19	22	23	1	89.7
5	10	N/A	N/A	N/A	21	22	24	24	1	88.4
6	5	N/A	N/A	N/A	22	22	24	24	1	88.4
7	3	N/A	N/A	N/A	23	24	25	26	1	86.1
8	3	N/A	N/A	N/A	24	25	26	26	1	86.1
9	2.6	N/A	N/A	N/A	24	25	26	27	1	85.0
10	3.3	30	N/A	N/A	24	27	32	32	1	80.3
11	1.6	12	N/A	N/A	28	31	33	34	1	78.7
12	1.3	12	N/A	N/A	28	31	34	35	1	78.0
13	2.4	10	N/A	N/A	27	32	36	36	1	77.2
14	1.4	7	N/A	N/A	31	33	36	37	1	76.5
15	0.8	5	N/A	N/A	32	34	37	38	1	75.9
16	1.3	5	N/A	N/A	32	38	41	41	1	74.0
17	0.9	3.4	20	N/A	35	39	42	42	1	73.4
18	0.9	3.0	17	N/A	36	39	43	43	1	72.8
19	0.4	2.7	10	31	38	42	44	45	2	56.9
20	0.8	2.3	6.5	12.8	40	44	N/A	45	5	41.9
21	1.0	2.2	7	12.2	39	43	N/A	45	5	41.9
22	1.0	2.0	7.5	18.5	40	42	N/A	45	4	45.2
23	0.5	1.5	5	8.5	42	N/A	N/A	45	8	35.9
24	0.5	1.3	4	7	43	N/A	N/A	45	9	34.5
25	0.7	1.3	4	6.8	43	N/A	N/A	45	10	33.3
26	0.6	1.3	3.5	4.7	N/A	N/A	N/A	45	13	30.5
27	0.3	0.8	1.7	2	N/A	N/A	N/A	45	33	22.4

[a]stirrer speed (rpm), bead loading (-), bead size (μm).[b]time required for the mill outlet temperature (°C) to reach the specified temperature; N/A: this temperature was not reached within 60 min milling. [c]mill outlet temperature at the specified milling time (min). N/A: mill shut down at 45 °C for additional cooling prior to the specified milling time.

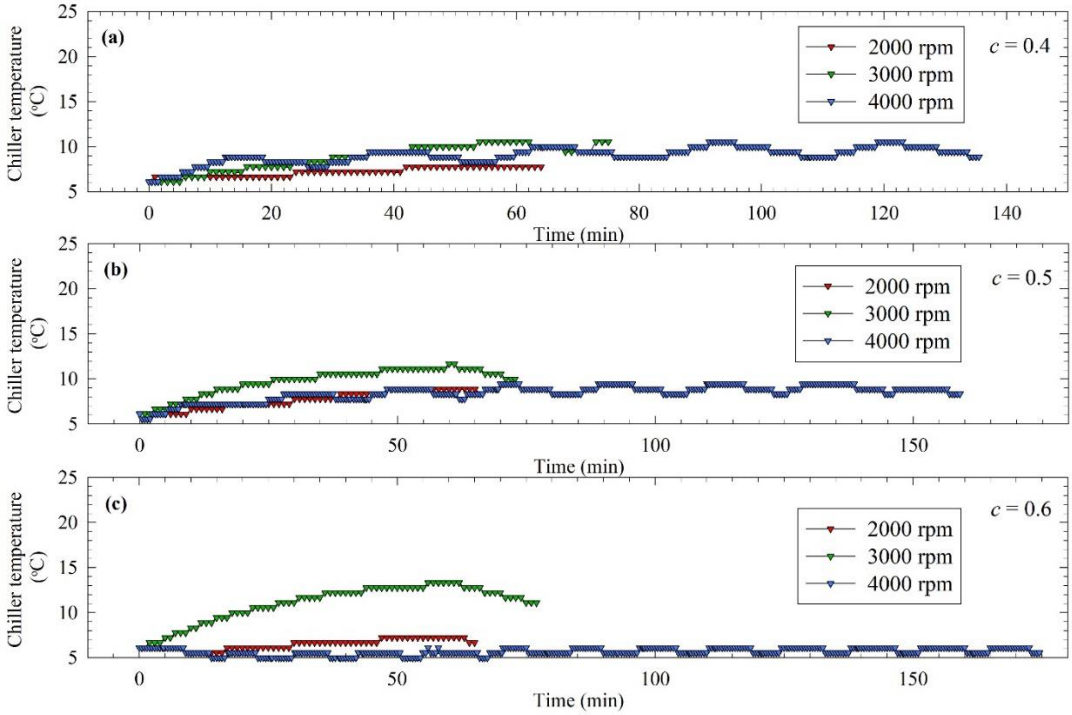

Figure C.1 Impact of stirrer speed on the timewise evolution of chiller liquid temperature for D_b = 400 µm beads at various loadings: (a) c = 0.4 (Runs 2, 11, 20), (b) c = 0.5 (Runs 5, 14, 23), and (c) c = 0.6 (Runs 8, 17, 26).

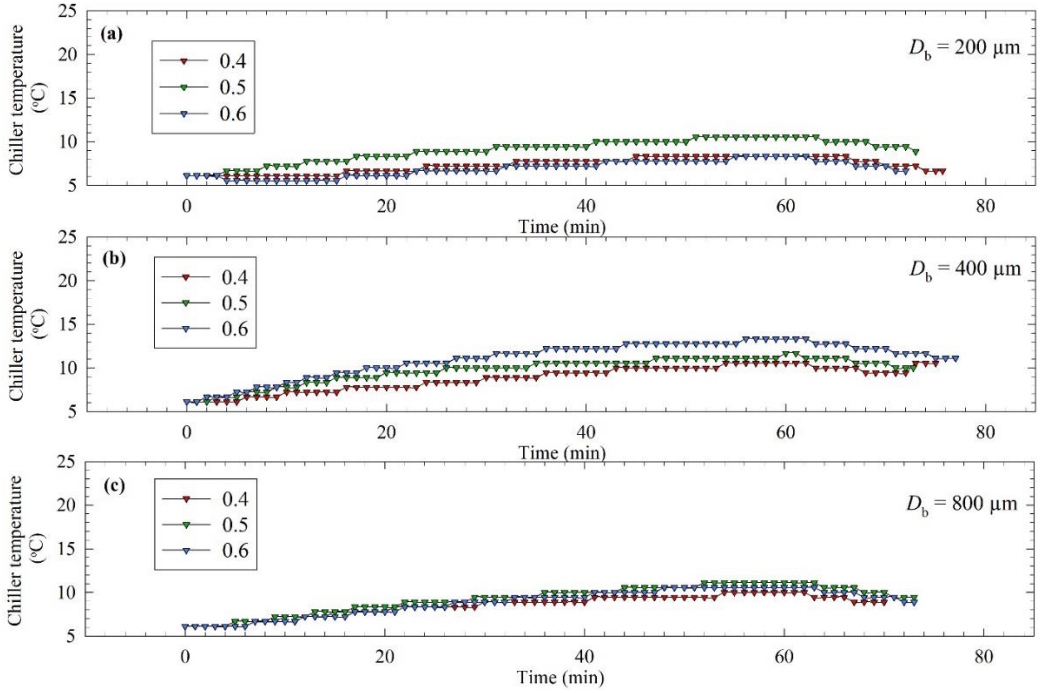

Figure C.2 Impact of bead loading on the timewise evolution of chiller liquid temperature for ω = 3000 rpm and various bead sizes: (a) D_b = 200 µm (Runs 10, 13, 16), (b) D_b = 400 µm (Runs 11, 14, 17), and (c) D_b = 800 µm (Runs 12, 15, 18).

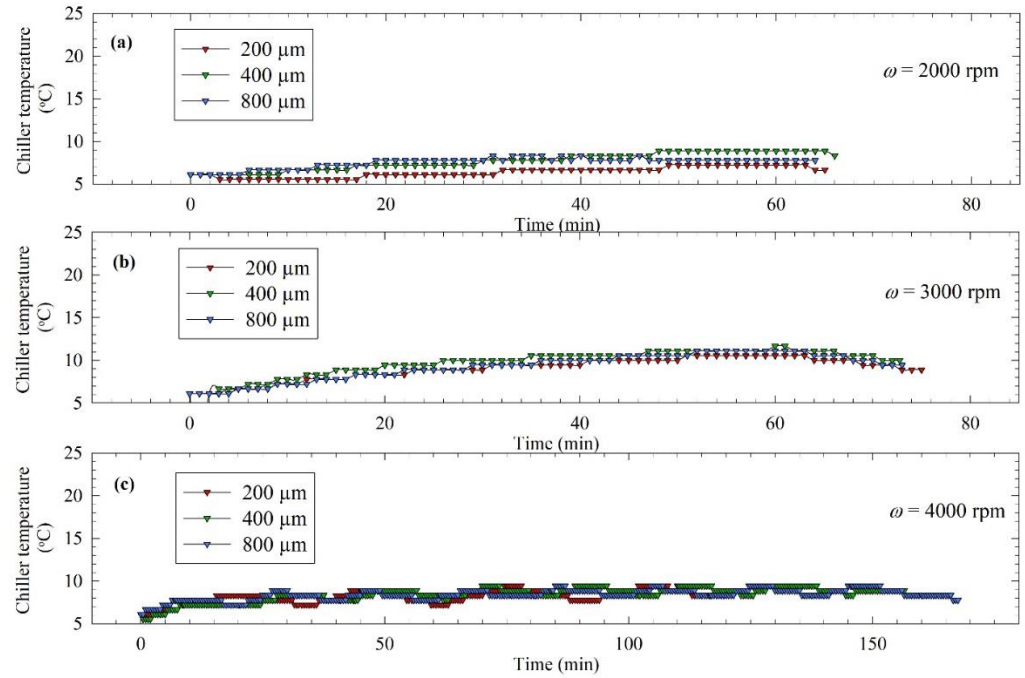

Figure C.3 Impact of bead size on the timewise evolution of chiller liquid temperature for c = 0.5 and various stirrer speeds: (a) ω = 2000 rpm (Runs 4–6), (b) ω = 3000 rpm (Runs 13–15), and (c) ω = 4000 rpm (Runs 22–24).

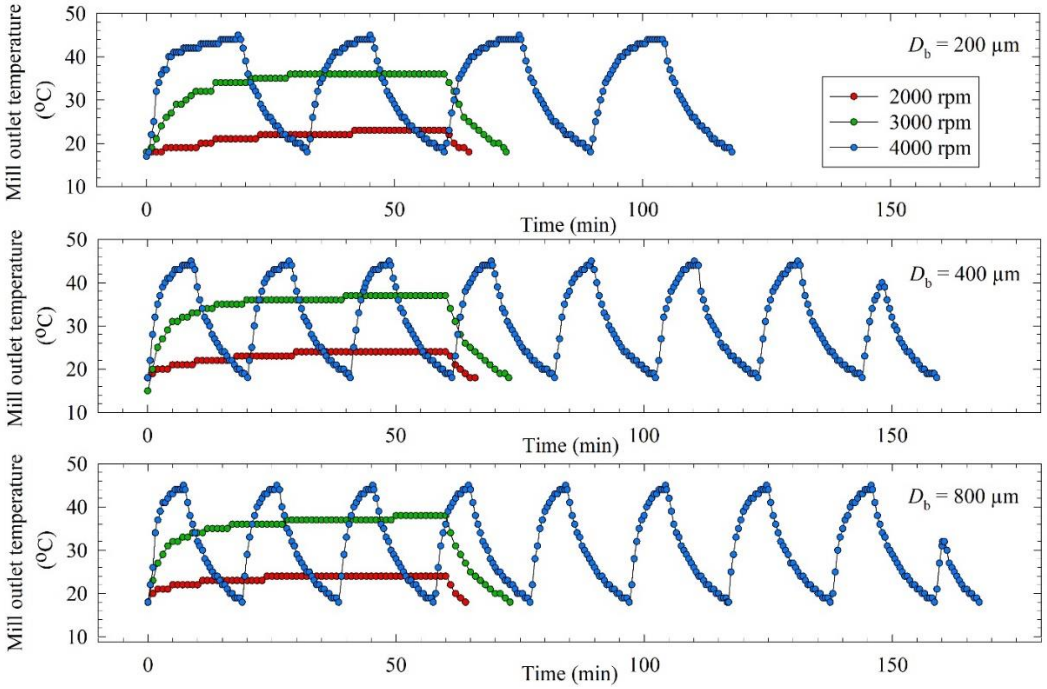

Figure C.4 Impact of stirrer speed on the timewise evolution of mill outlet temperature for c = 0.5 at various bead sizes: (top) D_b = 200 µm (Runs 4, 13, 22), (middle) D_b = 400 µm (Runs 5, 14, 23), and (bottom) D_b = 800 µm (Runs 6, 15, 24).

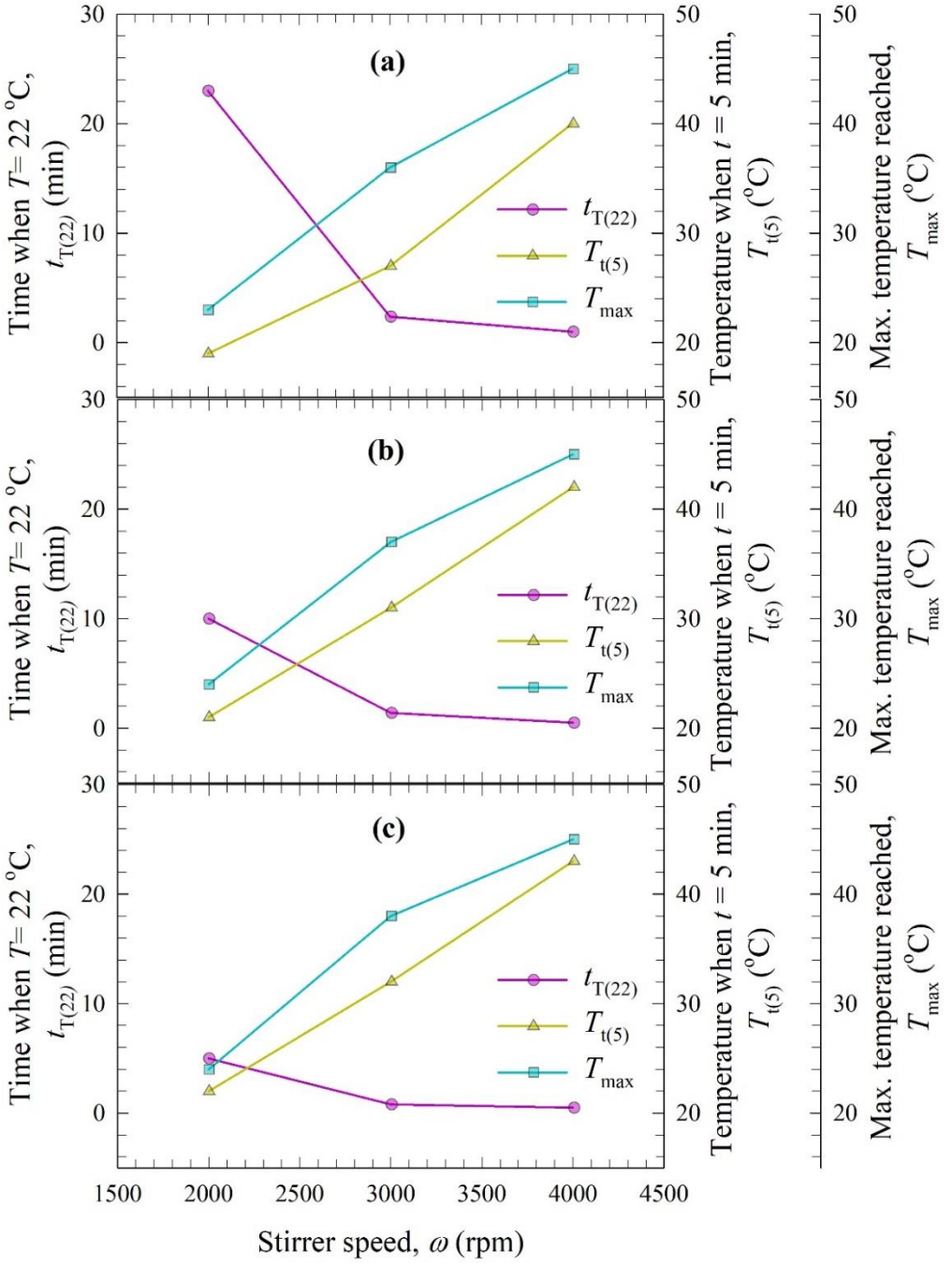

Figure C.5 Impact of stirrer speed on the characteristic time and temperatures for c = 0.5 at various bead sizes: (a) D_b = 200 μm (Runs 4, 13, 22), (b) D_b = 400 μm (Runs 5, 14, 23), and (c) D_b = 800 μm (Runs 6, 15, 24).

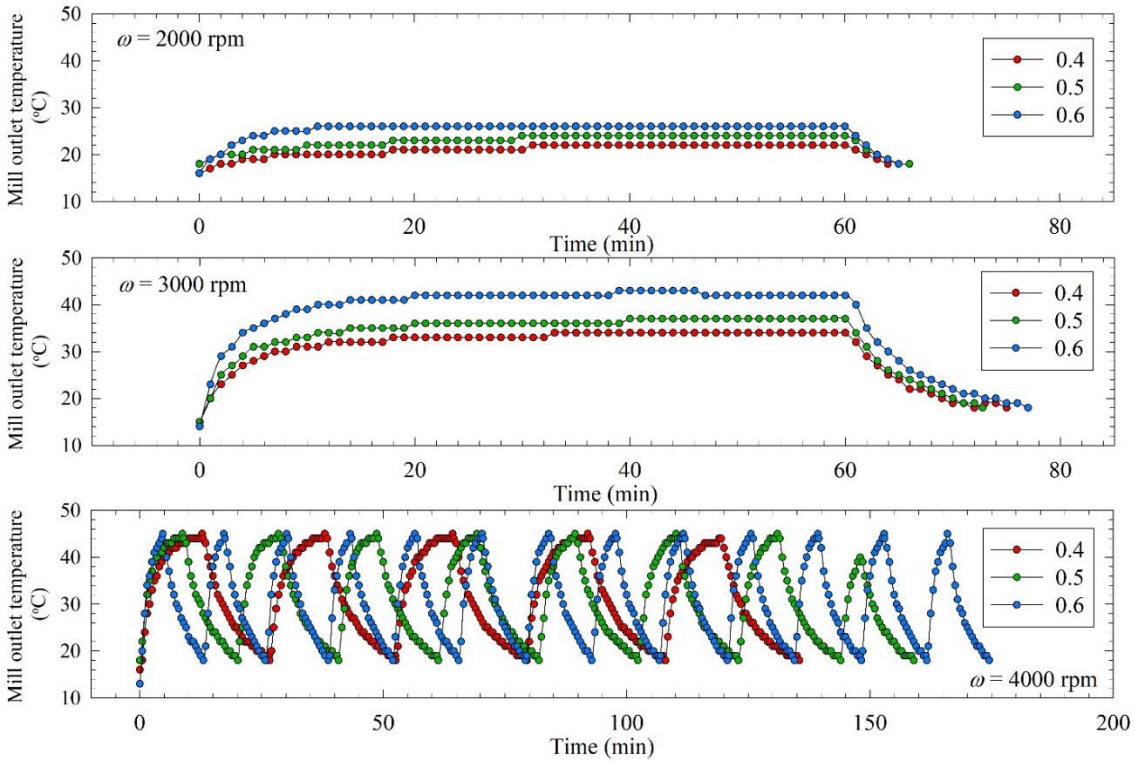

Figure C.6 Impact of bead loading on the timewise evolution of mill outlet temperature for D_b = 400 µm at various stirrer speeds: (top) ω = 2000 rpm (Runs 2, 5, 8), (middle) ω = 3000 rpm (Runs 11, 14, 17), and (bottom) ω = 4000 rpm (Runs 20, 23, 26).

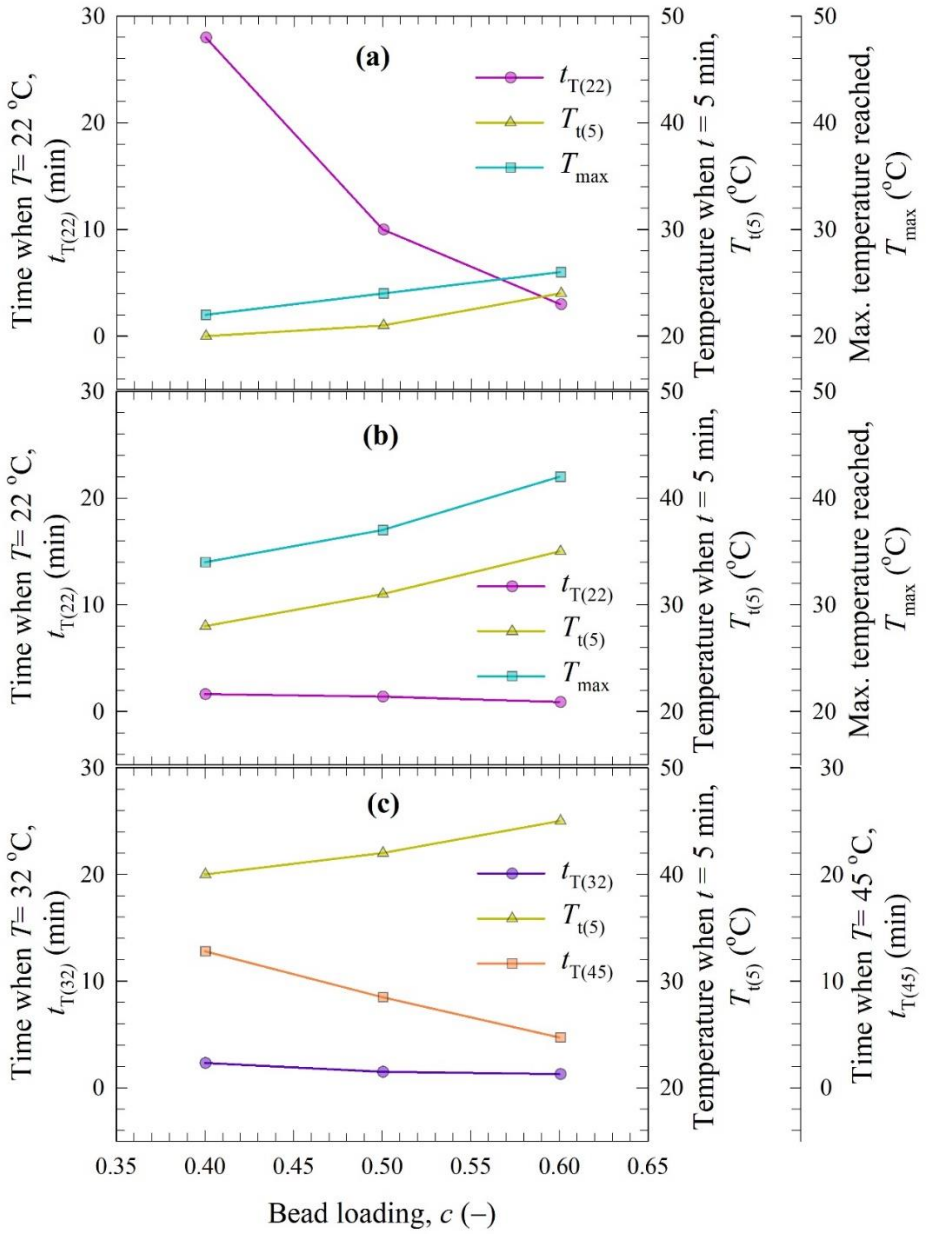

Figure C.7 Impact of bead loading on the characteristic time and temperatures for D_b = 400 µm at various stirrer speeds: (a) ω = 2000 rpm (Runs 2, 5, 8), (b) ω = 3000 rpm (Runs 11, 14, 17), and (c) ω = 4000 rpm (Runs 20, 23, 26).

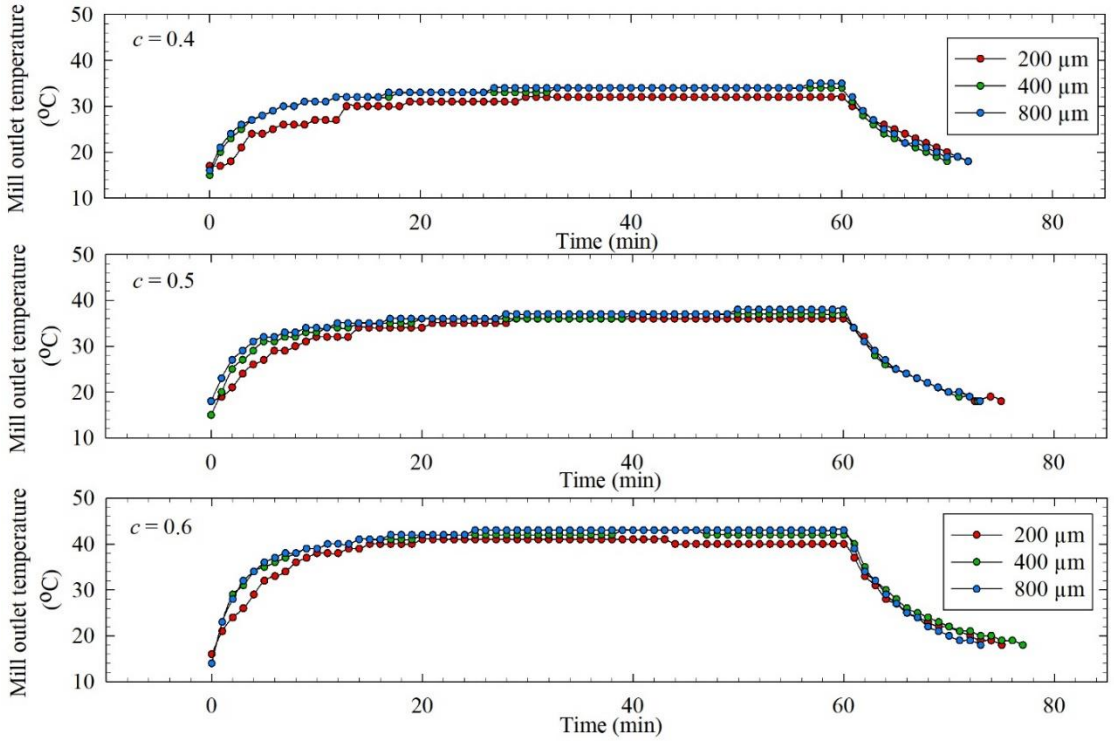

Figure C.8 Impact of bead size on the timewise evolution of mill outlet temperature for ω = 3000 rpm at various bead loadings: (top) c = 0.4 (Runs 10–12), (middle) c = 0.5 (Runs 13–15), and (bottom) c = 0.6 (Runs 16–18).

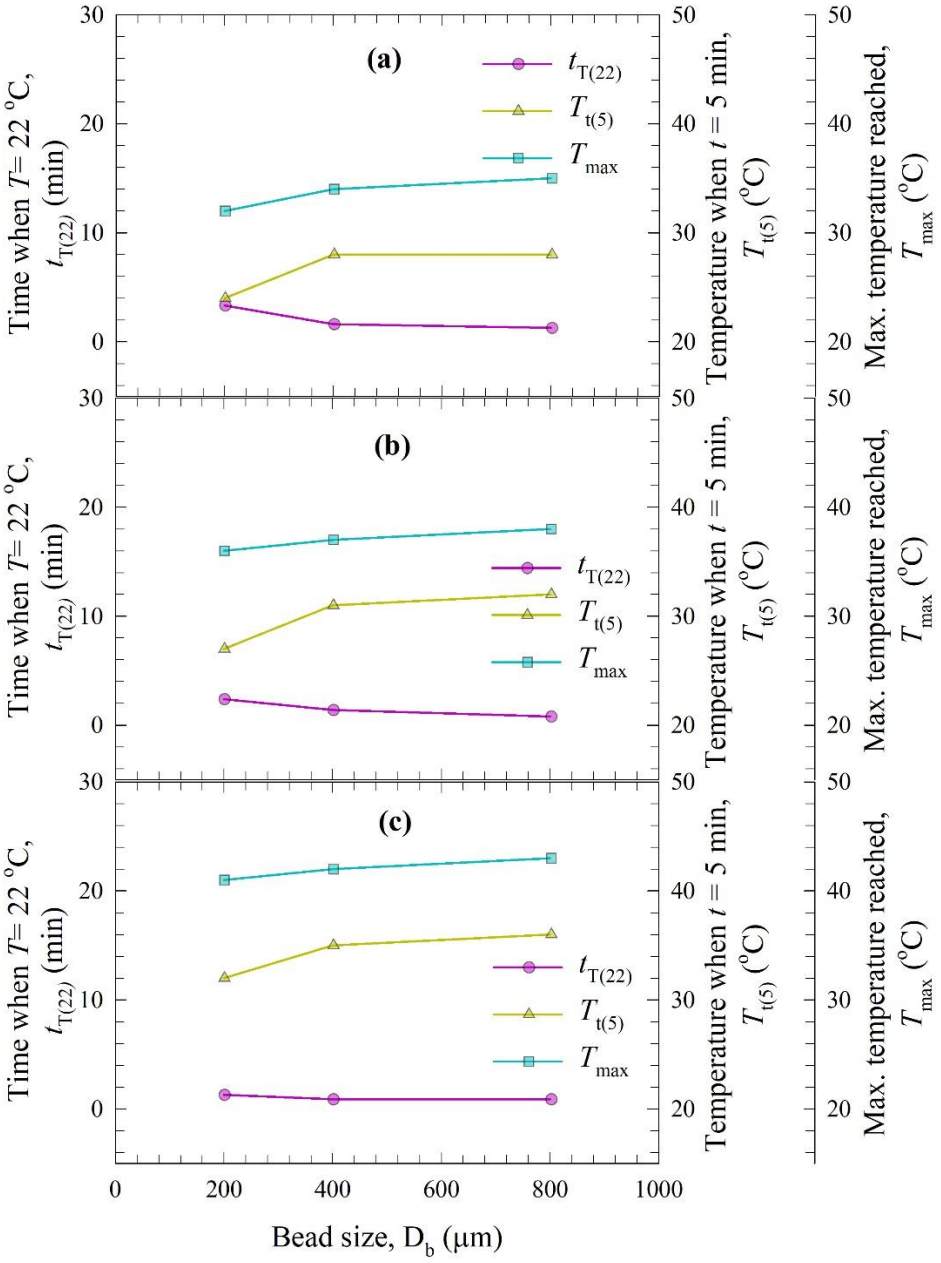

Figure C.9 Impact of bead size on the characteristic time and temperatures for ω = 3000 rpm with varying bead loadings: (a) c = 0.4 (Runs 10–12), (b) c = 0.5 (Runs 13–15), and (c) c = 0.6 (Runs 16–18).

APPENDIX D

SUPPLEMENTARY DATA FOR CHAPTER 5

This appendix contains the derivation of some correlations used for enthalpy balance model, as well as supportive figures and tables which was studied in Chapter 5.

D.1 Derivation of Heat Removed by the Chiller

The integration of a differential enthalpy balance for the coolant (chiller liquid) passing through the jacket (51) of the milling chamber leads to following expression for the heat removal rate from the milling chamber and overall enthalpy balance for the chiller liquid:

$$Q_{\mathrm{ch}} = UA_{\mathrm{m}} \frac{T_{\mathrm{ch,in}} - T_{\mathrm{ch,out}}}{\ln((T_{\mathrm{ch,in}} - T_{\mathrm{s,m}})/(T_{\mathrm{ch,out}} - T_{\mathrm{s,m}}))} \tag{D.1}$$

$$m_{\mathrm{ch}} C_{\mathrm{p,ch}} \left(T_{\mathrm{ch,out}} - T_{\mathrm{ch,in}}\right) = -Q_{\mathrm{ch}} = UA_{\mathrm{m}} \frac{T_{\mathrm{ch,out}} - T_{\mathrm{ch,in}}}{\ln((T_{\mathrm{ch,in}} - T_{\mathrm{s,m}})/(T_{\mathrm{ch,out}} - T_{\mathrm{s,m}}))} \tag{D.2}$$

In the derivation of the above expressions, one assumes plug flow of the chiller liquid inside the jacket (51) and makes a pseudo steady-state approximation due to time-dependence of the variables along with the well-mixedness assumption for the suspension in the mill and the holding tank (spatial invariance of $T_{\mathrm{s,m}}$ and $T_{\mathrm{s.ht}}$). The chiller liquid temperature entering the milling chamber $T_{\mathrm{ch,in}}$ was measured and recorded for each sampling time. Rearrangement of Equation D.2 yields

$$\ln((T_{\mathrm{ch,in}} - T_{\mathrm{s,m}})/(T_{\mathrm{ch,out}} - T_{\mathrm{s,m}})) = \frac{UA_{\mathrm{m}}}{m_{\mathrm{ch}} C_{\mathrm{p,ch}}} \tag{D.3}$$

This equation can be simplified by defining number of transfer units (NTU) as follows:

$$\frac{UA_{\mathrm{m}}}{m_{\mathrm{ch}} C_{\mathrm{p,ch}}} = \mathrm{NTU} \qquad \ln\left(\frac{T_{\mathrm{ch,in}} - T_{\mathrm{s,m}}}{T_{\mathrm{ch,out}} - T_{\mathrm{s,m}}}\right) = \mathrm{NTU} \tag{D.4}$$

$$T_{\mathrm{ch,out}} = T_{\mathrm{s,m}} + (T_{\mathrm{ch,in}} - T_{\mathrm{s,m}}) \exp(-\mathrm{NTU}) \tag{D.5}$$

which is identical to Equation (5.7) in the main text. Continuing derivation as:

$$T_{\mathrm{ch,in}} - T_{\mathrm{ch,out}} = T_{\mathrm{ch,in}}(1 - \exp(-\mathrm{NTU})) - T_{\mathrm{m}}(1 - \exp(-\mathrm{NTU})) = -(T_{\mathrm{ch,in}} - T_{\mathrm{s,m}})(1 - \exp(-\mathrm{NTU})) \quad \text{(D.6)}$$

The r.h.s. of Equation (D.2) could be rewritten with NTU as follows:

$$Q_{\mathrm{ch}} = UA_{\mathrm{m}}\left(T_{\mathrm{ch,in}} - T_{\mathrm{ch,out}}\right)/\mathrm{NTU} \quad \text{(D.7)}$$

By inserting Equation (D.6) and NTU definition into Equation (D.7), Equation (5.6) was obtained. Equation (5.8) was obtained in a similar fashion.

D.2 Overall Heat Transfer Coefficient Calculation

Overall heat transfer coefficient *U* for the mill chamber and holding tank was calculated from [218]:

$$\frac{1}{U} = \frac{1}{h_{\mathrm{B}}} + \frac{(R_{\mathrm{o}} - R_{\mathrm{i}})A_i}{k_{\mathrm{wall}}A_{\mathrm{lm}}} + \frac{A_{\mathrm{i}}}{A_{\mathrm{o}}h_{\mathrm{j}}} \quad \text{(D.8)}$$

where h_{B} is the heat transfer coefficient of the liquid (product batch) inside the mill chamber or the holding tank, h_{j} is the heat transfer coefficient of the jacket side chiller liquid, *R* and *A* are the radius and surface area of the respective chambers, where i and o indices stand for inside and outside. A_{lm} is the logarithmic mean of inside and outside areas. k_{wall} is the thermal conductivity of the wall, which is zirconia for mill chamber with 2.5 W/m°C [219] and stainless steel for holding tank with 15 W/m°C [220]. When *U* is written in the form as in Equation (D.8), the surface area in *UA* is taken as A_{i}. h_{B} was calculated using:

$$h_{\mathrm{B}} = \frac{kA_2}{D}\mathrm{Re}^{2/3}\,\mathrm{Pr}^{1/3}, \qquad \mathrm{Re} = \frac{D^2N\rho}{\mu}, \qquad \mathrm{Pr} = \frac{C_{\mathrm{p}}\mu}{k} \quad \text{(D.9)}$$

in which *k* is the thermal conductivity of the liquid, A_2 is a constant that depends on agitator type, which was taken as 0.54 for mill chamber (disk agitator) and 0.36 for holding tank (paddle agitator). *D* is the diameter of the chamber, Re is the Reynolds number, and Pr is the Prandtl number. *N* is the stirrer speed (1/s), μ is viscosity and ρ is density. For the mill chamber, *k*, μ and ρ were found for the bead–suspension mixture as follows [194, 221]:

$$k_{\mathrm{mix}} = \frac{k_{\mathrm{b}} + (n-1)k_{\mathrm{s}} + (n-1)(k_{\mathrm{b}} - k_{\mathrm{s}})c}{k_b + (n-1)k_s - (k_b - k_s)c} k_{\mathrm{b}} \quad \text{(D.10)}$$

$$\mu_{\mathrm{mix}} = \mu_{\mathrm{L}} \left[1 + 2.5c + 10c^2 + 0.0019 \exp(20c)\right], \quad \text{(D.11)}$$

$$\rho_{\mathrm{mix}} = \rho_{\mathrm{b}}\, c + \rho_{\mathrm{L}}\, (1 - c)$$

where k_{b} and k_{s} are thermal conductivities of the beads and the suspension, respectively. k_{b} is 1.8 W/m°C [222] and k_{s} is assumed to be equal to that of water, i.e., 0.607 W/m°C [223]. n was taken as 3 for spherical beads [221]. c is the bead loading. μ_{L} and ρ_{L} are the viscosity and density of the drug pre-suspension, which were measured as 198 mPa.s and 1030 kg/m^3. For h_{j}, the following correlation [218] was used:

$$h_{\mathrm{j}} = \frac{k_{\mathrm{j}} A_1}{D_{\mathrm{j}}} \mathrm{Re}_{\mathrm{j}}^{2/3}\, \mathrm{Pr}_{\mathrm{j}}^{b}, \qquad \mathrm{Re}_{\mathrm{j}} = \frac{D_{\mathrm{j}} v \rho_{\mathrm{j}}}{\mu_{\mathrm{j}}} \quad \text{(D.12)}$$

Here, A_1 and b are constants that are recommended to be 0.0265 and 0.3, respectively, for a cooling system (jacket). v is the jacket liquid velocity. ρ_{j}, μ_{j}, and Pr_{j} were taken as 1.13 g/cm^3, 1.448 mPa.s, and 15 respectively, for the glycol–water mixture [224] used in our chiller.

D.3 Power Number Correlation with Reynolds Number and Process Parameters

As power consumption governs the heat generation during the WSMM, it is important to estimate from a correlation. It is common to correlate the dimensionless power number N_{p}, a.k.a, Newton number,

$$N_{\mathrm{p}} = \frac{P}{D^5 N^3 \rho} \quad \text{(D.13)}$$

to Reynolds number Re and the process parameters. Here, N is the stirrer speed and D is the diameter of the mill stirrer. The use of N_{p}–Re correlation is a common practice in WSMM literature [198]. These correlations can be developed based on the suspension properties for the Re as in [137] or the mixture (suspension–bead) properties [34, 193]. We

have adopted the latter approach and calculated the mixture viscosities μ_m and densities ρ_m as follows [194]:

$$\mu_m = \mu_L[1 + 2.5c + 10c^2 + 0.0019\exp(20c)] \quad (D.14)$$

$$\rho_m = \rho_b c + \rho_L(1 - c) \quad (D.15)$$

$$Re_m = \frac{\rho_m N D^2}{\mu_m} \quad (D.16)$$

Re_m changes mostly with the varying stirrer speed in each run as can be seen in Table D.1. In order to capture the impact of all process parameters, N_p is not only correlated with Re_m but also with the dimensionless numbers of the bead size and bead loading: D_b/D and c/c_{lim}, where c_{lim} = 0.63 is the packing limit of the monodispersed spherical beads [147]. A power-law correlation was found by fitting the parameters using Minitab 18 as follows:

$$N_p = 0.89 Re_m^{-0.33}(D_b/D)^{0.105}(c/c_{lim})^{-1.44} \quad (D.17)$$

Equation (D.17) can be re-written after plugging in the defining equations of N_p and Re_m as follows:

$$P = 0.89\rho_m^{0.67} N^{2.67} D^{4.235} \mu_m^{0.33} D_b^{0.105}(c/c_{lim})^{-1.44} \quad (D.18)$$

It should be noted that Equation (D.18) is not fully explicit in terms of c-dependence because μ_m and ρ_m depend on c as per Equations (D.14) and (D.15). One can easily plug Equations (D.14) and (D.15) into Equation (D.18) to obtain a fully explicit dependence of P on c. Equations (D.17) and (D.18) are not intended for scale-up; additional geometric factors are needed for scale-up (2), and the experiments did not make use of data from any large-scale equipment with different geometric factors in this chapter.

D.4 Supportive Tables and Figures

Table D.1 Viscosity, Density, Reynolds Number, Initial–Final Power Consumption, and Calculated Power Number

Run no.	μ_L (mPa·s)[a]	ρ_L (kg/m^3)[a]	Re_L (–)[a]	μ_m (mPa.s)[b]	ρ_m (kg/m^3)[b]	Re_m (–)[b]	P_0 (kJ/min)	P_f (kJ/min)	$N_{p,0}$ (–)[b]	$N_{p,f}$ (–)[b]
1	168	1030	999	1560	3020	316	2.40	2.40	0.213	0.213
2	175	1030	962	1620	3020	304	2.40	2.40	0.213	0.213
3	175	1030	959	1620	3020	303	2.40	2.40	0.213	0.213
4	158	1030	1060	7360	3520	78	3.00	2.40	0.229	0.183
5	163	1030	1030	7610	3520	75	3.00	2.40	0.229	0.183
6	166	1030	1010	7740	3520	74	3.60	3.00	0.274	0.229
7	150	1030	1120	47300	4010	14	3.60	3.00	0.240	0.200
8	151	1030	1120	47600	4010	14	4.80	3.60	0.320	0.240
9	149	1030	1130	47000	4010	14	4.80	4.80	0.320	0.320
10	150	1030	1690	1390	3020	534	4.80	3.60	0.126	0.095
11	163	1030	1540	1510	3020	489	6.00	4.80	0.158	0.126
12	165	1030	1530	1530	3020	484	6.00	4.80	0.158	0.126
13	108	1030	2340	5020	3520	171	6.60	5.40	0.149	0.122
14	118	1030	2140	5500	3520	157	7.80	6.00	0.176	0.135
15	120	1030	2100	5600	3520	154	7.80	6.00	0.176	0.135
16	51.3	1030	4920	16200	4010	61	8.40	6.00	0.166	0.119
17	71.5	1030	3530	22500	4010	44	9.60	7.20	0.190	0.142
18	83.1	1030	3040	26200	4010	37	10.8	7.80	0.214	0.154
19	106	1030	3180	980	3020	1010	10.2	7.80	0.113	0.086
20	105	1030	3210	972	3020	1010	12.6	7.80	0.140	0.086
21	138	1030	2440	1280	3020	772	12.0	7.80	0.133	0.086
22	66.3	1030	5070	3090	3520	371	13.8	9.60	0.131	0.091
23	67.5	1030	4990	3140	3520	365	15.6	10.8	0.149	0.103
24	91.8	1030	3670	4280	3520	269	15.6	10.8	0.149	0.103
25	25.7	1030	13100	8100	4010	162	18.0	13.2	0.150	0.110
26	32.8	1030	10300	10300	4010	127	21.0	13.2	0.175	0.110
27	30.7	1030	10900	9700	4010	135	24.0	18.6	0.200	0.155

[a]Properties of the milled suspension (measured), [b]properties of the suspension–bead mixture (estimated by correlations).

Table D.2 Cycle Numbers During WSMM and Particle Size Statistics of the Milled Suspensions

Run no.	Total no. cycles[a]	d_{10} (μm)	d_{50} (μm)	d_{90} (μm)	Span[b]
1	1	0.178	0.314	0.566	1.24
2	1	0.190	0.326	0.592	1.23
3	1	0.212	0.400	1.63	3.56
4	1	0.158	0.263	0.454	1.14
5	1	0.115	0.296	0.490	1.18
6	1	0.185	0.335	0.661	1.42
7	1	0.120	0.204	0.344	1.10
8	1	0.123	0.238	0.382	1.09
9	1	0.090	0.241	0.468	1.53
10	1	0.122	0.199	0.325	1.02
11	1	0.113	0.221	0.421	1.39
12	1	0.167	0.317	0.642	1.50
13	1	0.120	0.174	0.249	0.741
14	1	0.121	0.175	0.246	0.719
15	1	0.071	0.223	0.446	1.68
16	1	0.111	0.162	0.235	0.769
17	1	0.112	0.162	0.234	0.755
18	1	0.102	0.165	0.258	0.944
19	2	0.116	0.172	0.250	0.776
20	5	0.111	0.173	0.256	0.841
21	5	0.085	0.244	0.490	1.66
22	4	0.109	0.159	0.232	0.779
23	8	0.111	0.162	0.235	0.769
24	9	0.105	0.196	0.384	1.42
25	10	0.103	0.149	0.223	0.803
26	13	0.106	0.154	0.229	0.799
27	33	0.106	0.179	0.329	1.24

[a]One cycle: milling–cooling followed by cooling only. [b]span $= (d_{90} - d_{10})/d_{50}$.

Table D.3 Estimated Parameters and Associated Statistics Upon Fitting T_{rise} vs. P and $P\xi$

T_{rise} to P (MSE = 2.62)[a]			T_{rise} to $P\xi$ (MSE = 4.38)[a]			T_{rise} to $\omega/\omega_{\max}$, $c/c_{\lim}$, D_b/D (MSE = 7.30)[b]		
Parameter	Estimate	Standard error of estimate	Parameter	Estimate	Standard error of estimate	Parameter	Estimate	Standard error of estimate
β_1	27.63	1.27	β_1	26.70	1.23	β_1	84.68	27.92
β_2	1.70	0.16	β_2	2.39	0.30	β_2	2.23	0.19
β_3	3.95×10^{-4}	4.51×10^{-5}	β_3	8.94×10^{-4}	1.22×10^{-4}	β_3	0.91	0.23
						β_4	0.16	0.06

[a]Equations in the form of $y = \beta_1 \exp(-\exp(\beta_2 - \beta_3 x))$ with x being predictor and y being response. [b]Equation in the form of $y = \beta_1 x_1^{\beta_2} x_2^{\beta_3} x_3^{\beta_4}$ with x_1, x_2, x_3 being predictors and y being response.

Table D.4 Mean Squared Error (MSE) and Mean Absolute Error (MAE) of the Model Predictions For ξ, P_0, And P_f in the Training and Test Runs

Model	ξ (-)				P_0 (J/min)				P_f (J/min)			
	Train		Test		Train		Test		Train		Test	
	MSE (-)	MAE (-)	MSE (-)	MAE (-)	MSE (J^2/min^2)	MAE (J/min)	MSE (J^2/min^2)	MAE (J/min)	MSE (J^2/min^2)	MAE (J/min)	MSE (J^2/min^2)	MAE (J/min)
Power-law	3.09×10^{-3}	4.90×10^{-2}	1.25×10^{-2}	2.10×10^{-1}	6.68×10^{5}	1.54×10^{4}	2.24×10^{6}	2.13×10^{3}	7.92×10^{6}	6.06×10^{4}	3.39×10^{6}	3.25×10^{3}
Linear regression	3.29×10^{-3}	5.02×10^{-2}	3.91×10^{-3}	5.06×10^{-2}	3.33×10^{6}	1.42×10^{3}	1.19×10^{6}	8.98×10^{2}	2.09×10^{6}	1.02×10^{3}	5.49×10^{5}	6.38×10^{2}
Lasso regression	7.85×10^{-3}	7.45×10^{-2}	6.40×10^{-3}	7.46×10^{-2}	3.33×10^{6}	1.42×10^{3}	1.19×10^{6}	9.00×10^{2}	2.09×10^{6}	1.02×10^{3}	5.49×10^{5}	6.38×10^{2}
Ridge regression	3.44×10^{-3}	5.20×10^{-2}	4.16×10^{-3}	5.50×10^{-2}	3.33×10^{6}	1.42×10^{3}	1.03×10^{6}	9.16×10^{2}	2.54×10^{6}	1.05×10^{3}	4.80×10^{5}	5.57×10^{2}
Elastic net regression	7.85×10^{-3}	7.45×10^{-2}	6.40×10^{-3}	7.46×10^{-2}	3.33×10^{6}	1.42×10^{3}	5.09×10^{6}	1.78×10^{3}	9.79×10^{6}	2.37×10^{3}	2.12×10^{6}	1.22×10^{3}
Decision tree	0.00	0.00	1.08×10^{-2}	8.50×10^{-2}	4.35×10^{6}	1.52×10^{3}	9.72×10^{6}	2.76×10^{3}	0.00	0.00	3.31×10^{6}	1.68×10^{3}
Gradient boost	1.12×10^{-4}	8.01×10^{-3}	1.07×10^{-2}	8.34×10^{-2}	2.08×10^{7}	3.67×10^{3}	9.80×10^{6}	2.76×10^{3}	5.44×10^{3}	5.87×10^{1}	3.28×10^{6}	1.66×10^{3}
Random forest	5.63×10^{-4}	1.91×10^{-2}	9.62×10^{-3}	8.65×10^{-2}	0.00	0.00	1.04×10^{7}	2.98×10^{3}	1.74×10^{5}	2.71×10^{2}	3.58×10^{6}	1.74×10^{3}
k-nearest neighborhood	2.22×10^{-3}	3.99×10^{-2}	2.62×10^{-3}	4.15×10^{-2}	1.08×10^{4}	7.14×10^{1}	3.17×10^{4}	1.68×10^{2}	3.25×10^{6}	1.06×10^{3}	8.06×10^{4}	2.40×10^{2}
Support vector regressor	4.92×10^{-3}	6.03×10^{-2}	5.23×10^{-3}	6.60×10^{-2}	3.33×10^{6}	1.42×10^{3}	9.13×10^{6}	2.76×10^{3}	1.61×10^{7}	3.02×10^{3}	3.52×10^{6}	1.80×10^{3}
Multilayer perceptron	7.90×10^{-3}	6.63×10^{-2}	1.88×10^{-2}	1.17×10^{-1}	3.33×10^{6}	1.42×10^{3}	7.12×10^{7}	7.92×10^{3}	5.21×10^{7}	6.10×10^{3}	3.71×10^{7}	5.80×10^{3}

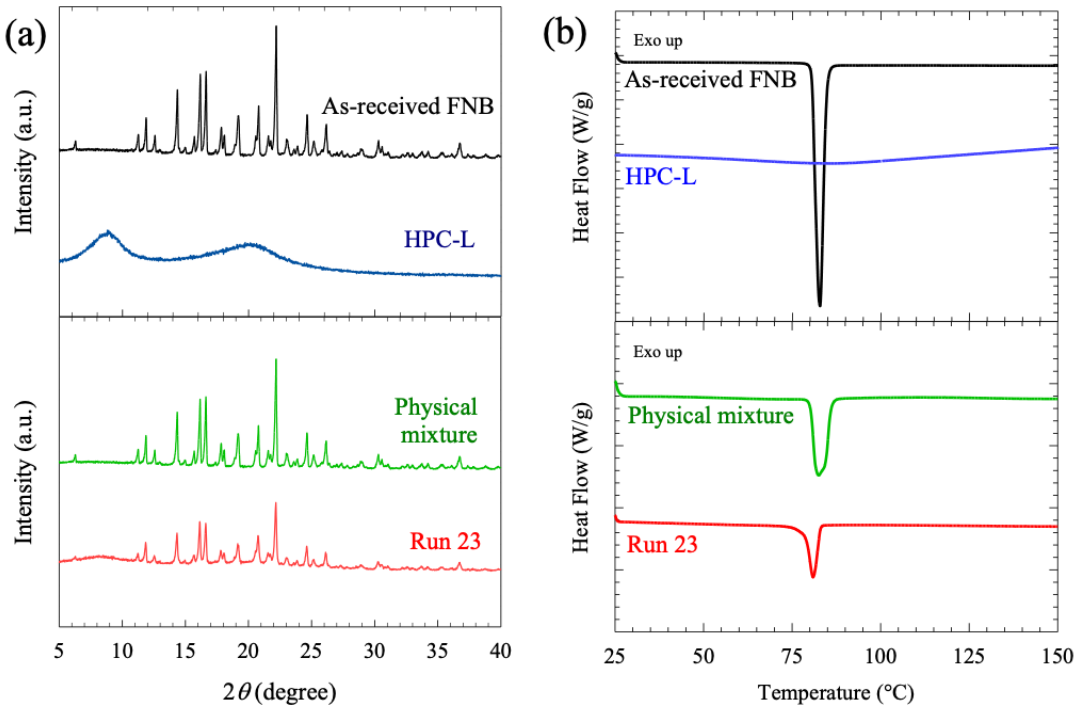

Figure D.1 **(a)** XRD of as-received drug, polymer, physical mixture, and milled and overnight dried suspension (Run 23) and **(b)** DSC traces of as-received drug, polymer, physical mixture, and milled and overnight dried suspension (Run 23), Adapted from Guner et al. (ref. [29] of the main text).

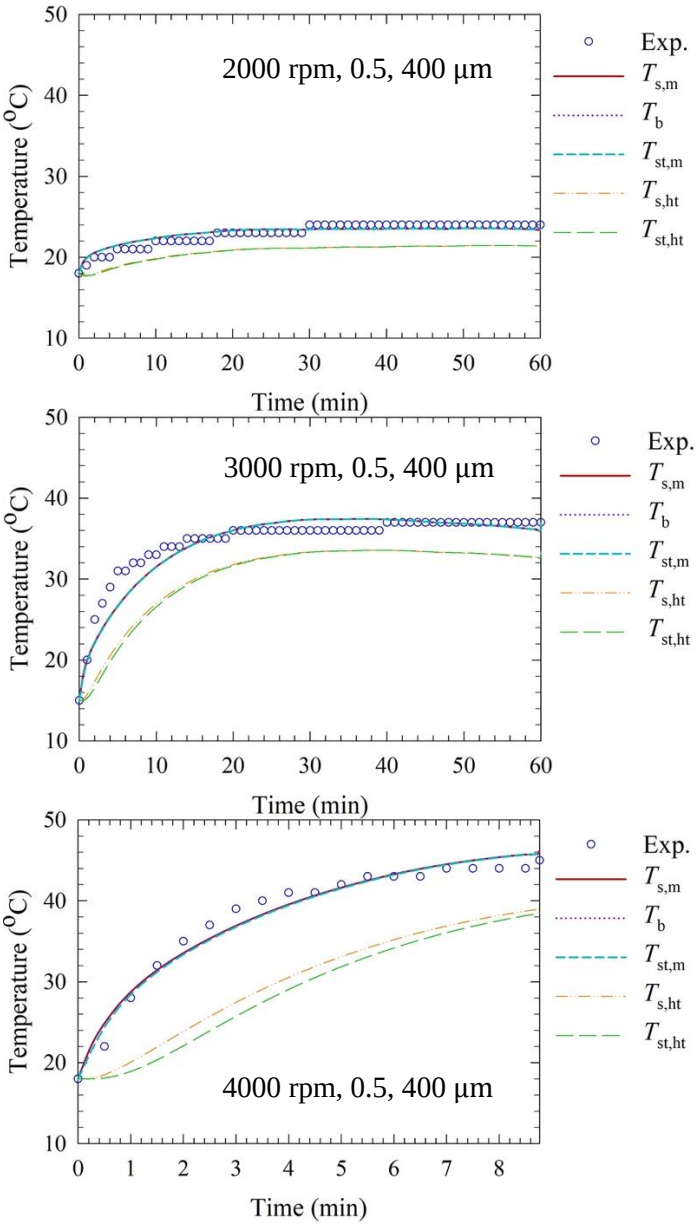

Figure D.2 Measured mill outlet temperature, simulated temperature of the suspension, the beads, and the stirrer in the mill chamber as well as that of the suspension and the stirrer in the holding tank when 400 µm beads at 0.5 fractional loading were stirred at 2000 rpm (top), 3000 rpm (middle), and 4000 rpm (bottom).

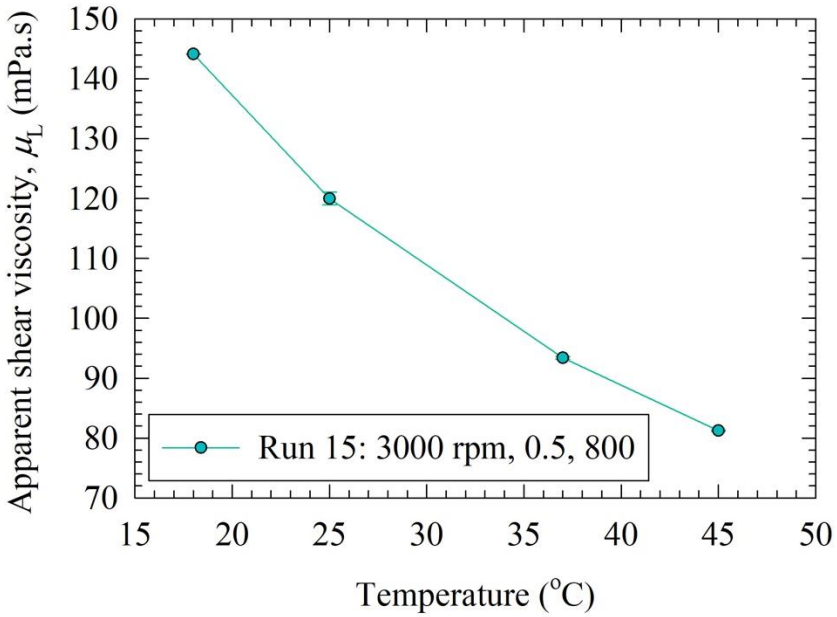

Figure D.3 The effect of temperature on the apparent shear viscosity of a milled FNB suspension (Run 15).

APPENDIX E

SUPPLEMENTARY DATA FOR CHAPTER 6

This appendix contains the statistics of the models used for the lumped parameter model study which was introduced in Chapter 6.

Table E.1 Mean Squared Error (MSE) and Mean Absolute Error (MAE) of the Model Predictions for Q_{gen} and UA in the Training and Test Tests

Model name	Q_{gen} (J/min)				UA (J/min°C)			
	Train		Test		Train		Test	
	MSE	MAE	MSE	MAE	MSE	MAE	MSE	MAE
Power law	3.28×10^{5}	4.64×10^{2}	2.86×10^{5}	4.50×10^{2}	8.28×10^{2}	22.0	5.48×10^{2}	19.4
Linear regression	1.27×10^{6}	9.23×10^{2}	1.55×10^{6}	9.27×10^{2}	9.53×10^{2}	24.0	1.00×10^{3}	22.2
Lasso regression	1.27×10^{6}	9.22×10^{2}	1.56×10^{6}	9.28×10^{2}	9.70×10^{2}	24.0	1.13×10^{3}	23.3
Ridge regression	1.55×10^{6}	9.98×10^{2}	1.27×10^{6}	8.86×10^{2}	1.05×10^{3}	25.0	8.52×10^{2}	19.9
Elastic net regression	6.00×10^{6}	2.03×10^{3}	1.66×10^{6}	1.15×10^{3}	2.57×10^{3}	40.1	8.44×10^{2}	24.8
Decision tree	0.00	0.00	2.69×10^{6}	1.45×10^{3}	0.00	0.00	1.84×10^{3}	39.4
Gradient boost	8.66×10^{3}	7.40×10^{1}	2.51×10^{6}	1.38×10^{3}	4.64×10^{1}	5.21	1.34×10^{3}	33.7
Random forest	1.18×10^{5}	2.72×10^{2}	3.01×10^{6}	1.50×10^{3}	1.60×10^{2}	10.0	1.63×10^{3}	36.3
K nearest neighborhood	1.58×10^{6}	9.30×10^{2}	3.63×10^{5}	4.62×10^{2}	8.88×10^{2}	22.4	4.32×10^{2}	16.9
Support vector regressor	1.09×10^{7}	2.48×10^{3}	2.11×10^{6}	1.18×10^{3}	3.66×10^{3}	46.3	6.83×10^{2}	22.4
Multilayer perceptron	2.37×10^{7}	3.79×10^{3}	1.01×10^{7}	3.11×10^{3}	2.07×10^{3}	39.5	1.06×10^{3}	29.4

APPENDIX F

SUPPLEMENTARY DATA FOR CHAPTER 7

This appendix contains supplementary tables and figures used for the zirconia-polystyrene bead mixture study which was described in Chapter 7.

Table F.1 Average Stirrer Power per Unit Volume P_w, Apparent Shear Viscosity μ_L and Density ρ_L of the Milled Drug Suspensions (Measured), Power-Law Model Parameters as well as Dynamic Mixture Viscosity μ_M and Mixture Density ρ_M of the Slurries (Estimated)

Run No.	P_w (W/m^3)	μ_L (mPa·s)[a]	μ_0 (mPa·s^q)[b]	q (–)[b]	R^2 (–)[b]	ρ_L (kg/m^3)	μ_m (mPa·s)[c]	ρ_m (kg/m^3)[d]
1	2.81×10^5	160	222	0.92	0.97	1030	829	1030
2	5.31×10^5	148	203	0.92	0.94	1030	767	1470
3	5.73×10^5	137	215	0.89	0.95	1030	711	1900
4	6.15×10^5	121	164	0.93	0.98	1030	625	2340
5	8.65×10^5	119	170	0.91	0.98	1030	616	2770
6	4.90×10^5	118	188	0.89	0.99	1030	5520	1040
7	5.73×10^5	96.6	134	0.92	0.99	1030	4500	1650
8	6.98×10^5	87.0	109	0.95	0.94	1020	4050	2270
9	9.06×10^5	67.2	89.4	0.93	0.99	1030	3130	2890
10	9.48×10^5	57.4	74.0	0.94	0.99	1030	2680	3520
11	1.03×10^6	144	216	0.91	0.94	1020	748	1030
12	1.16×10^6	111	144	0.94	0.96	1020	576	1460
13	1.28×10^6	97.9	144	0.91	0.95	1020	507	1890
14	1.36×10^6	90.8	119	0.94	0.97	1020	471	2330
15	1.49×10^6	67.4	82.3	0.95	0.98	1030	349	2770
16	1.16×10^6	81.0	113	0.92	0.98	1030	3780	1030
17	1.61×10^6	71.0	91.5	0.94	0.95	1030	3310	1650
18	2.07×10^6	49.7	64.2	0.94	0.98	1030	2320	2270
19	2.11×10^6	34.4	36.7	0.97	0.95	1030	1600	2890
20	2.49×10^6	32.5	38.6	0.96	0.91	1030	1520	3520

[a]Taken at the shear rate γ of 1000 1/s. [b]$\mu = \mu_0\gamma^{q-1}$ [c]$\mu_m = \mu_L[1 + 2.5c + 10c^2 + 0.0019\exp(20c)]$ [d]$\rho_m = c[\rho_{YSZ}c_{YSZ} + \rho_{CPS}(1 - c_{YSZ})] + (1-c)\rho_L$

Table F.2 The Time it Takes Drug Particle Median Size d_{50} to Reach 0.25 μm t_{d50} and d_{90} to Reach 0.5 μm t_{d90} and Estimated Parameters of the *n*th-order Kinetic Model (Equation (7.1)) Obtained via Fitting to the Evolution of the Median Particle Size

Run No.	Stirrer Speed ω (rpm)	Bead Loading c (-)	CPS:YSZ (v/v, %)	Characteristic Milling Times[a]		Parameters of the *n*th-order Kinetic Model Fit			
				t_{d50} (min)	t_{d90} (min)	d_{lim} (μm)	k (μm^{1-n}/min)	n	R^2
1	3000	0.35	100:0	94.5	83.0	0.161	0.105	1.86	0.989
2	3000	0.35	75:25	83.0	69.3	0.152	0.130	1.89	0.990
3	3000	0.35	50:50	53.2	46.6	0.118	0.168	2.09	0.998
4	3000	0.35	25:75	49.6	44.4	0.134	0.202	2.02	0.996
5	3000	0.35	0:100	46.7	41.7	0.133	0.217	2.06	0.995
6	3000	0.50	100:0	26.5	23.6	0.158	0.432	1.90	0.996
7	3000	0.50	75:25	23.9	20.8	0.159	0.520	1.89	0.997
8	3000	0.50	50:50	22.2	19.4	0.143	0.513	2.07	0.999
9	3000	0.50	25:75	19.8	18.8	0.142	0.569	2.06	0.997
10	3000	0.50	0:100	18.8	17.3	0.142	0.686	2.09	0.997
11	4000	0.35	100:0	50.6	41.1	0.152	0.215	1.95	0.995
12	4000	0.35	75:25	36.5	32.3	0.129	0.275	2.10	0.997
13	4000	0.35	50:50	29.2	29.2	0.129	0.340	2.10	0.997
14	4000	0.35	25:75	30.5	32.0	0.146	0.438	2.03	0.998
15	4000	0.35	0:100	26.8	28.3	0.137	0.461	2.10	0.997
16	4000	0.50	100:0	17.7	16.8	0.154	0.806	1.96	0.996
17	4000	0.50	75:25	14.1	15.1	0.143	0.939	2.12	0.999
18	4000	0.50	50:50	11.3	11.1	0.146	1.034	2.05	0.999
19	4000	0.50	25:75	10.4	10.7	0.144	1.153	2.08	0.998
20	4000	0.50	0:100	9.23	8.38	0.143	1.283	2.12	0.998

[a]Calculated by Hermite interpolation.

Table F.3 Microhydrodynamic Parameters Calculated Using the Lun Model for Runs with CPS Alone and YSZ Alone

Run No.	g_0 (–)	θ (m^2/s^2)	u_b (m/s)	ν (kHz)	σ_b^{max} (GPa)	α_b (μm)	a (mHz)	$\Pi\sigma_y$ (J^2/m^{6}s)
1[a]	5.62	1.28×10^{-3}	5.72×10^{-2}	2.15	1.84×10^{-2}	3.82	15.9	1.90×10^{12}
5[b]	5.62	4.32×10^{-3}	1.05×10^{-1}	4.32	1.58	2.41	16.7	2.73×10^{16}
6[a]	13.5	7.41×10^{-4}	4.34×10^{-2}	5.60	1.65×10^{-2}	3.42	61.7	4.55×10^{12}
10[b]	13.5	2.35×10^{-3}	7.74×10^{-2}	10.9	1.40	2.13	61.5	6.05×10^{16}
11[a]	5.62	5.15×10^{-3}	1.15×10^{-1}	4.31	2.43×10^{-2}	5.04	55.5	1.16×10^{13}
15[b]	5.62	1.24×10^{-2}	1.77×10^{-1}	7.31	1.94	2.97	43.0	1.07×10^{17}
16[a]	13.5	2.50×10^{-3}	7.98×10^{-2}	10.3	2.11×10^{-2}	4.37	184	2.22×10^{13}
20[b]	13.5	9.53×10^{-3}	1.56×10^{-1}	22.0	1.85	2.82	217	3.73×10^{17}

[a]CPS alone (100:0 CPS:YSZ), [b]YSZ alone (0:100 CPS:YSZ)

Table F.4 Values for Characteristic Milling Times (t_{d50} and t_{d90}), Specific Energy Consumed during t_{d50} (E_{td50}), Specific Energy Consumed During t_{d90} (E_{td90}), and Merit Scores

Run No.	t_{d50} (min)	t_{d90} (min)	E_{td50} (kJ/g)	E_{td90} (kJ/g)	Merit Score (–) w_1=1, w_2=w_3=1	w_2=0.1, w_1=w_3=1	w_1=0.1, w_2=w_3=1	w_3=0.1, w_1=w_2=1
1	94.5	83.0	6.38	5.60	0.56	0.85	0.56	1.27
2	83.0	69.3	10.6	8.83	0.48	0.92	0.48	0.82
3	53.2	46.6	7.31	6.41	0.71	1.43	0.71	1.19
4	49.6	44.4	7.31	6.55	0.74	1.52	0.74	1.20
5	46.7	41.7	9.69	8.64	0.63	1.54	0.63	0.92
6	26.5	23.6	3.11	2.77	1.56	2.91	1.56	2.77
7	23.9	20.8	3.28	2.85	1.59	3.18	1.59	2.66
8	22.2	19.4	3.72	3.24	1.52	3.33	1.52	2.37
9	19.8	18.8	4.30	4.09	0.91	1.45	1.37	1.12
10	18.8	17.3	4.27	3.94	0.91	1.44	1.40	1.11
11	50.6	41.1	12.5	10.2	0.42	0.84	0.51	0.54
12	36.5	32.3	10.1	8.96	0.49	0.94	0.64	0.61
13	29.2	29.2	8.97	8.98	0.53	0.98	0.74	0.64
14	30.5	32.0	10.0	10.5	0.49	0.92	0.67	0.58
15	26.8	28.3	9.57	10.1	0.50	0.92	0.72	0.58
16	17.7	16.8	4.93	4.66	0.80	1.28	1.28	0.94
17	14.1	15.1	5.46	5.84	0.68	1.05	1.22	0.75
18	11.3	11.1	5.61	5.55	0.60	0.88	1.22	0.65
19	10.4	10.7	5.28	5.41	0.61	0.88	1.28	0.65
20	9.2	8.4	5.52	5.00	0.55	0.77	1.24	0.58

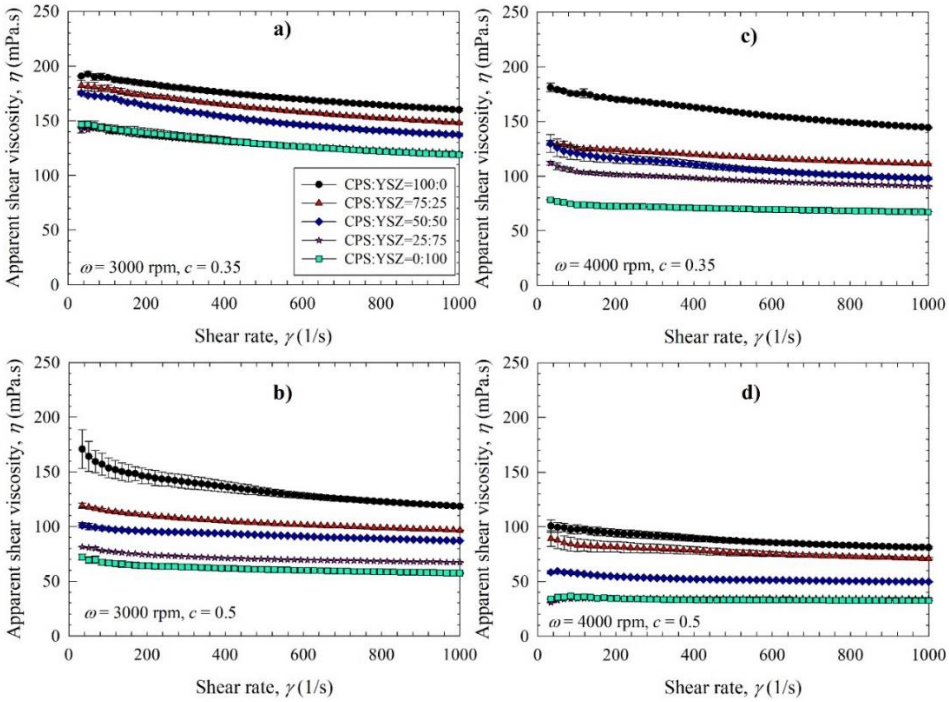

Figure F.1 Effects of CPS:YSZ ratio on apparent shear viscosity vs. shear rate of the milled FNB suspensions at various stirrer speeds ω and bead loadings c: (a) ω = 3000 rpm, c = 0.35, (b) ω = 3000 rpm, c = 0.5, (c) ω = 4000 rpm, c = 0.35, and (d) ω = 4000 rpm, c = 0.5.

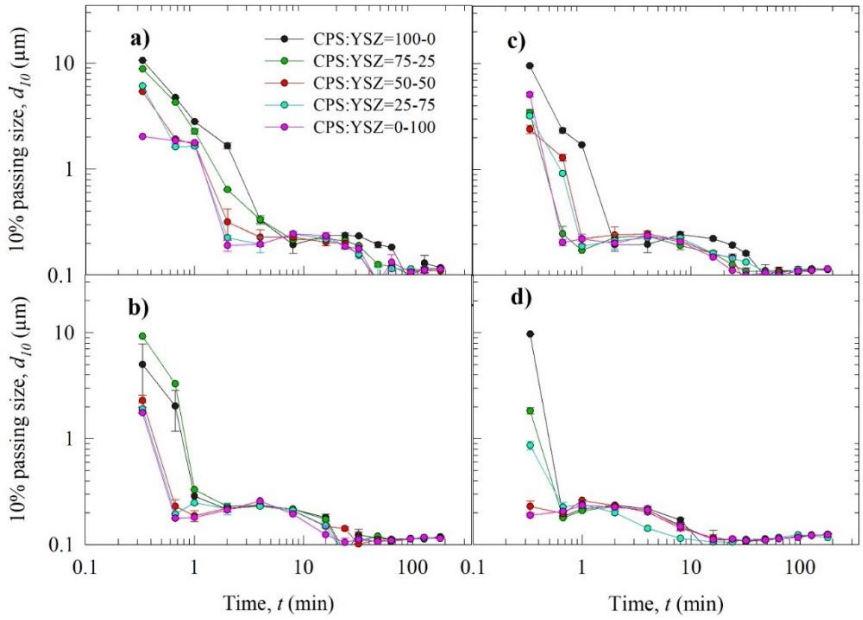

Figure F.2 Effects of CPS:YSZ volume percentages on the time-wise evolution of d_{10} during the milling of FNB particles at various stirrer speeds ω and bead loadings c: (a) ω = 3000 rpm, c = 0.35, (b) ω = 3000 rpm, c = 0.5, (c) ω = 4000 rpm, c = 0.35, and (d) ω = 4000 rpm, c = 0.5.

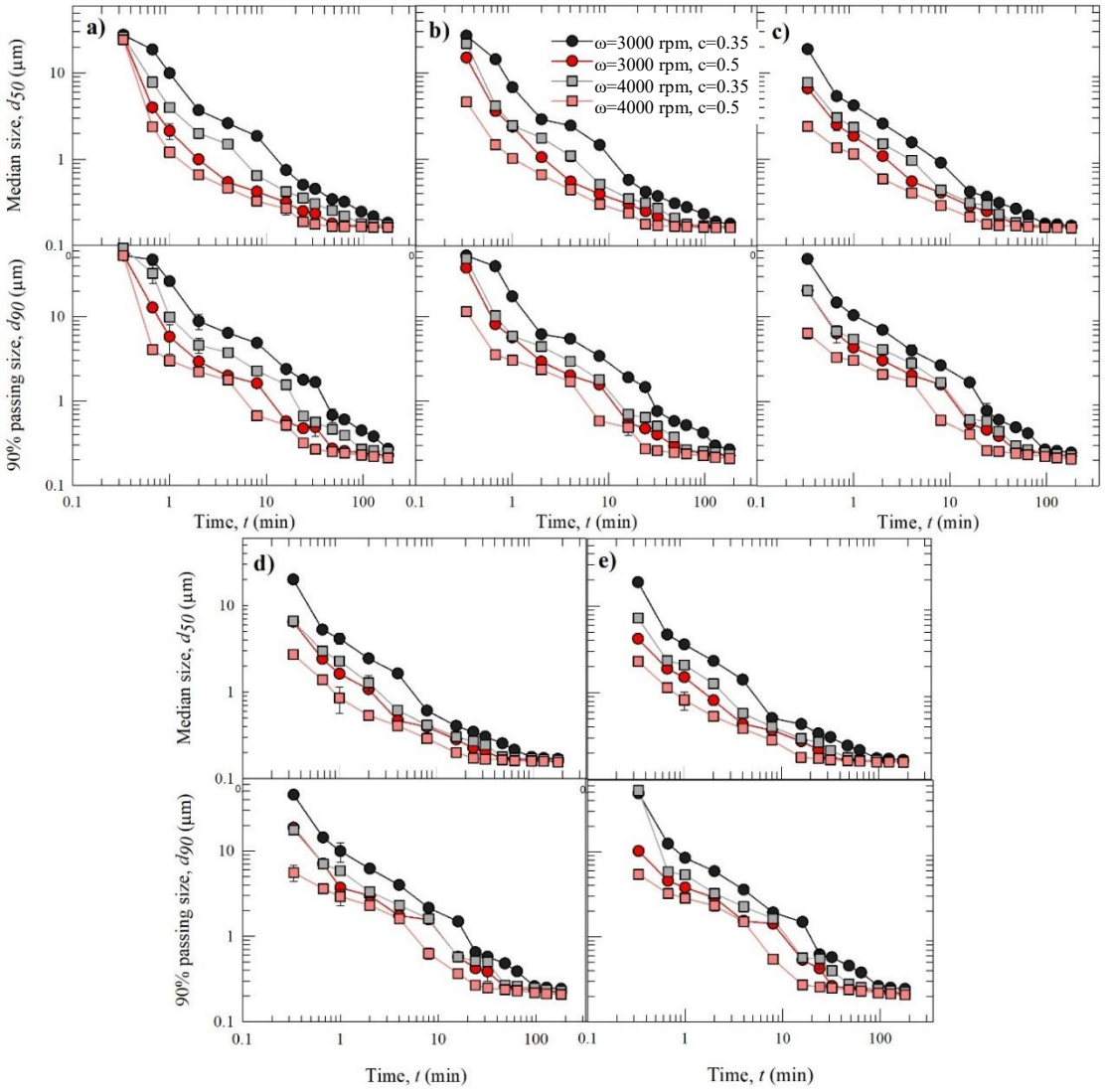

Figure F.3 Effects of the stirrer speed ω and the bead loading c on the time-wise evolution of d_{50} and d_{90} during the milling of FNB particles at various volume percentages of the CPS:YSZ bead mixtures: (a) 100:0, (b) 75:25 (c) 50:50, (d) 25:75 and (e) 0:100.

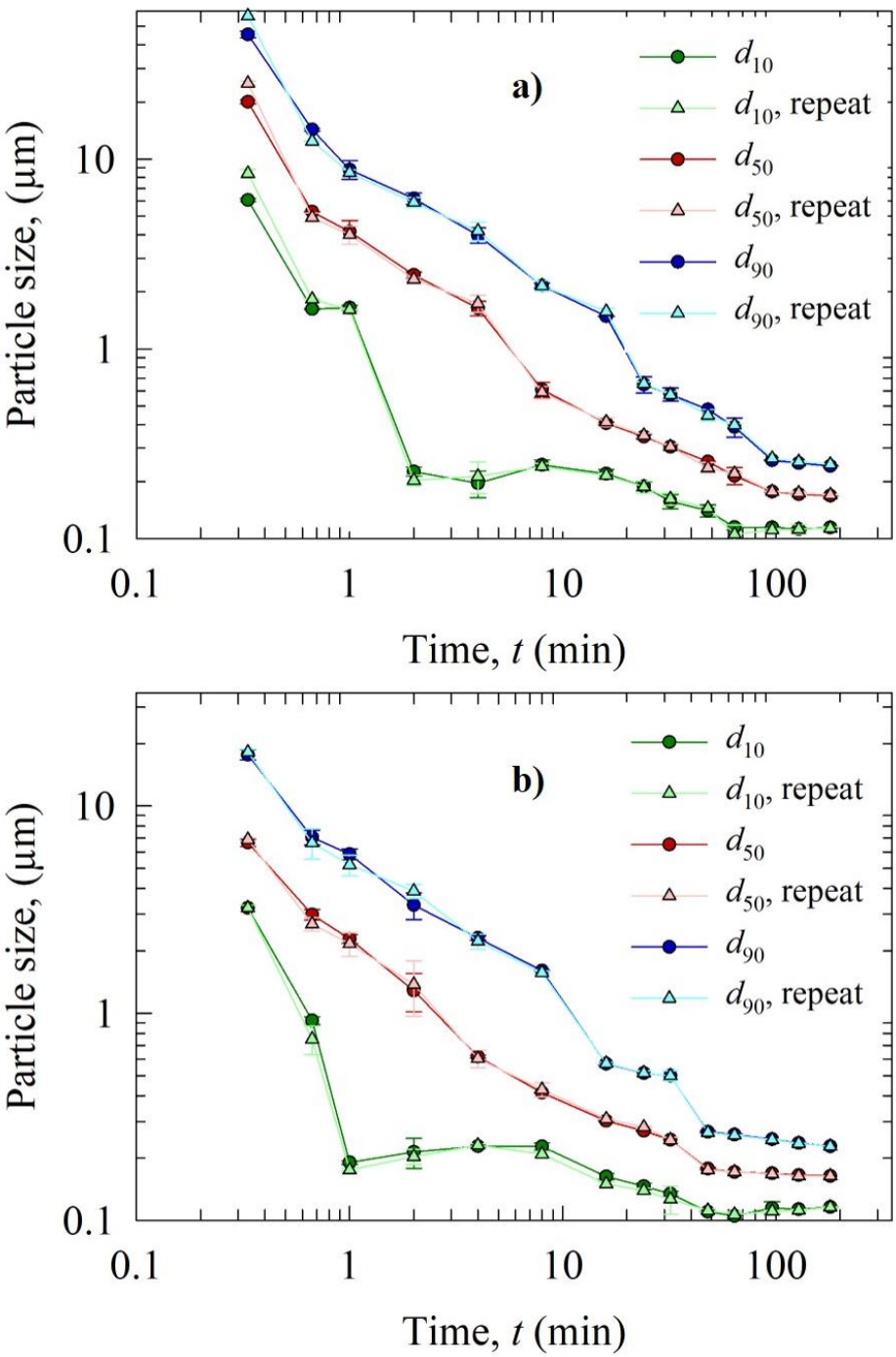

Figure F.4 Time-wise evolution of d_{10}, d_{50} and d_{90} during wet stirred media milling of (a) Run 4 and (b) Run 14. Circles represent the experimental data in the original runs, while triangles represent the experimental data in the repeated runs.

APPENDIX G

SUPPLEMENTARY DATA FOR CHAPTER 8

This appendix has supportive tables to the bead size mixtures study as referred and explained in Chapter 8.

Table G.1 Power per Unit Volume, Apparent Viscosity, and MHD Parameters

Run No.	P_w (W/m^3)	μ_L (mPa.s)	g_0 (-)	θ (m^2/s^2)	u_b (m/s)	v (kHz)	σ_b^{max} (GPa)	α_b (μm)	a (mHz)	$\Pi\sigma_y$ (J^2/m^{6}s)
1	4.90×10^{5}	119	5.62	1.93×10^{-4}	2.22×10^{-2}	3.30	0.846	0.357	5.53	3.15×10^{15}
2	5.31×10^{5}	102	5.62	4.54×10^{-4}	3.40×10^{-2}	3.71	1.00	0.579	6.40	5.14×10^{15}
3	5.73×10^{5}	104	5.62	7.70×10^{-4}	4.43×10^{-2}	3.81	1.12	0.816	6.40	6.36×10^{15}
4	5.73×10^{5}	100	5.62	1.41×10^{-3}	5.99×10^{-2}	3.87	1.26	1.22	6.23	7.86×10^{15}
5	5.73×10^{5}	113	5.62	1.67×10^{-3}	6.52×10^{-2}	3.64	1.30	1.47	5.41	7.31×10^{15}
6	5.73×10^{5}	93	5.62	3.61×10^{-3}	9.58×10^{-2}	3.97	1.52	2.31	5.95	1.09×10^{16}
7	8.23×10^{5}	51.0	13.5	1.85×10^{-4}	2.17×10^{-2}	11.1	0.839	0.354	34.0	1.47×10^{16}
8	8.23×10^{5}	66.6	13.5	2.63×10^{-4}	2.59×10^{-2}	9.68	0.900	0.519	24.9	1.24×10^{16}
9	9.06×10^{5}	72.6	13.5	4.26×10^{-4}	3.29×10^{-2}	9.71	1.00	0.725	23.9	1.44×10^{16}
10	8.23×10^{5}	70.9	13.5	6.99×10^{-4}	4.22×10^{-2}	9.36	1.09	1.06	21.1	1.55×10^{16}
11	9.06×10^{5}	72.4	13.5	1.01×10^{-3}	5.08×10^{-2}	9.71	1.18	1.33	22.0	1.87×10^{16}
12	9.90×10^{5}	63.8	13.5	2.20×10^{-3}	7.48×10^{-2}	10.6	1.38	2.09	24.3	2.82×10^{16}
13	1.36×10^{6}	76.8	5.62	8.27×10^{-4}	4.59×10^{-2}	6.84	1.11	0.478	20.5	2.09×10^{16}
14	1.41×10^{6}	81.2	5.62	1.51×10^{-3}	6.19×10^{-2}	6.75	1.28	0.736	18.8	2.44×10^{16}
15	1.45×10^{6}	70.4	5.62	2.85×10^{-3}	5.52×10^{-2}	7.31	1.45	1.06	20.8	3.48×10^{16}
16	1.41×10^{6}	73.7	5.62	4.57×10^{-3}	0.108	6.98	1.59	1.55	18.0	3.64×10^{16}
17	1.49×10^{6}	82.1	5.62	5.84×10^{-3}	0.122	6.80	1.67	1.89	16.7	3.72×10^{16}
18	1.57×10^{6}	107	5.62	8.50×10^{-3}	0.147	6.09	1.80	2.74	12.9	3.34×10^{16}
19	1.78×10^{6}	27.1	13.5	7.47×10^{-4}	4.36×10^{-2}	22.3	1.11	0.468	119	8.97×10^{16}
20	1.78×10^{6}	40.5	13.5	9.40×10^{-4}	4.89×10^{-2}	18.3	1.16	0.670	78.4	6.48×10^{16}
21	1.91×10^{6}	30.9	13.5	2.03×10^{-3}	7.19×10^{-2}	21.1	1.36	0.991	97.5	1.10×10^{17}
22	1.91×10^{6}	52.0	13.5	2.16×10^{-3}	7.41×10^{-2}	16.4	1.37	1.33	58.3	6.72×10^{16}
23	1.91×10^{6}	47.7	13.5	3.08×10^{-3}	8.86×10^{-2}	16.9	1.47	1.66	59.8	7.94×10^{16}
24	1.99×10^{6}	59.0	13.5	4.66×10^{-3}	0.109	15.5	1.60	2.43	47.7	7.48×10^{16}
T1	7.40×10^{5}	68.8	8.37	2.49×10^{-4}	2.52×10^{-2}	6.86	0.890	0.376	17.8	9.84×10^{15}
T2	1.16×10^{6}	124	8.37	6.47×10^{-4}	4.06×10^{-2}	6.38	1.08	0.788	14.0	1.14×10^{16}
T3	1.20×10^{6}	94.9	8.37	3.65×10^{-3}	9.64×10^{-2}	7.30	1.52	2.31	15.4	2.50×10^{16}
T4	2.40×10^{5}	142	4.56	5.53×10^{-4}	3.75×10^{-2}	1.83	1.04	0.937	1.75	1.64×10^{15}

Table G.2 Supportive Data such as Specific Time for Median Particle Size to Reach 0.20 μm, Power Consumption, Number of Milling Cycles, Merit Scores and Cost of the Beads for Each Run

Run No.	t_{d50} (min)	P (kW)	N_{mc} (#)	Merit Score (-)[a]	Merit Score (-)[b]	Price ($)
1	25.2	0.047	1	74.4	64.2	92.3
2	37.7	0.050	1	61.7	48.5	72.4
3	40.8	0.053	1	63.7	50.8	52.5
4	39.7	0.053	1	44.5	29.7	59.6
5	36.2	0.053	1	67.5	55.4	39.7
6	38.0	0.053	1	63.2	50.2	26.9
7	12.4	0.073	6	78.0	72.7	132
8	11.4	0.073	8	76.6	72.4	103
9	11.6	0.080	7	73.7	67.6	75.0
10	11.7	0.073	10	74.4	70.8	85.1
11	12.1	0.080	12	70.7	67.0	56.7
12	14.3	0.087	11	65.8	59.6	38.5
13	17.4	0.117	28	49.6	46.9	92.3
14	25.1	0.120	38	44.9	45.2	72.4
15	16.5	0.123	46	38.2	38.7	52.5
16	18.3	0.120	49	37.5	38.9	59.6
17	15.2	0.127	48	38.7	40.2	39.7
18	22.5	0.133	61	31.4	33.9	26.9
19	4.62	0.150	56	34.5	37.1	132
20	5.71	0.150	75	30.0	37.0	103
21	7.12	0.160	77	27.5	33.1	75.0
22	6.23	0.160	75	27.6	32.7	85.1
23	6.83	0.160	78	26.8	32.2	56.7
24	9.65	0.167	106	20.7	29.7	38.5

[a]Merit score calculated via $1/k$, P and N_{mc}. [b]Merit score calculated via $1/k$ and P (without N_{mc}).

Table G.3 Root Mean Squared Errors of the Machine Learning Models Based on MHD and Process Parameters

Model	MHD parameters		Process parameters	
	Train[a]	Test	Train[a]	Test
Linear regression	0.346	0.241	0.553	0.493
Lasso regression	0.806	0.358	0.806	0.358
Ridge regression	0.332	0.213	0.523	0.491
Elastic net regression	0.440	0.180	0.518	0.465
Decision tree	0.400	0.526	0.474	0.116
Gradient boost	0.394	0.361	0.508	0.179
Random forest	0.414	0.308	0.489	0.198
k-nearest neighborhood	0.382	0.242	0.472	0.643
Multilayer perceptron	0.427	0.236	0.426	0.151

[a]RMSE of the leave-one-out cross validated predictions are reported

REFERENCES

1. Zhang X, Xing H, Zhao Y, Ma Z. Pharmaceutical dispersion techniques for dissolution and bioavailability enhancement of poorly water-soluble drugs. Pharmaceutics. 2018;10(3):74.

2. Amidon GL, Lennernäs H, Shah VP, Crison JR. A theoretical basis for a biopharmaceutic drug classification: The correlation of in vitro drug product dissolution and in vivo bioavailability. Pharmaceutical Research. 1995;12(3):413-20.

3. Kasim NA, Whitehouse M, Ramachandran C, Bermejo M, Lennernäs H, Hussain AS, Junginger HE, Stavchansky SA, Midha KK, Shah VP, Amidon GL. Molecular properties of who essential drugs and provisional biopharmaceutical classification. Molecular Pharmaceutics. 2004;1(1):85-96.

4. Takagi T, Ramachandran C, Bermejo M, Yamashita S, Yu LX, Amidon GL. A provisional biopharmaceutical classification of the top 200 oral drug products in the united states, great britain, spain, and japan. Molecular Pharmaceutics. 2006;3(6):631-43.

5. Ku MS, Dulin W. A biopharmaceutical classification-based right-first-time formulation approach to reduce human pharmacokinetic variability and project cycle time from first-in-human to clinical proof-of-concept. Pharmaceutical Development and Technology. 2012;17(3):285-302.

6. Benet LZ, Wu C-Y, Custodio JM. Predicting drug absorption and the effects of food on oral bioavailability. Bulletin Technique Gattefosse. 2006;99:9-16.

7. Leeson PD. Molecular inflation, attrition and the rule of five. Advanced Drug Delivery Reviews. 2016;101:22-33.

8. Li P, Zhao L. Developing early formulations: Practice and perspective. International Journal of Pharmaceutics. 2007;341(1):1-19.

9. Singh MC, Sayyad A, Sawant S. Review on various techniques of solubility enhancement of poorly soluble drugs with special emphasis on solid dispersion. Journal of Pharmaceutical Research. 2010;3(10):249-50.

10. Li M, Azad M, Davé R, Bilgili E. Nanomilling of drugs for bioavailability enhancement: A holistic formulation-process perspective. Pharmaceutics. 2016

11. Hancock BC, Parks M. What is the true solubility advantage for amorphous pharmaceuticals? Pharmaceutical Research. 2000;17(4):397-404.

12. Marsac PJ, Konno H, Taylor LS. A comparison of the physical stability of amorphous felodipine and nifedipine systems. Pharmaceutical Research. 2006;23(10):2306-16.

13. Shamblin SL, Tang X, Chang L, Hancock BC, Pikal MJ. Characterization of the time scales of molecular motion in pharmaceutically important glasses. The Journal of Physical Chemistry B. 1999;103(20):4113-21.

14. Wu T, Yu L. Surface crystallization of indomethacin below Tg. Pharmaceutical Research. 2006;23(10):2350-5.

15. Tanaka Y, Inkyo M, Yumoto R, Nagai J, Takano M, Nagata S. Nanoparticulation of probucol, a poorly water-soluble drug, using a novel wet-milling process to improve in vitro dissolution and in vivo oral absorption. Drug Development and Industrial Pharmacy. 2012;38(8):1015-23.

16. Müller RH, Peters K. Nanosuspensions for the formulation of poorly soluble drugs 1. Preparation by a size-reduction technique. International Journal of Pharmaceutics. 1998;160:229.

17. Bhakay A, Rahman M, Dave RN, Bilgili E. Bioavailability enhancement of poorly water-soluble drugs via nanocomposites: Formulation–processing aspects and challenges. Pharmaceutics. 2018;10(3):86.

18. Kesisoglou F, Panmai S, Wu Y. Nanosizing — oral formulation development and biopharmaceutical evaluation. Advanced Drug Delivery Reviews. 2007;59(7):631-44.

19. Noyes AA, Whitney WR. The rate of solution of solid substances in their own solutions. Journal of American Chemical Society. 1897;19(12):930-4.

20. Zhang X, Guan J, Ni R, Li LC, Mao S. Preparation and solidification of redispersible nanosuspensions. Journal of Pharmaceutical Sciences. 2014;103(7):2166-76.

21. Bhakay A, Merwade M, Bilgili E, Dave RN. Novel aspects of wet milling for the production of microsuspensions and nanosuspensions of poorly water-soluble drugs. Drug Development and Industrial Pharmacy. 2011;37(8):963-76.

22. Lee J. Drug nano-and microparticles processed into solid dosage forms: Physical properties. Journal of Pharmaceutical Sciences. 2003;92(null):2057.

23. Liversidge GGC, K.C.; Bishop, J.F.; Czekai, D.A. Surface modified drug nanoparticles. US Patent No. 5,145,684. Washington DC: U.S. Patent and Trademark Office; 1992.

24. Beck C, Dalvi SV, Dave RN. Controlled liquid antisolvent precipitation using a rapid mixing device. Chemical Engineering Science. 2010;65(21):5669-75.

25. De Zordi N, Moneghini M, Kikic I, Grassi M, Del Rio Castillo AE, Solinas D, Bolger MB. Applications of supercritical fluids to enhance the dissolution behaviors of furosemide by generation of microparticles and solid dispersions. European Journal of Pharmaceutics and Biopharmaceutics. 2012;81(1):131-41.

26. Imperiale JC, Bevilacqua G, Rosa PdTVe, Sosnik A. Production of pure indinavir free base nanoparticles by a supercritical anti-solvent (sas) method. Drug Development and Industrial Pharmacy. 2014;40(12):1607-15.

27. Knieke C, Rawtani A, Davé R. Concentrated fenofibrate nanoparticle suspensions from melt emulsification for enhanced drug dissolution. Chemical Engineering & Technology. 2014;37.

28. Bhakay A, Vizzotti E, Li M, Davé R, Bilgili E. Incorporation of fenofibrate nanoparticles prepared by melt emulsification into polymeric films. Journal of Pharmaceutical Innovation. 2016;11(1):53-63.

29. Salazar J, Ghanem A, Müller RH, Möschwitzer JP. Nanocrystals: Comparison of the size reduction effectiveness of a novel combinative method with conventional top-down approaches. European Journal of Pharmaceutics and Biopharmaceutics. 2012;81(1):82-90.

30. Rabinow BE. Nanosuspensions in drug delivery. Nature Reviews Drug Discovery. 2004;3(9):785-96.

31. Peltonen L, Hirvonen J. Pharmaceutical nanocrystals by nanomilling: Critical process parameters, particle fracturing and stabilization methods. Journal of Pharmacy and Pharmacology. 2010;62(11):1569-79.

32. Bilgili E, Guner G. Mechanistic modeling of wet stirred media milling for production of drug nanosuspensions. American Association of Pharmaceutical Scientists PharmSciTech. 2020;22(1):2.

33. Li M, Alvarez P, Bilgili E. A microhydrodynamic rationale for selection of bead size in preparation of drug nanosuspensions via wet stirred media milling. International Journal of Pharmaceutics. 2017;524(1):178-92.

34. Eskin D, Zhupanska O, Hamey R, Moudgil B, Scarlett B. Microhydrodynamics of stirred media milling. Powder Technology. 2005;156(2):95-102.

35. Kwade A. Wet comminution in stirred media mills — research and its practical application. Powder Technology. 1999;105(1):14-20.

36. Merisko-Liversidge E, Liversidge GG, Cooper ER. Nanosizing: A formulation approach for poorly-water-soluble compounds. European Journal of Pharmaceutical Sciences. 2003;18(2):113-20.

37. Bhakay A, Davé R, Bilgili E. Recovery of bcs class II drugs during aqueous redispersion of core–shell type nanocomposite particles produced via fluidized bed coating. Powder Technology. 2013;236:221-34.

38. Bitterlich A, Laabs C, Busmann E, Grandeury A, Juhnke M, Bunjes H, Kwade A. Challenges in nanogrinding of active pharmaceutical ingredients. Chemical Engineering & Technology. 2014;37(5):840-6.

39. Cerdeira AM, Mazzotti M, Gander B. Miconazole nanosuspensions: Influence of formulation variables on particle size reduction and physical stability. International Journal of Pharmaceutics. 2010;396(1-2):210-8.

40. Wu L, Zhang J, Watanabe W. Physical and chemical stability of drug nanoparticles. Advanced Drug Delivery Reviews. 2011;63(6):456-69.

41. Ghosh I, Bose S, Vippagunta R, Harmon F. Nanosuspension for improving the bioavailability of a poorly soluble drug and screening of stabilizing agents to inhibit crystal growth. International Journal of Pharmaceutics. 2011;409(1):260-8.

42. Van Eerdenbrugh B, Vermant J, Martens JA, Froyen L, Van Humbeeck J, Augustijns P, Van den Mooter G. A screening study of surface stabilization during the production of drug nanocrystals. Journal of Pharmaceutical Sciences. 2009;98(6):2091-103.

43. George M, Ghosh I. Identifying the correlation between drug/stabilizer properties and critical quality attributes (CQAs) of nanosuspension formulation prepared by wet media milling technology. European Journal of Pharmaceutical Sciences. 2013;48(1):142-52.

44. Choi J-Y, Yoo JY, Kwak H-S, Uk Nam B, Lee J. Role of polymeric stabilizers for drug nanocrystal dispersions. Current Applied Physics. 2005;5(5):472-4.

45. Lee J, Choi JY, Park CH. Characteristics of polymers enabling nano-comminution of water-insoluble drugs. International Journal of Pharmaceutics. 2008;355(1):328-36.

46. Knieke C, Azad MA, Davé RN, Bilgili E. A study of the physical stability of wet media-milled fenofibrate suspensions using dynamic equilibrium curves. Chemical Engineering Research and Design. 2013;91(7):1245-58.

47. Bilgili E, Li M, Afolabi A. Is the combination of cellulosic polymers and anionic surfactants a good strategy for ensuring physical stability of bcs class II drug nanosuspensions? Pharmaceutical Development and Technology. 2016;21(4):499-510.

48. Basa S, Muniyappan T, Karatgi P. Production and in vitro characterization of solid dosage form incorporating drug nanoparticles. Drug Development and Industrial Pharmacy. 2008;34(null):1209.

49. Merisko-Liversidge E, Liversidge GG. Nanosizing for oral and parenteral drug delivery: A perspective on formulating poorly-water soluble compounds using wet media milling technology. Advanced Drug Delivery Reviews. 2011;63(6):427-40.

50. Van Eerdenbrugh B, Van den Mooter G, Augustijns P. Top-down production of drug nanocrystals: Nanosuspension stabilization, miniaturization and transformation into solid products. International Journal of Pharmaceutics. 2008;364(1):64-75.

51. Li M, Lopez N, Bilgili E. A study of the impact of polymer–surfactant in drug nanoparticle coated pharmatose composites on dissolution performance. Advanced Powder Technology. 2016;27(4):1625-36.

52. Yalkowsky SH, Roseman T. Techniques of solubilization of drugs. New York City, NY: Marcel Dekker; 1981.

53. Verma S, Kumar S, Gokhale R, Burgess DJ. Physical stability of nanosuspensions: Investigation of the role of stabilizers on ostwald ripening. International Journal of Pharmaceutics. 2011;406(1):145-52.

54. Azad M, Afolabi A, Bhakay A, Leonardi J, Davé R, Bilgili E. Enhanced physical stabilization of fenofibrate nanosuspensions via wet co-milling with a superdisintegrant and an adsorbing polymer. European Journal of Pharmaceutics and Biopharmaceutics. 2015;94:372-85.

55. Bhakay A, Azad M, Vizzotti E, Dave RN, Bilgili E. Enhanced recovery and dissolution of griseofulvin nanoparticles from surfactant-free nanocomposite microparticles incorporating wet-milled swellable dispersants. Drug Development and Industrial Pharmacy. 2014;40(11):1509-22.

56. Azad M, Arteaga C, Abdelmalek B, Davé R, Bilgili E. Spray drying of drug-swellable dispersant suspensions for preparation of fast-dissolving, high drug-loaded, surfactant-free nanocomposites. Drug Development and Industrial Pharmacy. 2015;41(10):1617-31.

57. Afolabi A, Akinlabi O, Bilgili E. Impact of process parameters on the breakage kinetics of poorly water-soluble drugs during wet stirred media milling: A microhydrodynamic view. European Journal of Pharmaceutical Sciences. 2014;51:75-86.

58. Bilgili E, Dave R, Bhakay A, Azad M. Systems and methods for superdisintegrant-based composite particles for dispersion and dissolution of agents. US Patent No. 9,452,107. Washington, DC: U.S. Patent and Trademark Office; 2016.

59. Malamatari M, Taylor KMG, Malamataris S, Douroumis D, Kachrimanis K. Pharmaceutical nanocrystals: Production by wet milling and applications. Drug Discovery Today. 2018;23(3):534-47.

60. Afolabi A. Batch and continuous production of stable dense suspensions of drug nanoparticles in a wet stirred media mill. PhD Thesis, New Jersey Institute of Technology, Otto H York Department of Chemical,Department of Chemical, Biological and Pharmaceutical Engineering, Newark, NJ, USA, 2013. 2013.

61. Kawatra SK. Advances in comminution. Littleton, CO: Society for Mining, Metallurgy, and Exploration; 2006.

62. Bilgili E, Afolabi A. A combined microhydrodynamics–polymer adsorption analysis for elucidation of the roles of stabilizers in wet stirred media milling. International Journal of Pharmaceutics. 2012;439(1):193-206.

63. Li M, Yaragudi N, Afolabi A, Dave R, Bilgili E. Sub-100nm drug particle suspensions prepared via wet milling with low bead contamination through novel process intensification. Chemical Engineering Science. 2015;130:207-20.

64. Juhnke M, Märtin D, John E. Generation of wear during the production of drug nanosuspensions by wet media milling. European Journal of Pharmaceutics and Biopharmaceutics. 2012;81(1):214-22.

65. Siewert C, Moog R, Alex R, Kretzer P, Rothenhäusler B. Process and scaling parameters for wet media milling in early phase drug development: A knowledge based approach. European Journal of Pharmaceutical Sciences. 2018;115:126-31.

66. Bilgili E, Capece M, Afolabi A. Modeling of milling processes via DEM, PBM, and microhydrodynamics. In: Pandey P, Bharadwaj R, editors. Predictive modeling of pharmaceutical unit operations. Sawston, Cambridge, UK: Woodhead Publishing; 2016. p. 159-203.

67. Nakach M, Authelin J-R, Tadros T, Galet L, Chamayou A. Engineering of nano-crystalline drug suspensions: Employing a physico-chemistry based stabilizer selection methodology or approach. International Journal of Pharmaceutics. 2014;476(1):277-88.

68. Shah S, Parmar B, Soniwala M, Chavda J. Design, optimization, and evaluation of lurasidone hydrochloride nanocrystals. American Association of Pharmaceutical Scientists PharmSciTech. 2016;17(5):1150-8.

69. Singh SK, Srinivasan KK, Gowthamarajan K, Singare DS, Prakash D, Gaikwad NB. Investigation of preparation parameters of nanosuspension by top-down media milling to improve the dissolution of poorly water-soluble glyburide. European Journal of Pharmaceutics and Biopharmaceutics. 2011;78(3):441-6.

70. Nakach M, Authelin J-R, Perrin M-A, Lakkireddy HR. Comparison of high pressure homogenization and stirred bead milling for the production of nano-crystalline suspensions. International Journal of Pharmaceutics. 2018;547(1):61-71.

71. Singare DS, Marella S, Gowthamrajan K, Kulkarni GT, Vooturi R, Rao PS. Optimization of formulation and process variable of nanosuspension: An industrial perspective. International Journal of Pharmaceutics. 2010;402(1):213-20.

72. Mahesh KV, Singh SK, Gulati M. A comparative study of top-down and bottom-up approaches for the preparation of nanosuspensions of glipizide. Powder Technology. 2014;256:436-49.

73. Shah SR, Parikh RH, Chavda JR, Sheth NR. Glibenclamide nanocrystals for bioavailability enhancement: Formulation design, process optimization, and pharmacodynamic evaluation. Journal of Pharmaceutical Innovation. 2014;9(3):227-37.

74. Ahuja BK, Jena SK, Paidi SK, Bagri S, Suresh S. Formulation, optimization and in vitro–in vivo evaluation of febuxostat nanosuspension. International Journal of Pharmaceutics. 2015;478(2):540-52.

75. Sharma OP, Patel V, Mehta T. Design of experiment approach in development of febuxostat nanocrystal: Application of soluplus® as stabilizer. Powder Technology. 2016;302:396-405.

76. Patel PJ, Gajera BY, Dave RH. A quality-by-design study to develop nifedipine nanosuspension: Examining the relative impact of formulation variables, wet media milling process parameters and excipient variability on drug product quality attributes. Drug Development & Industrial Pharmacy. 2018;44(12):1942-52.

77. Jog R, Burgess DJ. Comprehensive quality by design approach for stable nanocrystalline drug products. International Journal of Pharmaceutics. 2019;564:426-60.

78. Zuo J, de Araujo GLB, Stephano MA, Zuo Z, Bou-Chacra NA, Löbenberg R. Design space approach in the development of esculetin nanocrystals by a small-scale wet-bead milling process. Journal of Drug Delivery Science and Technology. 2020;55:101486.

79. Ding Z, Wang L, Xing Y, Zhao Y, Wang Z, Han J. Enhanced oral bioavailability of celecoxib nanocrystalline solid dispersion based on wet media milling technique: Formulation, optimization and in vitro/in vivo evaluation. Pharmaceutics. 2019;11(7):328.

80. Karakucuk A, Celebi N. Investigation of formulation and process parameters of wet media milling to develop etodolac nanosuspensions. Pharmaceutical Research. 2020

81. Lehocký R, Pěček D, Štěpánek F. Scale-up from batch to flow-through wet milling process for injectable depot formulation. European Journal of Pharmaceutical Sciences. 2016;95:122-9.

82. Nakach M, Authelin J-R, Agut C. New approach and practical modelling of bead milling process for the manufacturing of nanocrystalline suspensions. Journal of Pharmaceutical Sciences. 2017;106(7):1889-904.

83. Medarević D, Djuriš J, Ibrić S, Mitrić M, Kachrimanis K. Optimization of formulation and process parameters for the production of carvedilol nanosuspension by wet media milling. International Journal of Pharmaceutics. 2018;540(1):150-61.

84. Kumar S, Shen J, Zolnik B, Sadrieh N, Burgess DJ. Optimization and dissolution performance of spray-dried naproxen nano-crystals. International Journal of Pharmaceutics. 2015;486(1):159-66.

85. Parmar K, Patel J, Sheth N. Formulation and optimization of embelin nanosuspensions using central composite design for dissolution enhancement. Journal of Drug Delivery Science and Technology. 2015;29:1-7.

86. Patel J, Dhingani A, Garala K, Raval M, Sheth N. Design and development of solid nanoparticulate dosage forms of telmisartan for bioavailability enhancement by integration of experimental design and principal component analysis. Powder Technology. 2014;258:331-43.

87. Annapragada A, Adjei A. Numerical simulation of milling processes as an aid to process design. International Journal of Pharmaceutics. 1996;136(1):1-11.

88. Cerdeira AM, Gander B, Mazzotti M. Role of milling parameters and particle stabilization on nanogrinding of drug substances of similar mechanical properties. Chemical Engineering & Technology. 2011;34(9):1427-38.

89. Monteiro A, Afolabi A, Bilgili E. Continuous production of drug nanoparticle suspensions via wet stirred media milling: A fresh look at the rehbinder effect. Drug Development and Industrial Pharmacy. 2013;39(2):266-83.

90. Parker N, Rahman M, Bilgili E. Impact of media material and process parameters on breakage kinetics–energy consumption during wet media milling of drugs. European Journal of Pharmaceutics and Biopharmaceutics. 2020;153:52-67.

91. Bel Fadhel H, Frances C, Mamourian A. Investigations on ultra-fine grinding of titanium dioxide in a stirred media mill. Powder Technology. 1999;105(1):362-73.

92. Varinot C, Berthiaux H, Dodds J. Prediction of the product size distribution in associations of stirred bead mills. Powder Technology. 1999;105(1):228-36.

93. Frances C. On modelling of submicronic wet milling processes in bead mills. Powder Technology. 2004;143-144:253-63.

94. Bilgili E, Hamey R, Scarlett B. Nano-milling of pigment agglomerates using a wet stirred media mill: Elucidation of the kinetics and breakage mechanisms. Chemical Engineering Science. 2006;61(1):149-57.

95. Sommer M, Stenger F, Peukert W, Wagner NJ. Agglomeration and breakage of nanoparticles in stirred media mills—a comparison of different methods and models. Chemical Engineering Science. 2006;61(1):135-48.

96. Hennart SLA, Wildeboer WJ, van Hee P, Meesters GMH. Identification of the grinding mechanisms and their origin in a stirred ball mill using population balances. Chemical Engineering Science. 2009;64(19):4123-30.

97. Li H, Ndjamo A, Sauriol P, Patience GS. Optimization of lifepo4 wet media milling and regressive population balance modeling. Advanced Powder Technology. 2017;28(3):1000-7.

98. Hennart SLA, van Hee P, Drouet V, Domingues MC, Wildeboer WJ, Meesters GMH. Characterization and modeling of a sub-micron milling process limited by agglomeration phenomena. Chemical Engineering Science. 2012;71:484-95.

99. Theuerkauf J, Schwedes J. Theoretical and experimental investigation on particle and fluid motion in stirred media mills. Powder Technology. 1999;105(1):406-12.

100. Gers R, Anne-Archard D, Climent E, Legendre D, Frances C. Two colliding grinding beads: Experimental flow fields and particle capture efficiency. Chemical Engineering & Technology. 2010;33(9):1438-46.

101. Gers R, Climent E, Legendre D, Anne-Archard D, Frances C. Numerical modelling of grinding in a stirred media mill: Hydrodynamics and collision characteristics. Chemical Engineering Science. 2010;65(6):2052-64.

102. Winardi S, Widiyastuti W, Septiani EL, Nurtono T. Simulation of solid-liquid flows in a stirred bead mill based on computational fluid dynamics (CFD). Materials Research Express. 2018;5(5):054002.

103. Jayasundara CT, Yang RY, Yu AB. Discrete particle simulation of particle flow in a stirred mill: Effect of mill properties and geometry. Industrial & Engineering Chemistry Research. 2012;51(2):1050-61.

104. Jayasundara CT, Yang RY, Yu AB, Curry D. Discrete particle simulation of particle flow in isamill—effect of grinding medium properties. Chemical Engineering Journal. 2008;135(1):103-12.

105. Yang RY, Jayasundara CT, Yu AB, Curry D. DEM simulation of the flow of grinding media in isamill. Minerals Engineering. 2006;19(10):984-94.

106. Gudin D, Kano J, Saito F. Effect of the friction coefficient in the discrete element method simulation on media motion in a wet bead mill. Advanced Powder Technology. 2007;18(5):555-65.

107. Gudin D, Turczyn R, Mio H, Kano J, Saito F. Simulation of the movement of beads by the DEM with respect to the wet grinding process. AIChE Journal. 2006;52(10):3421-6.

108. Yamamoto Y, Soda R, Kano J, Saito F. DEM simulation of bead motion during wet bead milling using an enlarged particle model. International Journal of Mineral Processing. 2012;114-117:93-9.

109. Yamamoto Y, Soda R, Kano J, Saito F. Application of DEM modified with enlarged particle model to simulation of bead motion in a bead mill. Particuology. 2014;14:103-8.

110. Vocciante M, Trofa M, D'Avino G, Reverberi A. Nanoparticles synthesis in wet-operating stirred media: Preliminary investigation with dem simulations. Chemical Engineering Transactions. 2019;73:31-6.

111. Schilde C, Beinert S, Kwade A. Comparison of the micromechanical aggregate properties of nanostructured aggregates with the stress conditions during stirred media milling. Chemical Engineering Science. 2011;66(21):4943-52.

112. Jayasundara CT, Yang RY, Guo BY, Yu AB, Rubenstein J. Effect of slurry properties on particle motion in isamills. Minerals Engineering. 2009;22(11):886-92.

113. Jayasundara CT, Yang RY, Guo BY, Yu AB, Govender I, Mainza A, Westhuizen Avd, Rubenstein J. CFD–DEM modelling of particle flow in isamills – comparison between simulations and pept measurements. Minerals Engineering. 2011;24(3):181-7.

114. Jayasundara CT, Yang RY, Yu AB. Effect of the size of media on grinding performance in stirred mills. Minerals Engineering. 2012;33:66-71.

115. Nishiura D, Sakaguchi H, Shimosaka A. Wet dispersion mechanism of fine aggregates in multiphase flow with solid beads under simple shear. American Institute of Chemical Engineering Journal. 2014;60(12):4076-85.

116. Yamada Y, Sakai M. Lagrangian–lagrangian simulations of solid–liquid flows in a bead mill. Powder Technology. 2013;239:105-14.

117. Larsson S, Pålsson BI, Parian M, Jonsén P. A novel approach for modelling of physical interactions between slurry, grinding media and mill structure in wet stirred media mills. Minerals Engineering. 2020;148:106180.

118. Cleary PW, Sinnott MD. Computational prediction of performance for a full scale isamill: Part 2 – wet models of charge and slurry transport. Minerals Engineering. 2015;79:239-60.

119. Ndimande CB, Cleary PW, Mainza AN, Sinnott MD. Using two-way coupled DEM-SPH to model an industrial scale stirred media detritor. Minerals Engineering. 2019;137:259-76.

120. Oliveira ALR, Rodriguez VA, de Carvalho RM, Powell MS, Tavares LM. Mechanistic modeling and simulation of a batch vertical stirred mill. Minerals Engineering. 2020;156:106487.

121. Beinert S, Fragnière G, Schilde C, Kwade A. Multiscale simulation of fine grinding and dispersing processes: Stressing probability, stressing energy and resultant breakage rate. Advanced Powder Technology. 2018;29(3):573-83.

122. Beinert S, Fragnière G, Schilde C, Kwade A. Analysis and modelling of bead contacts in wet-operating stirred media and planetary ball mills with CFD–DEM simulations. Chemical Engineering Science. 2015;134:648-62.

123. Beinert S, Schilde C, Gronau G, Kwade A. CFD-discrete element method simulations combined with compression experiments to characterize stirred-media mills. Chemical Engineering & Technology. 2014;37(5):770-8.

124. Fragnière G, Beinert S, Overbeck A, Kampen I, Schilde C, Kwade A. Predicting effects of operating condition variations on breakage rates in stirred media mills. Chemical Engineering Research and Design. 2018;138:433-43.

125. Breitung-Faes S, Kwade A. Mill, material, and process parameters – a mechanistic model for the set-up of wet-stirred media milling processes. Advanced Powder Technology. 2019;30(8):1425-33.

126. Breitung-Faes S, Kwade A. Use of an enhanced stress model for the optimization of wet stirred media milling processes. Chemical Engineering & Technology. 2014;37(5):819-26.

127. Flach F, Breitung-Faes S, Kwade A. Model based process optimization of nanosuspension preparation via wet stirred media milling. Powder Technology. 2018;331:146-54.

128. Flach F, Konnerth C, Peppersack C, Schmidt J, Damm C, Breitung-Faes S, Peukert W, Kwade A. Impact of formulation and operating parameters on particle size and grinding media wear in wet media milling of organic compounds – a case study for pyrene. Advanced Powder Technology. 2016;27(6):2507-19.

129. Ohenoja K, Illikainen M. Effect of operational parameters and stress energies on stirred media milling of talc. Powder Technology. 2015;283:254-9.

130. Knieke C, Romeis S, Peukert W. Influence of process parameters on breakage kinetics and grinding limit at the nanoscale. American Institute of Chemical Engineering Journal. 2011;57(7):1751-8.

131. Strobel A, Schwenger J, Wittpahl S, Schmidt J, Romeis S, Peukert W. Assessing the influence of viscosity and milling bead size on the stressing conditions in a stirred media mill by single particle probes. Chemical Engineering Research and Design. 2018;136:859-69.

132. Eskin D, Zhupanska O, Hamey R, Moudgil B, Scarlett B. Microhydrodynamic analysis of nanogrinding in stirred media mills. American Institute of Chemical Engineering Journal. 2005;51(5):1346-58.

133. Gidaspow D. Multiphase flow and fluidization: Continuum and kinetic theory descriptions. Cambridge, MA: Academic press; 1994.

134. Wylie JJ, Koch DL, Ladd AJC. Rheology of suspensions with high particle inertia and moderate fluid inertia. Journal of Fluid Mechanics. 2003;480:95-118.

135. Sangani AS, Mo G, Tsao HK, Koch DL. Simple shear flows of dense gas-solid suspensions at finite stokes numbers. Journal of Fluid Mechanics. 1996;313:309-41.

136. Carnahan NF, Starling KE. Equation of state for nonattracting rigid spheres. The Journal of Chemical Physics. 1969;51(2):635-6.

137. Mannheim V. Empirical and scale-up modeling in stirred ball mills. Chemical Engineering Research and Design. 2011;89(4):405-9.

138. Azad M, Guner G, Afolabi A, Davé R, Bilgili E. Impact of solvents during wet stirred media milling of cross-linked biopolymer suspensions. Advanced Powder Technology. 2021;32(12):4562-75.

139. Maughan MR, Carvajal MT, Bahr DF. Nanomechanical testing technique for millimeter-sized and smaller molecular crystals. International Journal of Pharmaceutics. 2015;486(1):324-30.

140. Hertz H, Jones D, Schott G. Miscellaneous papers by H. Hertz. Jones and Schott, London, Macmillan. 1896.

141. Strobel A, Romeis S, Wittpahl S, Herre P, Schmidt J, Peukert W. Characterization of stressing conditions in mills – a comprehensive research strategy based on well-characterized model particles. Powder Technology. 2017;305:652-61.

142. Bilgili E. Personal communication with GlaxoSmithKline and Tridiagonal. 2021.

143. Bilgili E, Scarlett B. Population balance modeling of non-linear effects in milling processes. Powder Technology. 2005;153(1):59-71.

144. Stražišar J, Runovc F. Kinetics of comminution in micro- and sub-micrometer ranges. International Journal of Mineral Processing. 1996;44-45:673-82.

145. Wang S, Liu G, Lu H, Yinghua B, Ding J, Zhao Y. Prediction of radial distribution function of particles in a gas−solid fluidized bed using discrete hard-sphere model. Industrial & Engineering Chemistry Research. 2009;48(3):1343-52.

146. Ma D, Ahmadi G. An equation of state for dense rigid sphere gases. The Journal of Chemical Physics. 1986;84(6):3449-50.

147. Liu G. Application of the two-fluid model with kinetic theory of granular flow in liquid–solid fluidized beds. Granularity in Materials Science. 2018:2.

148. Lun CKK, Savage SB. A simple kinetic theory for granular flow of rough, inelastic, spherical particles. Journal of Applied Mechanics. 1987;54(1):47-53.

149. Guner G, Kannan M, Berrios M, Bilgili E. Use of bead mixtures as a novel process optimization approach to nanomilling of drug suspensions. Pharmaceutical Research. 2021;38(7):1279-96.

150. Guner G, Yilmaz D, Bilgili E. Kinetic and microhydrodynamic modeling of fenofibrate nanosuspension production in a wet stirred media mill. Pharmaceutics. 2021;13(7):1055.

151. Azad M, Guner G, Afolabi A, Davé R, Bilgili E. Impact of solvents during wet stirred media milling of cross-linked biopolymer suspensions. Advanced Powder Technology. 2021;32:4562–75.

152. Bitterlich A, Laabs C, Krautstrunk I, Dengler M, Juhnke M, Grandeury A, Bunjes H, Kwade A. Process parameter dependent growth phenomena of naproxen nanosuspension manufactured by wet media milling. European Journal of Pharmaceutics and Biopharmaceutics. 2015;92:171-9.

153. Van Eerdenbrugh B, Froyen L, Van Humbeeck J, Martens JA, Augustijns P, Van den Mooter G. Drying of crystalline drug nanosuspensions—the importance of surface hydrophobicity on dissolution behavior upon redispersion. European Journal of Pharmaceutical Sciences. 2008;35(1-2):127-35.

154. Aleandri S, Schönenberger M, Niederquell A, Kuentz M. Temperature-induced surface effects on drug nanosuspensions. Pharmaceutical Research. 2018;35(3):1-11.

155. NISSO: Nisso hpc | nippon soda co., ltd. Nissoexcipients.Com. . https://www.nissoexcipients.com/hpc-e/care_stable (2022). Accessed May 12, 2022.

156. Beirowski J, Inghelbrecht S, Arien A, Gieseler H. Freeze-drying of nanosuspensions, part 3: Investigation of factors compromising storage stability of highly concentrated drug nanosuspensions. Journal of Pharmaceutical Sciences. 2012;101(1):354-62.

157. Cerdeira AM, Mazzotti M, Gander B. Formulation and drying of miconazole and itraconazole nanosuspensions. International Journal of Pharmaceutics. 2013;443(1-2):209-20.

158. Zuo B, Sun Y, Li H, Liu X, Zhai Y, Sun J, He Z. Preparation and in vitro/in vivo evaluation of fenofibrate nanocrystals. International Journal of Pharmaceutics. 2013;455(1-2):267-75.

159. Bose S, Schenck D, Ghosh I, Hollywood A, Maulit E, Ruegger C. Application of spray granulation for conversion of a nanosuspension into a dry powder form. European Journal of Pharmaceutical Sciences. 2012;47(1):35-43.

160. Kumar S, Xu X, Gokhale R, Burgess DJ. Formulation parameters of crystalline nanosuspensions on spray drying processing: A doe approach. International Journal of Pharmaceutics. 2014;464(1-2):34-45.

161. Toziopoulou F, Malamatari M, Nikolakakis I, Kachrimanis K. Production of aprepitant nanocrystals by wet media milling and subsequent solidification. International Journal of Pharmaceutics. 2017;533(2):324-34.

162. Garcia F, Le Bolay N, Frances C. Changes of surface and volume properties of calcite during a batch wet grinding process. Chemical Engineering Journal. 2002;85(2-3):177-87.

163. Descamps M, Willart J. Perspectives on the amorphisation/milling relationship in pharmaceutical materials. Advanced Drug Delivery Reviews. 2016;100:51-66.

164. Meng T, Qiao F, Ma S, Gao T, Li L, Hou Y, Yang J. Exploring the influence factors and improvement strategies of drug polymorphic transformation combined kinetic and thermodynamic perspectives during the formation of nanosuspensions. Drug Development and Industrial Pharmacy. 2022(just-accepted):1-44.

165. Guner G, Yilmaz D, Eskin D, Bilgili E. Effects of bead packing limit concentration on microhydrodynamics-based prediction of breakage kinetics in wet stirred media milling. Powder Technology. 2022;403:117433.

166. Guner G, Elashri S, Mehaj M, Seetharaman N, Yao HF, Clancy DJ, Bilgili E. An enthalpy-balance model for timewise evolution of temperature during wet stirred media milling of drug suspensions. Pharmaceutical Research. 2022;39(9):2065-82.

167. Patel CM, Chakraborty M, Murthy Z. Enhancement of stirred media mill performance by a new mixed media grinding strategy. Journal of Industrial and Engineering Chemistry. 2014;20(4):2111-8.

168. Altun O, Prziwara P, Breitung-Faes S, Kwade A. Impacts of process and design conditions of dry stirred milling on the shape of product size distribution. Minerals Engineering. 2021;163:106806.

169. Jamzad S, Fassihi R. Role of surfactant and pH on dissolution properties of fenofibrate and glipizide—a technical note. American Association of Pharmaceutical Scientists PharmSciTech. 2006;7(2):17-22.

170. Capece M, Bilgili E, Davé R. Insight into first-order breakage kinetics using a particle-scale breakage rate constant. Chemical Engineering Science. 2014;117:318-30.

171. Fuerstenau DW, De A, Kapur PC. Linear and nonlinear particle breakage processes in comminution systems. International Journal of Mineral Processing. 2004;74:S317-S27.

172. Cho H, Waters MA, Hogg R. Investigation of the grind limit in stirred-media milling. International Journal of Mineral Processing. 1996;44-45:607-15.

173. H Scott F. Elements of chemical reaction engineering. Hoboken, NJ: Prentice Hall Profesional; 2006.

174. Barani K, Balochi H. First-order and second-order breakage rate of coarse particles in ball mill grinding. Physicochemical Problems of Mineral Processing. 2016;52.

175. Austin LG, Bagga P. An analysis of fine dry grinding in ball mills. Powder Technology. 1981;28(1):83-90.

176. Austin LG, Shah J, Wang J, Gallagher E, Luckie PT. An analysis of ball-and-race milling. Part i. The hardgrove mill. Powder Technology. 1981;29(2):263-75.

177. Cao J, Cheng Z, Fang Y, Jing H, Huang J, Wang Y. Simulation and experimental studies on fluidization properties in a pressurized jetting fluidized bed. Powder Technology. 2008;183(1):127-32.

178. Tatsumi S, Murayama Y, Hayakawa H, Sano M. Experimental study on the kinetics of granular gases under microgravity. Journal of Fluid Mechanics. 2009;641:521-39.

179. Ashby MF, Cebon D. Materials selection in mechanical design. Le Journal de Physique IV. 1993;3(7):1-9.

180. Srikar VT, Turner KT, Andrew Ie TY, Spearing SM. Structural design considerations for micromachined solid-oxide fuel cells. Journal of Power Sources. 2004;125(1):62-9.

181. Geißler S. Small scale processing of nanoscopic formulations for preclinical development of poorly soluble compounds. Chemistry, Pharmacy and Earth Sciences. Vürzburg, Germany: Johannes Gutenberg University; 2016.

182. James G, Witten D, Hastie T, Tibshirani R. An introduction to statistical learning. New York City, NY: Springer; 2013.

183. Team RC. R: A language and environment for statistical computing. 2013.

184. Ginestet C. Ggplot2: Elegant graphics for data analysis. Wiley Online Library; 2011.

185. Onoue S, Takahashi H, Kawabata Y, Seto Y, Hatanaka J, Timmermann B, Yamada S. Formulation design and photochemical studies on nanocrystal solid dispersion of curcumin with improved oral bioavailability. Journal of Pharmaceutical Sciences. 2010;99(4):1871-81.

186. Konnerth C, Damm C, Schmidt J, Peukert W. Mechanical activation of trans-stilbene during wet grinding. Advanced Powder Technology. 2014;25(6):1808-16.

187. Feng T, Pinal R, Carvajal MT. Process induced disorder in crystalline materials: Differentiating defective crystals from the amorphous form of griseofulvin. Journal of Pharmaceutical Sciences. 2008;97(8):3207-21.

188. Żarów A, Zhou B, Wang X, Pinal R, Iqbal Z. Spectroscopic and x-ray diffraction study of structural disorder in cryomilled and amorphous griseofulvin. Applied Spectroscopy. 2011;65(2):135-43.

189. Diemer RB. Applications of the linear mass-sectional breakage population balance to various milling process configurations. American Association of Pharmaceutical Scientists PharmSciTech. 2021;22(3):1-17.

190. Savage SB. Streaming motions in a bed of vibrationally fluidized dry granular material. Journal of Fluid Mechanics. 1988;194:457-78.

191. Kwan CC, Chen YQ, Ding YL, Papadopoulos DG, Bentham AC, Ghadiri M. Development of a novel approach towards predicting the milling behaviour of pharmaceutical powders. European Journal of Pharmaceutical Sciences. 2004;23(4):327-36.

192. Vogel L, Peukert W. Breakage behaviour of different materials—construction of a mastercurve for the breakage probability. Powder Technology. 2003;129(1):101-10.

193. Nagata S. Mixing: Principles and applications. Ultimo, Australia: Halsted press; 1975.

194. Gillies RG, Shook CA. Modelling high concentration settling slurry flows. The Canadian Journal of Chemical Engineering. 2000;78(4):709-16.

195. Epelle EI, Gerogiorgis DI. CFD modelling and simulation of drill cuttings transport efficiency in annular bends: Effect of particle sphericity. Journal of Petroleum Science and Engineering. 2018;170:992-1004.

196. Cornelissen JT, Taghipour F, Escudié R, Ellis N, Grace JR. CFD modelling of a liquid–solid fluidized bed. Chemical Engineering Science. 2007;62(22):6334-48.

197. Fogel'Son R, Likhachev E. Temperature dependence of viscosity. Technical Physics. 2001;46(8):1056-9.

198. Schönstedt B, Jacob H-J, Schilde C, Kwade A. Scale-up of the power draw of inline-rotor–stator mixers with high throughput. Chemical Engineering Research and Design. 2015;93:12-20.

199. Green DW, Perry RH. Perry's chemical engineers' handbook. McGraw-Hill Education; 2008.

200. Watterson S, Hudson S, Svärd M, Rasmuson ÅC. Thermodynamics of fenofibrate and solubility in pure organic solvents. Fluid Phase Equilibria. 2014;367:143-50.

201. Joshi H, Wilson T. Calorimetric studies of dissolution of hydroxypropyl methylcellulose e5 (HPMC e5) in water. Journal of Pharmaceutical Sciences. 1993;82(10):1033-8.

202. Tojo T, Atake T, Mori T, Yamamura H. Heat capacity and thermodynamic functions of zirconia and yttria-stabilized zirconia. The Journal of Chemical Thermodynamics. 1999;31(7):831-45.

203. Coleman T, Branch MA, Grace A. Optimization toolbox. For Use with MATLAB User's Guide for MATLAB 5, Version 2, Relaese II. 1999.

204. Pedregosa F, Varoquaux G, Gramfort A, Michel V, Thirion B, Grisel O, Blondel M, Prettenhofer P, Weiss R, Dubourg V. Scikit-learn: Machine learning in python. the Journal of machine Learning research. 2011;12:2825-30.

205. Li M, Alvarez P, Orbe P, Bilgili E. Multi-faceted characterization of wet-milled griseofulvin nanosuspensions for elucidation of aggregation state and stabilization mechanisms. Aaps Pharmscitech. 2018;19(4):1789-801.

206. Guner G, Seetharaman N, Elashri S, Mehaj M, Bilgili E. Analysis of heat generation during the production of drug nanosuspensions in a wet stirred media mill. International Journal of Pharmaceutics. 2022;624:122020.

207. Barrios ANS, Silva JBC, Rodrigues AR, Coelho RT, Braghini Junior A, Matsumoto H. Modeling heat transfer in die milling. Applied Thermal Engineering. 2014;64(1):108-16.

208. Xi SQ, Zhou JG, Wang XT. Research on temperature rise of powder during high energy ball milling. Powder Metallurgy. 2007;50(4):367-73.

209. Bilgili E, Rahman M, Palacios D, Arevalo F. Impact of polymers on the aggregation of wet-milled itraconazole particles and their dissolution from spray-dried nanocomposites. Advanced Powder Technology. 2018;29(12):2941-56.

210. Hecq J, Deleers M, Fanara D, Vranckx H, Amighi K. Preparation and characterization of nanocrystals for solubility and dissolution rate enhancement of nifedipine. International Journal of Pharmaceutics. 2005;299(1):167-77.

211. Prasher CL. Crushing and grinding process handbook. Hoboken, NJ: Wiley; 1987.

212. Kataoka M, Masaoka Y, Yamazaki Y, Sakane T, Sezaki H, Yamashita S. In vitro system to evaluate oral absorption of poorly water-soluble drugs: Simultaneous analysis on dissolution and permeation of drugs. Pharmaceutical Research. 2003;20(10):1674-80.

213. Yue J, Klein B. Effects of bead size on ultrafine grinding in a stirred bead mill. In: Kawatra SK, editor. Advances in comminution. Littleton, CO: Society for Mining, Metallurgy, and Exploration, Inc.; 2006. p. 87-98.

214. Iddir H, Arastoopour H. Modeling of multitype particle flow using the kinetic theory approach. AIChE Journal. 2005;51(6):1620-32.

215. Fan R, Fox RO. Segregation in polydisperse fluidized beds: Validation of a multi-fluid model. Chemical Engineering Science. 2008;63(1):272-85.

216. Shao J. Linear model selection by cross-validation. Journal of the American statistical Association. 1993;88(422):486-94.

217. Molinaro AM, Simon R, Pfeiffer RM. Prediction error estimation: A comparison of resampling methods. Bioinformatics. 2005;21(15):3301-7.

218. Geankoplis CJ, Hersel AA, Lepek DH. Transport processes and separation process principles. Prentice hall Boston, MA, USA; 2018.

219. Zhao H, Yu F, Bennett TD, Wadley HNG. Morphology and thermal conductivity of yttria-stabilized zirconia coatings. Acta Materialia. 2006;54(19):5195-207.

220. Peet M, Hasan H, Bhadeshia H. Prediction of thermal conductivity of steel. International Journal of Heat and Mass Transfer. 2011;54(11-12):2602-8.

221. Khan A, Ali HM, Nazir R, Ali R, Munir A, Ahmad B, Ahmad Z. Experimental investigation of enhanced heat transfer of a car radiator using ZnO nanoparticles in H2O–ethylene glycol mixture. Journal of Thermal Analysis and Calorimetry. 2019;138(5):3007-21.

222. Schlichting K, Padture N, Klemens P. Thermal conductivity of dense and porous yttria-stabilized zirconia. Journal of Materials Science. 2001;36(12):3003-10.

223. Ramires ML, Nieto de Castro CA, Nagasaka Y, Nagashima A, Assael MJ, Wakeham WA. Standard reference data for the thermal conductivity of water. Journal of Physical and Chemical Reference Data. 1995;24(3):1377-81.

224. Bohne D, Fischer S, Obermeier E. Thermal, conductivity, density, viscosity, and prandtl-numbers of ethylene glycol-water mixtures. Berichte der Bunsengesellschaft für physikalische Chemie. 1984;88(8):739-42.